

Decoding the Impact of Obesity Long Noncoding RNAs  
on Murine Liver Energy Homeostasis

Inaugural-Dissertation

zur

Erlangung des Doktorgrades

der Mathematisch-Naturwissenschaftlichen Fakultät

der Universität zu Köln



vorgelegt von

Nils Rouven Hansmeier

aus Beckum

Köln, Oktober 2018

Berichterstatter:

Prof. Dr. Jan-Wilhelm Kornfeld

Prof. Dr. Aleksandra Trifunovic

Tag der mündlichen Prüfung:

26. 11. 2018

Die vorliegende Arbeit entstand auf Anregung und unter Leitung von

Prof. Dr. Jan-Wilhelm Kornfeld

am Max-Planck-Institut für Stoffwechselforschung

in Köln



---

MAX PLANCK INSTITUTE  
FOR METABOLISM RESEARCH  
COLOGNE

## Table of contents

List of abbreviations	V
List of figures	VI
Abstract	VII
Chapter 1 - Introduction	1
1.1. The obesity pandemic - worldwide burden of the 21st century	1
1.1.1. Comorbidities of the global obesity pandemic	2
1.1.2. Obesity-associated metabolic syndrome and type 2 diabetes mellitus	3
1.2. The liver - central regulator of energy homeostasis	4
1.2.1. Hepatic regulation of glucose homeostasis	5
1.2.2. Molecular mechanisms of hepatic energy homeostasis	6
1.2.2.1. Glucose uptake and release	7
1.2.2.2. Hepatic gluconeogenesis	7
1.2.2.3. Fatty acid beta-oxidation	9
1.2.2.4. Fatty acid synthesis	10
1.2.2.5. Insulin signaling in hepatocytes	10
1.3. The noncoding genome - a neglected layer of genomic regulators	13
1.3.1. Regulation of hepatic energy homeostasis by long noncoding RNAs	15
1.3.2. CRISPR/Cas9-mediated genome engineering	17
1.3.3. The therapeutical potential of RNA interference-based agents	18
1.4. Research objectives	19
Chapter 2 - Materials	20
2.1. General materials	20
2.2. Technical equipment	22
2.3. Chemicals	23
2.4. Molecular biology reagents	26
2.5. Antibodies	27
2.6. PCR primer	28
2.7. Primer for SYBR™ Green Quantitative PCR	30
2.8. TaqMan® Assays	32
2.9. RNA Oligonucleotides	32
2.10. Antisense Locked Nucleic Acid (LNA™) GapmeRs	33
2.11. Chromatin immunoprecipitation sequencing (ChIP-Seq) data	33
2.12. Human Liver Biopsies	33
2.13. Software	34

Chapter 3 - Methods	36
3.1. Molecular biological methods	36
3.1.1. Polymerase chain reaction (PCR)	36
3.1.2. Agarose gel electrophoresis	36
3.1.3. High fidelity polymerase chain reaction (HiFi-PCR)	37
3.1.4. Addition of A'-overhangs	37
3.1.5. DNA ligation	38
3.1.6. Transformation of competent bacteria	38
3.1.7. Small scale plasmid DNA isolation	39
3.1.8. Large scale plasmid DNA isolation	40
3.1.9. DNA sequencing	40
3.1.10. Generation of DNA templates for single guide RNA (sgRNA) synthesis	40
3.1.11. DNA extraction from agarose gels	41
3.1.12. sgRNA synthesis	41
3.1.13. DNA digestion	42
3.1.14. sgRNA purification	42
3.1.15. T7 endonuclease I assay	43
3.1.16. Reverse transcription	44
3.1.17. Quantitative real-time PCR (qPCR)	44
3.1.18. RNA sequencing	45
3.1.19. RNA integrity measurement	46
3.2. Cell biological methods	47
3.2.1. Eukaryotic cell culture	47
3.2.2. Mycoplasma test	49
3.2.3. Transfection of primary murine hepatocytes with LNA oligonucleotides	49
3.2.4. Metabolic stimulation of primary murine hepatocytes	50
3.2.5. Transfection of NSC-34 cells with CRISPR/Cas9 components	51
3.3. Biochemical methods	51
3.3.1. Genomic DNA extraction from mouse tails	51
3.3.2. Subcellular fractionation	52
3.3.3. Total RNA isolation from subcellular fractions	52
3.3.4. Total RNA isolation from primary hepatocytes	53
3.3.5. Total RNA isolation from liver tissue	53
3.3.6. Total protein isolation from primary hepatocytes	54
3.3.7. Total protein isolation from liver tissue	54
3.3.8. SDS-PAGE	55



3.3.9. Western blot analysis	56
3.4. Mouse procedures	57
3.4.1. Animal care	57
3.4.2. Experimental mouse models	57
3.4.3. Genotyping of mice	58
3.4.4. Experimental diets	59
3.4.5. In vivo LNA application	59
3.4.6. Assessment of body weight progression	59
3.4.7. Intraperitoneal insulin tolerance test (ITT)	59
3.4.8. Intraperitoneal glucose tolerance test (GTT)	59
3.4.9. Indirect calorimetry analysis	60
3.4.10. Isolation of primary murine hepatocytes	60
3.4.11. Mouse model generation	61
3.5. Computational methods	62
3.5.1. Coding potential predictions	62
3.5.2. GuideRNA design	63
3.5.3. RNA sequencing data analysis	63
Chapter 4 - Results	64
4.1. Hepatic lncRNA expression inversely correlates with mRNA expression in response to metabolic states	64
4.1.1. Transcriptome profiling reveals global hepatic lncRNA downregulation in obesity mouse models	64
4.1.2. Hepatic lncRNA expression is dynamically adapted to organismal energy states	65
4.1.3. Anticorrelative regulation of lncRNAs and mRNAs in human liver biopsies	67
4.2. In vitro screening for metabolically relevant lncRNAs implicated in liver energy homeostasis	69
4.2.1. Identification of liver-enriched lncRNAs regulated upon chronic obesity, food satiety and food deprivation	69
4.2.2. Further characterisation of selected lncRNA candidates by expression profiling and coding predictions	71
4.2.3. Candidate expression levels in primary hepatocytes are mediated by metabolic stimuli	72
4.3. Generation of lncRNA-deficient mouse models using CRISPR/Cas9-mediated genome engineering	74
4.3.1. Targeting strategies to abrogate lncRNA candidate expression	74
4.3.2. In vitro validation of sgRNA activity using T7 endonuclease I assays	76
4.3.3. In vivo targeting approach - strategy for pronuclear microinjection	77

4.3.4. Generation of a mouse line deficient for lincIRS2-exon 1 (lincIRS2 $\Delta/\Delta$ )	78
4.3.5. Generation of a mouse line deficient for Gm15441-exon 1 (Gm15441 $\Delta/\Delta$ )	80
4.4. Gm15441-Exon 1 deficiency does not affect fertility or Txnip expression, but results in ablation of Gm15441 expression	81
4.5. LincIRS2 deficiency impacts on liver energy homeostasis by regulating expression levels of gluconeogenic and lipogenic genes	83
4.5.1. LincIRS2 deficiency does not affect fertility or body weight, but results in hyperglycemia in lincIRS2 $\Delta/\Delta$ mice	83
4.5.2. Indirect calorimetry analysis indicates unaltered energy expenditure and substrate mobilisation in lincIRS2 $\Delta/\Delta$ mice	85
4.5.3. LincIRS2 $\Delta/\Delta$ mice exhibit altered expression levels of key gluconeogenic and lipolytic genes	86
4.5.4. Knockdown of lincIRS2 in primary hepatocytes results in altered expression of key metabolic genes in response to metabolic stimuli	88
4.5.5. Knockdown of lincIRS2 indicates impaired insulin tolerance in LNA-treated mice	90
4.5.6. Knockdown of lincIRS2 results in reduced AKT phosphorylation in liver	92
<b>Chapter 5 - Discussion</b>	<b>93</b>
5.1. Hepatic lncRNA expression adapts to chronic and acute nutrient challenges	93
5.2. Selection procedure for liver-enriched lncRNAs proves sufficient to identify metabolically-instructive candidate transcripts	94
5.3. Successful generation of in vivo mouse models to study lncRNA-mediated metabolic networks	96
5.4. Genetic lincIRS2 deficiency results in hyperglycemia and impacts on expression of key metabolic enzymes	99
5.5. Reduction of lincIRS2 levels affects gluconeogenic and lipogenic gene expression and reduces insulin-mediated AKT phosphorylation	100
5.6. Future Perspectives	102
<b>Chapter 6 - Appendix</b>	<b>105</b>
6.1. Summary	105
6.2. Zusammenfassung	106
6.3. Supplemental figures	107
6.5. Acknowledgements	123
6.6. Eidesstattliche Erklärung	124
6.7. Curriculum vitae	125

## List of abbreviations

2WA+B	2-Way ANOVA test + Bonferroni	lncRNA	Long noncoding RNA
AL	<i>Ad libitum</i>	min	Minutes
ASO	Antisense oligonucleotide	miRNA	MicroRNA
BAT	Brown adipose tissue	mRNA	Messenger RNA
bp	Basepairs	NCD	Normal chow diet
BW	Body weight	NHEJ	Non-homologous end joining
ChiP-Seq	Chromatin immunoprecipitation sequencing	O <sub>2</sub>	Oxygen
chr	Chromosome	P2T-TT	Paired two-tailed t-test
CO <sub>2</sub>	Carbondioxide	PCA	Principal component analysis
CPAT	Coding potential assessment tool	PCR	Polymerase chain reaction
		PNS	Parasympathetic nervous system
CPC	Coding potential calculator	qPCR	Quantitative real-time PCR
CRISPR	Clustered regularly interspaced short palindromic repeats	RER	Respiratory exchange ratio
crRNA	CRISPR RNA	RF	Refeeding
Ctrl	Control	RNA	Ribonucleotid acid
d	Deleted	RNA-Seq	RNA sequencing
DNA	Desoxyribonucleotid acid	RNP	Ribonucleoprotein
DSB	Double strand break	rpm	Rounds per minute
FA	Fasting	rRNA	Ribosomal RNA
FD	Forskolin + Dexamethasone	RT	Room temperature
FPKM	Fragments per kilobase of exon per million reads	s	Seconds
GCG	Glucagon	s.e.m.	Standard error of the mean
gRNA	Guide RNA	SCAT	Subcutaneous white adipose tissue
GTT	Glucose tolerance test	sgRNA	Single guide RNA
H3K4me <sup>3</sup>	Histone 3 lysine 4 trimethylation	siRNA	Small inhibitory RNA
H3K27ac	Histone 3 lysine 27 acetylation	SM	Skeletal muscle
HDR	Homology-directed repair	snoRNA	Small nucleolar RNA
HFD	High-fat diet	snRNA	Small nuclear RNA
hrs	Hrs	SNS	Sympathetic nervous system
Ins	Insulin	T2DM	Type 2 diabetes mellitus
ITT	Insulin tolerance test	T7E1	T7 Endonuclease I
KID	Kidney	tracrRNA	Trans-activating CRISPR RNA
KO	Knockout	TCA	Tricarboxylic acid cycle
KS	Kolgomorov-Smirnov test	TSS	Transcriptional start site
LIV	Liver	UP2T-TT	Unpaired two-tailed t-test
LNA	Locked nucleic acid	VAT	Visceral white adipose tissue
		WT	Wildtype

## List of figures

Figure	Page
1. Worldwide mean body mass index (BMI) of males aged 18 years or more	2
2. Maintenance of physiological blood glucose levels by hepatic glycogenesis, glycogenolysis and gluconeogenesis	6
3. Key enzymes of the gluconeogenesis pathway	8
4. Insulin-mediated signaling mechanisms to regulate glucose and lipid metabolism in hepatocytes	12
5. Cellular processes regulated by long noncoding RNAs	14
6. Transcriptome profiling of two independent mouse model systems of obesity	65
7. Transcriptome profiling in livers of differentially-fed mice	66
8. Transcriptome profiling in liver biopsies of human patients	68
9. Identification of liver-enriched lncRNA transcripts regulated by chronic obesity and short-term changes in nutrient availability	70
10. Additional characteristics of selected lncRNA candidates	71
11. Metabolic regulation of selected lncRNA candidates in primary hepatocytes	73
12. Gene targeting approach to abrogate <i>lincIRS2</i> expression	75
13. Gene targeting approach to abrogate <i>Gm15441</i> expression	75
14. Validation of sgRNA activity using T7 endonuclease I assays	76
15. Experimental setup of the <i>in vivo</i> gene targeting strategy	78
16. Generation of a gene-edited <i>lincIRS2</i> <sup>Δ</sup> allele	79
17. Generation of a gene-edited <i>Gm15441</i> <sup>Δ</sup> allele	80
18. Physiological impact of allele <i>Gm15441</i> <sup>Δ</sup>	82
19. Physiological impact of allele <i>lincIRS2</i> <sup>Δ</sup> (I)	83
20. Physiological impact of allele <i>lincIRS2</i> <sup>Δ</sup> (II)	84
21. Indirect calorimetric analysis of the <i>lincIRS2</i> <sup>Δ/Δ</sup> mouse line	86
22. Gene expression analysis of key metabolic genes in the <i>lincIRS2</i> <sup>Δ/Δ</sup> mouse line	87
23. Gene expression analysis of key metabolic genes upon lincIRS2 knockdown in primary hepatocytes (I)	89
24. Gene expression analysis of key metabolic genes upon lincIRS2 knockdown in primary hepatocytes (II)	90
25. Knockdown of lincIRS2 transcript levels does not elicit hyperglycemia, but impairs insulin tolerance	91
26. Reduced insulin-induced AKT phosphorylation in lincIRS2 LNA-treated mice	92

## Abstract

Long noncoding RNAs (lncRNAs) have recently been recognised as multifaceted regulators of gene expression across multiple cellular and developmental contexts, yet their contribution to liver energy homeostasis remains poorly understood. Using global transcriptome profiling we demonstrate that both chronic and acute nutrient challenges elicit global anticorrelative transcriptional responses of protein-coding mRNAs and lncRNAs in liver. To address if lncRNAs functionally contribute to the control of liver metabolism, we performed *in vitro* characterisation of regulated hepatic lncRNAs and selected metabolically-responsive lncRNAs Gm15441 and lincIRS2 for further characterisations *in vivo*. Through CRISPR/Cas9-mediated genome engineering we generated deletion alleles of both selected lncRNAs and verified that expression of the respective transcripts were successfully abrogated in *in vivo* mouse models. Finally, we show that lincIRS2 deficiency causes hyperglycemia and impaired insulin tolerance in *in vivo* mouse models and provide evidence that lincIRS2 is essential for proper glucose homeostasis and insulin-evoked suppression of hepatic glucose production by impacting on AKT phosphorylation and gluconeogenic, lipolytic and lipogenic gene expression. Collectively, we propose the concept that nutrient-sensitive lncRNA lincIRS2 is transcriptionally coupled to alterations of systemic nutrient states and functions as molecular relay controlling liver energy homeostasis.

# Chapter 1 - Introduction

## 1.1. The obesity pandemic - worldwide burden of the 21st century

As a consequence of the current obesogenic environment, composed of inexpensive calorically dense food and an overall reduction in physical activity due to modern technologies, contemporary human societies are facing an unprecedented rise in rates of overweight and obesity. Between 1975 and 2016 the worldwide prevalence of obesity has nearly tripled, with more than 1.9 billion adults, aged 18 years or older, being overweight in 2016, out of which more than 600 million were obese [1]. Proportionally, 39 % of worldwide adults aged 18 years and over are considered being overweight and 13 % being obese [1]. Overweight and obesity is defined by the World Health Organization (WHO) as abnormal or excessive fat accumulation that presents a risk to the individual's health status [2]. As a crude population-level measure of overweight and obesity the WHO is utilising the body mass index (BMI), which is defined by a person's weight in kilograms divided by the square of his height in meters ( $\text{kg}/\text{m}^2$ ). By definition, a person with a BMI equal to or more than 25 is generally considered overweight and a person with a BMI greater than or equal to 30 is considered obese [2].

Once perceived as a problem of high-income countries, nowadays every region worldwide, except parts of sub-Saharan Africa and Asia, are impacted by the obesity pandemic, resulting in more deaths linked to overweight and obesity than to underweight in the affected countries [1]. As overweight and obesity are associated with accelerated ageing [3], morbidity [4] and increased risk of death [5], a recent study found that a BMI higher than 24.9 globally accounted for 4 million deaths and 120 million disability-adjusted years of life in 2015 [6]. The results further illustrate the massive global burden on healthcare systems due to overweight and obesity.

International genome-wide association studies have hitherto identified over 60 genetic risk markers implicated to elevated susceptibility to overweight and obesity [7]. Yet, the 32 most common genetic variants only account for less than 1.5 % of the overall inter-individual differences in BMI and thus, regarding the dramatic rise of global obesity over the last decades, point to other more influential risk factors beyond genetics [8]. Known non-genetic obesity risk factors not only include individual diet and lifestyle [9] as well as socioeconomic risk factors such as poverty [10] or education [11], but also behavioral and environmental risk factors that transfer obesity susceptibility to subsequent offspring generations, such as parental smoking [12], parental famine exposure [13] or parental obesity [14]. Although largely preventable, the combination of the aforementioned risk factors and their compounding interactions with each other signal a devastating trend towards prevalent obesity, which is underpinned by the fact that the incidence of overweight and obesity among children had dramatically risen from 4 % in 1975 to more than 18 % in 2016 [1]. Substantiated by dire projections forecasting the entire US population to be overweight or obese by the year 2048 [15], obesity turned from a historically rare disease of the affluent into a global pandemic that not only represents an economic burden for today's health care systems, but also an inevitable challenge for future generations to come.

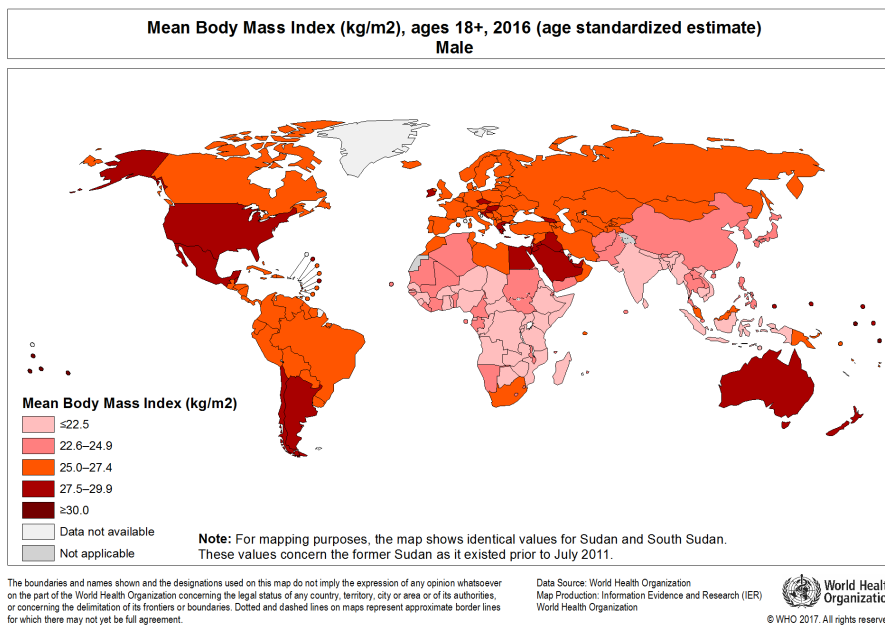


**Figure 1: Worldwide mean body mass index (BMI) of males aged 18 years or more.** Global map depicting mean BMIs of the adult male population (ages 18+) by nation. The BMI is defined by an individual's weight in kilograms divided by the square of his height in meters (kg/m<sup>2</sup>). According to WHO standards, a person with a BMI equal or higher than 25 is considered overweight (orange) and a person with a BMI equal or higher than 30 is considered obese (dark red). The graphic was created by the WHO and taken from [1]. Authorisation for reproducing WHO copyrighted material was permitted (license ID: 264641).

### 1.1.1. Comorbidities of the global obesity pandemic

Overweight and obesity are closely linked with a plethora of concomitant health consequences that, although diverse and oftentimes unrelated, ultimately elevate the risk of total mortality [16, 17]. Recent studies indicate that overweight and obesity in adulthood result in a decrease in life expectancy by an estimated 4-7 years [18] and attribute 15 % of all deaths in the USA in the year 2000 to excess body weight [19]. The most prominent obesity-associated diseases include a clinically vast spectrum of malignancies, ranging from stroke and cardiovascular diseases, certain cancer subtypes, impaired immunological responses, and neurodegenerative diseases, to the metabolic syndrome and type 2 diabetes mellitus (T2DM). Excess body fat is frequently accompanied by hypertension and hyperlipidemia, an elevated amount of triglycerides, cholesterol and phospholipids in the bloodstream, both of which constitute the major risk factors for ischemic heart disease and stroke, the leading cause of death worldwide [20-22].

In both men and women, high BMI is significantly associated with higher incidences of certain kind of cancers, such as cancers of the esophagus, colon and rectum, kidney, liver, pancreas, gallbladder and specific forms of leukaemia [23-26]. Significant correlations were also observed for higher rates of death from cancers of the stomach and prostate in men and for death from cancers of the cervix, ovary, uterus and postmenopausal breast tissue in women [27-29]. Collectively, around 6 % of all cancers diagnosed in 2007 were classified as attributable to obesity [30]. Meta studies surveying hospital stays and surgical complications in trauma centres demonstrated that obese patients had double the risk of major complications during surgery [31], were more often affected by surgical-site infections [32] and ultimately were diagnosed with worse prognoses compared to non-obese patients suffering from the same etiology [33]. In concert with impaired immunological responses during hospital infections [32], obese patients showed reduced vaccine efficacy and serological response to vaccination [34].

Despite the tremendous list of obesity-associated diseases already mentioned, the major individual and economic burden correlating with excess body weight is provoked by neurodegenerative diseases and T2DM (see next chapter). Obesity-related impairment of glucose homeostasis regulation has been associated with a higher risk to develop neurodegenerative diseases, such as multiple sclerosis and dementia, as well as Alzheimer's, Parkinson's and Huntington's disease [35]. Overweight during midlife elevates the risk to suffer from Alzheimer's disease or any kind of dementia by 35 and 26 %, respectively [36].

Although its comorbidities are variable in severity and disease characteristic, obesity is a fundamental contributor to the incidence of noncommunicable diseases and death across the globe and burdens global health care systems in myriad modalities.

### 1.1.2. Obesity-associated metabolic syndrome and type 2 diabetes mellitus

The metabolic syndrome is classified by a clustering of interrelated physiological and metabolic traits that collectively confer a 2-fold risk to develop cardiovascular diseases and a 5-fold risk to develop T2DM [37]. The five hallmarks of the metabolic syndrome are comprised of abdominal obesity, hypertension, high levels of blood glucose (hyperglycemia) and triglycerides (hypertriglyceridemia) and low levels of high-density lipoprotein (HDL), all of which are diagnosed significantly more frequently in overweight and obese people [38]. In fact, a recent study calculated that 70 % of obese people exhibit all five hallmarks of the metabolic syndrome [39] and as truncal obesity constitutes both a syndrome and a cause for hypertension, hyperglycemia and hypertriglyceridemia, obese people are predisposed to develop cardiovascular diseases and T2DM [40, 41]. Promoted by the ascending share of population being overweight or obese, the worldwide number of adults suffering from T2DM has increased from 30 million patients in 1980 to more than 422 million patients in 2014 [42]. Compared to normal weight people, the risk of developing type 2 diabetes is three-fold higher in people being overweight and seven-fold higher in people being obese [43]. Yet, not every overweight or obese individual suffers from diabetes; however, more than 80 % of all diabetes patients are overweight or obese [44].

Diabetes is characterised by permanent hyperglycemia and clinically diagnosed when fasting blood glucose levels exceed more than 7.0 mmol/L blood plasma [45]. Causative for the sustained elevation of blood glucose levels in diabetic patients are defects in physiological insulin signaling, mainly by impaired insulin sensitivity and secretion, which results in diminished clearance of glucose and triglycerides from the blood plasma by insulin-mediated uptake into peripheral organs [46]. Although a series of pharmacological interventions as well as changes in diet and physical activity can improve health outcomes of diabetic patients and facilitate many diabetics to participate in normal life, the underlying impairment of glucose homeostasis can seriously impact on quality of life. If not well controlled, diabetic hyperglycemia may cause chronic damage, dysfunction and failure of various organ systems, especially blood vessels, kidneys, heart, eyes and nerves, which can ultimately result in circulatory disorders, kidney failure, ischemic heart attack, stroke, leg amputation and blindness [47].



Despite pharmacological interventions that can delay diabetes progression, such as metformin, sulphonylureas, GLP-1 analogues and DPP4 inhibitors, T2DM and its concomitant diseases still represents the eighth leading cause of death worldwide [45]. In 2012, 1.5 million deaths were directly caused by T2DM and additional 2.2 million deaths by cardiovascular and chronic kidney diseases resulting from the constantly elevated blood glucose levels [48]. Worryingly, 43 % of the 3.7 million deaths elicited by diabetes occur prematurely, before the patients reach the age of 70 years [48].

Nowadays obesity-associated T2DM affects approximately 8.5 % of the global adult population, aged 20-79 years, and caused approximately USD 727 billion dollars in health expenditures in 2017 [45], underpinning the urgent need to counteract the global obesity pandemic and its detrimental metabolic consequences.

## 1.2. The liver - central regulator of energy homeostasis

In vertebrates the liver not only represents the largest solid organ and the largest gland in the body, but also carries out more than 500 vital functions, encompassing detoxification of endogenous and exogenous substrates, synthesis of proteins essential for immune function and blood coagulation as well as storage, metabolism and redistribution of nutrients, vitamins and minerals [49]. Directly connected to the gastrointestinal tract via the portal vein, the liver constitutes the first contact site of the body with ingested dietary nutrients, potentially toxic chemicals, xenobiotics and all other resorbed substances [50]. Whereas the minerals iron, copper and potassium as well as fat-soluble vitamins, such as vitamin A, D, E, K and B12, are stored within the liver, harmful endogenous and exogenous substances are biochemically modified in a process called biotransformation, which increases the water solubility of the hazardous metabolites and allows excretion via urine or feces [51].

Responsible for the vast repertoire of liver functions are hepatocytes, the main cell type of the liver, which account for around 80 % of the liver's mass and express a plethora of metabolic enzymes enabling carbohydrate, protein and lipid biosynthesis, transformation and breakdown [52]. Besides synthesising and secreting essential circulating proteins, such as cargo proteins, components of the complement immune system and coagulation factors, hepatocytes also produce bile that is secreted into the small intestine and facilitates the absorption of lipids and other fat-soluble substances [53].

In conjunction with adipose tissue, the liver plays a key role in controlling lipid metabolism, as hepatocytes are the major source of fatty acid synthesis, which exported as lipoproteins provide an additional energy source and membrane structural components for peripheral tissues [54]. As hepatocytes take up 90 % of the intestinally absorbed glucose for further procession and redistribution [55], thereby precisely controlling blood glucose levels, the liver represents both the central hub governing whole body energy metabolism as well as the major metabolic organ regulating glucose homeostasis.

### 1.2.1. Hepatic regulation of glucose homeostasis

The liver is the key metabolic organ balancing blood glucose levels within a narrow physiological range in order to ensure the supply of peripheral organs with glucose, and hence survival of the organism, but also to prevent tissue damage by detrimental hyperglycemia. The tight hepatic regulation of glucose homeostasis is orchestrated by an intricate network of inter-organ interactions, including the pancreas, the brain, adipose tissue and skeletal muscle, all of which impact on the liver's capability to produce, store and release glucose into the circulation [56, 57].

By releasing glucoregulatory hormones into the blood stream, the pancreas regulates the hepatic production and release of glucose, known as hepatic gluconeogenesis, as well as hepatic glucose storage in the form of glycogen, known as glycogenesis, and its counterpart, the glycogen breakdown into glucose, called glycogenolysis [58]. When blood glucose levels are low, during sleep or in between meals, pancreatic  $\alpha$ -cells release the peptide hormone glucagon, which promotes hepatic glycogenolysis to increase endogenous blood glucose levels. In case of prolonged fasting, when hepatic glycogen stores are depleted, glucagon also triggers hepatocytes to *de novo* synthesise glucose through gluconeogenesis using other metabolites, such as free fatty acids, glycerol, lactate and amino acids [59]. During prolonged fasting periods, hepatic gluconeogenesis is the primary source of glucose production, accounting for 90 % of endogenously produced glucose [60]. Driven by elevated glucose levels in the postprandial state, pancreatic  $\beta$ -cells secrete insulin, another peptide hormone that acts antagonistically to glucagon and directly inhibits gluconeogenesis and raises glycogenolysis in hepatocytes. In addition, insulin also indirectly hinders hepatic glucose production through inhibition of free fatty acid and glycerol release by adipose tissue, major precursors of hepatic gluconeogenesis [61].

As the brain accounts for around 25 % of glucose utilisation, it also directly partakes in the regulation of hepatic glucose homeostasis via both the sympathetic nervous system (SNS) and the parasympathetic nervous system (PNS) [62]. The liver is highly innervated by hypothalamic neurons, which transmit both SNS signals to promote glucose production and mobilisation of fuels for extrahepatic tissues as well as PNS stimuli to lower glucose production and increase fuel storage in the liver [57].

The rate of hepatic gluconeogenesis is determined by two major factors: the availability of gluconeogenic substrates, like free fatty acids, glycerol, lactate and amino acids, as well as by the expression of gluconeogenic enzymes (see chapter 1.2.2.2.). Whereas amino acids result from general protein degradation during prolonged fasting, the other substrates are mainly produced and released by extrahepatic tissues as a response to elevated energy consumption and demand. During exercise or fasting, skeletal muscle produce high amounts of pyruvate, which is converted into lactate, released into the circulation and ultimately utilised by hepatocytes to synthesise glucose through gluconeogenesis [57]. In a similar role, adipose tissue contributes to the rate of hepatic gluconeogenesis by providing glycerogenic substrates, which are generated as a product of lipolysis, the breakdown of body fat. Upon exercise or fasting, adipocytes extract energy from triglyceride degradation, thereby generating and releasing free fatty acids and glycerol, both of

which serve as progenitors for hepatic glucose production and consequently limit gluconeogenesis [63].

Insulin action constitutes the main anabolic trigger balancing glucose uptake by the liver and peripheral tissues as well as hepatic glycogenesis and gluconeogenesis. However, people suffering from diminished insulin secretion and/or sensitivity as well as T2DM patients exhibit a pathological condition called insulin resistance, which is characterised by an insufficient cellular response towards insulin, leading to uncontrolled hepatic glucose production and decreased glucose uptake by peripheral tissues, hence ultimately resulting in chronic and detrimental hyperglycemia [64].

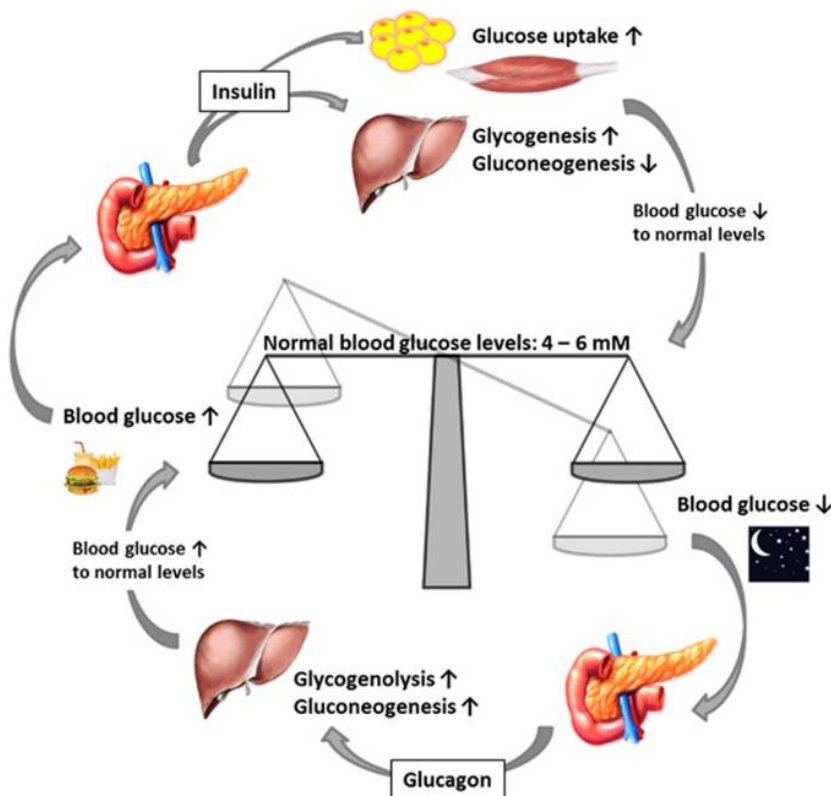


**Figure 2: Maintenance of physiological blood glucose levels by hepatic glycogenesis, glycogenolysis and gluconeogenesis.** Hormonal regulation, mainly by insulin and glucagon, precisely orchestrates liver function in order to maintain physiological blood glucose levels. In fed states with high blood glucose levels, insulin is released by the pancreas to stimulate glucose uptake by peripheral organs as well as glycogenesis, the storage of glucose in the liver in the form of glycogen. In addition, insulin inhibits hepatic production and release of glucose from the liver (gluconeogenesis, top). In fasted states with low blood glucose levels, glucagon is secreted by the pancreas to promote hepatic breakdown of glycogen into glucose (glycogenolysis) as well as hepatic gluconeogenesis (bottom). Figure taken from [59].

### 1.2.2. Molecular mechanisms of hepatic energy homeostasis

On a molecular level, hepatic energy homeostasis is orchestrated by a complex, yet not fully understood signaling network, involving several ramified and interwoven metabolic pathways that reciprocally stimulate or inhibit each other by a myriad of direct and indirect interactions.

For the understanding of this work, the regulatory pathways controlling glucose uptake and release, gluconeogenesis, fatty acid beta-oxidation, fatty acid synthesis and insulin signaling will be introduced. Yet, other intricate signaling networks contribute to liver energy homeostasis, i.a. mammalian target of rapamycin (mTOR), peroxisome proliferator-activated receptor (PPAR), cyclic AMP response element-binding protein (CREB), cAMP-dependent protein kinase (PKA), CCAAT-enhancer-binding protein (C/EBP) and peroxisome proliferator-activated receptor-gamma coactivator 1 $\alpha$  (PGC1 $\alpha$ ) signaling (reviewed in [65-70]).

### 1.2.2.1. Glucose uptake and release

Although several glucose transporters have been described (reviewed in [71]), hepatocytes predominantly control glucose uptake and release via glucose transporter-2 (GLUT2, also known as solute carrier family 2, member A2 or SLC2A2), a uniporter transporter protein that mediates bidirectional fluxes of glucose in and out of hepatocytes along a concentration gradient of glucose [50]. Interestingly, hepatocyte-specific deletion of GLUT2 abrogates hepatic glucose uptake in mice, but does not impinge on hepatic gluconeogenesis, pointing to alternative mechanisms of glucose release by hepatocytes [72]. In humans, mutations of GLUT2 result in Fanconi-Bickel syndrome, a rare type of glycogen storage disease which is characterised by hepatic glycogen accumulation, fasting hypoglycemia as well as glucose intolerance, underlining the key role of GLUT2 in hepatic glucose uptake and release [73].

In contrast to GLUT2, which constitutes a low-affinity glucose transporter, but is highly expressed in response to elevated blood glucose levels, also high-affinity glucose transporters which shuttle glucose close to maximum velocity are expressed in liver, such as glucose transporter-1 (GLUT1, also known as solute carrier family 2, member A1 or SLC2A1) and glucose transporter-4 (GLUT4, also known as solute carrier family 2, member A4 or SLC2A4) [74]. Humans with mutations of GLUT1 develop De Vivo disease, a severe disruption of brain glucose supply due to impaired glucose transport across the blood brain barrier, which leads to cerebral energy deficiency and cognitive impairments, yet no apparent malfunctions in liver energy metabolism [75]. Targeted disruption of GLUT4 in murine adipocytes and muscle impact on liver energy homeostasis as affected mice exhibit fasting hyperglycemia and glucose intolerance, underlining the importance of inter-tissue interactions to regulate liver energy homeostasis [76]. Yet, both GLUT1 as well as GLUT4 deficiency do not directly impinge on hepatic glucose homeostasis, pointing to GLUT2 as the main regulator of hepatic glucose uptake and release.

### 1.2.2.2. Hepatic gluconeogenesis

During short-term fasting the liver mainly generates and releases glucose through glycogenolysis. However, during prolonged fasting, when glycogen stores are depleted, hepatocytes *de novo* synthesise glucose through gluconeogenesis by converting other metabolites such as lactate, pyruvate, glycerol and amino acids to glucose 6-phosphate [61]. The gluconeogenic substrates are mostly delivered to the liver through circulation from extrahepatic tissues, such as skeletal muscle or adipose tissue. During fasting or exercise, skeletal muscle release amino acids as well as lactate, which can be converted to pyruvate, whereas adipose tissue provides hepatocytes with fatty acids and glycerol, all of which are metabolised to oxaloacetate in the hepatic mitochondrial tricarboxylic acid (TCA) cycle [57].

The key rate-limiting enzymes controlling gluconeogenesis are phosphoenolpyruvate carboxykinase (PCK1), which triggers the conversion of oxaloacetate to phosphoenolpyruvate, fructose 1,6-bisphosphatase (FBP1) which mediates dephosphorylation of fructose 1,6-bisphosphate to glucose 6-phosphate and glucose 6-phosphatase, subunit C (G6PC) which

facilitates dephosphorylation of glucose 6-phosphate to glucose (reviewed in [77], see also Figure 3). The expression levels of PCK1 and G6PC, and thus the rate of hepatic gluconeogenesis, are tightly controlled by numerous gluconeogenic transcription factors, which translate extracellular cues, such as metabolic hormones [78], nutrient availability [79] and inflammatory cytokines [80], into gluconeogenic transcriptional responses.

The predominant role of PCK1 in hepatic gluconeogenesis has been demonstrated in several transgenic mouse models. Whereas systemic deletion of PCK1 in mice results in severe hypoglycemia leading to early postnatal death [81], mice with hepatocyte-specific deletion of PCK1 are viable, but are incapable of producing glucose via gluconeogenesis when fasted, leading to accumulation of TCA metabolites and the development of dramatic hepatic steatosis, a triglyceride fat accumulation [82]. Concordantly, transgenic mice overexpressing PCK1 are hyperglycemic and show increased basal rates of glucose production from pyruvate, demonstrating that the increase of PCK1 alone is sufficient to elevate hepatic gluconeogenesis and thus hepatic glucose output [83]. In humans, mutations have been reported that alter the activity or the subcellular localisation of PCK1, leading to severe and persistent hypoglycemia and/or liver failure and premature death, further underlining the vital role of PCK1 in hepatic gluconeogenesis [84-86].

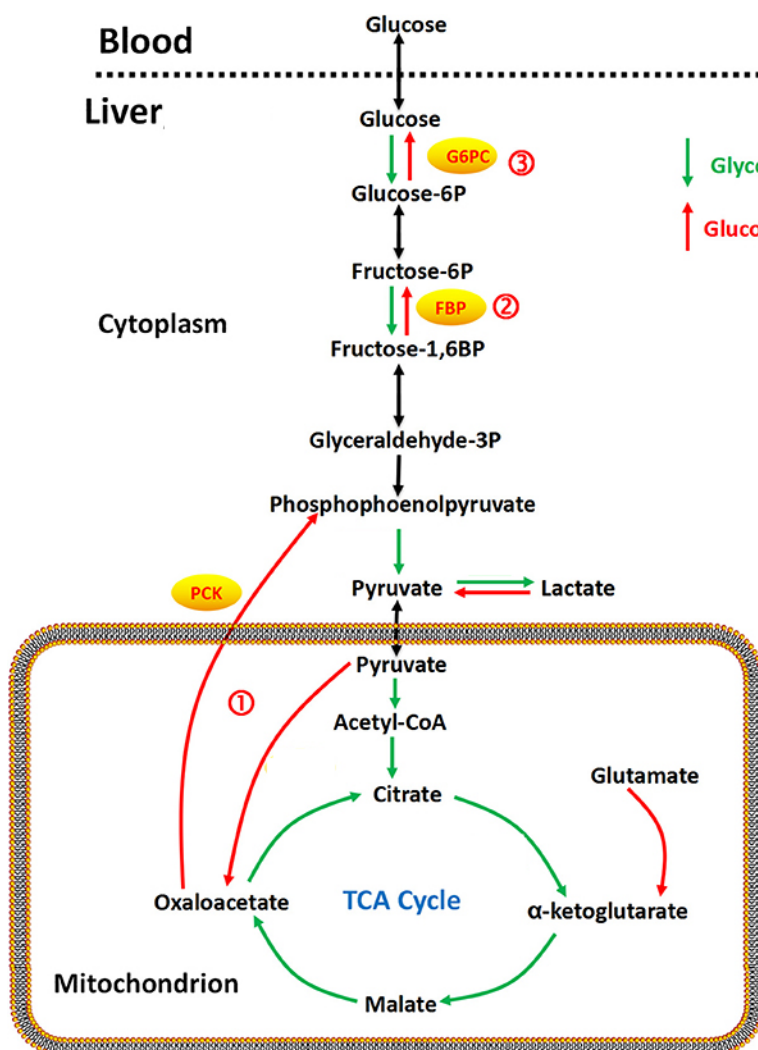


**Figure 3: Key enzymes of the gluconeogenesis pathway.** During hepatic gluconeogenesis, glucose is generated by a multistep enzymatic conversion of metabolic substrates, such as pyruvate, lactate or glutamate, all of which are metabolised to oxaloacetate in the mitochondrial tricarboxylic acid (TCA) cycle. The three rate-limiting enzymes of gluconeogenesis are (1) phosphoenolpyruvate carboxykinase (PCK) which converts oxaloacetate to phosphoenolpyruvate, (2) fructose 1,6-bisphosphatase (FBP) which facilitates dephosphorylation of fructose 1,6-bisphosphate to glucose 6-phosphate and (3) glucose 6-phosphatase, subunit C (G6PC) which exerts dephosphorylation of glucose 6-phosphate to glucose. Figure adapted from [87].

In another study, a transgenic mouse model was generated overexpressing the human *Fbp1* gene specifically in the liver, which results in glucose intolerance and enhanced hepatic glucose production, demonstrating that enhanced expression of FBP1 can increase hepatic glucose output [88]. In humans, several mutations of the *Fbp1* gene have been reported, all of which cause reduced or absent *Fbp1* activity and ultimately hypoglycemia and lactic acidosis, as defined by the accumulation of lactate in the bloodstream due to impaired lactate utilisation by gluconeogenesis [89-91].

To assess the metabolic consequences of G6PC deficiency, other studies generated transgenic mice with hepatocyte-specific deletions of *G6pc*, which develop lactic acidosis and hepatic steatosis due to glycogen and triglyceride accumulation [92, 93]. Interestingly, mice with liver-specific *G6pc* deficiency show normal blood glucose levels owing to compensatory glucose production from extrahepatic tissues, especially by the kidney and the intestines, pointing to alternative metabolic pathways that can overcome hepatic *G6pc* deficiency [94]. In contrast, humans with *G6pc* deficiency develop glycogen storage disease I, which is clinically manifested by hypoglycemia and hepatic accumulation of glycogen and fat, illustrating the significance of G6PC in controlling hepatic gluconeogenesis [95].

### 1.2.2.3. Fatty acid beta-oxidation

Besides glucose and amino acids, fatty acids can also be metabolised in hepatocytes to generate energy for metabolic homeostasis. The major pathway for the degradation of fatty acids is fatty acid beta-oxidation, which predominantly takes place in mitochondria and not only provides energy for hepatocytes, but also generates ketone bodies which are released into the circulation and provide metabolic fuels for extrahepatic tissues [96].

The important rate-limiting enzymes participating in fatty acid beta-oxidation are carnitine palmitoyltransferase 1 (CPT1), which shuttles the metabolic substrate acyl-CoA into mitochondria, acyl-CoA oxidase 1 (ACOX1), which catalyses the first step of the beta-oxidation pathway, and hydroxylacyl-CoA dehydrogenase (HADH), which mediates the final step of the beta-oxidation pathway (reviewed in [97]).

Transgenic mice homozygously lacking *Cpt1* expression die early during gestation, yet heterozygous *Cpt1*-deficient mice are viable and exhibit hypoglycemia as well as elevated levels of free fatty acids when fasted, pointing to impairments in physiological fatty acid conversion [98]. In concert with the *Cpt1* mouse model, humans affected by *Cpt1* mutations suffer from reduced levels of ketone bodies and blood glucose during fasting, a medical condition called hypoketotic hypoglycemia, which further indicates *Cpt1* to play an essential role in metabolising fatty acids to ketone bodies and cellular energy stores that can be utilised to generate glucose [99].

Homozygous mice deficient for *Acox1* expression are viable, but display growth retardation and accumulation of fatty acids in blood and in hepatocytes, resulting in alterations of hepatocyte morphology and hepatic steatosis [100]. Mutations of *Acox1* in humans lead to the development of adrenoleukodystrophy, a disease that is characterised by accumulation of very long chain fatty

acids throughout the body, emphasising the critical role of *Acox1* in hepatic fatty acid utilisation and beta-oxidation [101].

Transgenic mice deficient for *Hadh* have low birth weight and die within the first two days of life due to neonatal hypoglycemia, accumulation of fatty acid metabolites and resulting severe hepatic steatosis [102]. Humans suffering from mutations in *Hadh* develop hyperinsulinemic hypoketotic hypoglycemia, a metabolic condition featuring high levels of insulin as well as low levels of ketone bodies and blood glucose, which not only substantiates the key role of *Hadh* in fatty acid metabolism, but also points to undiscovered pathways linking fatty acid metabolism with insulin secretion by pancreatic  $\beta$ -cells [103].

#### 1.2.2.4. Fatty acid synthesis

In the fed state, when excess nutrients are available, the liver not only metabolises carbohydrates into glucose and subsequently glycogen, but also converts glucose into fatty acids, the main long-term form of energy storage within the body. Important enzymes controlling hepatic *de novo* lipogenesis are acetyl-CoA carboxylase alpha (ACACA), which catalyses carboxylation of acetyl-CoA to malonyl-CoA, the rate-limiting step of lipogenesis [57], fatty acid binding protein 4 (FABP4), which mediates fatty acid uptake and transport [104], and sterol regulatory element-binding protein-1 (SREBP1), a transcription factor that activates the transcription of key genes in fatty acid biosynthesis [105].

In mice, *Acaca* deficiency is embryonically lethal as homozygous *Acaca* knockout mice not properly develop and die during early embryonic development, demonstrating a vital function of ACACA not only in hepatic lipogenesis, but also in systemic energy metabolism [106].

Interestingly, mice deficient for *Fabp4* do not show developmental or metabolic alterations, most likely due to other fatty acid binding proteins compensating for the loss of FABP4. Yet, when exposed to diet-induced obesity, *Fabp4* deficient mice do not develop insulin resistance or diabetes, indicating that FABP4 links fatty acid metabolism to the development of detrimental metabolic alterations, such as peripheral insulin resistance or pancreatic  $\beta$ -cell dysfunction [107].

Elevated hepatic levels of SREBP1 protein have been detected in both obese mice [108] as well as in diabetic patients [109], both of which showed increased expression of SREBP1 target genes, higher rates of hepatic fatty acid synthesis and hepatic steatosis. In addition, hepatocyte-specific deletion of SCAP, an escort protein necessary for SREBP1 nuclear transport, reduced fatty acid synthesis and hepatic steatosis in mice with diet-induced obesity, suggesting that SREBP1 not only regulates fatty acid biosynthesis, but also contributes to the development of hepatic steatosis [110].

#### 1.2.2.5. Insulin signaling in hepatocytes

The anabolic hormone insulin is a major mediator of hepatic metabolism as postprandial insulin-mediated signaling simultaneously regulates the rates of hepatic lipogenesis, glycogenesis and gluconeogenesis as well as protein synthesis [111]. Binding of insulin to the insulin receptor (IR) tyrosine kinase results in conformational change-induced activation of the IR kinase activity, autophosphorylation of IR subunits and subsequently the recruitment and phosphorylation of

insulin receptor substrate (IRS) proteins, which act as molecular scaffolds and recruit and mediate other signaling complexes [112].

The major signaling pathway linking insulin action to metabolic responses is facilitated by phosphatidylinositol 3-kinases (PI3K), which are activated by IRS proteins and catalyse the phosphorylation of phosphatidylinositol 4,5-bisphosphate (PIP<sub>2</sub>) phospholipids to phosphatidylinositol 3,4,5-triphosphate (PIP<sub>3</sub>), important second messenger lipid molecules [113]. Membrane-bound PIP<sub>3</sub> triggers phosphoinositide-dependent kinase 1 (PDK-1) activity, which results in recruitment and phosphorylation of several downstream kinases, such as phosphorylation of threonine residue 308 (Thr308) of protein kinase B (also known as AKT), the key signaling molecule for several essential metabolic pathways [114]. Yet, for full kinase activity AKT is also phosphorylated at serine residue 473 (Ser473) by the mammalian target of rapamycin complex 2 (mTORC2), another protein complex regulated by insulin and nutrient availability [115]. Once fully activated by PDK-1 and mTORC2, AKT mediates phosphorylation of several downstream targets, such as glycogen synthase kinase 3 (GSK-3), forkhead box protein O1 (FOXO1) and tuberous sclerosis complex protein 2 (TSC-2). AKT-mediated phosphorylation of glycogenesis repressor GSK-3 results in GSK-3 kinase inactivation and thus enhances the rate of glycogen synthesis [116]. By phosphorylation-induced degradation of TSC-2, AKT activates mammalian target of rapamycin complex 1 (mTORC1), a master regulator of cell growth and proliferation that induces lipid synthesis via sterol regulatory element-binding protein 1 (SREBP1) activation as well as protein synthesis [117]. Phosphorylation of the transcription factor FOXO1 by AKT leads to nuclear exclusion and degradation of FOXO1, resulting in reduced FOXO1-mediated expression of the key gluconeogenic genes glucose-6-phosphate, catalytic subunit (*G6pc*) and phosphoenolpyruvate carboxykinase 1 (*Pck1*) [118]. In addition, the combination of FOXO1 degradation and mTORC1 activation increases the expression of glucokinase, the rate-limiting enzyme in glycogen synthesis and glycolysis, which contributes to increased glycolytic flux and promotes hepatic lipogenesis [111].

Mice lacking hepatocyte-specific expression of *Foxo1* exhibit decreased rates of glycogenolysis and gluconeogenesis, resulting in neonatal and fasted hypoglycemia [119]. Yet, the blunted glucose production of *Foxo1*-deficient mice is normalised when *Akt* is concomitantly ablated in liver, indicating that additional signaling pathways contribute to insulin-stimulated hepatic glucose production, such as other members of the FOXO protein family [120]. Indeed, triple-transgenic mice deficient for the forkhead box O proteins FOXO1, FOXO3 and FOXO4 show increased rates of hypoglycemia compared to FOXO1-deficient mice, indicating that FOXO3 and FOXO4 also mediate hepatic gluconeogenesis [121]. In addition, hepatic glucose output is also orchestrated by FOXO6, as hepatocyte-specific deletion of FOXO6 causes fasting hypoglycemia in mice and overexpression of a constitutively active FOXO6 variant in mice resulted in elevated rates of hepatic glucose output [122].

The main molecules transmitting signals from the insulin receptor to the intracellular signaling pathways are insulin receptor substrate 1 (IRS-1) and insulin receptor substrate 2 (IRS-2), both of which have mutated alleles in humans that are associated with reduced insulin sensitivity and obesity [123, 124]. Knockout mice deficient for *Irs-1* display impaired systemic insulin action and



growth retardation [125]. In contrast, *Irs-2*-deficient knockout mice also show impaired systemic insulin signaling, but only exhibit growth retardation in specific tissues, such as pancreatic islet cells, which in combination with defective hepatic insulin signaling results in premature development of diabetes [126]. Hepatocyte-specific deletion of *Irs-1* and *Irs-2* in mice completely abrogates hepatic insulin action and results in increased hepatic gluconeogenesis, hyperglycemia and T2DM, underlining not only the importance of IRS-1 and IRS-2 as key transmitters of insulin signaling, but also the impact of hepatic insulin signaling itself in the context of blood glucose control and development of T2DM [127].

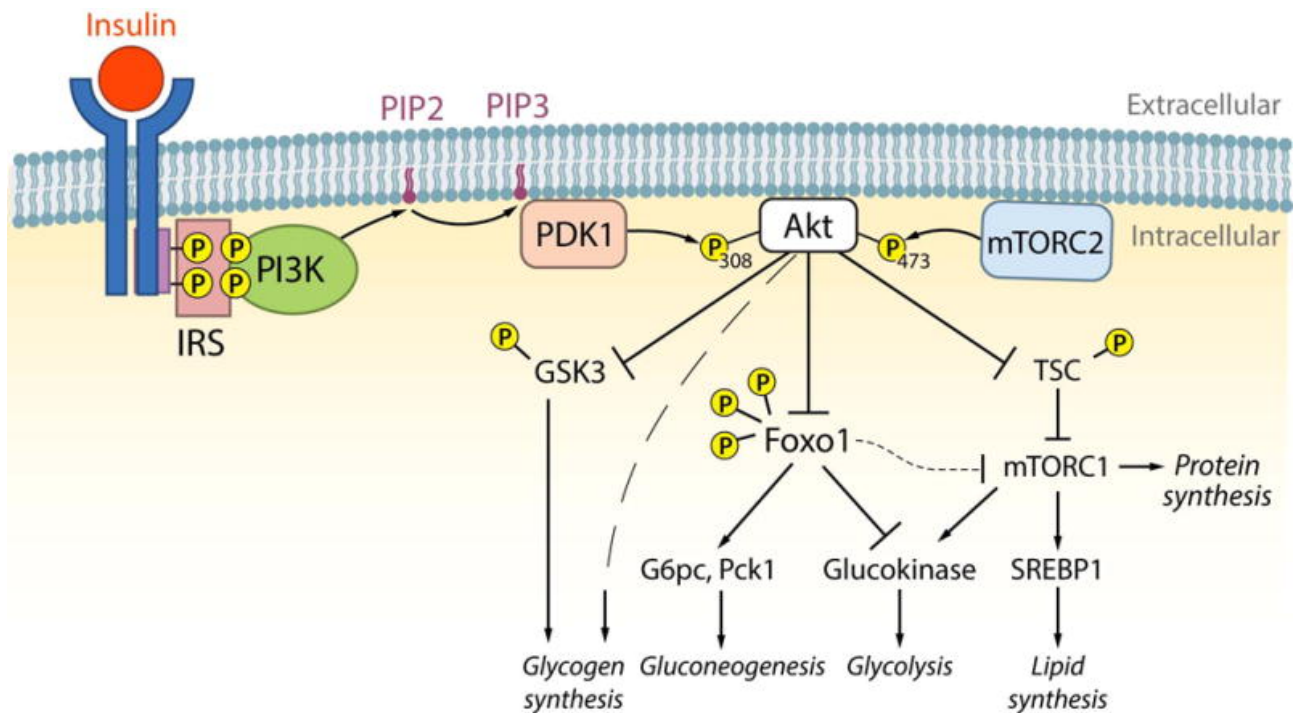


**Figure 4: Insulin-mediated signaling mechanisms to regulate glucose and lipid metabolism in hepatocytes.** Extracellular binding of insulin to the insulin receptor (blue) results in autophosphorylation of the receptor, followed by recruitment and phosphorylation of insulin receptor substrates (IRS). IRS proteins recruit and activate phosphatidylinositol 3-kinases (PI3K), which trigger the phosphorylation of phosphatidylinositol 4,5-bisphosphate (PIP<sub>2</sub>) to phosphatidylinositol 3,4,5-triphosphate (PIP<sub>3</sub>), which in turn promotes phosphoinositide-dependent kinase-1 (PDK1) to phosphorylate the protein kinase AKT at threonine residue 308 (Thr308). AKT is also phosphorylated at serine residue 473 (Ser473) by the mammalian target of rapamycin complex 2 (mTORC2), another protein complex regulated by insulin. Once fully activated, AKT phosphorylates several downstream effectors mediating multiple metabolic pathways, such as glycogen synthesis, gluconeogenesis, glycolysis and lipid synthesis. In addition to indirect pathways inducing glycogen synthesis (dashed lines), AKT directly stimulates glycogen synthesis by phosphorylation-mediated inhibition of glycogen synthase kinase 3 (GSK-3) activity. AKT-induced phosphorylation of the transcription factor forkhead box protein O1 (FOXO1) results in polyubiquitination and degradation of FOXO1, thus reducing expression of the key gluconeogenic genes glucose-6-phosphate, catalytic subunit (*G6pc*) and phosphoenolpyruvate carboxykinase 1 (*Pck1*). Additionally, FOXO1 degradation leads to increased expression of glucokinase, the rate-limiting enzyme controlling both glycogen synthesis and glycolysis by converting glucose to glucose-6-phosphate. Finally, activated AKT induces protein as well as lipid synthesis by phosphorylating the tuberous sclerosis (TSC) protein complex, leading to activation of mammalian target of rapamycin complex 1 (mTORC1), which in turn induces lipid synthesis via sterol regulatory element-binding protein 1 (SREBP1) activation as well as protein synthesis. Figure taken from [111].

### 1.3. The noncoding genome - a neglected layer of genomic regulators

In recent years, advances in whole-genome transcriptome analyses and tremendous efforts by multinational sequencing consortia have led to the discovery that the vast majority of mammalian genomes is pervasively transcribed in a highly dynamic and cell type-specific pattern [128]. Yet, whereas only about 1.2 % of mammalian genomes encode for proteins, most transcribed genes fall into the category of noncoding RNAs (ncRNAs), which are not translated into proteins, but facilitate various fundamental cellular functions [129]. Among others, processes enabled or regulated by ncRNAs include translation (transfer RNAs and ribosomal RNAs) [130], splicing (small nuclear RNAs) and RNA editing (small nucleolar RNAs) [131] as well as gene expression (microRNAs, small interfering RNAs and piwi-associated RNAs) [132-134]. However, the largest portion of mammalian transcriptomes is constituted by a heterogenous and hitherto mostly uncharacterised class of ncRNAs, termed long noncoding RNAs (lncRNAs), which comprises all noncoding RNA transcripts longer than 200 nucleotides. In humans, more than 68 % of all genes transcribed are lncRNAs [135] and systematic databases, such as the NONCODE database, report more than 96000 human and 87000 murine lncRNA genes, which express more than 172000 and 131000 different lncRNA transcripts, respectively [136]. Owing to the arbitrary classification of lncRNAs and the resulting huge numbers of transcripts, lncRNA genes are inherently diverse in terms of genome locus and transcription product. Whereas some lncRNA genes are found far away from annotated gene loci (large intergenic noncoding RNAs or lincRNAs), other lncRNA genes are transcribed from the opposite strand of protein-coding genes (natural antisense transcripts or NATs) or are even part of protein-coding gene loci, as lncRNA genes that are situated in intronic regions (intronic lncRNAs) or lncRNA genes that are transcribed by a bidirectional promotor of a protein-coding gene (promotor upstream transcripts or PROMPTs) (reviewed in [137]). Additionally, lncRNA genes can also harbor transcriptional units for other ncRNAs, such as miRNAs [138], snoRNAs [139] or circular RNAs (circRNAs), which are covalently closed RNA loops that are formed by backsplicing of exons or lariat introns and exhibit increased RNA stability due to circularisation (reviewed in [140]).

Although just a few lncRNA genes have been ascribed to specific molecular mechanisms to date, the reported functions cover a broad range of fundamental cellular processes, including X-chromosome inactivation [141], telomere maintenance [142], gene imprinting [143] and cell differentiation [144]. Depending on their subcellular localisation and exerted functions, lncRNAs can be broadly classified into three groups: (1) lncRNAs that are strictly localised in the nucleus and execute their actions on genes adjacent to their own gene locus (cis-regulatory functions), (2) lncRNAs that are mainly localised in the nucleus and execute their actions on genes distant to their own gene locus (trans-regulatory functions) and finally (3) lncRNAs that predominantly localise and function in the cytoplasm (reviewed [137]). Cis-regulatory lncRNAs can mediate the expression of neighboring genes by recruiting transcription factors, chromatin organisers or chromatin modifiers to their site of transcription, thereby either enhancing or inhibiting the transcriptional activity of adjacent genes (reviewed in [145]). A well studied cis-regulatory human lncRNA is HOXA transcript at the distal tip (HOTTIP), which has been shown to regulate the expression of multiple adjacent

*Hoxa* genes. When brought in close proximity to the *Hoxa* gene locus via chromosomal looping, HOTTIP binds the histone methyltransferase complex WDR5-MLL, which facilitates transcriptional activation of the *Hoxa* gene locus via methylation of histone H3 on lysine residue 4 (H3K4me3) [146].

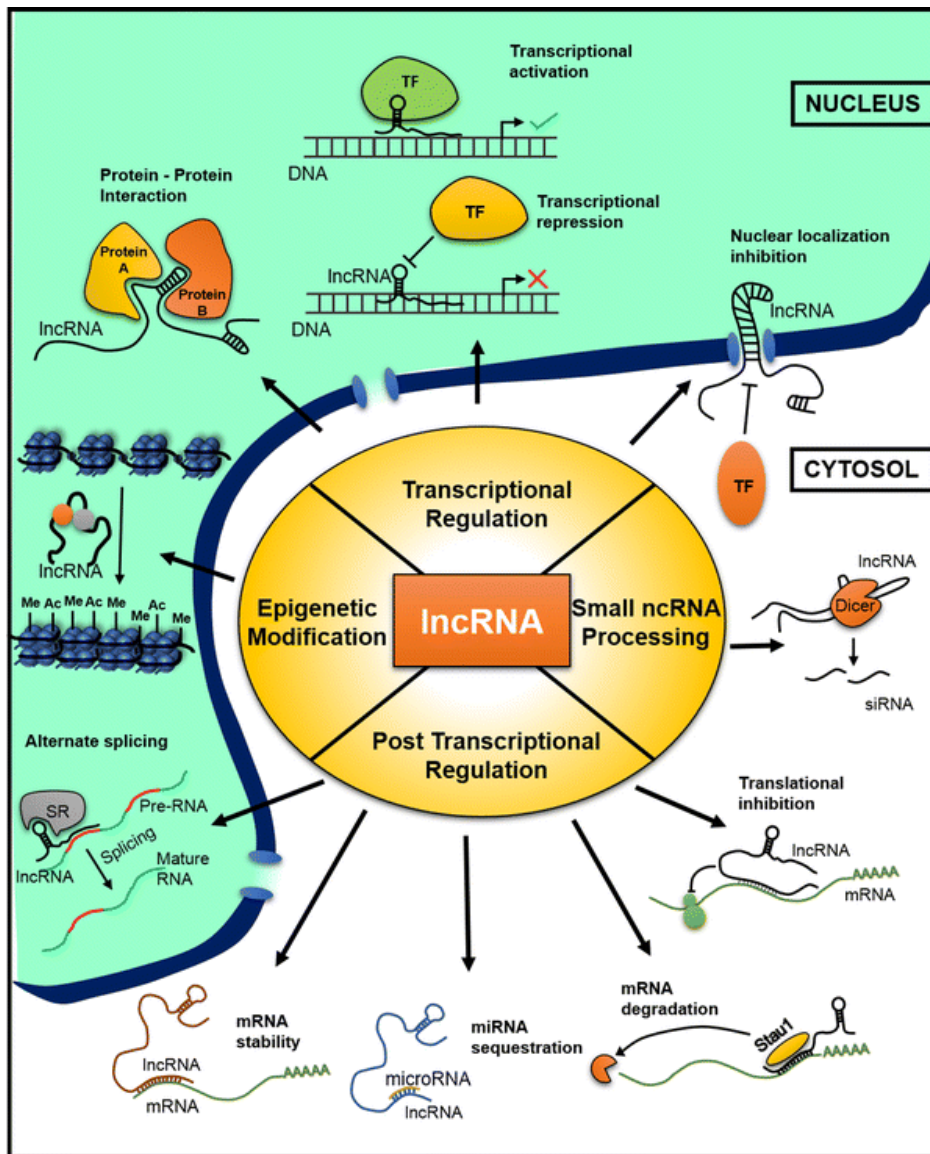


**Figure 5: Cellular processes regulated by long noncoding RNAs.**

Long noncoding RNAs (lncRNAs) control a plethora of various cellular mechanisms, such as transcriptional and post transcriptional regulation, epigenetic modification as well as small noncoding RNA (ncRNA) processing. Transcriptional regulation by lncRNAs includes scaffolding functions to enable protein-protein interactions as well as modulations of the activity, subcellular localisation or DNA-binding capacity of transcription factors and other proteins. By mediating activity and DNA binding of DNA methyltransferases and chromatin modifier proteins, lncRNAs can also facilitate epigenetic modifications at specific genomic regions like DNA methylation or histone modifications. Posttranscriptionally, lncRNAs moderate the regulation of splicing, translation or degradation of other RNA molecules and can also sequester, and thus inactivate, other ncRNAs molecules, such as

miRNAs. Via binding to Dicer, the main enzyme involved in RNA processing, lncRNAs mediate processing of other RNA species or get processed themselves to generate inhibitory small interfering RNA (siRNA) molecules. Figure taken from [147].

In contrast to cis-regulatory lncRNAs, trans-regulatory lncRNAs perform their functions far from their sites of synthesis, for instance by binding to RNA-binding proteins, such as members of the heterogenous nuclear ribonucleoprotein family (hnRNPs), which modulate gene expression, alternative splicing and mRNA stability (reviewed in [148]). Additional functions exerted by lncRNAs *in trans* include scaffolding for protein-protein interactions [149], modulation of protein activity or localisation [150] and multiplex epigenetic silencing in response to major cellular pathways [151, 152]. A prominent example for trans-regulatory lncRNAs is HOX Antisense Intergenic RNA (HOTAIR), a human lncRNA that acts as molecular scaffold binding two well-studied chromatin

modifying complexes, the polycomb repressive complex 2 (PRC2) and lysine-specific histone demethylase 1A (LSD1). By guiding these chromatin modifiers to the *Hoxd* gene locus, which is located on another chromosome than the HOTAIR transcription site, the HOTAIR lncRNA mediates epigenetic silencing of the *Hoxd* gene locus *in trans* [153].

Cytoplasmic lncRNAs can also influence gene expression of other genes, but they perform their actions either on cytoplasmic proteins by binding to specific phosphorylation sites [154] or by interacting with components of the translation machinery [155] or the RNA molecules to be translated [156]. In addition, recent studies reported that cytoplasmic lncRNAs can act as decoys for miRNAs [157] or proteins [158], thereby modulating expression levels of the RNA molecules usually targeted by the titrated miRNAs or proteins. Interestingly, some lncRNAs were shown to be posttranscriptionally processed to give rise to cytoplasmic inhibitory siRNAs or other small RNA molecules [128]. In case of metastasis associated lung adenocarcinoma transcript 1 (MALAT1), a highly expressed human lncRNA that is localised to nuclear speckles [159], the nascent MALAT1 transcript can be processed to a different transcripts that was called MALAT1-associated small cytoplasmic RNA (mascRNA) and is exclusively located within the cytoplasm [160].

In contrast to protein-coding genes, lncRNA expression is intriguingly tissue- or cell type-specific [161], which - in regard of the huge numbers and myriad functions exerted by lncRNAs - suggests versatile key regulatory roles of lncRNAs in specific cellular contexts and biological processes, such as development, adaptation to environmental cues and disease states.

### 1.3.1. Regulation of hepatic energy homeostasis by long noncoding RNAs

Despite the fact that just a few long noncoding RNAs (lncRNAs) have been functionally characterised to date, there is growing evidence that hepatic lipid and glucose metabolism is modulated by lncRNAs in mice as well as in humans. In humans, several lncRNAs have been described to have an impact on liver energy metabolism, i.a. the lncRNA colorectal neoplasia differentially expressed (CRNDE), which constitutes a downstream target of PI3K/AKT/mTOR signaling and mediates expression levels of 316 genes, some of which are associated with hepatic lipid and glucose metabolism [162], long intergenic non-coding RNA for kinase activation (LINK-A), which links PIP<sub>3</sub> and AKT to facilitate AKT enzymatic activation [163], and HCV regulated 1 (lncHR1), which suppresses lipogenesis transcription factor SREBP1c promoter activity, resulting in lower hepatic and plasma triglyceride levels [164]. However, due to the inevitable lack of human *in vivo* model systems, more insightful studies focusing on mechanisms regulating lncRNA expression and regulatory functions exerted by lncRNAs have been conducted in mice.

Gene expression analysis of murine key metabolic organs identified a liver-specific lncRNA, named liver-specific triglyceride regulator (lncLSTR), whose expression is significantly reduced in mice fasted for 24 hrs, but recovered when fasted mice were allowed to refeed for 4 hrs, indicating fluctuating expression of lncLSTR in response to the metabolic status [165]. Adenoviral-mediated knockdown of lncLSTR led to decreased levels of plasma triglycerides and glucose, both of which was implicated with lncLSTR-mediated alterations of bile acid synthesis and systemic lipid homeostasis [165].

In another study, the same group reported a lncRNA, called liver GCK repressor (lncLGR, previously labelled as 4632424N07), whose expression in mouse liver was significantly increased in mice fasted for 24 hrs and reverted to baseline expression when mice were allowed to refeed for 4 hrs after 24 hrs fasting [166]. Mechanistically, lncLGR was shown to repress the expression of the key metabolic enzyme glucokinase (GCK), resulting in suppressed hepatic GCK-mediated glycogenesis and glycogen storage during fasting [166].

In other studies hepatic fatty acid beta-oxidation was linked to the function of the lncRNA steroid RNA activator (SRA), which was initially described as transcriptional RNA co-activator for non-steroid nuclear receptors [167] and implicated to adipocyte differentiation and function [168]. Yet, upon high-fat diet-induced obesity, global SRA knockout mice not only exhibited reduced fat mass, but also reduced liver mass as well as lower levels of liver triglycerides and fatty acids, which pointed to additional hepatic functions of SRA in controlling lipid metabolism [169]. Indeed, hepatic SRA expression levels were reduced in mice fasted for 16 hrs and SRA was shown to inhibit hepatic FOXO1 transcriptional activity, thus reducing fatty acid beta-oxidation in liver in response to organismal energy levels [170].

Another lncRNA, which was demonstrated to mediate FOXO1-regulated metabolic signaling, is maternally expressed gene 3 (MEG3), a lncRNA that is upregulated in mice fed a high-fat diet [171]. Increased hepatic levels of MEG3 resulted in higher expression levels of FOXO1 as well as of gluconeogenic genes *G6pc* and *Pck1*, ultimately leading to elevated rates of hepatic gluconeogenesis. Conversely, knockdown of MEG3 in high-fat diet mice abrogated high-fat diet-induced hepatic triglyceride accumulation and facilitated higher hepatic glycogen content, demonstrating that lncRNA MEG3 not only mediates FOXO1-induced hepatic gluconeogenesis, but also glycogenesis in mouse liver [171].

Microarray analyses of mouse liver transcriptomes revealed 663 lncRNAs that were transcriptionally regulated by a 24 hour fasting regime. When mice were allowed to refeed for 4 hrs after 24 hrs fasting, 1723 hepatic lncRNAs showed significantly altered expression levels compared to mice subjected to 24 hour fasting. Interestingly, the fasting-induced regulation of 237 hepatic lncRNAs were completely reversed by refeeding, suggesting that lncRNA expression in liver is tightly and dynamically controlled by nutrient availability [172]. The same study identified a liver-specific lncRNA, labelled Gm16551, whose expression in mice is reduced by 24 hrs fasting and reinstated when 24 hrs fasting was followed by 4 hrs refeeding. Functionally, Gm16551 was identified as transcriptional target gene of lipogenesis transcription factor SREBP1c and implicated in a negative feedback loop attenuating SREBP1c activity and resulting hepatic lipogenesis. Liver-specific knockdown of Gm16551 expression in mice resulted in increased expression of key lipogenic enzymes and elevated circulating triglyceride levels. Consistently, hepatic overexpression of Gm16551 was shown to decrease lipogenic gene expression and increased levels of plasma triglycerides induced by liver-specific SREBP1c overexpression [172]. Another recent study employing high-throughput RNA sequencing of mouse livers identified 1320 liver-enriched lncRNAs that were transcriptionally regulated upon a 16 hour fasting regime [173]. By using an adenoviral overexpression vector, one of the identified lncRNAs, labelled Gm10768, was implicated in controlling hepatic gluconeogenesis, as Gm10768 overexpression in mouse liver resulted in

increased expression levels of the gluconeogenic genes *G6pc* and *Pck1* as well as in elevated insulin and glucose serum levels. In accordance, adenoviral-induced knockdown of hepatic Gm10768 in mouse liver led to significantly decreased expression levels of G6PC and PCK1 and lead to abated *de novo* hepatic glucose synthesis, improved glucose and insulin tolerance, and reduced serum levels of insulin and glucose [173]. Combining bioinformatic predictions of microRNA binding sites and Gm10768-specific luciferase reporter assays, Gm10768 was shown to interact with miR-214, a microRNA that has been identified as negative regulator of gluconeogenesis by suppressing FOXO1-associated transcriptional co-regulator activating transcription factor (ATF4) [174]. As Gm10768 overexpression antagonised miR-214 abundance and function in mouse liver, thus relieving ATF4 suppression and increasing gluconeogenic gene expression, lncRNA Gm10768 was identified as additional regulatory entity controlling hepatic gluconeogenesis in response to nutrient availability [173].

Collectively, an increasing number of recent studies demonstrated that lncRNAs represent multifaceted regulatory elements that fine-tune fundamental biological processes, like hepatic fatty acid and glucose metabolism. Importantly, the expression rates of most investigated lncRNAs correlate with specific disease states or metabolic abnormalities and, as shown in microarray and transcriptome analyses, the expression levels of a vast number of hepatic lncRNAs is dynamically fluctuating in response to nutrient availability, suggesting an important role for lncRNAs as dynamic relays facilitating rapid cellular adaptations to environmental cues.

### 1.3.2. CRISPR/Cas9-mediated genome engineering

In recent years, the clustered regularly interspaced short palindromic repeats (CRISPR)/Cas9 system has attracted increasing attention as simple, but efficient genome-editing tool. In CRISPR/Cas9 gene targeting systems, a three-component prokaryotic immune defense machinery is employed to specifically induce DNA double strand breaks (DSBs) at desired genomic positions [175]. CRISPR/Cas9-induced DSBs can be repaired by endogenous error-prone non-homologous end joining (NHEJ) or, if an additional donor template is provided, by homology-directed repair (HDR) [176]. Whereas NHEJ may result in random deletions and insertions of single nucleotides at the site of the DSB, eventually leading to gene-inactivating mutations, gene targeting via HDR can be used to precisely generate complex alleles [177].

Components of the CRISPR/Cas9 system include the RNA-guided DNA endonuclease CRISPR associated protein 9 (Cas9) as well as the guide RNA (gRNA), a RNA hybrid molecule composed of two different RNA molecules, known as the CRISPR RNA (crRNA) and the trans-activating RNA (tracrRNA) [178]. Whereas the spacer sequence of the crRNA determines the genomic sequence where a DSB will be induced by endonuclease Cas9, the tracrRNA is essential for crRNA maturation and the activity of the crRNA-tracrRNA-Cas9 ribonucleoprotein complex [179].

Using a 4-nucleotide linker, the 5' end of a tracrRNA can be fused to the 3' end of a crRNA to create a chimeric single guide RNA (sgRNA) molecule that exhibits all features of naturally occurring crRNA:tracrRNA hybrid molecules [176]. In this way, the gRNA hybrid can be produced as a single oligonucleotide, which may be beneficial for cost-intensive *in vitro* screenings.



In the last few years, CRISPR/Cas9 gene editing technology has been successfully established in several model organisms to facilitate targeted genetic mutations, including *Caenorhabditis elegans* [180], *Drosophila melanogaster* [181], *Danio rerio* [182] and *Mus musculus* [183]. However, to our knowledge CRISPR/Cas9-mediated genome engineering has not yet been used to generate lncRNA knockout mouse models and still remains an unexplored resource in the field of lncRNA biology.

### 1.3.3. The therapeutical potential of RNA interference-based agents

With microRNA-targeting therapeutics already reaching clinical development [184], lncRNAs have recently also been recognised as promising targets for RNA therapeutics. The main principle behind RNA therapeutic agents is a natural intracellular mechanism called RNA interference, which uses RNA molecules to inhibit the expression of other RNA molecules in a post-transcriptional manner [185]. Endogenous RNA molecules central to RNA interference are microRNAs (miRNAs) and small interfering RNAs (siRNAs), both of which are used as templates by the RNA-induced silencing complex (RISC) to cause sequence-specific targeting of other RNA species [185]. Gene silencing is achieved through imperfect base pairing between target RNAs and miRNAs, resulting in translation repression and finally RNA degradation, or through complement base pairing between target RNAs and siRNAs, followed by endonucleolytic cleavage of the target RNA (reviewed in [186]). Yet, whereas miRNAs and siRNAs are natural RNA templates produced by the organism to fine-tune expression of other genes in response to environmental cues or metabolic states, the endogenous RNAi machinery can also be exploited by exogenous RNA molecules like artificial siRNA or short hairpin RNA (shRNAs) therapeutics to specifically target expression of disease-associated genes, including lncRNAs [187]. However, RNA molecules are inherently unstable due to rapid degradation by the organism and hence require chemical modifications and/or delivery vehicles for efficient uptake by the targeted cell type [187].

In previous years, several studies have identified nucleic acid analogs with chemical modifications that promote RNA stability, target specificity and affinity, or decreased susceptibility to endonuclease degradation (reviewed in [188]). These modifications include 2'-O, 4'-C-methylene linked bicyclic ribonucleotides, which are known as locked nucleic acids (LNAs) and possess improved targeting potency and resistance to nucleases [189]. In combination with phosphorothioate-modified backbones that additionally increase nuclease resistance [190], LNA analogs can be utilised in single-stranded antisense oligonucleotides (ASO) that provide specific and efficient targeting of complementary RNA molecules. A very potent form of synthetic ASOs are GapmeRs, which are chimeric molecules containing a central block ('gap') of DNA nucleotides that mediate target recognition flanked by terminal LNA analogs that protect the ASO from exonuclease activity [191]. Upon binding of complementary RNA molecules to GapmeRs, the ubiquitously expressed ribonuclease H (RNase H) mediates cleavage of the RNA strand of the RNA-LNA heteroduplex, resulting in efficient degradation of the target RNA and the GapmeR remaining active after target RNA cleavage [192].

Collectively, RNA therapeutics such as LNA GapmeRs promise a molecular pharmaceutical approach enabling specific and versatile targeting of all genes expressed, including lncRNAs. Importantly, the high tissue specificity of lncRNAs allows site-specific manipulation of lncRNA expression levels without undesirable side effects in other tissues. However, improved delivery strategies need to be developed in order to guarantee effective and immuno-compatible transport of the agent through the body to ultimately fully harness the power of RNA-based therapeutics.

#### 1.4. Research objectives

Obesity has reached global epidemic dimensions and concomitant deregulations of glucose and lipid metabolism foster the development of obesity-associated diseases like cardiovascular pathologies and T2DM. The liver represents the central hub of energy homeostasis as it is not only the major site for carbohydrate and lipid biosynthesis, but also a precise regulator of blood glucose levels. Although many signaling pathways and key molecules controlling liver energy homeostasis have been identified, the molecular mechanisms integrating nutrient availability and organismal energy demand remain insufficiently understood.

Long noncoding RNAs represent a vast, yet poorly characterised class of functional RNA elements, some of which have been implicated in fine-tuning several major developmental processes in response to environmental cues or disease conditions. However, just a few studies have identified lncRNAs governing liver energy homeostasis and a multitude of lncRNA genes have not yet been ascribed to specific molecular functions.

By combining next-generation sequencing with RNA biology and mouse transgenics, the present study aimed to elucidate (1) if hepatic lncRNA expression globally correlates with metabolic conditions, such as obesity, T2DM and short-term alterations of nutrient availability, (2) if selected murine hepatic lncRNAs functionally contribute to the regulation of liver energy homeostasis *in vivo* and (3) how selected lncRNAs affect metaboregulatory signaling circuits.



## Chapter 2 - Materials

### 2.1. General materials

- Cell scraper [25 cm, 39 cm]  
(Product IDs: 83.1830, 83.1831, Sarstedt AG & Co., Nümbrecht, DE)
- Cell strainer, EASYstrainer™, 40 µm  
(Product ID: 542040, Greiner Bio-One GmbH, Kremsmünster, AT)
- Centrifugation tubes, Falcon®, polypropylene [15 ml, 50 ml]  
(Product IDs: 352096, 352070, Corning Corp., Corning, US)
- Ceramic beads, Precellys® zirconium oxide beads, 1.4 mm  
(Product ID: 03961-1-103, Cayman Chemical, Ann Arbor, US)
- Chromatography paper, Whatman™  
(Product ID: 3030-861, GE Healthcare, Chicago, US)
- Cover glasses, 24 x 32 mm  
(Product ID: 0102112, VWR International GmbH, Radnor, US)
- Cryo tubes, CryoPure®, 1.8 ml  
(Product ID: 72.379.005, Sarstedt AG & Co., Nümbrecht, DE)
- Density gradient medium, Percoll®  
(Product ID: GE17-0891-02, Sigma-Aldrich Chemie GmbH, Schnelldorf, DE)
- Disinfectant, Bacillol® AF  
(Product ID: 9733803, BODE Chemie GmbH, Hamburg, DE)
- Dispenser, Multipette® E3  
(Product ID: 4987000010, Eppendorf AG, Hamburg, DE)
- Dispenser-tips, Combitips advanced® [0.2 ml, 2.5 ml]  
(Product IDs: 613-2059, 613-2062, Eppendorf AG, Hamburg, DE)
- DNA gel loading dye, 6X  
(Product ID: R0611, Thermo Fisher Scientific, Waltham, US)
- DNA ladder mix, GeneRuler™  
(Product ID: SM0331, Thermo Fisher Scientific, Waltham, US)
- Dulbecco's modified eagle medium (DMEM), GlutaMAX™, high glucose (4.5g/l), 1X  
(Product ID: 10569010, Thermo Fisher Scientific, Waltham, US)
- Dulbecco's modified eagle medium (DMEM), low glucose (1g/l), 1X  
(Product ID: 11880036, Thermo Fisher Scientific, Waltham, US)
- Dulbecco's modified eagle medium (DMEM), no glucose, 1X  
(Product ID: 11966025, Thermo Fisher Scientific, Waltham, US)
- Dulbecco's phosphate-buffered saline (DPBS), 10X  
(Product ID: 14190169, Thermo Fisher Scientific, Waltham, US)
- Earle's balanced salt solution (EBSS), calcium, magnesium, phenol red, 1X  
(Product ID: 24010043, Thermo Fisher Scientific, Waltham, US)
- Earle's balanced salt solution (EBSS), no calcium, no magnesium, no phenol red, 1X  
(Product ID: 14155048, Thermo Fisher Scientific, Waltham, US)
- LB-Medium Powder, according to Miller  
(Product ID: A0954, AppliChem GmbH, Darmstadt, DE)
- L-Glutamine solution, 100X  
(Product ID: 25030081, Thermo Fisher Scientific, Waltham, US)
- Multichannel pipette, Transferpette® S-8  
(Product ID: 703708, Brand GmbH + CO KG, Wertheim, DE)
- Neubauer improved cell counting chamber, 0.01 mm  
(Product ID: N/A, W. Schreck, Hofheim am Taunus, DE)

- Needles, Sterican®, 0.45 x 12mm  
(Product ID: 4665457, B. Braun Melsungen AG, Melsungen, DE)
- Nitrocellulose western blotting membrane, Amersham™ Protran® Premium, 0,45 µm  
(Product ID: 10600047, GE Healthcare, Chicago, US)
- Non-essential amino acids (NEAA) solution, 100X  
(Product ID: 11140050, Thermo Fisher Scientific, Waltham, US)
- Nucleic acid staining solution, Midori Green Advance®  
(Product ID: 617004, Biozym Scientific GmbH, Hessisch Oldendorf, DE)
- Optical 384-well reaction plate with barcode, MicroAmp™  
(Product ID: 4309849, Thermo Fisher Scientific, Waltham, US)
- Optical adhesive film, MicroAmp™  
(Product ID: 4311971, Thermo Fisher Scientific, Waltham, US)
- Pasteur pipettes, non-sterile  
(Product ID: 612-1701, VWR International GmbH, Radnor, US)
- PCR lid strips, Multiply® 8-lid chain, flat  
(Product ID: 65.989.002, Sarstedt AG & Co., Nümbrecht, DE)
- PCR tubes, Multiply®-µStrip, 0.2 ml  
(Product ID: 72.985.002, Sarstedt AG & Co., Nümbrecht, DE)
- Penicillin-streptomycin solution, 10.000 U/ml  
(Product ID: 15140122, Thermo Fisher Scientific, Waltham, US)
- Petri dishes, 94 x 16 mm  
(Product ID: PP90, A. Hartenstein GmbH, Würzburg, DE)
- Pipetboy, accu-jet® pro  
(Product ID: 26300, Brand GmbH + CO KG, Wertheim, DE)
- Pipettes, Transferpette® S Starter Kit  
(Product ID: 613-3478, Brand GmbH + CO KG, Wertheim, DE)
- Pipette-tips [10 µl, 200 µl, 1000 µl]  
(Product IDs: 771255, 739265, 686271, Greiner Bio-One GmbH, Kremismünster, AT)
- Pipette-tips, filtered [0.5-10 µl, 5-100 µl, 50-1000 µl]  
(Product IDs: 732724, 732730, 732734, Brand GmbH + CO KG, Wertheim, DE)
- Pipette with tip, sterile [5 ml, 10 ml, 25 ml, 50 ml]  
(Product IDs: 606180, 607180, 760180, 768180, Greiner Bio-One GmbH, Kremismünster, AT)
- Precast gels, Mini-PROTEAN® TGX™, 10-well [4-15 %, 7.5 %]  
(Product IDs: 4561084, 4561023, Bio-Rad Laboratories, Inc., Hercules, US)
- Prestained protein ladder, PageRuler™, 10 to 180 kDa  
(Product ID: 26616, Thermo Fisher Scientific, Waltham, US)
- PVDF transfer pack, Trans-Blot® Turbo™ Mini  
(Product ID: 1704156, Bio-Rad Laboratories, Inc., Hercules, US)
- Reaction tubes, SafeSeal® [0.5 ml, 1.5 ml, 2.0 ml]  
(Product IDs: 72.704, 72.706, 72.695.600, Sarstedt AG & Co., Nümbrecht, DE)
- Reduced serum medium, Opti-MEM™  
(Product ID: 31985062, Thermo Fisher Scientific, Waltham, US)
- Syringes, Injekt®-F, 1 ml  
(Product ID: 9166017V, B. Braun Melsungen AG, Melsungen, DE)
- Tissue culture dish, TPP®, 15 cm  
(Product ID: Z707694, Sigma-Aldrich Chemie GmbH, Schnellendorf, DE)
- Tissue culture plate, Corning® BioCoat™, collagen I-coated [6-well, 12-well]  
(Product IDs: 356400, 356500, Corning Corp., Corning, US)
- Tissue culture plate, Falcon®, polystyrene [6-well, 12-well]  
(Product IDs: 353046, 353043, Corning Corp., Corning, US)

- Tissue culture plate, Falcon®, polystyrene ,10 cm  
(Product ID: 353003, Corning Corp., Corning, US)
- Tissue freezing medium  
(Product ID: 14020108926, Leica Biosystems Nussloch GmbH, Nussloch, DE)
- Water, BioXtra, for embryo transfer, sterile-filtered  
(Product ID: W1503, Sigma-Aldrich Chemie GmbH, Schnelldorf, DE)
- Western blocking reagent, solution  
(Product ID: 11921673001, Roche Diagnostics GmbH, Mannheim, DE)

## 2.2. Technical equipment

- Analysis system, Agilent 2100 Bioanalyzer  
(Agilent Technologies, Inc., Santa Clara, US)
- Analytical balances, Quintix® 124-1S & Quintix® 612-1S  
(Sartorius AG, Göttingen, DE)
- Blood glucose monitoring system + sensors, Contour® XT  
(Bayer Healthcare, Leverkusen, DE)
- Cell culture cabinet, Scanlaf Mars, safety class II  
(LaboGene ApS, Allorød, DK)
- Centrifuge, 5810 R  
(Eppendorf AG, Hamburg, DE)
- Chemiluminescence imaging system, Fusion Solo  
(Vilber Gourmet Deutschland GmbH, Eberhardzell, DE)
- CO<sub>2</sub>-Incubator, C 170  
(BINDER GmbH, Tuttlingen, DE)
- CO<sub>2</sub>-Incubator, Heracell™ 150i  
(Thermo Fisher Scientific, Waltham, US)
- Digital printer, P95DE  
(Mitsubishi Electric Corporation., Chiyoda, JP)
- Electrophoresis and blotting system, Mini-PROTEAN Tetra Cell  
(Bio-Rad Laboratories, Inc., Hercules, US)
- Electrophoretic transfer module, Mini Trans-Blot Cell  
(Bio-Rad Laboratories, Inc., Hercules, US)
- Fume cupboard, CC-30  
(Caspar & Co. Labora GmbH, Aachen, DE)
- Gel documentation system, FastGene® FAS V  
(Nippon Genetics Europe GmbH, Düren, DE)
- Gel electrophoresis chamber, PerfectBlue™ Mini  
(VWR International GmbH, Radnor, US)
- Homogenizer, FastPrep-24™ 5G  
(MP Biomedicals Germany GmbH, Eschwege, DE)
- Inverted microscope, DM IL LED  
(Leica Microsystems CMS GmbH, Wetzlar, DE)
- Laboratory freezer, Forma™ 88000  
(Thermo Fisher Scientific, Waltham, US)
- Laboratory freezer, LGex 3410 Mediline  
(Liebherr-International AG, Bulle, CH)
- Microcentrifuge, refrigerated, Micro Star 17R  
(VWR International GmbH, Radnor, US)
- Microplate reader, FilterMax™ F5  
(Molecular Devices, LLC, San José, US)

- PCR-Thermocycler, FlexCycler<sup>2</sup>  
(Analytik Jena AG, Jena, DE)
- PhenoMaster, Automated Home Cage Phenotyping  
(TSE Systems GmbH, Bad Homburg vor der Höhe, DE)
- Platform shaker, Polymax 1040  
(Heidolph Instruments GmbH & Co. KG, Schwabach, DE)
- Power Supply, PowerPac™ HC  
(Bio-Rad Laboratories, Inc., Hercules, US)
- Real-Time PCR System, QuantStudio™ 7 Flex  
(Applied Biosystems, Foster City, US)
- Refrigerator, KT 1730-26  
(Liebherr-International AG, Bulle, CH)
- Shaker, IKA® MS 3  
(IKA Werke GmbH & Co. KG, Staufen im Breisgau, DE)
- Spectrophotometer, NanoDrop™ ND-1000  
(NanoDrop Technologies, LLC, Wilmington, US)
- Thermoshaker, MKR 23  
(Hettich Benelux B.V., Geldermalsen, NL)
- Ultracentrifuge, Heraeus™ Megafuge™ 16R  
(Thermo Fisher Scientific, Waltham, US)
- Vortex mixer, Vortey-Genie 2  
(Scientific Industries, Inc., Bohemia, US)
- Water bath, model 1003  
(GFL Gesellschaft für Labortechnik mbH, Burgwedel, DE)
- Water purification system, Milli-Q® Advantage A10  
(Merck Millipore, Darmstadt, DE)
- Western blotting transfer system, Trans-Blot® Turbo™  
(Bio-Rad Laboratories, Inc., Hercules, US)

## 2.3. Chemicals

- 2-Propanol (isopropanol), for molecular biology, min. 99.5%  
(Product ID: I9516, Sigma-Aldrich Chemie GmbH, Schnelldorf, DE)
- 5-Bromo-4-chloro-3-indolyl-β-D-galactopyranoside (X-Gal), min. 99%  
(Product ID: R0404, Thermo Fisher Scientific, Waltham, US)
- β-Glycerophosphate disodium salt hydrate, min. 99%  
(Product ID: G9422, Sigma-Aldrich Chemie GmbH, Schnelldorf, DE)
- β-Mercaptoethanol, min. 99%  
(Product ID: A1108, AppliChem GmbH, Darmstadt, DE)
- Acetic acid, glacial, min. 90%  
(Product ID: BAKR9522, VWR International GmbH, Radnor, US)
- Acrylamide-bisacrylamide stock solution, Rotiphorese® Gel 30  
(Product ID: 3029, Carl Roth GmbH + Co. KG)
- Agarose, for molecular biology  
(Product ID: A9539, Sigma-Aldrich Chemie GmbH, Schnelldorf, DE)
- Agarose, UltraPure™  
(Product ID: 16500100, Thermo Fisher Scientific, Waltham, US)
- Ammonium persulfate (APS), pure  
(Product ID: 1610700, Bio-Rad Laboratories, Inc., Hercules, US)
- Ampicillin sodium salt, min. 91%  
(Product ID: A0839, AppliChem GmbH, Darmstadt, DE)

- Aprotinin, from bovine lung, 3-8 TIU/mg  
(Product ID: A3428, Sigma-Aldrich Chemie GmbH, Schnelldorf, DE)
- Bovine serum albumin (BSA), min. 98%  
(Product ID: A8806, Sigma-Aldrich Chemie GmbH, Schnelldorf, DE)
- Calcium chloride dihydrate (CaCl<sub>2</sub>-2H<sub>2</sub>O), min. 99%  
(Product ID: C7902, Sigma-Aldrich Chemie GmbH, Schnelldorf, DE)
- Chemiluminescence substrate, SuperSignal™ West Dura Extended Duration  
(Product ID: 34076, Thermo Fisher Scientific, Waltham, US)
- D-(+)-Glucose, min. 99.5%  
(Product ID: G7021, Sigma-Aldrich Chemie GmbH, Schnelldorf, DE)
- Dexamethasone, min. 97%  
(Product ID: D4902, Sigma-Aldrich Chemie GmbH, Schnelldorf, DE)
- Diethylpyrocarbonate (DEPC)-treated and sterile filtered water  
(Product ID: 95284, Sigma-Aldrich Chemie GmbH, Schnelldorf, DE)
- Dimethylformamide (DMF), min. 99%  
(Product ID: D4551, Sigma-Aldrich Chemie GmbH, Schnelldorf, DE)
- Dimethylsulfoxide (DMSO), 99 %  
(Product ID: 1096780100, Merck Millipore, Darmstadt, DE)
- DNA/RNA purification reagent, peqGOLD TriFast™  
(Product ID: 30-2010, VWR International GmbH, Radnor, US)
- Ethanol absolut, AnalaR NORMAPUR®, min. 99.8%  
(Product ID: 20821.296, VWR International GmbH, Radnor, US)
- Ethylene glycol-bis(2-aminoethylether)-tetraacetic acid (EGTA), min. 99%  
(Product ID: A0878, AppliChem GmbH, Darmstadt, DE)
- Ethylenediaminetetraacetic acid (EDTA), min. 98%  
(Product ID: E6758, Sigma-Aldrich Chemie GmbH, Schnelldorf, DE)
- Fetal Bovine Serum (FBS), South America Premium  
(Product ID: P30-3301, Pan - Biotech GmbH, Aidenbach, DE)
- Forskolin, min. 98%  
(Product ID: F3917, Sigma-Aldrich Chemie GmbH, Schnelldorf, DE)
- Glucagon, human recombinant, min. 95%  
(Product ID: G2044, Sigma-Aldrich Chemie GmbH, Schnelldorf, DE)
- Glucose-solution 20 %, ad us. vet.  
(Product ID: 2069.97.99 (prescription drug), bela-pharm GmbH & Co. KG, Vechta, DE)
- Glycine, biotechnology grade  
(Product ID: 444495D, VWR International GmbH, Radnor, US)
- Hydrochloric acid (HCl), 37%  
(Product ID: 211020, AppliChem GmbH, Darmstadt, DE)
- Insulin solution, human recombinant, 9.5 - 10.5 mg/ml  
(Product ID: I9278, Sigma-Aldrich Chemie GmbH, Schnelldorf, DE)
- Insulin solution, Insuman® Rapid, 40 I.E./ml  
(Product ID: 08923000, Sanofi-Aventis Deutschland GmbH, Frankfurt am Main, DE)
- Isopropyl-β-D-thiogalactopyranoside (IPTG), dioxane-free, min. 99%  
(Product ID: R0392, Thermo Fisher Scientific, Waltham, US)
- Isotonic sodium chloride solution, ad us. vet.  
(Product ID: 1409.99.99 (prescription drug), bela-pharm GmbH & Co. KG, Vechta, DE)
- Ketamin injection solution, Anesketin®, 100 mg/ml  
(Product ID: 401780.00.00 (prescription drug), Albrecht GmbH, Aulendorf, DE)
- Laemmli sample buffer, 4X  
(Product ID: 1610747, Bio-Rad Laboratories, Inc., Hercules, US)

- Magnesium chloride hexahydrate (MgCl<sub>2</sub>·6H<sub>2</sub>O), min. 99%  
(Product ID: M2393, Sigma-Aldrich Chemie GmbH, Schnelldorf, DE)
- Membrane staining solution, Ponceau S, 0.1 %  
(Product ID: P7170, Sigma-Aldrich Chemie GmbH, Schnelldorf, DE)
- Methanol, ROTIPURAN®, min. 99.9%  
(Product ID: 4627.1, Carl Roth GmbH + Co. KG)
- N-2-hydroxyethylpiperazine-N-2-ethane sulfuric acid (HEPES) buffer solution, 1M  
(Product ID: 15630049, Thermo Fisher Scientific, Waltham, US)
- N, N, N', N'-Tetramethylethylenediamin (TEMED), min. 99.5%  
(Product ID: A1148, AppliChem GmbH, Darmstadt, DE)
- Nonylphenylpolyethylenglycol (Nonidet™ P40), min. 99%  
(Product ID: A1694, AppliChem GmbH, Darmstadt, DE)
- Phenylmethylsulfonyl fluoride (PMSF), min. 98.5 %  
(Product ID: P7626, Sigma-Aldrich Chemie GmbH, Schnelldorf, DE)
- Phosphatase inhibitor tablets, PhosSTOP™  
(Product ID: 04906837001, Sigma-Aldrich Chemie GmbH, Schnelldorf, DE)
- Potassium chloride (KCl), min. 99%  
(Product ID: P9333, Sigma-Aldrich Chemie GmbH, Schnelldorf, DE)
- Protease inhibitor tablets, Complete™ Mini  
(Product ID: 4693159001, Roche Diagnostics, Rotkreuz, CH)
- RNase decontamination solution, RNaseZAP™  
(Product ID: R2020, Sigma-Aldrich Chemie GmbH, Schnelldorf, DE)
- RNase inhibitor, RNasin® Plus  
(Product ID: N2511, Promega GmbH, Mannheim, DE)
- Sodium acetate (NaAc), min. 99%  
(Product ID: S5636, Sigma-Aldrich Chemie GmbH, Schnelldorf, DE)
- Sodium chloride (NaCl), pure  
(Product ID: 443827W, VWR International GmbH, Radnor, US)
- Sodium dodecyl sulfate (SDS), min. 99%  
(Product ID: A1112, AppliChem GmbH, Darmstadt, DE)
- Sodium fluoride (NaF), min. 99 %  
(Product ID: S6776, Sigma-Aldrich Chemie GmbH, Schnelldorf, DE)
- Sodium hydroxide (NaOH), AnalaR NORMAPUR®, solid  
(Product ID: 28244.295, VWR International GmbH, Radnor, US)
- Sodium pyruvate solution, 100 mM  
(Product ID: 11360070, Thermo Fisher Scientific, Waltham, US)
- Transfection reagent, Lipofectamine™ 2000  
(Product ID: 11668019, Thermo Fisher Scientific, Waltham, US)
- Transfection reagent, Lipofectamine™ RNAiMAX  
(Product ID: 13778150, Thermo Fisher Scientific, Waltham, US)
- Trichlormethane (chloroform), min. 99.8 %  
(Product ID: 4432.1, Carl Roth GmbH + Co. KG)
- Tris-(hydroxymethyl)-aminomethane (Tris), AnalaR, solid  
(Product ID: 103156X, VWR International GmbH, Radnor, US)
- Tris hydrochloride (Tris-HCl), solid  
(Product ID: A3452, AppliChem GmbH, Darmstadt, DE)
- Trypan blue solution, 0.4%  
(Product ID: T8154, Sigma-Aldrich Chemie GmbH, Schnelldorf, DE)
- Trypsin-EDTA (0.5%), no phenol red, 10X  
(Product ID: 15400054, Thermo Fisher Scientific, Waltham, US)

- Trypsin inhibitor from *Glycine max* (soybean)  
(Product ID: T6522, Sigma-Aldrich Chemie GmbH, Schnelldorf, DE)
- Tween® 20 (polysorbate), for molecular biology  
(Product ID: 437082Q, VWR International GmbH, Radnor, US)
- Xylazine injection solution, Rompun® 2%  
(Product ID: 6293841.00.00 (prescription drug), Bayer Vital GmbH, Leverkusen, DE)

## 2.4. Molecular biology reagents

- Agilent RNA 600 Nano Kit  
(Product ID: 5067-1511, Agilent Technologies, Inc., Santa Clara, US)
- Agilent RNA 600 Pico Kit  
(Product ID: 5067-1513, Agilent Technologies, Inc., Santa Clara, US)
- Alt-R® S.p. Cas9 Nuclease 3NLS  
(Product ID: 1074181, Integrated DNA Technologies, Inc., Skokie, US )
- Cas9 mRNA (5meC, Psi)  
(Product ID: L-6125-20, TriLink BioTechnologies, Inc., San Diego, US)
- Collagenase, Type 4  
(Product ID: LS004189, Worthington Biochemical Corporation, Lakewood, US)
- DNase I (RNase-free)  
(Product ID: M0303, New England Biolabs GmbH, Ipswich, US)
- dNTP set, 100 mM solutions  
(Product ID: R0182, Thermo Fisher Scientific, Waltham, US)
- DreamTaq Green DNA Polymerase (5 U/µl)  
(Product ID: EP0714, Thermo Fisher Scientific, Waltham, US)
- ERRC RNA Spike-In Mix  
(Product ID: 4456740, Thermo Fisher Scientific, Waltham, US)
- High-Capacity cDNA Reverse Transcription Kit  
(Product ID: 4368814, Thermo Fisher Scientific, Waltham, US)
- High Fidelity PCR Master Kit  
(Product ID: 12140314001, Roche Diagnostics GmbH, Mannheim, DE)
- HiScribe™ T7 High Yield RNA Synthesis Kit  
(Product ID: E2040, New England Biolabs GmbH, Ipswich, US)
- MinElute PCR Purification Kit  
(Product ID: 28006, QIAGEN N.V., Venlo, NL)
- NEBNext® rRNA Depletion Kit (Human/Mouse/Rat)  
(Product ID: E6310, New England Biolabs GmbH, Ipswich, US)
- NEBNext® Ultra™ Directional RNA Library Prep Kit for Illumina®  
(Product ID: E7420, New England Biolabs GmbH, Ipswich, US)
- Nuclei EZ Prep Nuclei Isolation Kit  
(Product ID: NUC101, Sigma-Aldrich Chemie GmbH, Schnelldorf, DE)
- NucleoBond® Xtra Maxi  
(Product ID: 740414, Macherey-Nagel GmbH & Co., Düren, DE)
- NucleoSpin® RNA Kit  
(Product ID: 740955, Macherey-Nagel GmbH & Co., Düren, DE)
- PCR Mycoplasma Test Kit  
(Product ID: A3744, AppliChem GmbH, Darmstadt, DE)
- pGEM®-T Easy Vector System I  
(Product ID: A1360, Promega Corp., Madison, US)

- Phusion® High-Fidelity DNA Polymerase  
(Product ID: M0530, New England Biolabs GmbH, Ipswich, US)
- Pierce BCA Protein Assay Kit  
(Product ID: 23225, Thermo Fisher Scientific, Waltham, US)
- Proteinase K, recombinant, PCR grade  
(Product ID: 03115844001, Roche Diagnostics GmbH, Mannheim, DE)
- pX330-U6-Chimeric\_BB-CBh-hSpCas9 plasmid  
(Plasmid #42230, Addgene, Cambridge, US)
- QIAquick® Gel Extraction Kit  
(Product ID: 28706, QIAGEN N.V., Venlo, NL)
- QIAshredder® Cell Homogenization Kit  
(Product ID: 79656, QIAGEN N.V., Venlo, NL)
- Quick Start™ Bradford Protein Assay Kit 1  
(Product ID: 5000201, Bio-Rad Laboratories, Inc., Hercules, US)
- Ribo-Zero rRNA Removal Kit (Human/Mouse/Rat)  
(Product ID: RS-122-2001/2, Illumina, San Diego, US)
- RNase A, DNase and protease-free (10 mg/ml)  
(Product ID: EN0531, Thermo Fisher Scientific, Waltham, US)
- RNeasy® Mini Kit  
(Product ID: 74106, QIAGEN N.V., Venlo, NL)
- SYBR™ Select Master Mix  
(Product ID: 4472903, Thermo Fisher Scientific, Waltham, US)
- T4 DNA Ligase  
(Product ID: M0202, New England Biolabs GmbH, Ipswich, US)
- T7 Endonuclease I  
(Product ID: M0302, New England Biolabs GmbH, Ipswich, US)
- TaqMan™ Gene Expression Master Mix  
(Product ID: 4369016, Thermo Fisher Scientific, Waltham, US)
- TruSeq RNA Library Prep Kit v2  
(Product ID: MRZH116/124, Illumina, San Diego, US)
- TURBO DNA-free™ Kit  
(Product ID: AM1907, Thermo Fisher Scientific, Waltham, US)
- Ultracompetent cells, XL10-Gold®  
(Product ID: 200314, Agilent Technologies, Inc., Santa Clara, US)

## 2.5. Antibodies

Antigen	Source	Dilution	Company & Product ID
AKT (pan) (11E7)	Rabbit	1:1000	Cell Signaling Technology, ID: 4685
Calnexin (C-term. 575-593)	Rabbit	1:5000	Merck Millipore, ID: 208880
Phospho-AKT (Ser473)	Rabbit	1:1000	Cell Signaling Technology, ID: 9271
Rabbit (IgG)	Goat	1:5000	Sigma-Aldrich, ID: A6154



## 2.6. PCR primer

### Genotyping primer

4833411C07Rik-delta external PCR forward (#409)  
4833411C07Rik-delta external PCR reverse (#408)  
4833411C07Rik-delta internal PCR forward (#407)  
4833411C07Rik-delta internal PCR reverse (#410)  
Gm15441-delta external PCR forward (#411)  
Gm15441-delta external PCR reverse (#242)  
Gm15441-delta internal PCR forward (#239)  
Gm15441-delta internal PCR reverse (#240)

### Sequence (5' -> 3')

TGCGCAATAGGTCCCCACAAACAC  
TTTCTTTCTTTCTTTCTCGTCTGA  
GGTGGGGTCAGGAGCTTGTTTACT  
CTAGAAACAGACCACCAATCAGC  
GACCCCTTGTTCTTGTGTGGC  
AGAGCACAGACAGACAGACC  
TCTAGAGCCTGGAAAAGCGC  
CTCTAGCTCCCAAAGGCACC

### Primer for sgRNA synthesis

pX330-5' reverse primer

### Sequence (5' -> 3')

AAAAAGCACCGACTCGGTGCC

Gm15441-5'-1 (18)

TTAATACGACTCACTATAGGAGGCAGAACTCTACGGGAGTTTTAGAGCTAGAAATAGC

Gm15441-5'-2 (18)

TTAATACGACTCACTATAGGCCTTGGCTCACTAGGTGAGTTTTAGAGCTAGAAATAGC

Gm15441-3'-1 (18)

TTAATACGACTCACTATAGGTCCATCAGACTAGTCTGTGTTTTAGAGCTAGAAATAGC

Gm15441-3'-2 (18)

TTAATACGACTCACTATAGGCACCGTAGGCGGTTTCATTGTTTTAGAGCTAGAAATAGC

InclRS2-5'-1 (18)

TTAATACGACTCACTATAGGAGATGTTTATTTGTCGCGTTTTAGAGCTAGAAATAGC

InclRS2-5'-2 (18)

TTAATACGACTCACTATAGGTAAACACATTCCGGGTGGTTTTAGAGCTAGAAATAGC

InclRS2-3'-1 (18)

TTAATACGACTCACTATAGGCAGTCCTCAAATGCTGATGTTTTAGAGCTAGAAATAGC

InclRS2-3'-2 (18)

TTAATACGACTCACTATAGGAGCACTGAACAGCCAATCGTTTTAGAGCTAGAAATAGC

Gm15441-5'-1 (20)

TTAATACGACTCACTATAGGCCTGTTCTAAGCACCCCTGACGTTTTAGAGCTAGAAATAGC

Gm15441-5'-2 (20)

TTAATACGACTCACTATAGGCAAGGCAGAACTCTACGGGAGTTTTAGAGCTAGAAATAGC

Gm15441-3'-1 (20)

TTAATACGACTCACTATAGGAGTATTGAATGAACCGCCTAGTTTTAGAGCTAGAAATAGC

Gm15441-3'-2 (20)

TTAATACGACTCACTATAGGGCTCTCCTAAGTACCTGTGGGTTTTAGAGCTAGAAATAGC

InclRS2-5'-1 (20)

TTAATACGACTCACTATAGGTGTAGCGCTCTAGCTGCATCGTTTTAGAGCTAGAAATAGC

InclRS2-5'-2 (20)

TTAATACGACTCACTATAGGTCTAGCTGCATCGGGTTTGTGTTTTAGAGCTAGAAATAGC  
 InclRS2-3'-1 (20)  
 TTAATACGACTCACTATAGGAAATGGGACATCTATCAATGGTTTTAGAGCTAGAAATAGC  
 InclRS2-3'-2 (20)  
 TTAATACGACTCACTATAGGGTGTGCTCACACAGGCACTTGTTTTTAGAGCTAGAAATAGC

All sgRNA synthesis primer were designed using the CRISPR design tool and the CRISPOR prediction software.

Primer for T7 endonuclease assays

Sequence (5' -> 3')

Gm15441-5'-1 (18) forward	GCGCACGTTTAACTGACTCTC
Gm15441-5'-1 (18) reverse	ATAAGCAGCACCCCTCCATG
Gm15441-5'-2 (18) forward	CACAGAAGGGAGATAAAGCGC
Gm15441-5'-2 (18) reverse	TTGCCTTCCCTCACTGATGG
Gm15441-3'-1 (18) forward	ATCAGTGAGGGAAGGCAAGG
Gm15441-3'-1 (18) reverse	AGCAAGCCAGTATCACATGC
Gm15441-3'-2 (18) forward	ATGGAGGGGTGCTGCTTATC
Gm15441-3'-2 (18) reverse	GCAGGAAGGCTAACAGGAGG
InclRS2-5'-1 (18) forward	GGAGGAGACAGCAGTTGGG
InclRS2-5'-1 (18) reverse	TGTGTGTGTGCAATGCTCTC
InclRS2-5'-2 (18) forward	TTTTGTGCTGGTTGAGGTG
InclRS2-5'-2 (18) reverse	CACTTTGAGATGGGCTTGGC
InclRS2-3'-1 (18) forward	ACCGGGTGA ACTCTGTGTAG
InclRS2-3'-1 (18) reverse	GATTGGCTGTTCA GTGCTCTC
InclRS2-3'-2 (18) forward	TTGAGGACTGGAGAGATGGC
InclRS2-3'-2 (18) reverse	GTGCCTGTGTGTGTATGTGC
Gm15441-5'-1 (20) forward	GCTCCTACTCAGACCCTTGTTCC
Gm15441-5'-1 (20) reverse	CTCCCTGAGTTGCTTTTGGTC
Gm15441-5'-2 (20) forward	GAAGGGAGATAAAGCGCACG
Gm15441-5'-2 (20) reverse	ATGGGGAGCAAGCCGATAAG
Gm15441-3'-1 (20) forward	GACTAGTCTGATGGAGGCATC
Gm15441-3'-1 (20) reverse	TGTGTGTGTGTGTGAGAGAGAG
Gm15441-3'-2 (20) forward	TCAGCCTGCTTTCTTATATGGC
Gm15441-3'-2 (20) reverse	TGCAAACACAGACATGCACAC
InclRS2-5'-1 (20) forward	ACATTCCAGTAAGTTCCCCG
InclRS2-5'-1 (20) reverse	TCTCTTTCCTGTGCTCATGACC
InclRS2-5'-2 (20) forward	ACATTCCAGTAAGTTCCCCG
InclRS2-5'-2 (20) reverse	TCTTTCCTGTGCTCATGACCA
InclRS2-3'-1 (20) forward	GCACACACACATACAGGCAC
InclRS2-3'-1 (20) reverse	GGCTGTTGTTCTCTCTCGGG

InclRS2-3'-2 (20) forward	ATGAATGAATGAAGCTGGGC
InclRS2-3'-2 (20) reverse	AACAGGGTTATTTACACTTTG

If not stated otherwise, all primers have been designed using the Primer3web online tool.

All primer oligonucleotides have been purchased in 0.025  $\mu$ mole stocks from Sigma-Aldrich Chemie GmbH, Schnelldorf, DE.

## 2.7. Primer for SYBR™ Green Quantitative PCR

<u>Top15 lncRNAs</u>	<u>Sequence (5' -&gt; 3')</u>
4833411C07Rik-202 forward	TTTAATCGCCATGGAAACAGA
4833411C07Rik-202 reverse	TCGTGCTTTGGACTGTCAGA
4933404O12Rik-201 forward	TTGCCGCTGAAAACCTCTGGG
4933404O12Rik-201 reverse	TTGCCGCTGAAAACCTCTGGG
9030616G12Rik-201 forward	GTCAGAGAGGCATGCTTCCC
9030616G12Rik-201 reverse	CAGTAGCAGCCTTCCACCAG
B930025P03Rik-201 forward	CTCTCAGGAACGTCTCTCGG
B930025P03Rik-201 reverse	GGCTGTTGATGTCTTGGCTT
C730036E19Rik-201 forward	AGCAAGCAACCATTGAGACC
C730036E19Rik-201 reverse	TTCCTATGGGCTGTCGTTGT
Gm2788-201 forward	CTGACCGTCCCTTCATCCAC
Gm2788-201 reverse	GAAGAACCCAAACAAGCCACC
Gm2814-201 forward	TCTCCGTGACATGCTCAGAG
Gm2814-201 reverse	GCTGTGGTCCTTTGGGTTTC
Gm8883-203 forward	TGTGTTACACGTGAGGAGCG
Gm8883-203 reverse	AGCTGTTTCCATTGCTGGAG
Gm10319-202 forward	GGACTTGTTCCAATGTGTTTCC
Gm10319-202 reverse	TTTTGCTGAATTCGTGGGTT
Gm11342-203 forward	GCTAGGACCACAGTTGCAGG
Gm11342-203 reverse	GAATCTGTCAATCCCGGCGAC
Gm11789-005 forward	TTCTCCCTTTCCCTCCCCTC
Gm11789-005 reverse	AGGCTCACAGTCTGCAGTAAC
Gm12265-201 forward	GCTGGAGAACAAGGCTGCTC
Gm12265-201 reverse	GATGACAGAGACAGCCCAGG
Gm13775-201 forward	ATGAATGGGGAATGGTTAAACAG
Gm13775-201 reverse	TGTCAGAAGCCAGGATAATAGTG
Gm15441-202 forward	CCTTGCCTTCCCTCACTGAT
Gm15441-202 reverse	GATCAGACCATCCATCCTGG
Gm15611-201 forward	GAATGGACTCTAGCCAGCCC
Gm15611-201 reverse	CACCAAACCAGGCCTTTATGC

Gm16552-201 forward	TGGTGCACGCCTTTAATCCC
Gm16552-201 reverse	CTTGGAGGAGCTGGTTGTGG
<u>Housekeeping genes</u>	<u>Sequence (5' -&gt; 3')</u>
GAPDH forward	TGGCAAAGTGGAGATTGTTGCC
GAPDH reverse	AAGATGGTGTATGGGCTTCCCG
HPRT forward	TCATTATGCCGAGGATTTGG
HPRT reverse	GTCAGCAAAGAACTTATAGCCCC
<u>Other genes</u>	<u>Sequence (5' -&gt; 3')</u>
18s rRNA forward	AGTCCCTGCCCTTTGTACACA
18s rRNA reverse	CGATCCGAGGGCCTCACTA
ActB forward	TTGAACATGGCATTGTTACCAA
ActB reverse	TGGCATAGAGGTCTTTACGGA
DANCR forward	AACCCGTGACTGAATGGCTC
DANCR reverse	GACATGAAGAAGGGGTGGGG
Malat1 forward	AGGCGGGCAGCTAAGGA
Malat1 reverse	CCCCACTGTAGCATCACATCA
MT-RNR1 forward	ATTTCAATTGGCCGACAGCTA
MT-RNR1 reverse	AGGTAGAGCGGGGTTTATCG
Rpl37a forward	CATCGTCGGCAAGTACGGG
Rpl37a reverse	CACCGGCCACTGTTTTTCATG
Rps16 forward	GCTCATCAAGGTGAACGGAC
Rps16 reverse	ATTTGGGCCACATGTCCACC
TBP forward	CCAGACCCCACAACCTCTTCC
TBP reverse	ACAGCCAAGATTCACGGTAG
Txnip forward	GTCAGTGTCCCTGGCTCCAAGA
Txnip reverse	AGTCATCTCAGAGCTCGTCCG
U6 snRNA forward	GTGCTCGCTTCGGCAGCACA
U6 snRNA reverse	GGAACGCTTCACGAATTTGCGTGTCAT
U99 snoRNA forward	CCTCCTTTTCTTGGCGGGGA
U99 snoRNA reverse	CGTCTGAGGATAGAACCCGC

All primers have been designed using the Primer3web online tool and purchased in 0.025  $\mu$ mole stocks from Sigma-Aldrich Chemie GmbH, Schnelldorf, DE.

## 2.8. TaqMan® Assays

<u>TaqMan® assay</u>	<u>TaqMan® ID</u>
ACACA (Acetyl-coenzyme A carboxylase alpha)	Mm01304257_m1
ACOX1 (Acyl-coenzyme A oxidase 1, peroxisomal)	Mm01246834_m1
CPT1A (Carnitine palmitoyltransferase 1a, liver isoform)	Mm01231183_m1
FABP4 (Fatty acid binding protein 4)	Mm00445878_m1
FBP1 (Fructose biphosphatase 1)	Mm00490181_m1
FOXO1 (Forkhead box protein O1)	Mm00490671_m1
G6PC (Glucose-6-phosphate)	Mm00839363_m1
GAPDH (Glyceraldehyde-3-phosphate dehydrogenase)	Mm99999915_g1
HADHB (Trifunctional enzyme subunit beta, mitochondrial)	Mm00695255_g1
HPRT (Hypoxanthine guanine phosphoribosyl transferase 1)	Mm00446968_m1
IRS-1 (Insulin receptor substrate 1)	Mm01278327_m1
IRS-2 (Insulin receptor substrate 2)	Mm03038438_m1
PCK1 (Phosphoenolpyruvate carboxylase 1)	Mm01247058_m1
SLC2A1 (Solute carrier family 2 member 1)	Mm00441480_m1
SLC2A2 (Solute carrier family 2 member 2)	Mm00446229_m1
SLC2A4 (Solute carrier family 2 member 4)	Mm00436615_m1
SREBF1 (Sterol regulatory element binding transcription factor 1)	Mm00550338_m1

All TaqMan® assays have been purchased from Thermo Fisher Scientific, Waltham, US.

## 2.9. RNA Oligonucleotides

<u>Alt-R® CRISPR/Cas9 crRNAs</u>	<u>Sequence (5' -&gt; 3')</u>
4833411C07Rik 5'-crRNA	<b>GGCAGTTACATAATCACG</b> GCGTTTTAGAGCTATGCT
4833411C07Rik 3'-crRNA	CAGACTATGGCGGATAAGCA <b>GTTTTAGAGCTATGCT</b>
Gm15441 5'-crRNA	<b>GGCCTTGGCTCACTAGGTGAGTTTTAGAGCTATGCT</b>
Gm15441 3'-crRNA	<b>TTCCAGATGACTTTAGTTG</b> GTTTTAGAGCTATGCT

The part of the sequence highlighted in red represents the spacer sequence, whereas the other 16 nucleotides facilitate tracrRNA binding.

### Alt-R® CRISPR/Cas9 tracrRNA (Product ID: 1072532)

5'-GTTGGAACCATTCAAAACAGCATAGCAAGTTAAAATAAGGCTAGTCCGTTATCAACTTG  
AAAAAGTGGCACCGAGTCGGTGCTTTTT-3'

All RNA oligonucleotides have been purchased from Integrated DNA Technologies, Inc., Coralville, US.

## 2.10. Antisense Locked Nucleic Acid (LNA™) GapmeRs

<u>Target transcript</u>	<u>Sequence (5' -&gt; 3')</u>
4833411C07Rik	CTCGATTAACCTGATA
B930025P03Rik	ATCACGGATTGCTAAT
Gm15441	CTCGAAATGAATTGCG
Negative control (scramble)	AACACGTCTATACGC

All LNAs™ have been purchased from Exiqon A/S, Vedbaek, DK.

## 2.11. Chromatin immunoprecipitation sequencing (ChIP-Seq) data

<u>Histone modification</u>	<u>Mouse strain</u>	<u>Developmental stage</u>	<u>ENCODE project</u>
H3K4me3	C57BL/6	Postnatal (p=0)	ENCSR653AVN
H3K27Ac	C57BL/6	Postnatal (p=0)	ENCSR616TJM

ChIP-Seq data sets were generated by Bing Ren, University of California, San Diego, US, and are publicly available under the listed ENCODE project numbers.

## 2.12. Human Liver Biopsies

<u>Code</u>	<u>Group assignment</u>	<u>Age</u>	<u>BMI</u>	<u>Diagnosis</u>	<u>RIN</u>
0381 WSC	lean non-diabetic, male	52	24.5	rectal carcinoma	6.6
1311 WER	lean non-diabetic, male	62	24.8	gastric carcinoma	6.2
1651 HRU	lean non-diabetic, male	55	21.9	rectal carcinoma	7.0
3141 AZE	lean non-diabetic, male	74	22.9	colon carcinoma	5.2
0121 STR	obese non-diabetic, male	21	52.8	obesity	7.0
0311 RAN	obese non-diabetic, male	35	49.1	obesity	8.3
0861 NSC	obese non-diabetic, male	50	47.9	obesity	6.3
1941 JRO	obese non-diabetic, male	48	54.2	obesity	6.6
0951 LZU	obese diabetic, male	46	63.0	obesity	4.9
1781 DGR	obese diabetic, male	42	33.5	obesity	6.3
1701 GBO	overweight diabetic, male	76	27.0	colon carcinoma	7.9
3011 FHE	overweight diabetic, male	75	25.0	pancreas carcinoma	7.3

All samples were tested negative for hepatitis B (HBV) and hepatitis C (HCV). Sample preparation was previously described in [193]. The samples were kindly provided by Prof. Dr. Jörg Heeren, Institute for Biochemistry and Molecular Cell Biology, Medical Center Hamburg-Eppendorf, Hamburg, Germany.

## 2.13. Software

- 4Peaks, Nucleobytes B.V., version 1.8
- Atom, GitHub community, version 1.24.1
- Benchling Molecular Biology Design and Analysis Suite, Benchling Inc. web-based application, <https://benchling.com/> [March, 2018]
- biomaRt package, version 2.16.0  
designed as described in [194]
- Bowtie2, version 2.2.9  
designed as described in [195]
- Coding Potential Assessment Tool, version 1.2.4  
designed as described in [196]  
web-based application, <http://lilab.research.bcm.edu/cpat/> [March, 2018]
- Coding Potential Calculator  
designed as described in [197]  
web-based application, [http://cpc.cbi.pku.edu.cn/programs/run\\_cpc.jsp](http://cpc.cbi.pku.edu.cn/programs/run_cpc.jsp) [March, 2018]
- CorelDraw Graphics Suite X6, Corel corp.
- CRISPOR, version 4.3  
designed as described in [198]  
web-based application, <http://crispor.tefor.net/> [March, 2018]
- CRISPR Design Tool, Zhang Lab  
designed as described in [199]  
web-based application, [crispr.mit.edu](http://crispr.mit.edu) [March 2018]
- Cufflinks suite, version 2.2.1  
designed as described in [200]
- DESeq2, version 1.10.1  
designed as described in [201]
- EndNote™ X7, Thomas Reuters, version 7.8
- Ensemble BioMart [202]
- flexbar, version 3.4.0  
designed as described in [203]
- FUSION-CAPT, Vilber Lourmat Deutschland GmbH, version 16.15
- ImageJ, Wayne Rasband/NIH, version 1.48v
- Keynote, Apple Inc., version 7.3.1
- NanoDrop™ 1000 software, Thermo Fisher Scientific Inc., version 3.8.1
- Numbers, Apple Inc. version 4.3.1
- Pages, Apple Inc., version 6.3.1
- Primer3web, version 4.1.0  
designed as described in [204, 205]  
web-based application, <http://primer3.ut.ee/> [March, 2018]
- Prism, GraphPad Software Inc., version 7.0c
- PyRAT, Scionics Computer Innovation GmbH, version 3.6-365
- QuantStudio™ 6, Applied Biosystems, version 1.3
- QuickNGS, version 1.2.2  
designed as described in [206]
- R, R Core Team, version 3.1.2
- RStudio, RStudio Inc., version 1.0.136
- SeqBuilder™, DNASTAR Inc., version 14.1.0
- SeqMan Pro™, DNASTAR Inc., version 14.1.0
- SoftMax® Pro, Molecular Devices, version 6.3

- STAR, version 2.6.0c  
designed as described in [207]
- Tophat2, version 2.0.10  
designed as described in [208]



## Chapter 3 - Methods

### 3.1. Molecular biological methods

#### 3.1.1. Polymerase chain reaction (PCR)

Genotyping Polymerase Chain Reactions (PCRs) were performed using the DreamTaq™ Green DNA Polymerase Kit in a total reaction volume of 25 µL composed of:

- 2.5 µL DreamTaq™ Green Buffer (10X)
- 1 µL dNTP Mix (10mM)
- 0.25 µL Forward primer (10 µM)
- 0.25 µL Reverse primer (10 µM)
- 0.2 µL DreamTaq™ Green DNA Polymerase
- 2 µL Genomic template DNA
- 18.8 µL Millipore® H<sub>2</sub>O

PCR cycling parameters have been determined for each individual PCR according to the annealing temperature of the specific primer pair and the length of the DNA product (for protocols see 3.4.3.). All PCRs have been performed using FlexCycler<sup>2</sup> PCR-Thermocycler.

For subsequent applications requiring highly accurate DNA products proof-reading DNA polymerases have been used according to the manufacturer's protocols. Detailed information on the High Fidelity PCR Master Kit (HiFi-PCR, see 3.1.3.) or the Phusion DNA Polymerase Kit (sgRNA synthesis, see 3.1.10.) can be found in the respective chapter.

#### 3.1.2. Agarose gel electrophoresis

Amplified DNA fragments were electrophoretically separated by native gel electrophoresis. Via boiling, agarose was dissolved in 1X TBE buffer resulting in solutions with final agarose concentrations varying between 0.5 % and 2 %. For DNA visualization 5 µL Midori Green Advance® was added per 100 mL agarose solution. PCR samples originating from high-fidelity PCRs were mixed with the respective amount of 6X DNA gel loading dye before loading the samples into the gel, whereas other PCR samples were directly loaded into the gel. Loaded DNA fragments were separated at 80 – 130 V for varying time spans and visualized by UV-light on a FastGene® FAS V gel documentation system.

- 1X TBE buffer
- 89 mM Tris-Base
- 89 mM Boric acid
- 2 mM EDTA
- in Millipore® H<sub>2</sub>O, adjusted to pH 8.0

### 3.1.3. High fidelity polymerase chain reaction (HiFi-PCR)

DreamTaq™ Green DNA Polymerase lacks 5'→3' proof-reading capacity and thus has not been used for PCR reactions of important and/or limited samples. For the most accurate DNA sequencing results, PCR reactions were performed using the High Fidelity PCR Master Kit in a total reaction volume of 50 µL composed of:

	<u>Initial denaturation</u>	94°C	3 min	
25 µL MasterMix 1 (HF - Enzyme Mix)	Denaturation	94°C	10 s	
23 µL MasterMix 2 (HF - Water)	Annealing	58°C	45 s	14x
0.5 µL Forward primer (10 µM)	<u>Elongation</u>	68°C	2 min	
0.5 µL Reverse primer (10 µM)	Denaturation	94°C	10 s	
1 µL DNA template	Annealing	58°C	45 s	26x
	<u>Elongation</u>	68°C	3 min	
	Final elongation	68°C	3 min	
	Hold	4°C		

High fidelity PCR products lack 3'-end adenosine overhangs and thus cannot directly be integrated into stable plasmid vectors.

### 3.1.4. Addition of A'-overhangs

In order to achieve linear DNA fragments suitable for integration into the pGEM®-T Easy vector, high fidelity PCR reactions were incubated with the DreamTaq™ Green DNA Polymerase, which catalyzes a non-template directed addition of an adenine residue to the 3'-ends of both DNA strands. After completion of the initial high fidelity PCR reaction, 1 µL of DreamTaq™ Green DNA Polymerase was added to the reaction mix and incubated at 72°C for 10 min. DNA fragments were purified from the PCR reaction mix using the QIAquick® Gel Extraction Kit. Therefore, 150 µL of Buffer QG and 50 µL of isopropanol were added to the DNA solution and briefly vortexed, applied to a QIAquick® column and centrifuged for 1 min at 13000 x g. To remove remaining salt and agarose residues, the column was washed with 500 µL Buffer QG (2x) or 750 µL Buffer PE and centrifuged for 1 min at 13000 x g, respectively. Finally, bound DNA was eluted from the column by the addition of 25 µL Elution Buffer and centrifugation for 1 min at 13000 x g. Extracted DNA was immediately used in a DNA ligation reaction.

### 3.1.5. DNA ligation

For preservation of high fidelity PCR products modified DNA fragments (+ 3'-A overhangs) were integrated into the pGEM®-T Easy Vector System, a pre-linearised plasmid vector with 3'-T overhangs at the insertion site. The insertion site is located within a  $\beta$ -galactosidase gene (*lacZ*) whose expression is activated by isopropyl- $\beta$ -D-thiogalactopyranoside (IPTG) administration, but whose coding region is disrupted in case of a PCR product insertion.

DNA ligation reactions were performed at RT for 2-4 hrs in a total reaction volume of 10  $\mu$ L composed of:

- 5  $\mu$ L Rapid Ligation Buffer (2X)
- 1  $\mu$ L pGEM®-T Easy plasmid vector
- 1  $\mu$ L T4 DNA ligase
- 3  $\mu$ L PCR products (+ A'-overhangs)

Resulting DNA ligation reactions were immediately used for transformation of competent bacteria

### 3.1.6. Transformation of competent bacteria

Aliquots (100  $\mu$ L) of competent XL10-Gold® *E. coli* cells were thawed on ice for 20 mins, gently mixed with 2.5  $\mu$ L of DNA ligation products and incubated on ice for 20 mins. Following a heat-shock at 42°C for 45 s, the bacteria solution was kept on ice for 2 mins. Subsequently the solution was supplemented with 900  $\mu$ L LB medium, transferred to a 15 mL Falcon® tube and incubated for 90 mins at 37°C with constant shaking (300 rpm). After a short centrifugation (10 s, 1200 rpm), 900  $\mu$ L of the supernatant was removed and the remaining 100  $\mu$ L bacteria solution was plated on bacterial culture plates and incubated at 37°C overnight.

Following supplementation of bacterial culture plates with IPTG Solution and X-Gal Solution, bacterial clones carrying pGEM®-T Easy vectors with inserted DNA fragments could be detected by the lack of functional  $\beta$ -galactosidase protein (*lacZ*) and the resulting white appearance on the bacterial culture plates. These colonies have been used to inoculate bacterial cultures.

<u>Bacterial Culture Plates</u>	<u>Amp Solution</u>
14 g LB-Medium (autoclaved)	100 mg Ampicillin sodium salt
200 $\mu$ L Amp Solution	in 1 mL Millipore® H <sub>2</sub> O
400 $\mu$ L X-Gal Solution	
400 $\mu$ L IPTG Solution	<u>IPTG Solution</u>
in 400 mL Millipore® H <sub>2</sub> O	166.8 mg IPTG
[20 mL per plate]	in 7 mL Millipore® H <sub>2</sub> O
	<u>X-Gal Solution</u>
	140 mg X-Gal
	in 7 mL DMF

### 3.1.7. Small scale plasmid DNA isolation

15 mL Falcon® tubes containing 4 mL LB medium and ampicillin antibiotic (30 mg/mL) were inoculated with a single bacterial colony and incubated for 6-12 hrs at 37°C with constant shaking (180 rpm). Afterwards, 2 mL of the bacterial culture was centrifuged (1 min, 6000 x g) and the supernatant was discarded. The remaining pellet was resuspended in 100 µL ice-cold Solution I and incubated at RT for 5 mins. For cell lysis, 200 µL freshly prepared Solution II was added to the cell solution, which then was mixed by inverting and incubated on ice for 5 mins. By adding 150 µL ice-cold Solution III and vortexing the sample for 10 s, the lysate was neutralized and subsequently centrifuged (10 min, 6000 x g, 4°C). The supernatant was transferred to a reaction tube and plasmid DNA was precipitated by adding 400 µL ice-cold isopropanol to the solution. After another centrifugation step (10 min, 12000 x g, 4°C) the supernatant was discarded, while the DNA pellet was washed with 500 µL ice-cold ethanol (70 % v/v, in Millipore® H<sub>2</sub>O) and centrifuged again (10 min, 12000 x g, 4°C). The supernatant was removed completely by aspiration and the DNA pellet was resuspended in 30 µL TBE Buffer. Plasmid DNA concentrations were measured using a NanoDrop™ ND-1000 spectrophotometer and the samples were stored at -80°C.

<u>Solution I</u>		<u>Solution II</u>	
10 mM	EDTA	200 mM	NaOH
50 mM	Tris-Cl, pH 8.0	1 %	SDS (w/v)
50 mM	Glucose	in Millipore® H <sub>2</sub> O	
in Millipore® H <sub>2</sub> O			
<u>Solution III</u>		<u>TBE Buffer</u>	
5 M	NaAc	200 mM	Tris-Cl, pH 8.0
11.5 %	Glacial acetic acid (v/v)	10 mM	EDTA
in Millipore® H <sub>2</sub> O		36 mg/mL	RNAse A
		in Millipore® H <sub>2</sub> O	

### 3.1.8. Large scale plasmid DNA isolation

For large scale plasmid DNA isolation the NucleoBond® Xtra Maxi was used following the manufacturer's protocol. Briefly, 120 mL LB medium was supplemented with ampicillin (30 mg/mL) and inoculated with 50 µL of a preexisting bacterial culture. After incubating the culture overnight (37°C, 180 rpm) bacteria were harvested by centrifugation (15 min, 6000 x g, 4°C). The supernatant was discarded, whereas the pellet was resuspended in 8 mL Buffer RES and incubated at RT for 5 mins. For cell lysis, 8 mL Buffer LYS was added to the cell solution, which then was mixed by inverting the tube and incubated at RT for another 5 mins. The lysate was subsequently neutralized by adding 12 mL ice-cold Buffer NEU and thoroughly mixed, before being transferred onto a NucleoBond® Xtra Column Filter. The column filter was washed two times with 15 and 25 mL of Buffer WASH and the bound plasmid DNA was finally eluted from the column by adding 15 mL Buffer ELU. Eluted plasmid DNA was precipitated by adding 10.5 mL ice-cold isopropanol to the solution. After centrifugation (30 min, 15000 x g, 4°C) the supernatant was discarded, while the DNA pellet was washed in 4 mL ice-cold ethanol (70 % v/v, in Millipore® H<sub>2</sub>O) and centrifuged again (15 min, 15000 x g, 4°C). Finally, the supernatant was removed completely by aspiration and the DNA pellet was resuspended in 30 µL TBE Buffer. Plasmid DNA concentrations were measured using a NanoDrop™ ND-1000 spectrophotometer and the samples were stored at -80°C.

### 3.1.9. DNA sequencing

DNA plasmids harvested from bacterial cultures were diluted to a final concentration of 50 ng/µL and sent for custom DNA sequencing to GATC Biotech, Ebersberg, DE.

Integrated primer sequences on the pGEM®-T Easy Vector System which have been used as sequencing primers are M13 forward (M13Fwd) and M13 reverse (M13Rev).

### 3.1.10. Generation of DNA templates for single guide RNA (sgRNA) synthesis

In order to generate DNA templates for sgRNA synthesis, specific DNA oligonucleotides (forward primer, length of 58 or 60 bp) were designed for each sgRNA to be synthesized according to the following composition:

T7 promotor	-	5'-TTAATACGACTCACTATAGG-3'
gRNA of interest	-	variable (18-20 bp of specific gRNA)
pX330-5'tracrRNA	-	5'-GTTTTAGAGCTAGAAATAGC-3'

PCR reactions were performed using the Phusion® High-Fidelity DNA Polymerase in a total reaction volume of 50 µL composed as shown on the next page.

10 µL Phusion HF Buffer (5X)*				
1 µL dNTP Mix (10mM)	Initial denaturation	98°C	30 s	
2.5 µL sgRNA specific forward primer	Denaturation	98°C	10 s	
2.5 µL pX330-5' reverse primer	Annealing	60-72°C	15 s	40x
0.5 µL Phusion DNA Polymerase	Elongation	72°C	15 s	
1.5 µL DMSO (optional)	Final elongation	72°C	5 min	
200 ng pX330 plasmid DNA in Millipore® H <sub>2</sub> O	Hold	4°C		

\*For PCR products with high GC content (>70 %) Phusion HF Buffer was replaced by Phusion GC Buffer (5X) and 1.5 µL DMSO was added to the reaction mix.

Before proceeding to RNA synthesis DNA template PCR reactions were controlled for the appearance of a single specific band (120 or 122 bp) by agarose gel electrophoresis.

### 3.1.11. DNA extraction from agarose gels

Separated DNA fragments were extracted from agarose gels using the QIAquick® Gel Extraction Kit according to the manufacturer's protocol. Briefly, excised DNA-containing gel slices were weighed, mixed with three volumes of Buffer QG and incubated for 10 mins at 50°C with constant shaking (300 rpm). After complete dissolving of the agarose slice, 1 volume of isopropanol was added to the DNA solution, which then was briefly vortexed, applied to a QIAquick® column and centrifuged at 13000 x g for 1 min. To remove remaining salt and agarose residues, the column was washed with 500 µl Buffer QG (2x) or 750 µL Buffer PE, respectively, and centrifuged at 13000 x g for 1 min. Finally, bound DNA was eluted from the column by the addition of 25 µL Elution Buffer and centrifugation at 13000 x g for 1 min. Extracted DNA concentrations were measured using a NanoDrop™ ND-1000 spectrophotometer and directly used for RNA synthesis.

### 3.1.12. sgRNA synthesis

sgRNA oligonucleotides were synthesized using the HiScribe™ T7 High Yield RNA Synthesis Kit and previously generated sgRNA template DNA. GuideRNA PCR reactions were performed at 37°C for 16-18 hrs in a total reaction volume of 20 µL composed as shown on the next page. Before using the produced RNA oligonucleotides, sgRNA template DNA as well as other reaction components need to be removed by DNase treatment and RNA purification, respectively.

#### sgRNA synthesis mix

2  $\mu$ L Reaction Buffer (10X)  
1.5  $\mu$ L T7 RNA Polymerase Mix  
1.5  $\mu$ L ATP Nucleotide Mix (100 mM)  
1.5  $\mu$ L CTP Nucleotide Mix (100 mM)  
1.5  $\mu$ L GTP Nucleotide Mix (100 mM)  
1.5  $\mu$ L UTP Nucleotide Mix (100 mM)  
200 ng sgRNA template DNA  
in Millipore® H<sub>2</sub>O

#### 3.1.13. DNA digestion

In order to remove the DNA template used for sgRNA synthesis, the RNA synthesis reaction mix was subjected to DNase I treatment as shown below and incubated at 37°C for 15min.

20  $\mu$ L RNA synthesis reaction mix  
10  $\mu$ L DNase I Buffer (10X)  
2  $\mu$ L DNase I  
70  $\mu$ L RNase-free H<sub>2</sub>O

Finally, DNase I activity was heat-inactivated by incubating the reaction at 75°C for 10 min.

#### 3.1.14. sgRNA purification

After removal of sgRNA template DNA, the RNA oligonucleotides were purified from the DNase reaction mix using the NucleoSpin® RNA Kit according to the manufacturer's protocol. Briefly, the sgRNA reaction mix was mixed with 600  $\mu$ L of a Buffer RA1 - absolute ethanol premix with ratio 1:1 and loaded onto a NucleoSpin® RNA Column. After centrifugation (30 s, 11000 x g) the column was placed in a new Collection Tube and washed with 200  $\mu$ L Buffer RAW2 (centrifugation: 30 s, 11000 x g), 600  $\mu$ L Buffer RA3 (centrifugation: 30 s, 11000 x g) and 250  $\mu$ L Buffer RA3 (centrifugation: 2 min, 11000 x g), respectively. Bound RNA was finally eluted from the column by the addition of 50  $\mu$ L RNase-free H<sub>2</sub>O and centrifugation at 11000 x g for 1 min. Resulting sgRNA samples were split in two 22  $\mu$ L aliquots, which were directly snap-frozen in liquid nitrogen and then stored at -80°C, and one 6  $\mu$ L aliquot, which was used to determine RNA concentration and integrity. sgRNA concentrations were measured using a NanoDrop™ ND-1000 spectrophotometer and the remaining 5  $\mu$ L sgRNA aliquot was run on an agarose gel to validate RNA product consistency and integrity. Importantly, before running the gel, the sgRNA aliquot was incubated at 65°C for 30 mins to dissolve secondary RNA structures. High-quality synthesis results in a strong single band (length: 18 or 20 bp) with no other RNA products or background contaminations.

### 3.1.15. T7 endonuclease I assay

Functionality of synthesized sgRNAs was tested *in vitro* by transfecting Cas9 mRNA and the sgRNA to be tested into NSC-34 cells (for details see 3.2.1.) and subsequently by analysing genomic DNA of transfected cells for CRISPR/Cas9-mediated mutations at the locus of interest. To detect genomic variations at the potentially mutated genomic loci, specific PCR primer pairs were designed for each sgRNA with the following characteristics:

- standardized primer annealing temperature of 60°C
- resulting PCR product of 400 - 800 bp length
- resulting PCR product containing the targeted CRISPR/Cas9 cutting site at its center

Before utilising designed primer pairs for T7 Endonuclease I assays, all PCR reactions have been tested with unmodified genomic DNA for a specific and strong single band. Verified primer pairs have been used with genomic DNA of transfected cells in a total reaction volume of 25 µL composed of:

2.5 µL DreamTaq™ Green Buffer (10X)	<u>Initial denaturation</u>	95°C	2 min
1 µL dNTP Mix (10mM)	Denaturation	95°C	30 s
0.25 µL Forward primer (1 µM)	Annealing	60°C	30 s 35x
0.25 µL Reverse primer (1 µM)	<u>Elongation</u>	72°C	1 min
0.2 µL DreamTaq™ Green DNA Polymerase	Final elongation	72°C	5 min
2 µL Genomic DNA	Hold	4°C	
in Millipore® H <sub>2</sub> O			

In case of functional synthesized sgRNAs, the PCR reaction yields different DNA amplicons with unmodified as well as mutated genomic sequences of the locus of interest. By boiling the PCR products as shown below, identical double-stranded DNA homoduplexes were separated from each other and randomly re-annealed with other single-stranded DNA sequences, allowing the formation of DNA heteroduplexes comprised of unmodified as well as mutated DNA sequences.

95°C	10 min	45°C	1 min
85°C	1 min	35°C	1 min
75°C	1 min	25°C	1 min
65°C	1 min	25°C	hold
55°C	1 min		

DNA heteroduplexes feature base pair mismatches at the mutated genomic locus and can be visualized on an agarose gel after the re-annealed PCR products were subjected to T7 Endonuclease I assays. In this assay DNA heteroduplexes are incubated with T7 Endonuclease I, a mismatch-specific DNA endonuclease that recognizes base-substitution mismatches as well as mismatches resulting from genomic deletions or insertions. Due to the position of the CRISPR/Cas9 cutting site at the center of the PCR product, cleavage of heteroduplexes by T7 Endonuclease I results in two PCR fragments of similar size.



### T7 Endonuclease I Assay

10 µL	Re-annealed PCR product		
1.1 µL	NEBuffer 2	37°C	60 min
0.3 µL	T7 Endonuclease I		

After T7 Endonuclease I assays the PCR reactions were analyzed for cleaved DNA fragments of the specific PCR product by agarose gel electrophoresis (see 3.1.2.).

### 3.1.16. Reverse transcription

In order to convert single-stranded RNA molecules into more stable, double-stranded complementary DNA (cDNA) molecules, total RNA solutions were subjected to reverse transcription using the High-Capacity cDNA Reverse Transcription Kit according to the manufacturer's protocol. The synthesis of cDNA molecules in this protocol is based on random hexamer primers (6 bp DNA oligonucleotides), which allow conversion of all possible RNA sequences. Depending on total RNA abundance the RNA solutions used for cDNA synthesis were equally diluted to RNA concentrations of 400 ng/µL or 200 ng/µL.

2 µL	10X RT Buffer		
2 µL	Random hexamer primers	Pre-primer extension	25°C 10 min
0.8 µL	dNTP Mix	cDNA synthesis	37°C 2 hrs
1 µL	Reverse Transcriptase	Inactivation	85°C 15 min
2 µg	RNA solution	Hold	4°C
	in Millipore® H <sub>2</sub> O		

After the RT-PCR reaction, 180 µL Millipore® H<sub>2</sub>O was added to the PCR sample and the diluted cDNA molecules were stored at -20°C or directly used for RNA expression analysis in quantitative PCR (qPCR) experiments.

### 3.1.17. Quantitative real-time PCR (qPCR)

To quantify the expression of specific RNA molecules, prior synthesized cDNA solutions of the cells or tissue of interest were subjected to quantitative PCR (qPCR) analysis using a QuantStudio™ 7 Flex Real-Time PCR System. For RNA molecules with commercially available gene expression assays the TaqMan™ Gene Expression Master Mix was used in combination with the respective transcript-specific TaqMan® Gene Expression Assays. For noncoding RNA genes and other genes with no available TaqMan® Gene Expression Assay the SYBR™ Select Master Mix was used in combination with self-designed and tested DNA primers.

### SYBR Green-based qPCRs

5  $\mu$ L SYBR Select Master Mix (10X)

0.25  $\mu$ L Forward primer (1  $\mu$ M)

0.25  $\mu$ L Reverse primer (1  $\mu$ M)

2.5  $\mu$ L Millipore® H<sub>2</sub>O

2  $\mu$ L cDNA solution

Initial denaturation 95°C 2 min

Denaturation 95°C 30 s

Annealing 60°C 30 s 40x

Elongation 72°C 1 min

Final elongation 72°C 5 min

Hold 4°C

### TaqMan™-based qPCRs

6  $\mu$ L TaqMan™ Master Mix

0.3  $\mu$ L TaqMan™ probes

4  $\mu$ L cDNA solution

Relative expression of target RNA molecules was adjusted for total RNA content by measuring expression of housekeeping genes (HPRT and/or GAPDH) and calculated by the  $2^{-\Delta\Delta CT}$  method (as described in [209]).

All TaqMan® assays as well as the DNA primer used for qPCR experiments can be found in the materials section (2.7. & 2.8.).

### 3.1.18. RNA sequencing

Before isolated RNA solutions could be sent for sequencing, remaining traces of DNA were removed using the TURBO DNA-free™ Kit as shown below:

5  $\mu$ L 10X TURBO DNase Buffer

1  $\mu$ L TURBO DNase

37°C 30 min

5  $\mu$ g RNA solution

in RNase-free H<sub>2</sub>O

TURBO DNase activity was inactivated by adding 5  $\mu$ L of DNase Inactivation Reagent and incubating the reaction mix at RT for 5 min. After centrifugation (2 min, 10000 x g, RT) the supernatant was transferred to an RNase-free tube and tested for RNA concentration and integrity. RNA concentrations were measured using a NanoDrop™ ND-1000 spectrophotometer and the samples were diluted to 100 ng/ $\mu$ L. 1  $\mu$ L of the RNA sample was used to examine RNA integrity (see 3.1.19.) and the remaining samples were stored at -80°C.

RNA sequencing experiments were performed at (1) the Max Planck-Genome-centre Cologne, Cologne, DE (obesity mouse models) or at (2) the Cologne Center for Genomics, Cologne, DE (others) with the following conditions:

- Sample input: 1 µg of total RNA (100 ng/µL)
- rRNA depletion: (1) NEBNext® rRNA Depletion Kit (Human/Mouse/Rat)  
(2) Ribo-Zero rRNA Removal Kit (Human/Mouse/Rat)
- cDNA library preparation: (1) NEBNext® Ultra™ Directional RNA Library Prep Kit for Illumina®  
(2) TruSeq RNA Library Prep Kit v2
- Normalization: ERCC RNA Spike-In (ThermoFisher)
- Sequencing platform: HiSeq2500, paired-end flow cells (Obesity Experiment)  
HiSeq4000, paired-end flow cells (Feeding Experiment)  
HiSeq4000, paired-end flow cells (Human Liver Biopsies)
- Sequencing conditions: 2 x 100 bp read length, strand-specific (Obesity Experiment)  
2 x 75 bp read length, strand-specific (Feeding Experiment)  
2 x 75 bp read length, strand-specific (Human Liver Biopsies)
- Sequencing depth: 150-200 million reads per sample

### 3.1.19. RNA integrity measurement

RNA molecules are more prone to degradation than DNA molecules due to their chemical structure and the high prevalence of RNase enzymes. Thus, in order to obtain high-quality RNA sequencing results, it is critical to control RNA samples for intact RNA molecules.

RNA integrity of samples intended to be sequenced were measured using an Agilent 2100 Bioanalyzer Analysis System in combination with the Agilent RNA 600 Pico Kit for samples containing low amounts of RNA (less than 5 ng/µL) or the Agilent RNA 600 Nano Kit for samples containing higher amounts of RNA (more than 5 ng/µL). This system provides a detailed assessment of the 18S to 28S ribosomal RNA (rRNA) ratio and generates a RNA Integrity Number (RIN) for each given sample to interpret the respective RNA degradation.

Both kits were performed according to the respective manufacturer's protocols and only samples yielding high RNA Integrity Numbers (RIN ≥ 8.0 for murine RNA, RIN ≥ 6.0 for human RNA) were sent for sequencing.

## 3.2. Cell biological methods

### 3.2.1. Eukaryotic cell culture

The following cell lines have been used during the *in vitro* experiments described in this thesis:

#### NSC-34

Mouse motor neuron-like hybrid cells (NSC-34) have been used as *in vitro* system for sgRNA validation. The NSC-34 cell line was produced by fusion of motor neuron enriched, embryonic mouse spinal cord cells with mouse neuroblastoma cells [210, 211] and provide a robust *in vitro* system with high proliferative capacity that can be maintained on standard cell culture plates.

NSC-34 cells were kindly provided by Robin Schwarzer (Lab of Manolis Pasparakis, CECAD Research Center, Cologne).

#### NSC-34 Medium

DMEM GlutaMAX™, high glucose (4.5 g/L)

10% FBS

1% L-Glutamine solution

1% Penicillin-streptomycin solution

#### Primary murine hepatocytes

Primary murine hepatocytes have been used as *in vitro* system for all experiments concerning long noncoding RNA expression analysis. Hepatocytes are the major cell type in mouse liver and isolated primary hepatocytes resemble an appropriate *in vitro* cell culture system for the study of liver metabolic functions. Yet, primary hepatocytes gradually lose cuboidal morphology as well as differentiated, liver-specific functions after 4-5 days in culture.

Primary hepatocytes were freshly isolated for each experiment (as described in 3.4.10.) and maintained on collagen I-coated cell culture plates. Due to gradual loss of hepatocyte-specific morphology and marker expression, primary hepatocytes were not maintained in culture for more than 4 days.

#### Attachment Medium

DMEM, low glucose (1 g/L)

10% FBS

1% L-Glutamine solution

1% Penicillin-streptomycin solution

#### Fasting Medium

DMEM, low glucose (1 g/L)

1% L-Glutamine solution

1% Penicillin-streptomycin solution

All eukaryotic cells were maintained under controlled conditions (37°C, 10% CO<sub>2</sub>) in C170 or Heracell 150i™ CO<sub>2</sub> incubators.

### Passage

Tissue culture dishes harboring adherent eukaryotic cells were washed with PBS and then incubated with 5 mL trypsin solution at 37°C for 10 mins. Trypsinization was stopped by adding 15 mL PBS and detached cells were collected by centrifugation (5 min, 300 x g), resuspended in 10 mL of fresh medium and reseeded on fresh tissue culture dishes.

### Counting

In order to determine the amount of cells in a given cell suspension, cells were collected by centrifugation (5 min, 300 x g) and resuspended in 10 mL of the respective buffer. 10 µL of the cell suspension were mixed with 10 µL trypan blue solution to achieve a final dilution of 1:1. Finally, cell numbers were determined by using a Neubauer improved cell counting chamber.

### Storage

For long-term storage, eukaryotic cells were detached from tissue culture dishes by incubation with trypsin solution (10 min, 37°C), pelleted by centrifugation (5 min, 300 x g) and resuspended in 10 mL freezing medium. Finally, 1.5 mL of cell suspension was transferred to CryoPure® cryotubes, which have been placed in a freezing container filled with isopropanol and subsequently stored at -80°C for 2 days before being placed in liquid nitrogen (-196°C).

#### Freezing Medium

95 % (v/v) NSC-34 Medium

5 % (v/v) DMSO

### Thawing cells

Before taking frozen cells into culture, preserved cells were tested for mycoplasma contaminations (see 3.2.2.). Mycoplasma-negative samples were then mixed with 500 µL of pre-warmed (37°C) culture medium and gradually transferred to a 15 mL Falcon® tube containing 8.5 mL of culture medium. After centrifugation (5 min, 1200 x g, RT) the supernatant was discarded and the cell pellet resuspended in 10 mL culture medium. Finally, varying amounts (6 mL, 3 mL, 1 mL) of the cell suspension were mixed with the respective amount of culture medium (total volume 25 mL) and seeded on 15 cm cell culture dishes.

### 3.2.2. Mycoplasma test

Mycoplasma species are a genus of bacteria which resemble the most common contaminants in laboratory cell culture and may induce changes in cell growth and metabolism [212]. Thus, all cell suspensions taken into culture have been tested for mycoplasma contaminations using the PCR Mycoplasma Test Kit as shown below:

#### Cell Suspension PCR

35  $\mu$ L Millipore® H<sub>2</sub>O

10  $\mu$ L Reaction Mix

5  $\mu$ L Cell Suspension

Initial denaturation 94°C 30 s

Denaturation 94°C 30 s

Annealing 60°C 2 min 35 x

Elongation 72°C 1 min

#### Positive Control PCR

39  $\mu$ L Millipore® H<sub>2</sub>O

10  $\mu$ L Reaction Mix

1  $\mu$ L Positive Control Template

Denaturation 94°C 30 s

Annealing 60°C 2 min

Final elongation 75°C 5 min

#### Negative Control PCR

40  $\mu$ L Millipore® H<sub>2</sub>O

10  $\mu$ L Reaction Mix

Hold 4°C

PCRs of mycoplasma-positive samples produce a band at 270 bp and were not taken into culture, but directly discarded.

### 3.2.3. Transfection of primary murine hepatocytes with LNA oligonucleotides

Freshly isolated primary hepatocytes were counted and seeded on collagen I-coated cell culture plates according to the specific experimental setup:

- Protein expression analysis: 6-well plates, 400000 cells per well, 2 mL medium
- RNA expression analysis: 12-well plates, 250000 cells per well, 1 mL medium

The cells were seeded in the respective amount of Attachment Medium and allowed to adhere to the cell culture plates for 2 hrs. Afterwards the medium was changed to the same volume of Fasting Medium and the cells were incubated overnight.

On the next morning, the cells were controlled for viability and hepatocyte-specific morphology, before being transfected with LNA antisense oligonucleotides (ASO) to reduce target gene expression. The cell culture medium was replaced by 800  $\mu$ L of fresh Fasting Medium and then 200  $\mu$ L of TFX Mix was added dropwise.

#### TFX Mix

DMEM, low glucose (1 g/L)  
Lipofectamine RNAiMAX (6  $\mu$ L / 100  $\mu$ L solution)  
LNA ASO (100 nM / 100  $\mu$ L solution)

To ensure a robust target gene downregulation the cells were incubated for another 24 hrs, before being stimulated with metabolic reagents.

### 3.2.4. Metabolic stimulation of primary murine hepatocytes

Primary hepatocytes were stimulated with metabolic reagents exactly 24 hrs after seeding or LNA transfection. Briefly, the Fasting medium was replaced by the same volume of the respective Stimulation Medium and the cells were incubated for varying durations. At the end of the respective stimulation the Stimulation Medium was removed and the cells were directly frozen at  $-20^{\circ}\text{C}$ . Three technical replicates (400.000 cells in 6-wells) were performed for each biological replicate.

#### Insulin Predilution Mix (1 $\mu$ M)

10 mL DMEM, low glucose (1 g/L)  
5.8  $\mu$ L Insulin, human recombinant

#### Insulin Stimulation Medium

DMEM, low glucose (1 g/L)  
Insulin Predilution Mix (10 nM / 100 nM total)

#### Glucagon Solution (1 mg/mL)

1 mL Millipore<sup>®</sup> H<sub>2</sub>O  
1 mg Glucagon, human recombinant

#### Glucagon Stimulation Medium

DMEM, low glucose (1 g/L)  
Glucagon Solution (3  $\mu$ M total)

#### Dexamethasone Solution (5 mM)

10 mL Ethanol (100 %)  
19.62 mg Dexamethasone, min. 97 %

#### Dexamethasone Predilution Mix (10 $\mu$ M)

10 mL DMEM, low glucose (1 g/L)  
20  $\mu$ L Dexamethasone solution

#### Forskolin Solution (10 mM)

10 mL DMSO (99 %)  
41.05 mg Forskolin, min. 98 %

#### Fasting Stimulation Medium

DMEM, low glucose (1 g/L)  
Dexamethasone Predilution Mix (100 nM total)  
Forskolin Solution (10  $\mu$ M total)

### 3.2.5. Transfection of NSC-34 cells with CRISPR/Cas9 components

In order to validate gRNA functionality, NSC-34 cells were seeded on a 12-well plate (100000 cells per well) and transfected with Cas9 mRNA (5meC, Psi) and the sgRNAs to be tested.

Briefly, cells were allowed to acclimatise to the cell culture plates for 24 hrs before starting the experiment. The TFX Mix was freshly prepared for every experiment and incubated at RT for 25 min, while the cells were washed twice with 1X PBS. Subsequently, 500  $\mu$ L of TFX Mix was added dropwise on every well and the cells were incubated in a CO<sub>2</sub> incubator. After 4 hrs of incubation 500  $\mu$ L of NSC-34 Medium was added on top of the TFX Mix and the cells were incubated for another 48 hrs. At the end of the experiment the medium was removed and 200  $\mu$ L Tail Lysis Buffer (see 3.3.1) was added to each well. After scraping the cells from the cell culture surface, the cell lysis solution was transferred into 1.5 mL reaction tubes and incubated for 2 hrs at 60°C, 800 rpm. Proteinase K activity was heat-inactivated by incubating the cell lysis solution for 15 min at 96°C. Finally, 800  $\mu$ L DNase-free H<sub>2</sub>O was added to the cell lysis solution and it was directly used as genomic DNA template in T7 Endonuclease I Assays (see 3.1.15.).

#### TFX Mix

Opti-MEM™ Reduced Serum Medium  
Lipofectamine® 2000 (8  $\mu$ L/mL solution)  
Cas9 mRNA (2  $\mu$ g/mL solution)  
gRNA to be tested (1  $\mu$ g/mL solution)

### 3.3. Biochemical methods

#### 3.3.1. Genomic DNA extraction from mouse tails

In order to achieve genomic DNA samples for genotyping PCR reactions (see 3.4.3.), small tail biopsies were lysed by Proteinase K digestion in 300  $\mu$ L Tail Lysis buffer and incubated overnight in a thermo mixer (56°C, 300 rpm). Finally, Proteinase K activity was heat-inactivated at 96°C for 15 minutes and the samples were directly used for subsequent PCR reactions or stored at 4°C.

#### Tail Lysis Buffer

50 mM            KCl  
10 mM            Tris-HCl, pH 8.3  
1.5 mM            MgCl<sub>2</sub>  
0.45 %            Tween® 20  
0.45 %            Nonidet™ P-40  
100  $\mu$ g/mL        Proteinase K  
in Millipore® H<sub>2</sub>O



### 3.3.2. Subcellular fractionation

Subcellular fractions were obtained using freshly isolated primary hepatocytes and the Nuclei Isolation Kit: Nuclei EZ Prep according to the manufacturer's protocol.

Briefly,  $5 \times 10^6$  cells were centrifuged (5 min, 300 g, 4°C) and the supernatant was discarded, whereas the cell pellet was resuspended in 10 mL PBS and centrifuged again (5 min, 300 g, 4°C). After removal of the supernatant, 4 mL ice-cold Nuclei EZ Lysis Buffer was added to the cell pellet and the reaction tube was vortexed briefly and kept on ice for 5 min. Following centrifugation (5 min, 300 g, 4°C), the supernatant was kept for later analysis (cytoplasmic fraction), while the pellet was again resuspended in 4 mL ice-cold Nuclei EZ Lysis Buffer, vortexed briefly and kept on ice for 5 min. After a final centrifugation (5 min, 300 g, 4°C) the supernatant was discarded and the nuclei pellet was resuspended in 200  $\mu$ L ice-cold Nuclei EZ Storage Buffer (nuclear fraction). If not directly processed for total RNA isolation, the cytoplasmic and nuclear fractions were stored at -80°C.

### 3.3.3. Total RNA isolation from subcellular fractions

Irrespective of the different volume of different subcellular fractions, 1 mL TriFast solution was added to the respective solution, homogenized by pipetting up and down and stored at RT for 10 min. During the incubation time, nucleoprotein complexes dissociate and release previously bound RNA molecules, which subsequently were separated from DNA molecules and proteins by adding 200  $\mu$ L chloroform to the sample. Following vigorous shaking and 3 min incubation at RT, the samples were centrifuged (15 min, 12000 x g, 4°C) to separate the reaction mixture into a lower red phenol-chloroform phase, an interphase containing DNA and protein partitions as well as in an upper colorless aqueous phase that contains RNA molecules. After transferring the aqueous phase to a fresh tube, RNA was precipitated by adding 500  $\mu$ L isopropanol, brief vortexing and incubation at RT for 10 min. After centrifugation (10 min, 12000 x g, 4°C), the supernatant was discarded, whereas the RNA pellet was washed with 1 mL ethanol (75 %, in DEPC-H<sub>2</sub>O), vortexed and pelleted by centrifugation (10 min, 12000 x g, 4°C). Subsequently, the supernatant was discarded and the RNA pellet was air-dried for 10 min, then resuspended in 50  $\mu$ L DEPC-H<sub>2</sub>O and heated at 55°C for 10 min. Finally, RNA concentrations were measured using a NanoDrop™ ND-1000 spectrophotometer, diluted to identical concentrations with DEPC-H<sub>2</sub>O and directly used for subsequent RT-PCR reactions or stored at -80°C.

### 3.3.4. Total RNA isolation from primary hepatocytes

Total RNA was isolated from primary hepatocytes using the RNeasy® Mini Kit according to the manufacturer's protocol.

Primary hepatocytes grow in a monolayer and were directly lysed on the cell culture dish by adding 350 µL Buffer RLT and 3.5 µL β-Mercaptoethanol. Using a cell scraper (12-well plate: 25 cm; 6-well plate: 39 cm) the cells were completely detached from the cell culture plate and subsequently loaded into a QIAshredder spin column and centrifuged at full speed for 2 min. Afterwards 350 µL ethanol (70 %, in Millipore® H<sub>2</sub>O) was added to the lysate and the mixture was loaded into a RNeasy spin column and centrifuged (15 s, 8000 x g). After discarding the flow-through, the column was loaded with 700 µL of Buffer RW1 and centrifuged again (15 s, 8000 x g). The flow-through was discarded again and the column was washed with 500 µL of Buffer RPE and centrifuged (15 s, 8000 x g). Once more the flow-through was discarded and the column was washed again with 500 µL of Buffer RPE and centrifuged (2 min, 8000 x g). To elute the RNA, the column was placed on a fresh reaction tube and 30 µL RNase-free H<sub>2</sub>O was directly added on the center of the spin column membrane. Following centrifugation (1 min, 8000 x g) RNA concentrations were measured using a NanoDrop™ ND-1000 spectrophotometer, diluted to 200 ng/µL and directly used for subsequent RT-PCR reactions or stored at -80°C.

### 3.3.5. Total RNA isolation from liver tissue

Before thawing frozen liver tissue, 1.5 mL reaction tubes were prepared for each tissue sample and loaded with a small volume of Precellys® zirconium oxide beads and 500 µL TriFast solution. Then small pieces of frozen liver tissue were cut on dry ice, directly transferred to the prepared reaction tubes and homogenized using a FastPrep-24™ 5G Homogenizer (program: mouse liver). After storing the homogenates at RT for 10 min, 200 µL chloroform was added to each sample and the samples were vigorously shaken and incubated at RT for 3 min. Following centrifugation (15 min, 12000 x g, 4°C) the reaction mixture was separated into a lower red phenol-chloroform phase, an interphase containing DNA and protein partitions as well as in an upper colorless aqueous phase that contains RNA molecules. After transferring the aqueous phase to a fresh tube, RNA was precipitated by adding 500 µL isopropanol, brief vortexing and incubation at RT for 10 min. After centrifugation (10 min, 12000 x g, 4°C), the supernatant was discarded, whereas the RNA pellet was washed with 1 mL ethanol (75 %, in DEPC-H<sub>2</sub>O), vortexed and pelleted by centrifugation (10 min, 12000 x g, 4°C). Subsequently, the supernatant was discarded and the RNA pellet was air-dried for 10 min, then resuspended in 50 µL DEPC-H<sub>2</sub>O and heated at 55°C for 10 min. Finally, RNA concentrations were measured using a NanoDrop™ ND-1000 spectrophotometer, diluted to identical concentrations with DEPC-H<sub>2</sub>O and directly used for subsequent RT-PCR reactions or stored at -80°C.

### 3.3.6. Total protein isolation from primary hepatocytes

To isolate total proteins from primary hepatocytes, 500  $\mu$ L RIPA Working Solution were directly added in the wells of frozen cell culture dishes. Using a cell scraper (12-well plate: 25 cm; 6-well plate: 39 cm) the cells were completely detached from the cell culture plate and transferred into 1.5 mL reaction tubes. For cell lysis the reaction tubes were snap-frozen in liquid nitrogen and thawed on dry ice for three consecutive times. Subsequently, the samples were centrifuged (10 min, 12000 x g, 4°C) and the pellet was discarded, while the supernatant was transferred to a new reaction tube. By using the Quick Start™ Bradford Protein Assay Kit and a FilterMax™ F5 microplate reader, the protein concentrations of the samples were measured at 595 nM and diluted to equivalent concentrations with RIPA Working Solution. Finally, the respective amount of 4X Laemmli Buffer (containing 5 %  $\beta$ -Mercaptoethanol) was added to every sample and the mixture was boiled at 96°C for 6 min, before being stored at -20°C.

<u>RIPA Buffer</u>		<u>RIPA Working Solution</u>	
150 mM	NaCl	5 mL	RIPA Buffer
50 mM	Tris-HCl, pH 7.5	1 x Complete™	Mini Protease Inhibitor tablet
1 mM	EDTA	1 x PhosSTOP™	Phosphatase Inhibitor tablet
1 %	Nonidet™ P-40		
0.1 %	Tween® 20 (v/v)		
	in Millipore® H <sub>2</sub> O		

### 3.3.7. Total protein isolation from liver tissue

Before thawing frozen liver tissue, 1.5 mL reaction tubes were prepared for each tissue sample, loaded with 500  $\mu$ L IP Lysis Buffer and kept on dry ice. Then small pieces of frozen liver tissue were cut on dry ice, directly transferred to the prepared reaction tubes and homogenized using a FastPrep-24™ 5G Homogenizer (program: mouse liver). Afterwards, the samples were incubated on ice for 45 min, centrifuged (45 min, 12000 x g, 4°C) and then 400  $\mu$ L of the supernatant was transferred to a fresh reaction tube. After another centrifugation step (45 min, 12000 x g, 4°C) 300  $\mu$ L of the supernatant was transferred to a fresh tube and 1  $\mu$ L of the supernatant was mixed with 39  $\mu$ L of IP Lysis Working Solution to assess the respective protein concentration. By using the Quick Start™ Bradford Protein Assay Kit and a FilterMax™ F5 microplate reader, the protein concentrations of the samples were measured at 595 nM and diluted to equivalent concentrations with IP Lysis Working Buffer. Finally, the respective amount of 4X Laemmli Buffer (containing 5 %  $\beta$ -Mercaptoethanol) was added to every sample and the mixture was boiled at 96°C for 6 min, before being stored at -20°C.

<u>IP Lysis Buffer</u>		<u>PMSF Solution (100 mM)</u>	
130 mM	NaCl	1 mL	isopropanol
50 mM	Tris-HCl, pH 7.4	17.4 mg	PMSF
5 mM	EDTA		
1 % (v/v)	Nonidet™ P-40	<u>NaF Solution (100 mM)</u>	
		1 mL	Millipore® H <sub>2</sub> O
		4.2 mg	NaF
<u>IP Lysis Working Buffer</u>			
15 mL	IP Lysis Buffer		
150 µL	NaF Solution		
150 µL	PMSF Solution		
2 x Complete™ Mini Protease Inhibitor tablet			

### 3.3.8. SDS-PAGE

Proteins lysates were separated according to their molecular weight by sodium dodecyl sulfate-polyacrylamide gel electrophoresis (SDS-PAGE). Samples as well as molecular weight protein markers were loaded into precast polyacrylamide gels, the gel chamber was filled with 1X SDS Running Buffer and proteins were subsequently separated in an electric field of 90-120 V for varying time spans.

For experiments with 12 samples polyacrylamide gels were prepared according to the following protocol:

<u>Separating Gel (10 mL, 8 %)</u>		<u>Stacking Gel (2 mL, 5 %)</u>	
4.625 mL	Millipore® H <sub>2</sub> O	1.375 mL	Millipore® H <sub>2</sub> O
2.675 mL	Rotiphorese® Gel 30	325 µL	Rotiphorese® Gel 30
2.5 mL	Tris-Cl (1.5 M), pH 8.8	250 µL	Tris-Cl (1.0 M), pH 6.8
100 µL	10 % SDS (in Millipore® H <sub>2</sub> O)	20 µL	10 % SDS (in Millipore® H <sub>2</sub> O)
100 µL	10 % APS (in Millipore® H <sub>2</sub> O)	20 µL	10 % APS (in Millipore® H <sub>2</sub> O)
6 µL	TEMED	2 µL	TEMED
<u>10X SDS Running Buffer</u>			
144 g	Glycine		
30 g	Tris(hydroxymethyl)aminomethane		
10 mL	SDS		
Millipore® H <sub>2</sub> O, up to 1 L			

### 3.3.9. Western blot analysis

After SDS-PAGE separated proteins were electrotransferred from the polyacrylamide gel to a previously activated PVDF membrane (30 s incubation in methanol). A transfer sandwich composed of three Whatman™ papers, the PVDF membrane (facing the anode), the polyacrylamide gel (facing the cathode) and three additional Whatman™ papers was assembled in 1X Transfer Buffer and placed in a ice-cooled blotting chamber filled with 1X Transfer Buffer. The electrotransfer was performed for 2 hrs with 200 mA per membrane.

After protein transfer the PVDF membrane was incubated with Ponceau solution to check for protein abundance. Afterwards, the membrane was rinsed with 1X TBS-T, cut into the membrane parts to be analyzed and incubated for 1 hour with 20 mL Blocking Solution with constant shaking. Following overnight incubation with 20 mL of the respective primary antibody solution (4°C, constant rotation, 200 rpm), the membrane parts were washed (3 x 10 mins, RT, shaking) with TBS-T and incubated with 20 mL of horseradish peroxidase (HRP)-coupled secondary antibodies (1 h, RT, permanent shaking). After additional washing with TBS-T (3 x 10 mins, RT, shaking), 500 µL of chemoluminescent substrate (mix 1:1) was applied on the membrane and the chemoluminescence originating from HRP-conjugated antibodies bound to the proteins of interest has been detected using a FastGene® FAS V gel documentation system.

#### 10X Transfer Buffer

144 g Glycine  
30 g Tris(hydroxymethyl)aminomethane  
Millipore® H<sub>2</sub>O, up to 1 L

#### 1X Transfer Buffer

200 mL Methanol  
100 mL 10X Transfer Buffer  
Millipore® H<sub>2</sub>O, up to 1 L

#### 20X Tris Buffered Saline (TBS)

175.4 g NaCl  
48 g Tris(hydroxymethyl)aminomethane  
Millipore® H<sub>2</sub>O, up to 900 mL  
adjust pH to 7.4 with HCl  
Millipore® H<sub>2</sub>O, up to 1 L

#### 1X Tween 20-Tris Buffered Saline (TBS-T)

50 mL 20X TBS  
1 mL Tween® 20  
Millipore® H<sub>2</sub>O, up to 1 L

#### Blocking Solution

18 mL Tween 20-Tris Buffered Saline  
2 mL Western Blocking Reagent

#### Antibody Solutions

19 mL Tween 20-Tris Buffered Saline  
1 mL Western Blocking Reagent  
Protein-specific Antibody

## 3.4. Mouse procedures

### 3.4.1. Animal care

Experimental animals were housed in individually ventilated cages (IVC Type II long) in a specific pathogen-free (SPF) research facility with controlled temperature (22-24°C), relative air moisture (50-70 %) and light/dark cycle (12h/12h). Care of animals was within institutional animal-care committee guidelines. Unless stated otherwise, animals were allowed *ab libitum* access to food and drinking water. After experimentation procedures or before tissue collection animals were sacrificed by cervical dislocation.

Animal housing and experimentation procedures were approved by local and regional authorities (Landesamt for Natur, Umwelt und Verbraucherschutz Nordrhein Westfalen) and can be found under the following internal reference numbers:

- 576.1.36.6.G 50/13 Be
- 84-02.04.2016.A460
- 84-02.05.40.14.134
- 84-02.05.40.16.009

### 3.4.2. Experimental mouse models

Wild type control mice were maintained on a C57BL/6N genetic background and purchased from Charles River Research Models and Services, Sulzfeld, DE, whereas diabetes model mice (C57BLKS/J *Lepr<sup>db/db</sup>*) as well as misty control mice (C57BLKS/J *Dock7<sup>m/m</sup>*) were purchased from The Jackson Laboratory, Bar Harbor, US.

The *Lepr<sup>db/db</sup>* mouse line is characterized by a G-to-T transversion in the leptin receptor gene *Lepr* resulting in premature transcript termination and subsequently leptin receptor deficiency. Homozygous *Lepr<sup>db</sup>* mice develop morbid obesity and chronic hyperglycemia by 3 to 4 weeks of age. Further disease characteristics are hyperinsulinemia, hyperglycemia, insulin resistance, glucose intolerance and abnormal pancreatic beta cell morphology [213-215].

As homozygous *Lepr<sup>db</sup>* mice are sterile, distributors of mouse models incorporated the misty mutation (*Dock7<sup>m</sup>*) into breeding stocks of the diabetes (db) mutation. The recessive coat color mutation misty is the result of a retrotransposon insertion into the gene *Dock7*, which is closely linked to the *Lepr* locus and therefore can be used as marker allele for the propagation of the db mutation. Yet, *Dock7<sup>m/m</sup>* mice not only exhibit a dilution of coat color, but also mild growth retardation, less inguinal adipose mass and the complete lack of brown adipose tissue [216].

Genome-edited mouse lines (*lincIRS2<sup>Δ</sup>*, *Gm15441<sup>Δ</sup>*) were generated by pronuclear injection of CRISPR/Cas9 components at the CECAD in vivo Research Facility, Cologne, DE. Donor oocytes originated from a C57BL/6N background and resulting offspring was maintained on a C57BL/6N background.

### 3.4.3. Genotyping of mice

In order to identify genome-edited mice, genomic DNA was extracted from tail biopsies (see 3.3.1.) and used as template in two independent genotyping PCR reactions (3.1.1.):

#### Genotyping protocol *linclRS2*<sup>Δ</sup> (#1)

Forward primer: #407	<u>Initial denaturation</u>	94°C	3 min	
Reverse primer: #410	Denaturation	94°C	30 s	
	Annealing	60°C	30 s	35x
<u>Expected fragments</u>	<u>Elongation</u>	72°C	1 min	
WT -> 555 bp	Final elongation	72°C	10 min	
KO -> no band	Hold	4°C	∞	

#### Genotyping protocol *linclRS2*<sup>Δ</sup> (#2)

Forward primer: #409	<u>Initial denaturation</u>	94°C	3 min	
Reverse primer: #408	Denaturation	94°C	30 s	
	Annealing	60°C	30 s	35x
<u>Expected fragments</u>	<u>Elongation</u>	72°C	1 min	
WT -> 762 bp	Final elongation	72°C	10 min	
KO -> 357 bp	Hold	4°C	∞	

#### Genotyping protocol *Gm15441*<sup>Δ</sup> (#1)

Forward primer: #239	<u>Initial denaturation</u>	94°C	3 min	
Reverse primer: #240	Denaturation	94°C	30 s	
	Annealing	60°C	30 s	35x
<u>Expected fragments</u>	<u>Elongation</u>	72°C	1:30 min	
WT -> 672 bp	Final elongation	72°C	10 min	
KO -> no band	Hold	4°C	∞	

#### Genotyping protocol *Gm15441*<sup>Δ</sup> (#2)

Forward primer: #241	<u>Initial denaturation</u>	94°C	3 min	
Reverse primer: #240	Denaturation	94°C	30 s	
	Annealing	60°C	30 s	35x
<u>Expected fragments</u>	<u>Elongation</u>	72°C	1:30 min	
WT -> 713 bp	Final elongation	72°C	10 min	
KO -> 306 bp	Hold	4°C	∞	

#### 3.4.4. Experimental diets

During maintenance and breeding all mice were fed a normal chow diet (NCD) containing 57 % carbohydrates, 34 % protein and 9 % fat. For diet-induced obesity experiments, mice were fed a high-fat diet (HFD) containing 54 % fat, 24 % protein and 22 % carbohydrates or a control diet (CD) containing 67 % carbohydrates, 20 % protein and 13 % fat.

Normal chow diet:	ssniff® R/M-H Low-Phytoestrogen	(Product-ID: V1554)
High-fat diet:	ssniff® EF acc. D12492 (I) mod.	(Product-ID: E15742)
Control diet:	ssniff® EF D12450B* mod. LS	(Product-ID: E15748)

All diets were purchased from ssniff Spezialdiäten GmbH, Soest, DE

#### 3.4.5. *In vivo* LNA application

Antisense LNA™ GapmeRs were administered to mice via intraperitoneal (IP) injection. Starting from 6 weeks of age mice were injected every two weeks with 10 mg LNA (diluted in 0.9 % NaCl solution) per kg of body weight.

#### 3.4.6. Assessment of body weight progression

Body weight of experimental mouse cohorts was assessed weekly for each individual mouse, starting from 6 weeks of age until euthanasia (week 18).

#### 3.4.7. Intraperitoneal insulin tolerance test (ITT)

Experimental mouse cohorts were subjected to an intraperitoneal insulin tolerance test at 11 weeks of age. Before starting the experiment mice were weighed and basal glucose levels were recorded. Following intraperitoneal administration of insulin (0.75 U/kg body weight, in 0.9 % NaCl solution) blood glucose levels were measured after 15 min, 30 min, 60 min and 90 min.

#### 3.4.8. Intraperitoneal glucose tolerance test (GTT)

Experimental mouse cohorts were subjected to an intraperitoneal glucose tolerance test at 12 weeks of age. After 16 hrs of overnight fasting mice were weighed and basal glucose levels were recorded. Following intraperitoneal administration of glucose (2 g/kg body weight, in 0.9 % NaCl solution) blood glucose levels were measured after 15 min, 30 min, 60 min and 120 min.



### 3.4.9. Indirect calorimetry analysis

Indirect calorimetric measurements were obtained using the TSE PhenoMaster platform. In detail, mice were allowed to adapt to single housing in metabolic cages (7.1 liter) for 4 days, followed by 3 days of indirect calorimetry measurements. Access to food and water were provided *ad libitum* and metabolic parameters were measured automatically by the monitoring system.

### 3.4.10. Isolation of primary murine hepatocytes

For each experiment primary murine hepatocytes were freshly isolated from male wild type mice of 12 to 20 weeks of age. Before surgery a peristaltic pump was equipped with a butterfly needle (0.45 x 12mm) and rinsed for 5 min with Ethanol (70 %) and for 5 min with Millipore® H<sub>2</sub>O. For high viability of cells it is critical to ensure that there are no air bubbles left in the tubing. During cleaning of the peristaltic pump Solution I, Solution II and Solution III were prepared and placed into a water bath at 40°C.

Mice were anaesthetised by intraperitoneal injection of freshly prepared Ketamin/Xylazine Mix (0.01 mL/g BW), fixed on the working platform and the abdominal cavity was opened. Intestinal organs were pushed aside to have free access to the inferior vena cava as well as to the portal vein. The peristaltic pump was slowly started perfusing Solution I, while the canula was inserted into the inferior vena cava. If the cannulation was successful, the liver instantly began to clear and the portal vein was cut to relieve the pressure and allow the fluid to leave the circulation. Once the portal vein was cut, the flow rate of the peristaltic pump was increased to 7-9 mL / minute and the liver was perfused with 75 mL of Solution I. Shortly before the reservoir of Solution I was depleted, 50 mL of Solution III was added to the same tube and used for the remaining perfusion. Before air bubbles could reach the liver, the perfusion was stopped and the canula as well as the gall bladder were removed from the perfused liver. Subsequently, the entire liver was carefully excised and transferred to a petri dish containing 10 mL of Solution II. By dissecting the lobes and gently shaking the liver, hepatocytes were brushed out of the liver and passed through a 40 µM cell strainer. The filtered cell solution was centrifuged two times (5 min, 200 g, 4°C) and resuspended in 10 mL of ice-cold Attachment Medium (see 3.2.1.). Afterwards, the cell solution was centrifuged again (5 min, 200 g, 4°C) and resuspended in 20 mL Attachment Medium and 16 mL Percoll Solution. After a final centrifugation (7 min, 200 g, 4°C) and removal of the supernatant (= dead cells), the cell pellet was resuspended in 10 mL of Attachment Medium and the primary hepatocytes were counted and seeded on collagen I-coated cell culture.

Solution I  
500 mL EBSS without Ca/Mg  
0.5 mL 0.5 M EGTA

Solution II  
500 mL EBSS with Ca/Mg  
5 mL HEPES

Solution III  
50 mL Solution II (pre-warmed)  
13 mg Collagenase IV  
2 mg Trypsin Inhibitor

Ketamin/Xylazine Mix  
6 mL 0.9 % NaCl solution  
1 mL Anesketin® Ketamin solution  
0.25 mL Rompun® Xylazine solution

Percoll Solution  
28 mL Percoll  
2 mL PBS (10X)

### 3.4.11. Mouse model generation

LncRNA-specific KO mouse models were generated by pronuclear injection of CRISPR/Cas9 ribonucleoprotein (RNP) complexes into zygotes of superovulated C57BL/6NRj females as described in [217].

Briefly, before injection target-specific CRISPR RNAs (crRNAs) were incubated with trans-activating crRNAs (tracrRNAs) to form annealed guideRNA (gRNA) molecules as shown below:

<u>crRNA:tracrRNA Solution</u>	
16 µL T <sub>10</sub> E <sub>0.1</sub> Buffer	95°C 5 min
2 µL crRNA #1 (100 µM)	cool down 5°C / min
2 µL crRNA #2 (100 µM)	RT hold
2 µL tracrRNA (100 µM)	

Subsequently, annealed gRNA molecules were incubated with Cas9 proteins to assemble functional RNP complexes as shown below:

<u>RNP Solution</u>	
21 µL T <sub>10</sub> E <sub>0.1</sub> Buffer	
2 µL Cas9 protein (5 µM)	RT 10 min
2 µL crRNA:tracrRNA Solution (10 µM)	

To achieve the Final Injection Solution additional Cas9 mRNA was added to the RNP solution and the solution was centrifuged (10 min, 12000 x g, 4°C) and kept on ice or directly used for injection.

Final Injection Solution

25 µL	RNP Solution
23.5 µL	T <sub>10</sub> E <sub>0.1</sub> Buffer
1.5 µL	Cas9 mRNA

Pronuclear injections of C57BL/6NRj zygotes were performed at the CECAD *in vivo* Research Facility, CECAD Research Center, Cologne, DE. 2-cell stage embryos were subsequently implanted into the oviduct of pseudopregnant 0.5 postcoital (p.c.) RjHan:NMRI females. Finally, offspring born from implanted embryos were genetically analyzed via DNA sequencing (3.1.9.) and - in case of CRISPR/Cas9-mediated genome-engineering of the desired locus - bred to create transgenic mouse lines.

Final Injection Solution composition

50 µL	T <sub>10</sub> E <sub>0.1</sub> Buffer
Cas9 protein	(32.7 ng/µL)
Cas9 mRNA	(30 ng/µL)
tracrRNA	(12.5 ng/µL)
crRNA #1	(12.5 ng/µL)
crRNA #2	(12.5 ng/µL)

T<sub>10</sub>E<sub>0.1</sub> Buffer

24.25 mL	embryo-tested H <sub>2</sub> O
500 µL	EDTA (5 mM)
209 µL	Tris-HCl (1 M)
40.85 µL	Tris-base (1 M)

### 3.5. Computational methods

#### 3.5.1. Coding potential predictions

Coding potentials of lncRNA candidates were predicted using transcript sequence data (in FASTA format) obtained from the Ensembl Genome Browser (Mus musculus, version GRCh38.p6) and the following web-based applications [196, 197]:

Coding Potential Calculator (CPC)

- Coding probability cutoff: 0.0
- Positive controls: *Gapdh* (*Gapdh-202*), *Hprt* (*Hprt-201*) and *Prox1* (*Prox1-202*)
- Negative controls: *LeXis* (*LeXis-202*), *Malat1* (*Malat1-201*) and *Neat1* (*Neat1-201*)

Coding Potential Assessment Tool (CPAT), version 1.2.4

- Species assembly: NCBI Build 37/mm9
- Coding probability cutoff: 0.44
- Positive controls: *Gapdh* (*Gapdh-202*), *Hprt* (*Hprt-201*) and *Prox1* (*Prox1-202*)
- Negative controls: *LeXis* (*LeXis-202*), *Malat1* (*Malat1-201*) and *Neat1* (*Neat1-201*)

### 3.5.2. GuideRNA design

Single guide RNAs (sgRNAs) have been designed using the CRISPOR online application [198] considering the following criteria:

- exclusion of sgRNAs with off-targets for 1- or 2 mismatches
- specificity score as high as possible, invariably higher than 50
- score of Moreno-Mateos algorithm as high as possible

Although high scores are desirable for all design algorithms, the algorithm by Moreno-Mateos [218] is best for sgRNAs expressed with a T7 promotor and thus needs to be privileged when designing sgRNAs intended for mouse oocyte injections.

#### Target locus for 4833411C07Rik sgRNA design

Mus musculus (GRCm38/mm10), genome coordinates: chr8:10,899,835-10,900,342

#### Target locus for Gm15441 sgRNA design

Mus musculus (GRCm38/mm10), genome coordinates: chr3:96,566,517-96,567,016

### 3.5.3. RNA sequencing data analysis

Mouse RNA-Seq data was processed utilising the GRCm38.p6 assembly of the mouse genome as gene sets from Ensembl release 90 [219]. Biotype and gene features were added manually using Ensembl BioMart [202]. The bioinformatic data analysis pipeline consists of five steps:

- (1) barcode and adapter removal using flexbar [203],
- (2) computational rRNA depletion by filtering reads that map to known murine rRNAs using Bowtie2 [195],
- (3) alignment of non-rRNA reads to the GRCm38.p6 reference genome using STAR [207],
- (4) transcript assembly using cufflinks followed by cuffmerge (Cufflinks suite 2.2.1) [220] and
- (5) differential gene expression analysis between experimental conditions using cuffdiff (Cufflinks suite 2.2.1) [200].

Human RNA-Seq data was analyzed using the QuickNGS workflow system based on Ensemble release 82 [206]. The bioinformatic data analysis pipeline consists of four steps:

- (1) alignment of reads to the GRCm38.p12 reference genome using Tophat2 [208],
- (2) transcript assembly using cufflinks followed by cuffmerge (Cufflinks suite 2.2.1) [220],
- (3) differential gene expression analysis between experimental conditions using DESeq2 [201] and
- (4) combination with multiple annotations using the biomaRt package [194].

## Chapter 4 - Results

### 4.1. Hepatic lncRNA expression inversely correlates with mRNA expression in response to metabolic states

#### 4.1.1. Transcriptome profiling reveals global hepatic lncRNA downregulation in obesity mouse models

In order to elucidate, if hepatic lncRNA expression correlates with metabolic disorders, such as obesity or T2DM, we performed global transcriptome profiling by performing RNA sequencing (RNA-Seq) in livers from four different cohorts of mice. This included (I) a diet-induced mouse model for obesity and (II) its control littermates as well as (III) a genetically-evoked mouse model for obesity and T2DM and (IV) its control breeding stock strain. In detail, we harvested seven metabolically relevant tissues (liver, kidney, brain, skeletal muscle, brown adipose tissue as well subcutaneous- and visceral white adipose tissue) from three mice of each respective groups: (I) 30 weeks-old wild type mice (male) that had been fed a high-fat diet (HFD) for 24 weeks, with beginning of HFD feeding at 6 weeks of age, (II) 30 weeks-old wild type mice (male) that had been fed a low-fat or normal chow diet (NCD) for 30 weeks, (III) 10 weeks-old *LepR<sup>db/db</sup>* mutant mice (male), a widely used genetic model for obesity and T2DM in mice [215], that had been fed a NCD for 10 weeks, and (IV) 10 weeks-old *Dock7<sup>m/m</sup>* mutant mice (male), which develop less adipose tissue and on average weigh 15 % less than wild type control mice [216], that had been fed a NCD for 10 weeks (Figure 6a).

RNA was extracted from the harvested tissues of the respective mouse models and used for rRNA-depleted (total) RNA-Seq. Liver samples yielded, on average, 201 million high-quality, paired-end RNA sequencing reads (range 184.3 million - 238.9 million), among which 90.9 % were mapped to the mouse genome assembly GRCm38 (for summarised read information see Supplemental Figure 1). Homogeneity of liver RNA-Seq data sets were confirmed by principle component analysis (PCA), which demonstrated little variance within experimental groups and separate clustering of different mouse models (Figure 6b).

For identification of hepatic lncRNAs that were differentially regulated between aforementioned mouse models, we performed differential gene expression analysis and detected 50 hepatic lncRNA transcripts that were differentially regulated between HFD and NCD mice and 83 hepatic lncRNA transcripts that exhibited differential expression levels between *LepR<sup>db/db</sup>* and *Dock7<sup>m/m</sup>* mutant mice (Figure 6c).

Intriguingly, when we globally compared the expression levels of hepatic transcripts, we observed a significant overrepresentation of downregulated lncRNA transcripts compared to protein-coding mRNAs in response to HFD feeding. Whereas protein-coding mRNAs generally displayed a profound tendency to upregulated transcription upon diet-induced obesity, most of the lncRNA transcripts were downregulated. Interestingly, we also found the same global trend of lncRNA downregulation and mRNA upregulation in the genetic-evoked obesity model system, albeit less pronounced than in the diet-induced obesity model system (Figure 6d + e).

Collectively, these results indicate that chronic obesity affects lncRNA expression levels, leading to lncRNA repression upon diet-induced as well as genetic-evoked obesity, and that global lncRNA and mRNA expression levels are independently and inversely regulated in obesity mouse models.

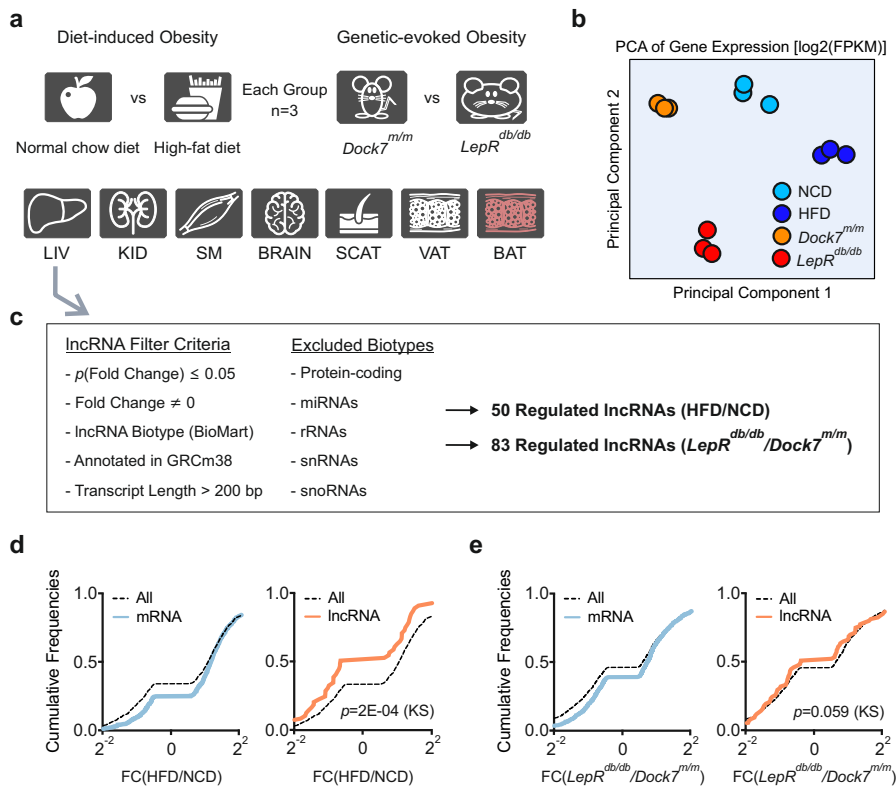


**Figure 6: Transcriptome profiling of two independent mouse model systems of obesity.**

(a) Schematic representation of the global transcriptome profiling approach using two independent mouse model systems of chronic obesity. Diet-induced obesity was represented by feeding male C57BL/6 mice a normal chow (NCD) or high-fat diet (HFD); genetic-evoked obesity by male *LepR*<sup>db/db</sup> and *Dock7*<sup>m/m</sup> mice (n=3 each). Livers (LIV), kidneys (KID), skeletal muscle (SM), brain (BRAIN), subcutaneous white adipose tissue (SCAT), visceral white adipose tissue (VAT) and brown adipose tissue (BAT) were harvested and sent for RNA sequencing. (b) Principal component analysis (PCA) score plot depicting

differences in gene expression between liver RNA-Seq data sets derived from the obesity mouse models cohorts NCD, HFD, *LepR*<sup>db/db</sup> and *Dock7*<sup>m/m</sup>. Gene expression was estimated using fragments per kilobase of exon per million reads [FPKM] values of the respective RNA-Seq data sets. (c) lncRNA-specific filter criteria of liver transcriptome data for identification of differentially regulated hepatic lncRNAs. (d-e) Cumulative frequency distribution of log<sub>2</sub>-transformed fold changes of hepatic mRNA (blue) and lncRNA (orange) expression between HFD and NCD mice (d) or *LepR*<sup>db/db</sup> and *Dock7*<sup>m/m</sup> mice (e). Graphs represent mean expression values with all data points plotted. Log<sub>2</sub>-transformed expression fold changes of all hepatic transcripts are shown as dotted black line. Statistical differences between mRNA and lncRNA expression changes were assessed using non-parametric Kolmogorov-Smirnov (KS) tests. p-values are given in the panels.

#### 4.1.2. Hepatic lncRNA expression is dynamically adapted to organismal energy states

In addition to the transcriptome data obtained from the chronic obesity mouse models, we also wanted to assess rapid transcriptional alterations of hepatic transcript expression upon short-term changes in nutrient availability. Therefore, three groups of C57BL/6 mice (male, 16 weeks-old, n=4) were subjected to a differential feeding experiment, with (I) a cohort being allowed to eat *ad libitum* for 16 hrs, (II) a cohort forced to fast for 16 hrs and (III) a cohort forced to fast for 16 hrs followed by 6 hrs of *ad libitum* refeeding. At the end of the respective feeding/fasting periods, we harvested the metabolically relevant tissues of the animals and performed total RNA-Seq of whole liver RNA in order to check for differential transcript expression upon the varying feeding conditions (Figure 7a).

On average, 137 million high-quality, paired-end RNA sequencing reads have been obtained from each liver sample (range 121,6 million - 149.9 million), among which 94.3 % were mapped to the mouse genome assembly GRCm38 (for summarised read information see Supplemental Figure 1). Principal component analysis confirmed homogeneity of liver RNA-Seq data sets with little variance within biological replicates and separate clustering of different experimental cohorts (Figure 7b).

To identify differentially expressed hepatic lncRNAs between experimental groups, we performed differential gene expression analysis and detected 92 lncRNAs with altered hepatic expression levels between mice fasted for 16 hrs compared to mice allowed to feed for 16 hrs. Additionally, 59 lncRNAs were identified that were differentially expressed in livers of mice allowed to refeed for 6 hrs after 16 hrs of fasting compared to mice fasting for 16 hrs (Figure 7c).

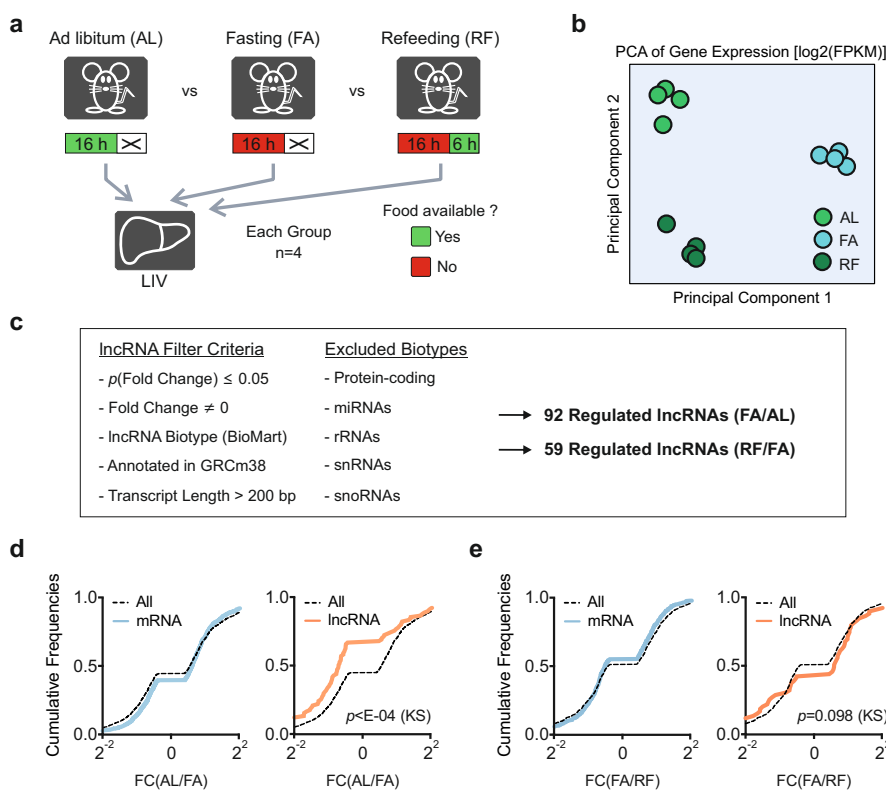


**Figure 7: Transcriptome profiling in livers of differentially-fed mice.**

(a) Schematic representation of the liver transcriptome profiling approach using three cohorts of male C57BL/6 mice (n=4 each) subjected to 16 hrs *ad libitum* feeding (AL), 16 hrs fasting (FA) or 16 hrs fasting followed by 6 hrs of *ad libitum* refeeding (RF). Livers (LIV) were harvested and sent for RNA sequencing. (b) Principal component analysis (PCA) score plot depicting differences in gene expression between liver RNA-Seq data sets derived from the differentially-fed mouse cohorts AL, FA and RF. Gene expression was estimated using fragments per kilobase of exon per million reads [FPKM] values

of the respective RNA-Seq data sets. (c) lncRNA-specific filter criteria of liver transcriptome data for identification of differentially regulated hepatic lncRNAs. (d-e) Cumulative frequency distribution of  $\log_2$ -transformed fold changes of hepatic mRNA (blue) and lncRNA (orange) expression between FA and AL mice (d) or RF and FA mice (e). Graphs represent mean expression values with all data points plotted.  $\log_2$ -transformed expression fold changes of all hepatic transcripts are shown as dotted black line. Statistical differences between mRNA and lncRNA expression changes were assessed using non-parametric Kolmogorov-Smirnov (KS) tests.  $p$ -values are given in the panels.

Similar to the expression data of the chronic obesity mouse models, we observed opposite transcriptional regulations for coding and long noncoding hepatic transcripts in the differentially-fed mouse cohorts. Global differential gene expression analysis between mice fasted for 16 hrs and *ad libitum* fed mice resulted in a significant upregulation of lncRNA transcripts as compared to mRNA transcripts. After 16 hrs of fasting, hepatic lncRNA regulation was globally upregulated in comparison to *ad libitum* fed mice, whereas hepatic mRNAs showed a tendency to global

downregulation (Figure 7d). Conversely, we detected a tendency towards global downregulation of lncRNAs between fasted mice allowed to short-term refeeding and fasted mice. But in contrast to the highly significant reciprocal regulation between fasted and *ad libitum* fed mice, the differential regulation between lncRNA and mRNA transcripts between refeed and fasted mice was not significant, but an inverted trend to the fasting-induced upregulation of lncRNAs (Figure 7e).

In conclusion, these results suggest a dynamic regulation of lncRNA expression levels in response to short-term alterations of nutrient availability, manifesting in increased global lncRNA expression upon fasting and diminished global lncRNA expression after only 6 hrs of refeeding after the fasting regime. In line with previous results obtained from the chronic obesity mouse models, global regulation of lncRNA levels again inversely correlates with global mRNA regulation.

#### 4.1.3. Anticorrelative regulation of lncRNAs and mRNAs in human liver biopsies

To corroborate the finding of inverse global regulations of lncRNA and mRNA transcripts in mouse models for chronic obesity and short-term changes in nutrient availability, we decided to analyse human liver biopsies for differential transcript regulation. Examined biopsies were part of a previously described cohort of human patients [193] and were selected according to the patient's gender (male) and body mass index (BMI) as well as to the fact if the patient was suffering from T2DM. In detail, we assembled three groups of human males (n=4), with (I) one group composed of lean (BMI: 21.9 - 24.8) and non-diabetic men, (II) one group consisting of obese (BMI: 47,9 - 54,2) and non-diabetic men and (III) one group made up of overweight or obese men (BMI: 27,0 - 63,0) with clinically-manifested T2DM (Figure 8a).

For each patient, total RNA-Seq was performed using whole liver RNA extracted from the respective liver biopsies. From each sample we obtained, on average, 138.2 million high-quality, paired-end RNA sequencing reads (range 127.6 million - 148.6 million), among which 87.6 % were mapped to the human genome assembly GRCh38 (for summarised read information see Supplemental Figure 1). Principal component analysis reflected heterogeneity of RNA-Seq data sets, potentially due to (apart from genetic differences) strong variance in patient's age (range 21-75 years) and disease etiology. Also, differences in lifestyle and diet could account for the high variance in these datasets. Highest differences were observed between RNA-Seq data sets of lean, non-diabetic patients, all of which were suffering from different types of cancer (see also 2.11.). However, data sets of obese, non-diabetic patients displayed transcriptional homogeneity and clustered together with data sets of obese diabetic patients, but not with overweight diabetic patients (Figure 8b). When performing differential gene expression analysis, we detected 297 hepatic lncRNA transcripts that were differentially regulated between lean, non-diabetic patients and obese, non-diabetic patients. In addition, we identified 504 hepatic lncRNA transcripts that exhibited altered expression levels between lean, non-diabetic patients and overweight or obese, diabetic patients (Figure 8c).



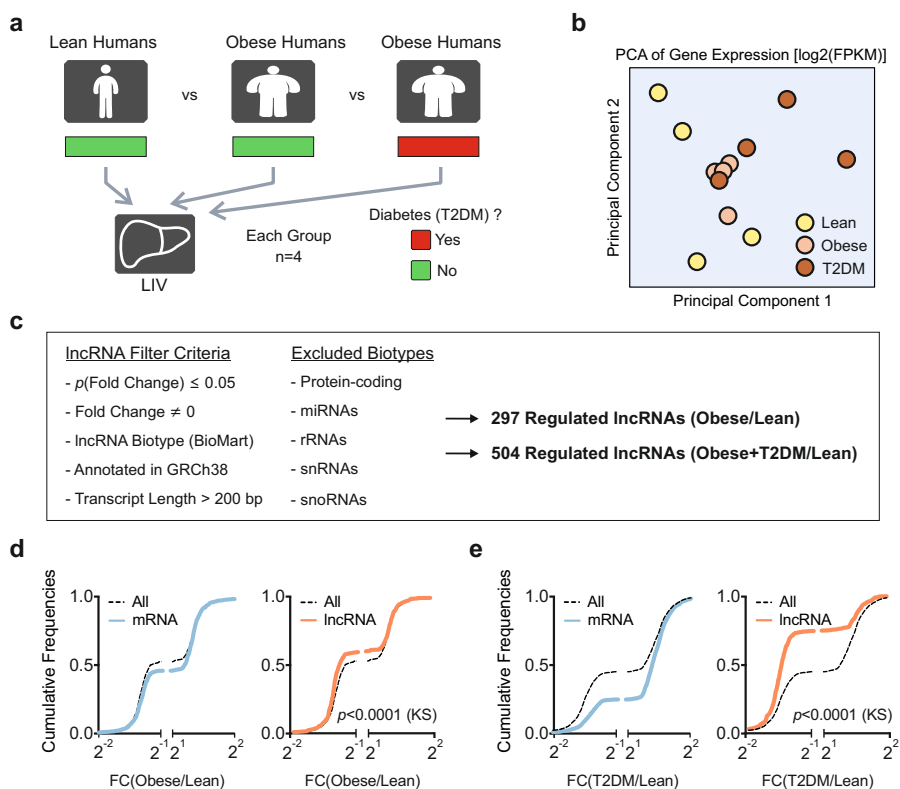


**Figure 8: Transcriptome profiling in liver biopsies of human patients.**

(a) Schematic representation of the transcriptome profiling approach using liver biopsies of three groups of male patients (n=4 each), with one group composed of lean, non-diabetic man (Lean), one group consisting of obese, non-diabetic man (Obese) and one group made up of obese/overweight man suffering from T2DM (T2DM). RNA extracted from livers biopsies (LIV) were sent for RNA sequencing. (b) Principal component analysis (PCA) score plot depicting differences in gene expression between liver RNA-Seq data sets derived from the patient groups Lean, Obese and T2DM. Gene expression was estimated using fragments per kilobase

of exon per million reads [FPKM] values of the respective RNA-Seq data sets. (c) LncRNA-specific filter criteria of liver transcriptome data for identification of differentially regulated hepatic lncRNAs. (d-e) Cumulative frequency distribution of log<sub>2</sub>-transformed fold changes of hepatic mRNA (blue) and lncRNA (orange) expression between the patient groups Obese and Lean (d) or T2DM and Lean (e). Graphs represent mean expression values with all data points plotted. Log<sub>2</sub>-transformed expression fold changes of all hepatic transcripts are shown as dotted black line. Statistical differences between mRNA and lncRNA expression changes were assessed using non-parametric Kolmogorov-Smirnov (KS) tests.  $p$ -values are given in the panels.

Consistent with the results of the murine RNA-Seq data, global differential gene expression analysis revealed inverse transcriptional regulations for lncRNAs and mRNAs in liver biopsies of the respective groups. Comparison of hepatic expression levels between lean, non-diabetic patients and obese, non-diabetic patients revealed a highly significant downregulation of lncRNA transcripts compared to mRNA transcripts upon obesity (Figure 8d). Interestingly, the same, yet even more pronounced correlation was found between lean, non-diabetic patients and obese/overweight patients suffering from T2DM (Figure 8e).

Taken together, these results reveal that human hepatic lncRNA regulation correlates with metabolic health in liver, more precisely a strong repression of hepatic lncRNAs was observed upon obesity and T2DM. Consistent with murine liver transcriptome data analysis, regulation of global lncRNA expression correlates reciprocally with global mRNA expression in human livers, indicating that anticorrelative regulation of hepatic lncRNAs is not only induced in mice in response to chronic or short-term nutrient challenges, but also in humans suffering from obesity or T2DM.

## 4.2. *In vitro* screening for metabolically relevant lncRNAs implicated in liver energy homeostasis

### 4.2.1. Identification of liver-enriched lncRNAs regulated upon chronic obesity, food satiety and food deprivation

To better explore how lncRNAs could partake in regulation of hepatic energy homeostasis, we screened the achieved murine transcriptome data for hepatic lncRNAs that could be further functionally investigated. Potential lncRNA candidates were selected according to three criteria, namely (I) tissue-selective expression in liver, (II) biological regulation across obesity and differentially-fed mouse models and (III) accurate bioinformatic attribution to annotated genes.

Tissue-specific expression of lncRNA transcripts was assessed by analysing RNA-Seq data of seven metabolically active tissues of an independent, NCD-fed cohort of 17-18 weeks-old C57BL6 mice [221]. Filtering normalised RNA-Seq data (in fragments per kilobase of exon per million reads [FPKM]) for liver-enriched lncRNA transcripts resulted in 372 potential candidates, whose RNA-Seq reads were predominantly found ( $FPKM[LIV]/FPKM[ALL] \geq 0.5$ ) in the liver samples (Figure 9a). When considering the biological regulation of the potential candidates in the mouse models of diet-induced and genetic-evoked obesity, we detected 61 lncRNA transcripts, which were consistently regulated in both mouse models (Figure 9b). After manually reviewing aligned RNA-Seq reads of potential candidates for proper alignment to annotated genes and precise exon-intron boundaries, we selected 15 lncRNA transcripts to be further investigated *in vitro*.

Differential expression of the selected candidate lncRNAs upon obesity was validated via qPCR gene expression analysis using total liver RNA of both the diet-induced as well as the genetic-evoked obesity mouse models (Figure 9c). Yet, owing to sporadic high variances among biological replicates, a significant regulation ( $p=0.05$ ) in both mouse model system for obesity could not be validated for all lncRNA transcripts.

Additionally, we performed qPCR gene expression analysis of the selected lncRNA candidates in livers of the differentially-fed mouse cohorts and detected strong transcriptional regulation of some transcripts in response to short-term alterations of nutrient availability.

Interestingly, transcriptional alterations caused by the 16 hrs fasting regime appeared to be reversed in re-fed mice, as most of the significantly regulated transcript levels abated to control levels when fasted mice were allowed to re-feed for 6 hrs (Figure 9d).

In conclusion, upon validation of previously obtained transcriptome data for liver-enriched lncRNA transcripts by qPCR, we found that 15 lncRNAs are regulated upon chronic obesity, some of which are strongly affected by alterations in feeding status and thus constitute interesting candidates for further investigations.

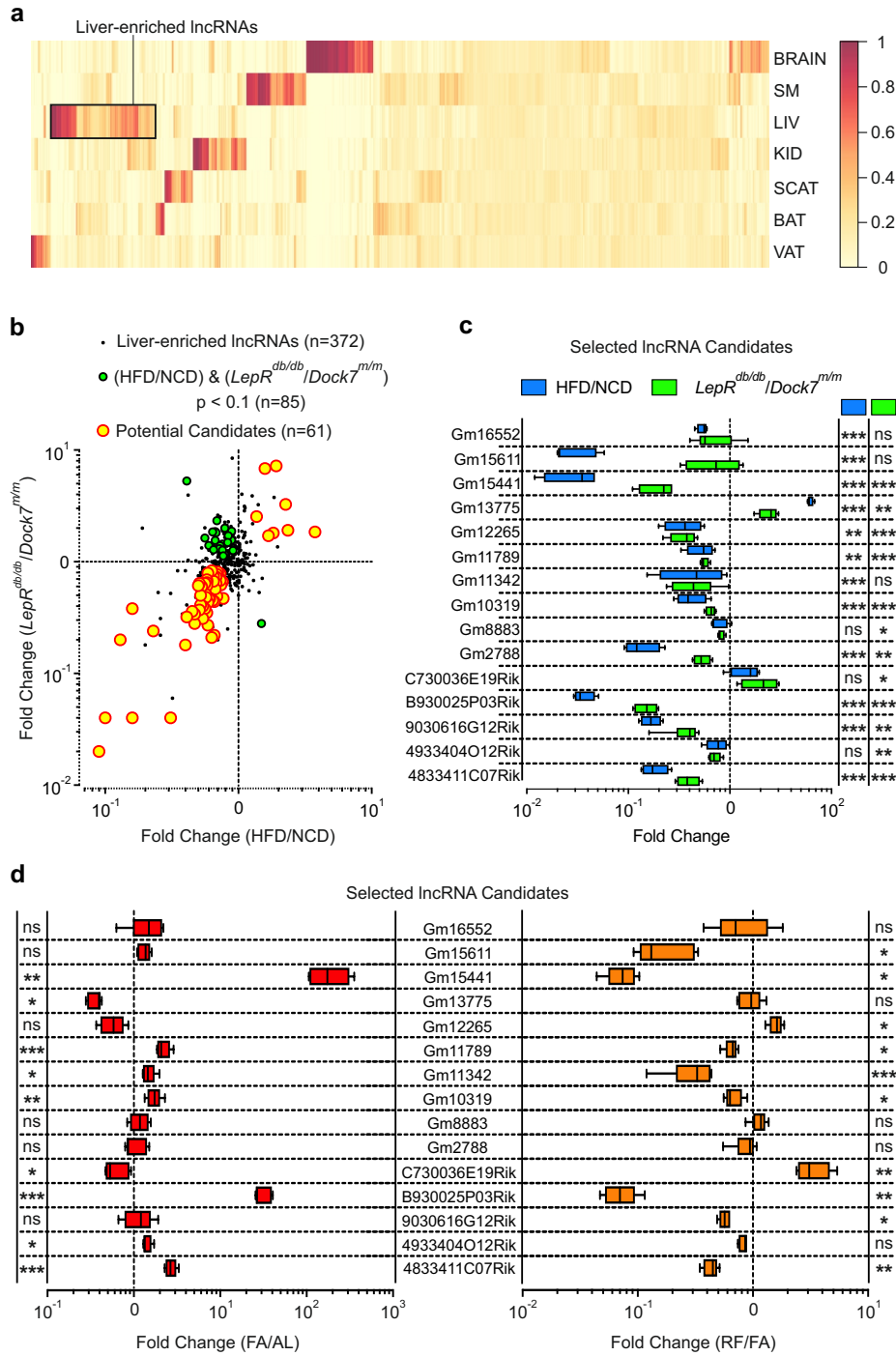


**Figure 9: Identification of liver-enriched lncRNA transcripts regulated by chronic obesity and short-term changes in nutrient availability.**

(a) Heatmap of fractional read counts for the tissues brain (BRAIN), skeletal muscle (SM), liver (LIV), kidney (KID), subcutaneous white adipose tissue (SCAT), brown adipose tissue (BAT) and visceral white adipose tissue (VAT) in RNA-Seq data of mouse models for chronic obesity. (b) Scatter plot depicting mean expression fold changes of liver-enriched lncRNAs between mice fed a high-fat diet (HFD) and mice fed a normal chow diet (NCD) as well as between *LepR<sup>db/db</sup>* and *Dock7<sup>m/m</sup>* mice (n=3 each). Black dots represent liver-enriched lncRNAs. Green dots indicate liver-enriched lncRNAs that are regulated ( $p=0.1$ ) in both mouse models of chronic obesity. Yellow dots show liver-enriched lncRNAs that are consistently regulated ( $p=0.1$ ) in both mouse models of chronic obesity. (c) qPCR gene expression analysis of selected lncRNA candidates between HFD-fed and NCD-fed mice as well as between *LepR<sup>db/db</sup>* and *Dock7<sup>m/m</sup>* mice (n=3

each). (d) qPCR gene expression analysis of selected lncRNA candidates between mice subjected to 16 hrs *ad libitum* feeding (AL), 16 hrs fasting (FA) or 16 hrs fasting followed by 6 hrs of *ad libitum* refeeding (RF) (n=4 each). Graphs (c+d) represent mean  $\pm$  s.e.m. Statistical differences were calculated using unpaired two-tailed t-tests (UP2T-TT). \* $p < 0.05$ ; \*\* $p < 0.01$ ; \*\*\* $p < 0.001$ ; ns, not significant.

#### 4.2.2. Further characterisation of selected lncRNA candidates by expression profiling and coding predictions

Before selecting lncRNA transcripts for further investigations, we aimed to gain more information about the previously selected list of transcripts.

Due to technical variability RNA sequencing results may be affected by inconsistent detection of exons at low levels of coverage [222]. Prompted by the low expression levels of most of our candidates, we intended to validate tissue-specific expression of the selected lncRNAs by performing qPCR gene expression analysis in the harvested tissues of C57BL/6 mice. Surprisingly, whereas liver-enriched expression of most of the transcripts could be confirmed, we also found two potential candidates with pronounced expression in several non-hepatic tissues (Figure 10a).

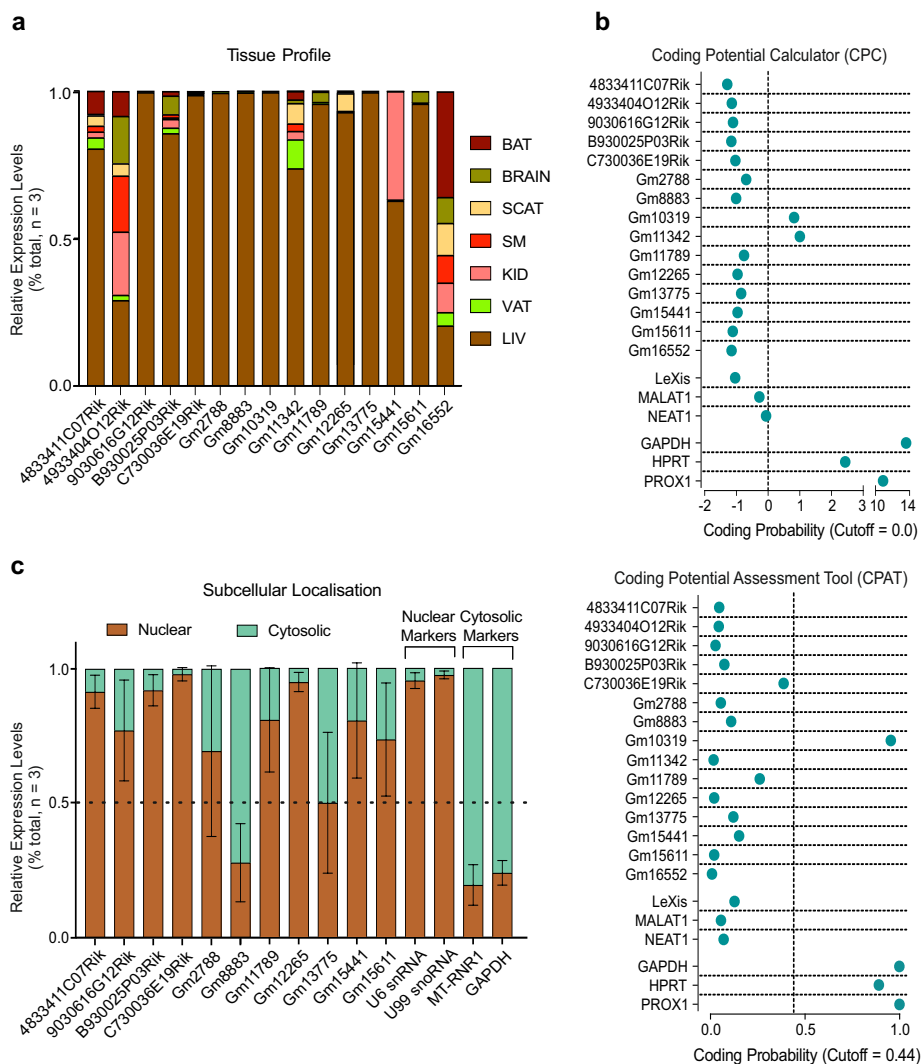


**Figure 10: Additional characteristics of selected lncRNA candidates.**

(a) qPCR gene expression analysis of selected lncRNA candidates in indicated tissues of C57BL/6 wildtype mice (n=3 each). BAT, brown adipose tissue; BRAIN, brain; SCAT, subcutaneous white adipose tissue; SM, skeletal muscle; KID, kidney; VAT, visceral white adipose tissue; LIV, liver. (b) Coding potential predictions of indicated lncRNA and mRNA transcripts using web-based transcript classifier tools. Published lncRNA (LeXis, MALAT1, NEAT1) and mRNA transcripts (GAPDH, HPRT, PROX1) were used as controls. (c) qPCR gene expression analysis of selected lncRNA candidates in nuclear and cytosolic subcellular fractions (n=3 each) derived from livers of 16-20 weeks-old C57BL/6 wildtype mice. Graphs (a+c) represent mean  $\pm$  s.e.m. abundance in the respective subcellular fraction relative to total abundance.

Recent studies suggested that putative lncRNAs can also encode for micropeptides, small peptides consisting of less than 100 amino acids [223, 224]. To exclude potential candidates with coding capabilities, we evaluated the coding potential of the selected lncRNAs by using the web-based transcript classifier tools, 'Coding Potential Calculator' (CPC, [197]) and 'Coding Potential Assessment Tool' (CPAT, [196]). Both algorithms concordantly verified the coding capabilities of

published control transcripts (LeXis, MALAT1, NEAT1, GAPDH, HPRT, PROX1), yet also predicted coding potentials for two selected lncRNAs, whereas the remaining lncRNA candidates were not predicted to encode for (micro-)peptides (Figure 10b).

After discarding four lncRNA candidates due to their abundant expression in multiple non-hepatic tissues or their predicted potential to encode for proteins, we further characterised the remaining 11 lncRNAs by assessing the localisation of their transcripts. As lncRNAs can execute their molecular functions both in the nucleus as well as in the cytoplasm, we examined subcellular fractions of wildtype primary hepatocytes for the expression of the candidate lncRNA transcripts. qPCR gene expression analysis revealed that most of the transcripts were predominantly found in nuclear fractions, while only one gene product strongly accumulated in cytoplasmic fractions. However, we also found several candidates with noticeable expression in both subcellular fractions, indicating that the corresponding transcripts could execute multiple functions in both the nuclear and cytoplasmic compartments (Figure 10c).

#### 4.2.3. Candidate expression levels in primary hepatocytes are mediated by metabolic stimuli

Next we wanted to investigate, whether selected lncRNAs are not only regulated by metabolic states, but could also affect energy homeostasis and hepatic metabolism. Thus, we aimed to generate *in vivo* mouse models with genetic loss of obesity-associated lncRNAs. We therefore manually reviewed our previously obtained RNA-Seq data and choose candidates for further investigations that were significantly regulated upon chronic obesity as well as dynamically expressed in response to short-term nutritional changes. We picked four transcripts fulfilling the aforementioned criteria, namely 4833411C07Rik, B930025P03Rik, Gm13775 and Gm15441, and performed metabolic stimulation of primary hepatocytes to check for differential gene expression of the selected transcripts (Figure 11a).

Indeed, transcript levels of 4833411C07Rik and Gm15441 displayed strong reductions after 6 hrs stimulation with the anabolic hormone insulin and were also regulated by fasting mimicking metabolites such as forskolin and dexamethasone. Yet, whereas alterations in 4833411C07Rik expression levels were consistent with the opposing physiological effects of insulin and forskolin/dexamethasone and consequentially increased after fasting stimulation, we surprisingly observed significant reductions of Gm15441 transcript levels in response to both metabolic stimuli. Transcript levels of B930025P03Rik and Gm13775 showed no significant alterations to 6 hrs insulin stimulation and only B930025P03Rik exhibited elevated expression levels upon 6 hrs fasting stimulation (Figure 11b-e).

Collectively, we demonstrated that expression of some selected lncRNA candidates are mediated by essential anabolic and catabolic stimuli. Yet, as we could only detect partial transcriptional responses of B930025P03Rik and Gm13775 to feeding and fasting mimicking metabolites and due to limitations in time and work load, we decided to exclusively select 4833411C07Rik and Gm15441 as final lncRNA candidates to be studied in *in vivo* mouse models.

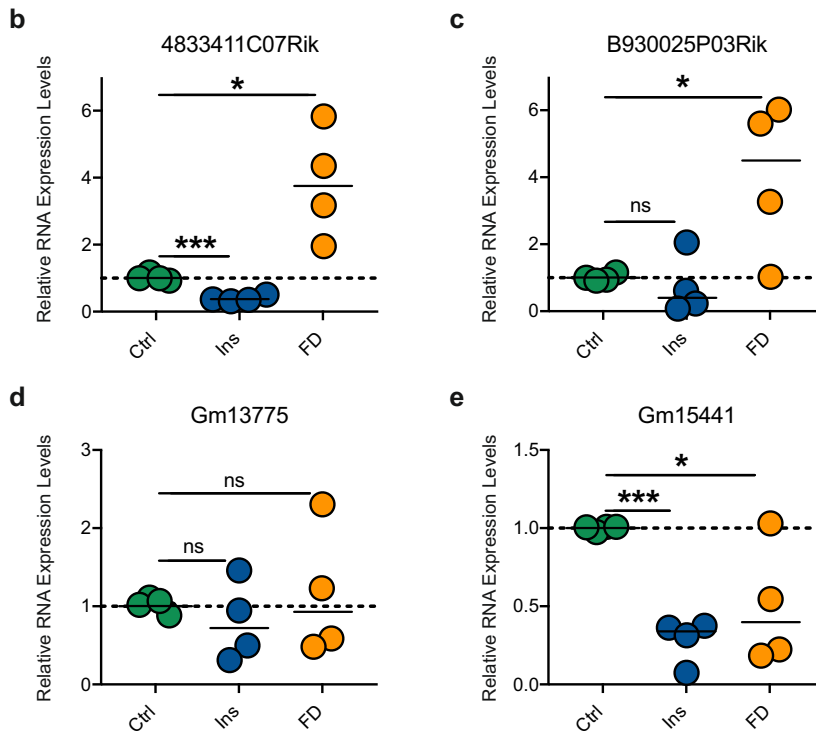
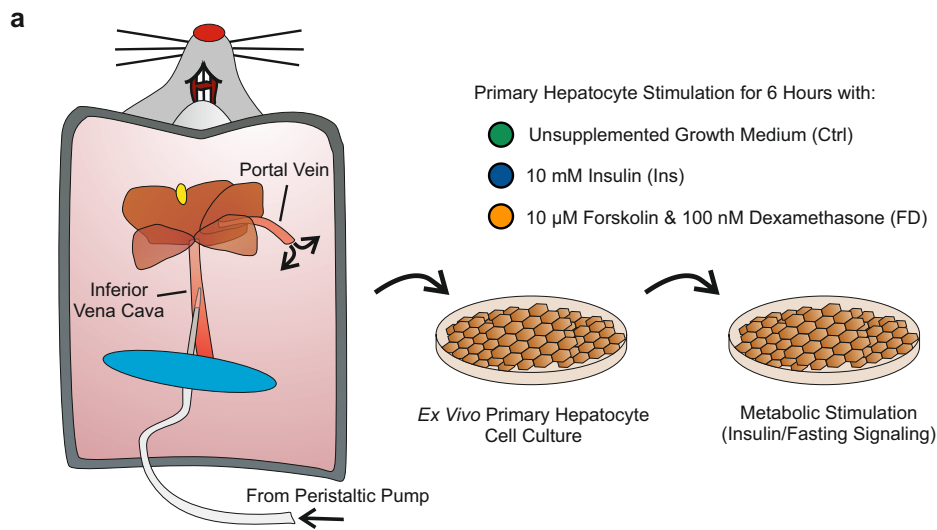


**Figure 11: Metabolic regulation of selected lncRNA candidates in primary hepatocytes.**

(a) Schematic representation of the experimental approach using 14-18 weeks-old C57BL/6 mice for isolation of primary hepatocytes, which were stimulated for 6 hrs with 10 nM insulin (Ins) or 10  $\mu$ M forskolin and 100 nM dexamethasone (FD). Unstimulated cells have been used as controls (Ctrl). (b-e) qPCR gene expression analysis of lncRNA candidates 4833411C07Rik (b), B930025P03Rik (c), Gm13775 (d) and Gm15441 (e) in stimulated primary hepatocytes (n=4). Measurements for each biological replicate were performed in 3 technical replicates. The expression value for the biological replicates was calculated as mean of respective technical replicates. Graphs represent mean expression values with

all data points shown. Statistical differences were calculated using unpaired two-tailed t-tests (UP2T-TT). \* $p < 0.05$ ; \*\*\* $p < 0.001$ ; ns, not significant.

### 4.3. Generation of lncRNA-deficient mouse models using CRISPR/Cas9-mediated genome engineering

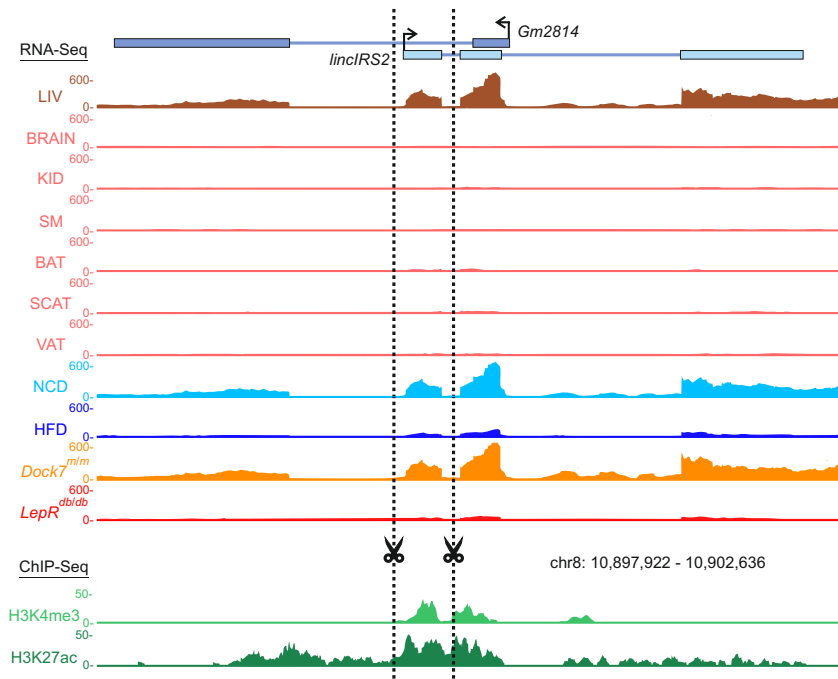
#### 4.3.1. Targeting strategies to abrogate lncRNA candidate expression

In order to study the systemic impact of lncRNAs 4833411C07Rik and Gm15441 on liver energy homeostasis, we sought to generate *in vivo* mouse model systems devoid of 4833411C07Rik or Gm15441 expression, respectively. Due to its positioning ca. 80 kb upstream of the well-described insulin receptor substrate 2 (*Irs-2*, see also Supplemental Figure 2), we termed 4833411C07Rik as *lincIRS2* in the following studies. To gain a comprehensive overview of the genomic loci to be targeted, we complemented the previously achieved RNA-Seq data with publicly available liver chromatin immunoprecipitation sequencing (ChIP-Seq) data for histone 3 lysine 4 trimethylation (H3K4me3) and histone 3 lysine 27 acetylation (H3K27ac) chromatin marks of postnatal (p=0) C57Bl/6 mice.

Tissue-specific RNA-Seq data tracks indicated liver-specific expression of *lincIRS2*, yet also showed expression of another hepatic lncRNA locus, *Gm2814*, which is located in antisense direction on the opposing DNA strand and is overlapping with exon 2 of *lincIRS2*. Interestingly, both genes exhibited identical transcriptional regulations in chronic obesity mouse models, suggesting a potential conjoint expression of both genes by a bidirectional promoter or other regulatory genomic elements. ChIP-Seq data revealed the occurrence of H3K4me3 chromatin marks in close proximity to the transcriptional start site (TSS) of *lincIRS2* and broad H3K27ac chromatin marks along the gene body, both of which are associated with active transcription of nearby genes [225]. To avoid removal of *Gm2814* transcriptional units and to impact on both isoforms expressed by *lincIRS2*, which differ in exon 3 and exon 4 composition, but share exon 1 (Supplemental Figure 3), we decided to exclusively delete *lincIRS2* exon 1. Of note, this targeting approach results in collateral elimination of genomic sites with accumulation of H3K4me3 and H3K27ac chromatin marks, which is an advantaged aspect of our targeting strategy to disrupt *lincIRS2* expression (Figure 12).

The targeting strategy for *Gm15441* is similar to *lincIRS2*, as *Gm15441* also partly overlaps with another transcript located in antisense direction on the opposing DNA strand, the protein-coding gene *Txnip*. Tissue-specific RNA-Seq data tracks suggested liver-enriched expression of *Gm15441*, with minor *Gm15441* expression in kidney, whereas the overlapping *Txnip* was expressed independently of *Gm15441* in multiple tissues. ChIP-Seq data tracks showed accumulations of H3K4me3 and H3K27ac chromatin marks in close proximity to the *Txnip* TSS and along its gene body, but only marginal chromatin marks for active transcription at the *Gm15441* TSS. Intriguingly, TXNIP is a well-studied modulator of energy metabolism, as it has been associated with regulation of cellular redox balance [226], hepatic glucose production [227], and diabetes in humans [228]. Due to the multiple contributions of TXNIP to liver energy metabolism, we aimed to avoid unnecessary disruptions of the *Txnip* locus or its gene function and decided to exclusively remove exon 1 of *Gm15441* (Figure 13).

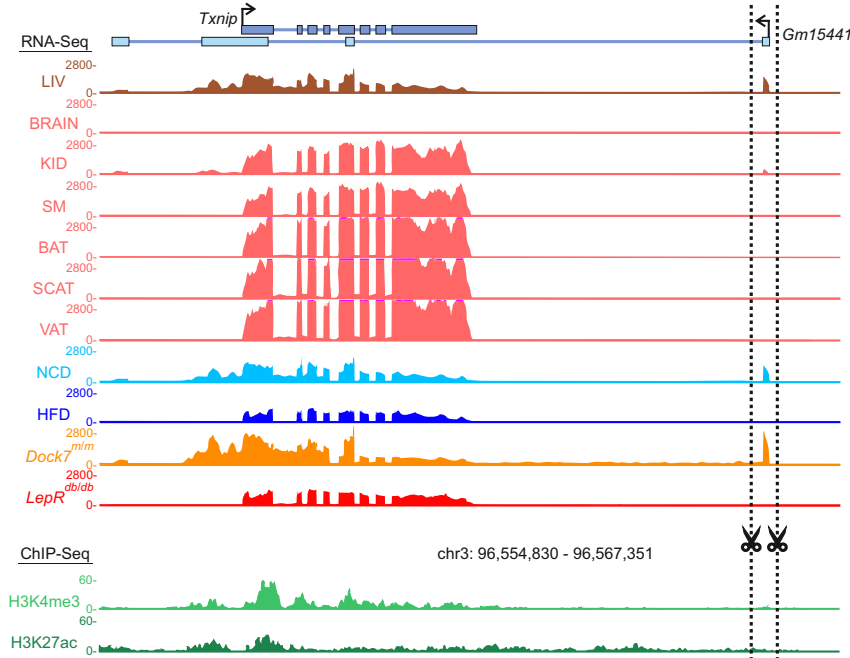




histone 3 lysine 4 trimethylation (H3K4me3, light green) and histone 3 lysine 27 acetylation (H3K27ac, dark green). Dotted lines show genomic sites targeted by CRISPR/Cas9-mediated genome engineering. BRAIN, brain; KID, kidney; SM, skeletal muscle; BAT, brown adipose tissue; SCAT, subcutaneous white adipose tissue; VAT, visceral white adipose tissue; LIV, liver.

**Figure 12: Gene targeting approach to abrogate *lincIRS2* expression.**

Illustration of RNA-Seq and ChIP-Seq data tracks of genomic region 8:10,897,922-10,902,636. Boxes represent annotated exons of *lincIRS2* and *Gm2814*, arrows indicate start site and direction of transcription. Upper histograms depict RNA-Seq read counts of indicated tissues in male 30 weeks-old C57BL/6 mice fed a normal chow diet (NCD) or liver RNA-Seq read counts in male 30 weeks-old C57BL/6 mice fed a normal chow diet (NCD, light blue), male 30 weeks-old C57BL/6 mice fed a high-fat diet (HFD, dark blue), male 10 weeks-old *Dock7<sup>m/m</sup>* mutant mice (orange) or male 10 weeks-old *LepR<sup>db/db</sup>* mutant mice (red). Lower histograms illustrate liver ChIP-Seq read counts in postnatal (day p=0) C57BL/6 mice of mixed sexes for



read counts in postnatal (day p=0) C57BL/6 mice of mixed sexes for histone 3 lysine 4 trimethylation (H3K4me3, light green) and histone 3 lysine 27 acetylation (H3K27ac, dark green). Dotted lines show genomic sites targeted by CRISPR/Cas9-mediated genome engineering. BRAIN, brain; KID, kidney; SM, skeletal muscle; BAT, brown adipose tissue; SCAT, subcutaneous white adipose tissue; VAT, visceral white adipose tissue; LIV, liver.

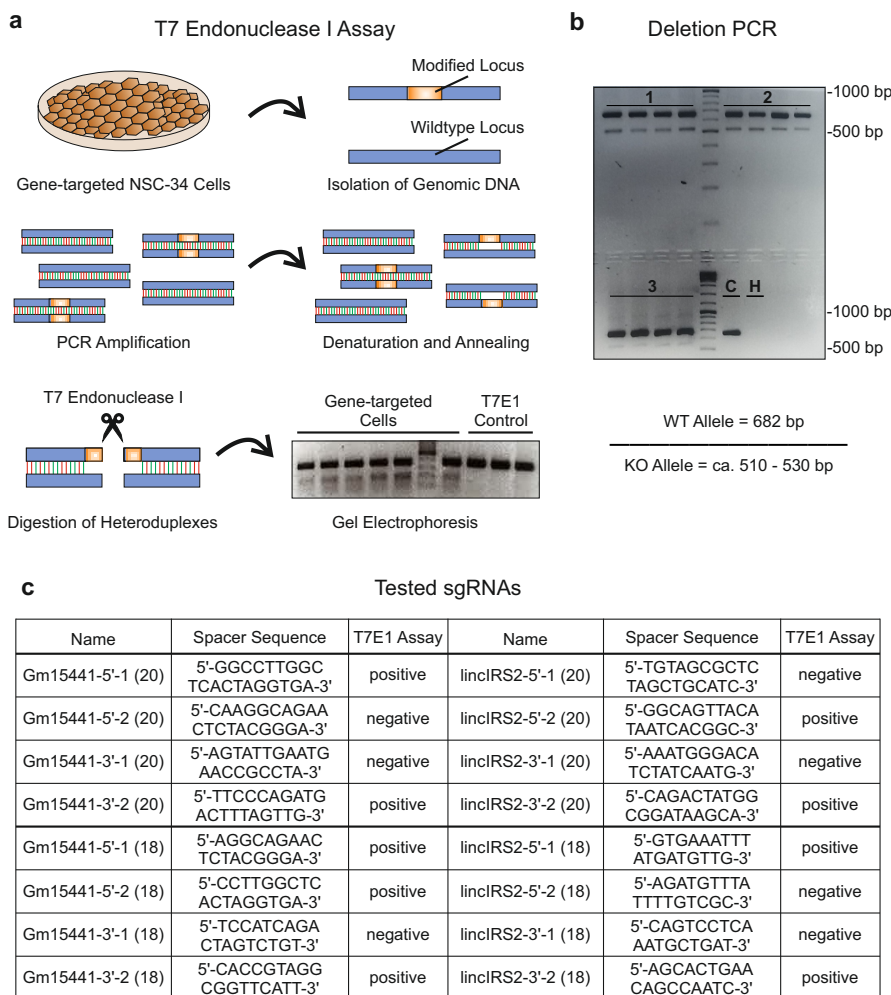
**Figure 13: Gene targeting approach to abrogate *Gm15441* expression.**

Illustration of RNA-Seq and ChIP-Seq data tracks of genomic region 3:96,554,830-96,567,351. Boxes represent annotated exons of *Gm15441* and *Txnip*, arrows indicate start site and direction of transcription. Upper histograms depict RNA-Seq read counts of indicated tissues in male 30 weeks-old C57BL/6 mice fed a normal chow diet (NCD) or liver RNA-Seq read counts in male 30 weeks-old C57BL/6 mice fed a normal chow diet (NCD, light blue), male 30 weeks-old C57BL/6 mice fed a high-fat diet (HFD, dark blue), male 10 weeks-old *Dock7<sup>m/m</sup>* mutant mice (orange) or male 10 weeks-old *LepR<sup>db/db</sup>* mutant mice (red). Lower histograms illustrate liver ChIP-Seq



#### 4.3.2. *In vitro* validation of sgRNA activity using T7 endonuclease I assays

Using the web-based applications CRISPR Design [199] and CRISPOR [198], we screened for suitable crRNA spacer sequences that could be used in the previously designed targeting approaches. Indeed, we identified crRNA spacer sequences flanking the first exons of *lincIRS2* and *Gm15441*, respectively, and selected two 20-nucleotide spacer sequences for each 5'- and 3'-end of the targeted regions. Upon simultaneous cleavage at both ends flanking the targeted exons, open genomic ends can be fused by endogenous end ligation repair mechanisms [229], ultimately resulting in the deletion of the flanked genomic region. As recent reports demonstrated that truncated gRNAs with 18 nucleotide spacer sequences exhibit increased target specificity [230], we additionally selected two 18-nucleotide spacer sequences for each genomic region to be targeted.



**Figure 14: Validation of sgRNA activity using T7 endonuclease I assays.**

(a) Schematic representation depicting the workflow of T7 endonuclease I (T7E1) assays. To detect genome-editing events induced by functional sgRNAs, genomic DNA is isolated from gene-targeted cells and the locus of interest is amplified via PCR. After denaturation and random re-annealing of DNA strands, the PCR products are incubated with T7E1, which results in cleavage of DNA heteroduplexes consisting of unmodified and gene-targeted DNA strands. Cleaved heteroduplexes can be detected by gel electrophoresis and demonstrate successful genome-editing by functional sgRNAs. To control for T7E1-specific appearance of additional bands, PCR products that have not been subjected to T7E1 digestion are also run on the same gel electrophoresis (T7E1 control). (b) Representative agarose gel displaying PCR reactions with primers flanking exon 1 of lincRNA Gm15441 using genomic DNA isolated from NSC-34 cells transfected with different combinations of sgRNAs, including [1] *Gm15441-5'-1 (20)* + *Gm15441-3'-2 (20)*, [2] *Gm15441-5'-1 (18)* + *Gm15441-3'-2 (18)* and [3] *Gm15441-5'-2 (18)* + *Gm15441-3'-2 (18)*. C, negative control PCR using genomic DNA from untransfected NSC-34 cells. H, H<sub>2</sub>O control PCR using no template DNA. (c) Table of sgRNAs that have been evaluated for genome-editing activity, including the crRNA spacer sequence and the outcome of the T7E1 assay. The length of the spacer sequences is indicated in brackets behind the name of the respective sgRNA.

reactions with primers flanking exon 1 of lincRNA Gm15441 using genomic DNA isolated from NSC-34 cells transfected with different combinations of sgRNAs, including [1] *Gm15441-5'-1 (20)* + *Gm15441-3'-2 (20)*, [2] *Gm15441-5'-1 (18)* + *Gm15441-3'-2 (18)* and [3] *Gm15441-5'-2 (18)* + *Gm15441-3'-2 (18)*. C, negative control PCR using genomic DNA from untransfected NSC-34 cells. H, H<sub>2</sub>O control PCR using no template DNA. (c) Table of sgRNAs that have been evaluated for genome-editing activity, including the crRNA spacer sequence and the outcome of the T7E1 assay. The length of the spacer sequences is indicated in brackets behind the name of the respective sgRNA.

Before using the selected crRNA sequences to generate *in vivo* mouse models, we wanted to validate spacer sequence activity *in vitro*. Synthesised single guide RNA (sgRNA) molecules containing the spacer sequence to be evaluated were examined for gene targeting efficiency by transfecting NSC-34 cells with pairs of sgRNAs and evaluating the occurrence of gene-editing events via sequence-specific T7 Endonuclease I (T7E1) assays. To improve the detection of gene-editing events, PCR primers for the amplification of the locus of interest were designed in such a way that T7E1-mediated cleavage of heteroduplexes results in two DNA fragments of equal lengths, which gives a strong single band during gel electrophoretic separation (Figure 14a). If both sites flanking the genomic region to be deleted were targeted by functional sgRNAs, the deletion event itself could also be visualized by standard PCR reactions using target region flanking genotyping primers (Figure 14b). Out of the 16 crRNA sequences evaluated, we detected four 20-nucleotide spacer sequences and five 18-nucleotide spacer sequences with detectable genome-editing events in T7E1 assays (Figure 14c).

Taken together, we successfully validated genome-editing capacity of nine selected crRNA spacer sequences using T7E1 assays and genotyping PCRs. However, in order to reduce undesirable off-target events, we selected the 20-nucleotide spacer sequences for the generation of lncRNA-deficient *in vivo* mouse models.

#### 4.3.3. In vivo targeting approach - strategy for pronuclear microinjection

To generate *in vivo* lncRNA mouse models, we decided to employ pronuclear injection (PNI) of CRISPR/Cas9 components into C57BL/6NRj zygotes, which were subsequently implanted into pseudopregnant RjHan:NMRI females. For maximum quality of the CRISPR components, synthetic crRNA and tracrRNA molecules were purchased from commercial distributors using the 20-nucleotide crRNA spacer sequences that have been validated *in vitro*. To enhance CRISPR/Cas9 genome-editing events, we additionally added Cas9 mRNA to the injection mix containing the guide RNA components (tracrRNA + 2x crRNAs) and Cas9 protein (Figure 15).

When using CRISPR PNI technology to generate genome-engineered mouse models, the developmental time point of the genome-editing event as well as the exact result of the CRISPR-induced genomic alteration occur in a random fashion [176]. Thus, the genomic alteration of the targeted locus can not only differ among individual animals of the F0 generation, but also in different somatic or gametic cells of the same animal (genetic mosaicism). In order to ensure stable germline transmission of the edited allele and ultimately the establishment of a new genome-edited mouse line, all animals obtained by CRISPR PNI as well as their F1 and F2 offspring have been monitored for the composition of the targeted locus by DNA sequencing.

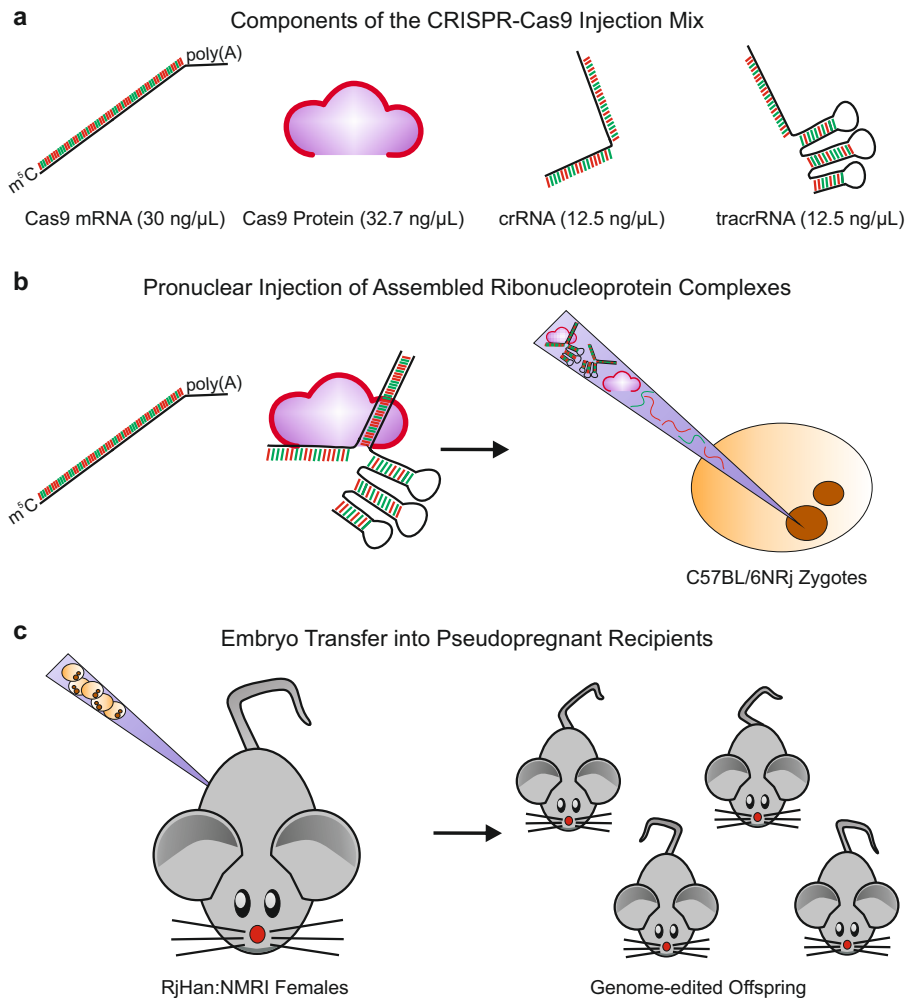


**Figure 15: Experimental setup of the *in vivo* gene targeting strategy.**

Schematic representation of the experimental approach to generate *in vivo* mouse models, depicting the (a) composition of the CRISPR-Cas9 injection mix, containing Cas9 mRNA, Cas9 protein as well as the gRNA components tracrRNA and crRNA, (b) pronuclear microinjection of assembled ribonucleoprotein complexes into C57BL/6NRj zygotes and (c) embryo transfer of 2-cell stage embryos into pseudopregnant RjHan:NMRI females. Concentrations of the injection components are indicated in the panel.

#### 4.3.4. Generation of a mouse line deficient for *linclRS2*-exon 1 (*linclRS2*<sup>ΔΔ</sup>)

Selected 20-nucleotide spacer sequences for *linclRS2* gene targeting flanked a genomic region of 415 bp, including entire *linclRS2* exon 1 and parts of *linclRS2* exon 2, but no transcriptional units of overlapping lncRNA gene *Gm2814* (Figure 16a+b). PNI of CRISPR/Cas9 components into zygotes yielded 115 viable 2-cell stage embryos, which subsequently were transferred into four pseudopregnant foster females. Unfortunately, only two females became pregnant and only gave birth to 7 pups in total (Supplemental Figure 3).

Although genotyping of CRISPR founder animals is not meaningful to determine the genomic configuration of progeny due to possible genetic mosaicism, we extracted genomic DNA from founder tail biopsies to check for CRISPR/Cas9-mediated alterations of the *linclRS2* locus in founder animals. Interestingly, two independent PCR reactions detected a truncated allele of the targeted locus matching the predicted size for a successful deletion event in one potential founder mouse (Figure 16c). Genotyping PCRs of F1 offspring showed deleted *linclRS2* alleles in progeny of the founder animal that previously showed an altered *linclRS2* allele in tail biopsy DNA, but no truncated *linclRS2* alleles in progeny of other potential founder animals. DNA sequencing of the positive founder line revealed identical genomic compositions among 21 sequenced animals of the F1 and F2 generation. In detail, CRISPR/Cas9-induced cleavage resulted in a 418 bp genomic

deletion, including the targeted 415 bp genomic region and three additional basepairs at the 5' Cas9 cutting site. Surprisingly, DNA sequencing also detected four additional basepairs that were removed close to the proximal Cas9 cutting site, which indicates multiple repair procedures of Cas9-induced DSB and ultimately results in a total loss of 422 bp in the *linclRS2*<sup>Δ</sup> allele (Figure 16d+e).

In conclusion, we successfully generated a truncated *linclRS2* allele, defined by a 422 bp genomic deletion comprising the gene-targeted exon 1 of *linclRS2*, but no transcriptional units of overlapping lncRNA gene *Gm2814*. Of note, CRISPR/Cas9-induced DSB repair resulted in a random 4 bp deletion outside the targeted genomic region, which not impinges on our gene targeting strategy, but has to be considered for further genome-editing approaches.

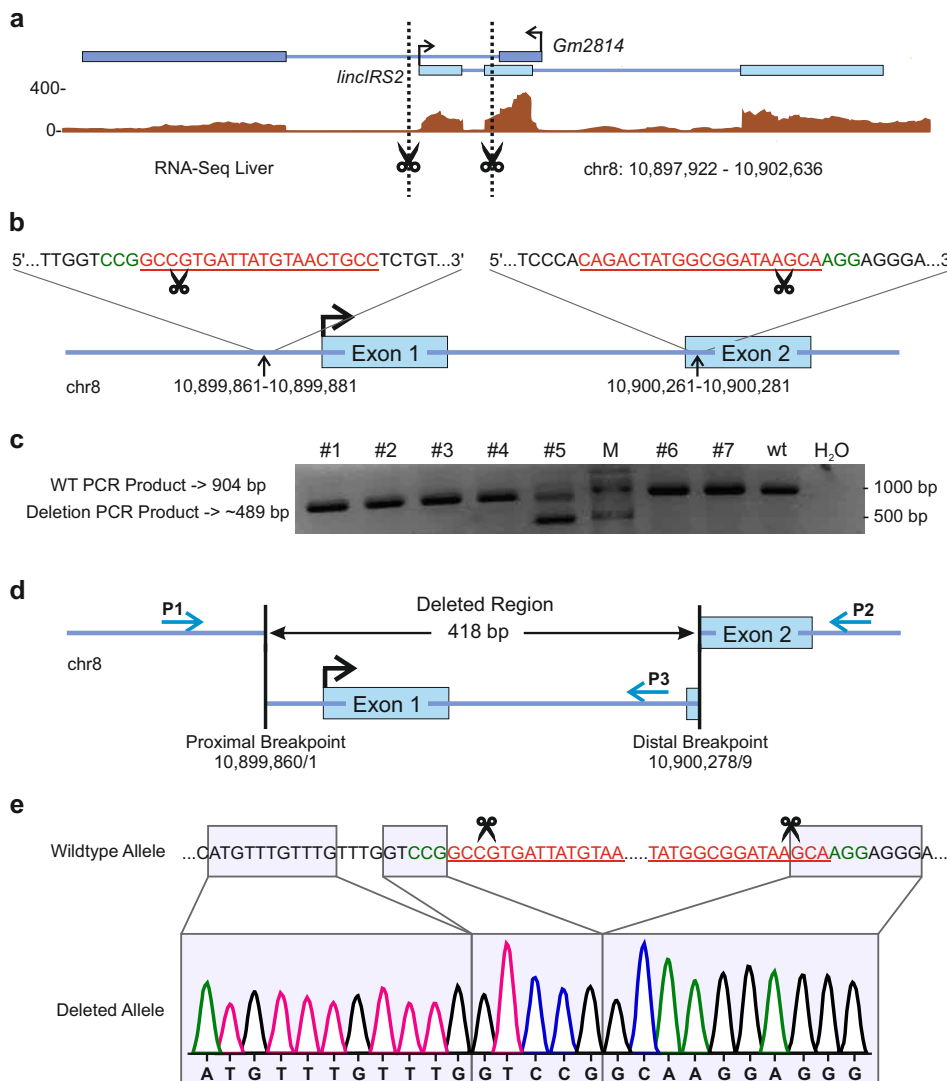


**Figure 16: Generation of a gene-edited *linclRS2*<sup>Δ</sup> allele.**

(a) Schematic illustration of the targeting strategy to delete exon 1 of *linclRS2*. Brown histograms represent RNA-Seq read counts in liver of 30 weeks-old C57BL/6 mice. Blue boxes indicate annotated exons of lncRNAs *linclRS2* (light blue) and overlapping *Gm2814* (dark blue). Dotted lines show genomic sites to be cleaved by CRISPR/Cas9-mediated genome engineering. (b) Schematic representation of the targeted *linclRS2* locus. Spacer sequences of Cas9-recruiting crRNAs are shown in red. Protospacer adjacent motifs necessary for Cas9 activity are shown in green. Black arrows indicate the genomic coordinates bound by crRNA spacer sequences. Scissors depict Cas9 cutting sites (c) Agarose gel electrophoresis of

amplified PCR products using genomic DNA isolated from 7 individual founder mice, which have been obtained by pronuclear injection of CRISPR/Cas9 components. M, marker; wt, C57BL/6 wildtype control mouse; H<sub>2</sub>O, no template control PCR. (d) Scheme of the genomic locus of founder #5, depicting the *linclRS2*<sup>Δ</sup> allele with proximal and distal breakpoints. Blue arrows indicate PCR primers P1, P2 and P3 used for genotyping and sequencing. (e) Chromatogram showing the genomic DNA sequence of the *linclRS2*<sup>Δ</sup> allele in comparison to the wildtype allele.

### 4.3.5. Generation of a mouse line deficient for *Gm15441*-exon 1 (*Gm15441*<sup>ΔΔ</sup>)

For gene targeting of *Gm15441*, we selected 20-nucleotide spacer sequences flanking a genomic region of 407 bp, which contains the entire exon 1 of *Gm15441*, yet still remains approximately 4.9 kb away from transcriptional units of overlapping protein-coding gene *Txnip* (Figure 17a+b). PNI of CRISPR/Cas9 components into zygotes resulted in 106 viable 2-cell stage embryos, which were transferred into five pseudopregnant foster females, out of which four females gave birth to 18 pups overall (Supplemental Figure 4).

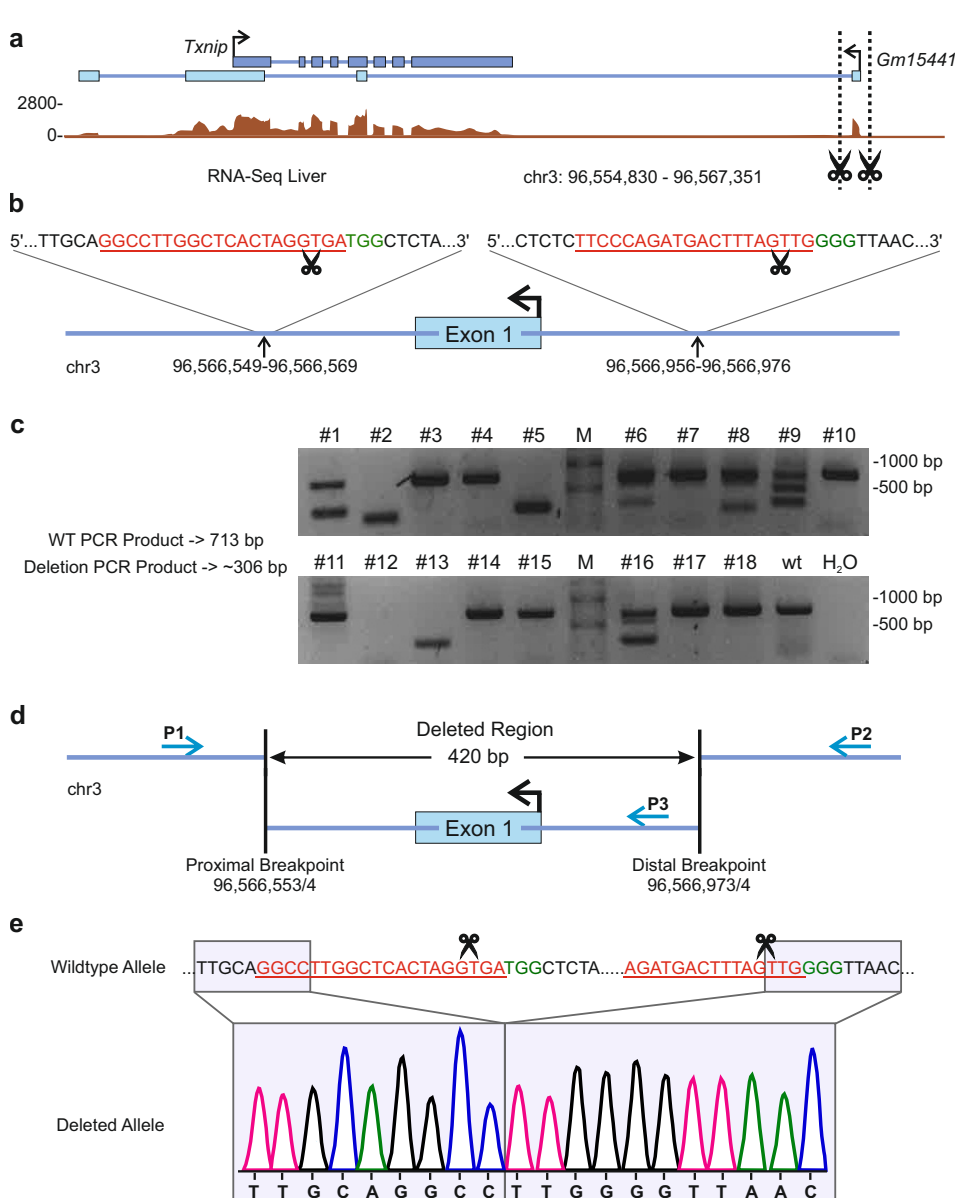


**Figure 17: Generation of a gene-edited *Gm15441*<sup>Δ</sup> allele.**

(a) Schematic illustration of the targeting strategy to delete exon 1 of *Gm15441*. Brown histograms represent RNA-Seq read counts in liver of 30 weeks-old C57BL/6 mice. Blue boxes indicate annotated exons of lncRNA *Gm15441* (light blue) and overlapping protein-coding *Txnip* (dark blue). Dotted lines show genomic sites to be cleaved by CRISPR/Cas9-mediated genome engineering. (b) Schematic representation of the targeted *Gm15441* locus. Spacer sequences of Cas9-recruiting crRNAs are shown in red. Protospacer adjacent motifs necessary for Cas9 activity are shown in green. Black arrows indicate the genomic coordinates bound by crRNA spacer sequences. Scissors depict Cas9 cutting sites. (c) Agarose gel electrophoresis of amplified PCR products using genomic DNA isolated from 18 individual founder mice, which have been obtained by

pronuclear injection of CRISPR/Cas9 components. M, marker; wt, C57BL/6 wildtype control mouse; H<sub>2</sub>O, no template control PCR. (d) Scheme of the genomic locus of founder #1, depicting the *Gm15441*<sup>Δ</sup> allele with proximal and distal breakpoints. Blue arrows indicate PCR primers P1, P2 and P3 used for genotyping and sequencing. (e) Chromatogram showing the genomic DNA sequence of the *Gm15441*<sup>Δ</sup> allele in comparison to the wildtype allele.

Genotyping of founder animal tail biopsies demonstrated multiple successful alterations of the *Gm15441* locus, including truncated alleles in range of predicted deletion events, but also unpredicted edited alleles with slightly increased or decreased genomic sizes. Interestingly, we also found four founder animals lacking the wildtype *Gm15441* allele, suggesting homozygous CRISPR/Cas9-mediated alterations of the *Gm15441* locus or genomic deletions of primer binding sequences (Figure 17c). Genotyping of F1 and F2 offspring validated successful germline transmission of truncated *Gm15441* alleles by four potential founder animals (#1, #6, #11 and #13). Strikingly, one founder animal that did not harbor truncated alleles of *Gm15441* in genomic tail biopsy DNA (#11) was found to give rise to a stable *Gm15441*<sup>Δ</sup> mouse line, which reflects genetic mosaicism among gametic and somatic cells in the respective F0 individual. DNA sequencing of positive founder lines showed identical genomic compositions among sequenced animals, but also identified minor variations of the genomic deletions (range 411 bp - 433 bp), potentially due to error-prone NHEJ repair of Cas9-induced DSBs (Supplemental Figure 4). For further studies we selected the truncated *Gm15441* allele of the first founder (#1), which is characterised by deletion of the targeted 407 bp genomic region and an additional loss of 13 nucleotides at the 5' Cas9 cutting site, ultimately resulting in a genomic deletion of 420 bp (Figure 17d+e). In conclusion, we demonstrated that the performed gene targeting strategy can result in the generation of multiple, stable *Gm15441*-deficient mouse lines with slightly varying genomic compositions, including genetic mosaicism among potential founder animals.

#### 4.4. *Gm15441*-Exon 1 deficiency does not affect fertility or *Txnip* expression, but results in ablation of *Gm15441* expression

To assess potential physiological effects of the *Gm15441*<sup>Δ</sup> allele, we monitored all mice of the selected *Gm15441*<sup>Δ</sup> mouse line for fecundity, genetic inheritance of the *Gm15441*<sup>Δ</sup> allele as well as for behavioural or morphological changes.

Breeding performance of mice harboring the selected *Gm15441*<sup>Δ</sup> allele showed unaltered fertility rates and genetic inheritance of the *Gm15441*<sup>Δ</sup> allele with no significant deviations from Mendelian inheritance (Figure 18a). Additionally, neither heterozygous nor homozygous mice carrying the selected *Gm15441*<sup>Δ</sup> allele exhibited noticeable behavioural alterations or developed visible morphological defects.

Gene expression analysis in livers of mice harboring wildtype, heterozygous or homozygous compositions of the *Gm15441*<sup>Δ</sup> allele identified highly significant reductions of *Gm15441* transcript levels (range 94 % - 97 % reduction) in homozygous *Gm15441*<sup>Δ/Δ</sup> mice, but no changes in *Gm15441* expression in heterozygous *Gm15441*<sup>wt/Δ</sup> mice. Unaltered *Gm15441* expression levels in heterozygous *Gm15441*<sup>wt/Δ</sup> mice indicate that the wildtype allele of *Gm15441* is sufficient to compensate the lack of *Gm15441* expression by the *Gm15441*<sup>Δ</sup> allele. Importantly, expression levels of overlapping protein-coding gene *Txnip* remained unaltered upon heterozygous or homozygous deletion of *Gm15441*-Exon 1 (Figure 18b).

Taken together, we report the generation of a stable and fertile *Gm15441*-deficient mouse lines, which is characterised by almost complete absence of *Gm15441* transcript expression, without

disruptions of the genomic locus of overlapping protein-coding gene *Txnip* or alterations of TXNIP expression levels. Yet, due to limitations in time and animal husbandry, we were not able to further characterise phenotypical parameters of *Gm15441*<sup>Δ/Δ</sup> mice.

**a** Inheritance of Allele *Gm15441*<sup>Δ</sup>

Parental Genotypes	Number of Breedings	Total Offspring	Pups per Breeding	Males	Females	Δ/Δ (in %)	wt/Δ (in %)	wt/wt (in %)	χ <sup>2</sup> -Test (P = 0.05)
F0 X wt/wt	3	29	9.66	13	---	0	23.07	76.93	n.s.
				---	16	0	31.25	68.75	n.s.
wt/Δ X wt/Δ	3	24	8	15	---	20	60	20	n.s.
				---	9	11.11	55.55	33.33	n.s.
wt/Δ X Δ/Δ	1	4	4	0	---	0	0	0	n.s.
				---	4	50	50	0	n.s.

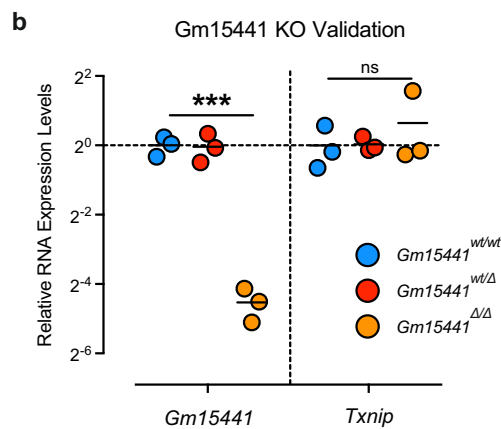


**Figure 18: Physiological impact of allele *Gm15441*<sup>Δ</sup>.**

(a) Table depicting genetic inheritance of the truncated allele *Gm15441*<sup>Δ</sup> in breedings of founder animals (F0) and their progeny. Statistical differences were calculated using chi-squared (χ<sup>2</sup>)-tests with significance level P=0.05. (b) qPCR gene expression analysis of lncRNA *Gm15441* and overlapping protein-coding gene TXNIP in mice harboring wildtype (*Gm15441*<sup>wt/wt</sup>), heterozygous (*Gm15441*<sup>wt/Δ</sup>) or homozygous (*Gm15441*<sup>Δ/Δ</sup>) compositions of the *Gm15441*<sup>Δ</sup> allele (n=3). Graphs represent mean expression values with all data points shown. Statistical differences were calculated using unpaired two-tailed t-tests (UP2T-TT). \*\*\*p<0.001; ns, not significant.



## 4.5. *linclRS2* deficiency impacts on liver energy homeostasis by regulating expression levels of gluconeogenic and lipogenic genes

### 4.5.1. *linclRS2* deficiency does not affect fertility or body weight, but results in hyperglycemia in *linclRS2<sup>Δ/Δ</sup>* mice

In order to evaluate putative physiological effects of the gene-edited *linclRS2<sup>Δ</sup>* allele, we controlled all mice harboring the *linclRS2<sup>Δ</sup>* allele for fecundity, genetic inheritance of the deleted allele as well as for changes in behaviour or morphology. Animals carrying heterozygous and homozygous genomic compositions of the *linclRS2<sup>Δ</sup>* allele demonstrated no noticeable alterations in behaviour or morphology and demonstrated conventional breeding performance and genetic inheritance of the *linclRS2<sup>Δ</sup>* allele with no significant deviations from Mendelian inheritance (Figure 19).

Inheritance of Allele *linclRS2<sup>Δ</sup>*

Parental Genotypes	Number of Breedings	Total Offspring	Pups per Breeding	Males	Females	$\Delta/\Delta$ (in %)	wt/ $\Delta$ (in %)	wt/wt (in %)	$\chi^2$ -Test (P = 0.05)
F0 X wt/wt	4	29	7.25	18	---	0	50	50	n.s.
				---	11	0	63.64	36.36	n.s.
wt/ $\Delta$ X wt/ $\Delta$	11	84	7.63	47	---	19.14	44.68	36.17	n.s.
				---	37	27.02	37.84	35.13	n.s.
wt/ $\Delta$ X $\Delta/\Delta$	1	4	4	4	---	25	75	0	n.s.
				---	0	0	0	0	n.s.
$\Delta/\Delta$ X $\Delta/\Delta$	2	14	7	5	---	100	0	0	---
				---	9	100	0	0	---

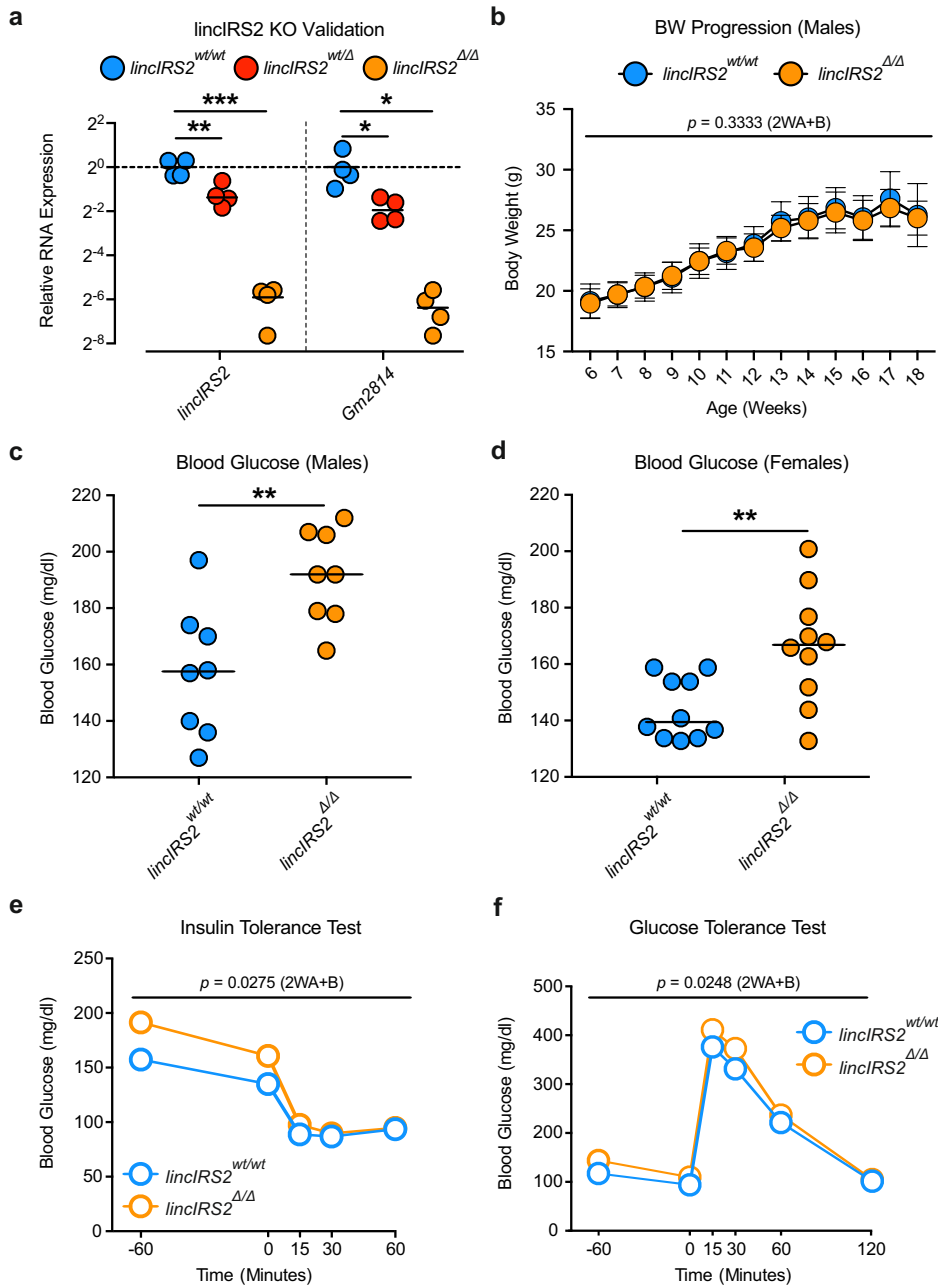
**Figure 19:** Physiological impact of allele *linclRS2<sup>Δ</sup>* (I).

Table depicting genetic inheritance of the truncated allele *linclRS2<sup>Δ</sup>* in breedings of founder animals (F0) and their progeny. Statistical differences were calculated using chi-squared ( $\chi^2$ )-tests with significance level P=0.05.

Gene expression analysis in liver showed significant reductions in *linclRS2* levels in both heterozygous and homozygous *linclRS2<sup>Δ</sup>* mice. Interestingly, *linclRS2* expression in heterozygous *linclRS2<sup>wt/Δ</sup>* mice was reduced to approximately half the wildtype *linclRS2* expression levels (range 26 % - 69 % reduction), whereas *linclRS2* expression was almost completely absent (range 98 % - 99 % reduction) in homozygous *linclRS2<sup>Δ/Δ</sup>* mice. This finding suggests that two wildtype alleles of *linclRS2* are necessary for conventional *linclRS2* expression and that one wildtype allele alone can not compensate for the lack of *linclRS2* expression by a *linclRS2<sup>Δ</sup>* allele. Importantly, we found similar reductions in expression levels of overlapping lncRNA Gm2814, pointing to interconnected transcriptional regulation of lncRNA genes *linclRS2* and *Gm2814*. Identical to *linclRS2*, we detected that Gm2814 expression was reduced to approximately half of wildtype Gm2814 expression levels (range 45 % - 74 % reduction) in heterozygous *linclRS2<sup>wt/Δ</sup>* mice and almost completely absent (range 98 % - 99 % reduction) in homozygous *linclRS2<sup>Δ/Δ</sup>* mice (Figure 20a).



To further characterise the systemic metabolic impact of *lincIRS2*, we examined metabolic parameters in cohorts of male wildtype and male *lincIRS2*<sup>Δ/Δ</sup> mice (n=8 each). Whereas body weight progression showed no differences in weight gain between wildtype and *lincIRS2*<sup>Δ/Δ</sup> mice (Figure 20b), we detected significantly elevated blood glucose levels in *lincIRS2*<sup>Δ/Δ</sup> mice (Figure 20c). To corroborate this finding, we also measured blood glucose levels in female siblings and again found significantly increased levels of blood glucose in *lincIRS2*<sup>Δ/Δ</sup> mice (Figure 20d).



**Figure 20: Physiological impact of allele *lincIRS2*<sup>Δ</sup> (II).**

(a) qPCR gene expression analysis of lncRNAs *lincIRS2* and *Gm2814* in male mice harboring wildtype (*lincIRS2*<sup>wt/wt</sup>, blue), heterozygous (*lincIRS2*<sup>wt/Δ</sup>, red) or homozygous (*lincIRS2*<sup>Δ/Δ</sup>, orange) compositions of the *lincIRS2*<sup>Δ</sup> allele (n=4). Graphs represent mean expression values with all data points shown. (b) Body weight progression in male mice with wildtype (*lincIRS2*<sup>wt/wt</sup>, blue) or homozygously deleted (*lincIRS2*<sup>Δ/Δ</sup>, orange) *lincIRS2* genotypes (n=8). Graphs represent mean body weight ± s.e.m. (c+d) Blood glucose levels in 11 weeks-old male (c) and female (d) siblings of the *lincIRS2*<sup>Δ</sup> mouse line homozygously carrying wildtype (*lincIRS2*<sup>wt/wt</sup>, blue) or deleted (*lincIRS2*<sup>Δ/Δ</sup>, orange) alleles of *lincIRS2* (n=8 each). Graphs represent mean blood glucose levels with all data points shown. (e+f) Blood glucose levels of male mice with wildtype (*lincIRS2*<sup>wt/wt</sup>, blue) or homozygously deleted (*lincIRS2*<sup>Δ/Δ</sup>, orange) genomic compositions of

the *lincIRS2*<sup>Δ</sup> allele (n=8) upon insulin (e) and glucose tolerance tests (f). The insulin tolerance test was performed with 11 weeks-old animals, the glucose tolerance test with 12 weeks-old animals. Insulin and glucose were administered at timepoint 0. Graphs represent mean blood glucose levels. Statistical differences were calculated using (a+c+d) unpaired two-tailed t-tests (UP2T-TT) or (b+e+f) two-way ANOVA with Bonferroni post-hoc test (2WA+B). *p*-values are given in the panels. \**p*<0.05; \*\**p*<0.01; \*\*\**p*<0.001.

With 11 and 12 weeks of age, respectively, we performed insulin and glucose tolerance tests with the cohorts of male mice to check for differential metabolic responses to intraperitoneal insulin or glucose administration. Indeed, *lincIRS2<sup>ΔΔ</sup>* mice exhibited significantly different blood glucose levels compared to wildtype mice in both the insulin tolerance test (Figure 20e) as well as in the glucose tolerance test (Figure 20f). Strikingly, 60 mins after insulin administration and 120 mins after glucose administration, we observed similar blood glucose levels between wildtype and *lincIRS2<sup>ΔΔ</sup>* mice, which suggests that hyperglycemia of *lincIRS2<sup>ΔΔ</sup>* mice can temporarily abate to wildtype levels.

Taken together, metabolic characterisation of *lincIRS2<sup>ΔΔ</sup>* mice demonstrated significant hyperglycemia in both male and female *lincIRS2*-deficient mice and showed strong tendencies towards impaired insulin and glucose resistance upon *lincIRS2* deficiency, all of which indicate that *lincIRS2* is essential for physiological hepatic glucose homeostasis *in vivo*.

#### 4.5.2. Indirect calorimetry analysis indicates unaltered energy expenditure and substrate mobilisation in *lincIRS2<sup>ΔΔ</sup>* mice

Since *lincIRS2<sup>ΔΔ</sup>* mice exhibit hyperglycemia, we next wanted to further survey potential metabolic consequences of *lincIRS2* deficiency by comparing (indirect) calorimetric metabolic parameters between wildtype and homozygous *lincIRS2<sup>ΔΔ</sup>* mice (n=8 each). Three-day indirect calorimetric measurements of 16 weeks-old wildtype and *lincIRS2<sup>ΔΔ</sup>* mice demonstrated no significant alterations in energy expenditure or respiratory exchange ratio as proxy for lipid versus carbohydrate substrate mobilisation, although we observed a tendency towards higher energy expenditure in *lincIRS2<sup>ΔΔ</sup>* mice (Figure 21a+b). As energy expenditure is calculated by oxygen (O<sub>2</sub>) consumption and carbon dioxide (CO<sub>2</sub>) production, we consequently found tendencies towards increased O<sub>2</sub> consumption and CO<sub>2</sub> production in *lincIRS2<sup>ΔΔ</sup>* mice (Figure 21c+d). Of note, the tendencies of increased energy expenditure, O<sub>2</sub> consumption and CO<sub>2</sub> production in *lincIRS2<sup>ΔΔ</sup>* mice were not linked to increased nutrition or activity, as we observed similar food (Figure 21e) and water intake (Figure 21f) as well as overall activity (Figure 21g+h) between wildtype and *lincIRS2<sup>ΔΔ</sup>* mice.

Taken together, indirect calorimetric measurements could not detect obvious differences in energy expenditure or substrate mobilisation between wildtype and *lincIRS2<sup>ΔΔ</sup>* mice, but point to elevated O<sub>2</sub> consumption and CO<sub>2</sub> production, consequently resulting in increased energy expenditure, in *lincIRS2<sup>ΔΔ</sup>* mice. However, due to the high variance among individual mice further studies are necessary to evaluate potentially increased energy expenditure of *lincIRS2<sup>ΔΔ</sup>* mice.

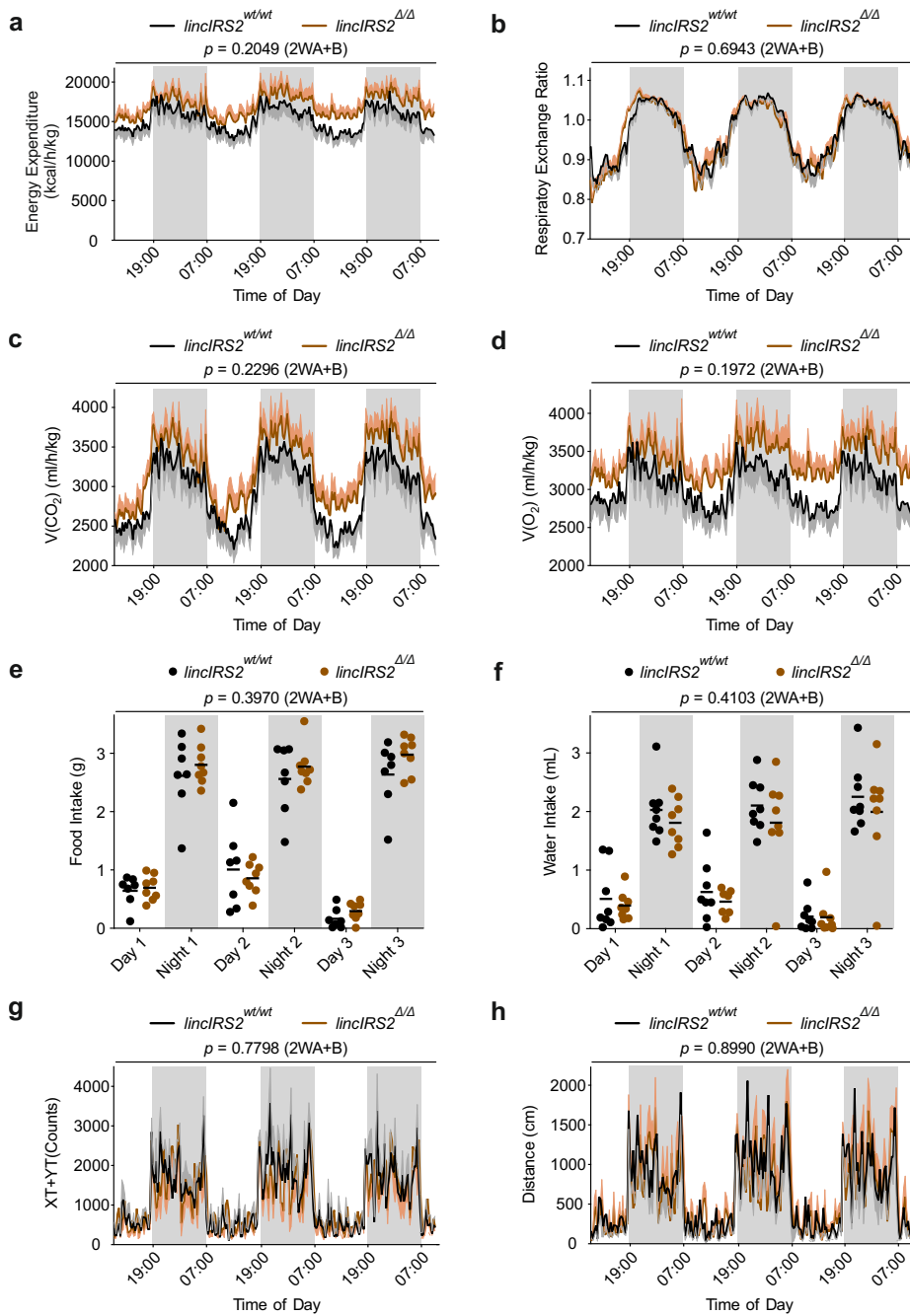


**Figure 21: Indirect calorimetric analysis of the *lincIRS2*<sup>Δ/Δ</sup> mouse line.**

Three-day indirect calorimetric determination of energy expenditure (a), respiratory exchange ratio - mediated assessment of substrate mobilisation (b), CO<sub>2</sub> production (c), O<sub>2</sub> consumption (d), food (e) and water intake (f) as well as movement counted in steps (g) or total distance covered (h) in 16 weeks-old mice harboring wildtype (*lincIRS2*<sup>wt/wt</sup>, black) or homozygous (*lincIRS2*<sup>Δ/Δ</sup>, orange) compositions of the *lincIRS2*<sup>Δ</sup> allele (n=8 each). Graphs represent mean ± s.e.m. (a, b, c, d, g, h) or mean food (e) or water (f) with all data points plotted. Statistical differences were calculated using two-way ANOVA with Bonferroni post-hoc test (2WA+B). *p*-values are given in the panels.

### 4.5.3. *lincIRS2*<sup>Δ/Δ</sup> mice exhibit altered expression levels of key gluconeogenic and lipolytic genes

To identify potential molecular effects affected by altered *lincIRS2* transcript levels, we examined the expression of key metabolic genes in livers of 18 weeks-old mice harboring wildtype (*lincIRS2*<sup>wt/wt</sup>), heterozygous (*lincIRS2*<sup>wt/Δ</sup>) or homozygous (*lincIRS2*<sup>Δ/Δ</sup>) compositions of the *lincIRS2*<sup>Δ</sup> allele (n=4). Loss of *lincIRS2* expression did not significantly change expression levels of metabolic genes controlling glucose transport or fatty acid synthesis. However, we observed genotype-dependent tendencies of altered expression levels for glucose transporters SLC2A2 and SLC2A4 as well as for lipogenesis enzymes ACACA and SREBP1. Interestingly, expression of

insulin signaling proteins showed a tendency to genotype-dependent transcriptional increases, including derepressed expression of insulin signaling proteins IRS-1 and IRS-2 as well as significantly increased expression levels of insulin-responsive transcription factor FOXO1 in heterozygous *lincIRS2<sup>wt/Δ</sup>* mice. Despite high variance among individual expression levels, we also detected strong genotype-dependent elevations of gluconeogenesis regulatory enzymes G6PC and PCK1 upon heterozygous and homozygous deletion of *lincIRS2*, with significantly increased PCK1 expression in *lincIRS2<sup>Δ/Δ</sup>* mice. In addition, fatty acid beta-oxidation rate-limiting enzymes ACOX1 and CPT1A demonstrated borderline significant derepressed expression levels in both heterozygous *lincIRS2<sup>wt/Δ</sup>* and homozygous *lincIRS2<sup>Δ/Δ</sup>* mice (Figure 22).

Collectively, these findings indicate multiple molecular interactions of *lincIRS2* and genes controlling major metabolic pathways, in particular hepatic gluconeogenesis and fatty acid beta-oxidation. Of note, monitored changes in expression levels were dependent upon the gene dosage of *lincIRS2*, as homozygous *lincIRS2<sup>Δ/Δ</sup>* mice exhibited stronger alterations as heterozygous *lincIRS2<sup>wt/Δ</sup>* mice. However, due to the limited number of animals tested and general high variance among individuals, further studies with more animals numbers are needed to corroborate the significant findings and observed tendencies.

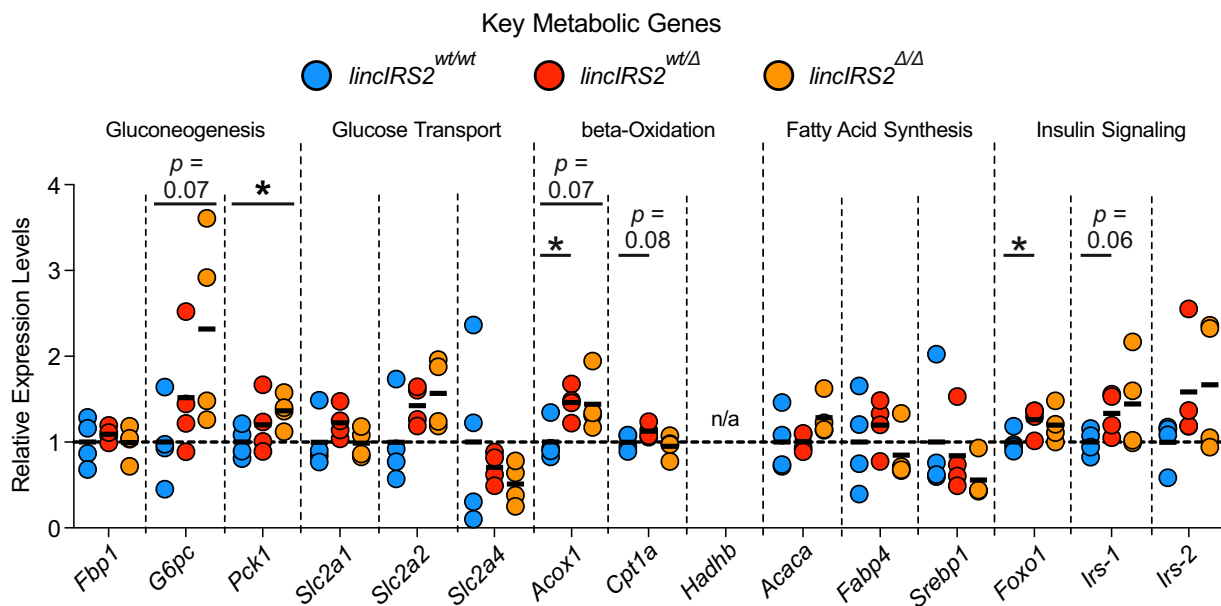


**Figure 22: Gene expression analysis of key metabolic genes in the *lincIRS2<sup>Δ/Δ</sup>* mouse line.**

(a) qPCR gene expression analysis of key metabolic genes in livers of 18 weeks-old mice harboring wildtype (*lincIRS2<sup>wt/wt</sup>*, blue), heterozygous (*lincIRS2<sup>wt/Δ</sup>*, red) or homozygous (*lincIRS2<sup>Δ/Δ</sup>*, orange) compositions of the *lincIRS2<sup>Δ</sup>* allele (n=4). Graphs represent mean expression values with all data points shown. Statistical differences were calculated using unpaired two-tailed t-tests (UP2T-TT). *p*-values are given in the panels. \**p*<0.05.

#### 4.5.4. Knockdown of *linclRS2* in primary hepatocytes results in altered expression of key metabolic genes in response to metabolic stimuli

In order to investigate molecular interactions of *linclRS2*, primary hepatocytes were isolated from 14-18 weeks-old C57BL/6 mice, transfected with antisense oligonucleotides (ASOs) to reduce *linclRS2* gene expression and evaluated for expression of key metabolic genes in response to 6 hrs metabolic stimuli (Figure 23a). Using locked nucleic acid ASOs (LNA GapmeRs [192]) specifically targeting the shared exon 2 of both *linclRS2* isoforms, we could significantly reduce *linclRS2* gene expression (range of mean reduction 46 % - 75 %) in primary hepatocytes grown in unsupplemented growth medium or grown in growth medium supplemented with insulin, forskolin and dexamethasone, or glucagon. As expected, we also observed alterations of *linclRS2* expression levels in response to the respective metabolic stimuli, including *linclRS2* downregulation after insulin stimulation and *linclRS2* upregulation by both fasting mimicking stimulations (Figure 23b).

*LinclRS2* knockdown in primary hepatocytes grown in unsupplemented control medium did not significantly change expression levels of key metabolic genes controlling gluconeogenesis, glucose transport, beta-oxidation, fatty acid synthesis or insulin signaling (Figure 23c). However, we detected alterations in gene expression for genes of all aforementioned metabolic processes when transfected primary hepatocytes were stimulated with insulin (Figure 24a), forskolin and dexamethasone (Figure 24b) or glucagon (Figure 24c).

Despite high variance among biological replicates, gluconeogenesis regulatory enzymes FBP1, G6PC and PCK1 exhibited similar transcriptional regulations upon the respective metabolic stimulations, including significantly reduced insulin-induced repression of G6PC and PCK1 expression levels as well as significantly blunted increases of G6PC and PCK1 expression levels upon fasting mimicking stimulations. Metabolic genes encoding for glucose transporters showed no significant alterations in expression levels, but tendencies to reduced insulin-induced upregulation of *Slc2a1* and diminished glucagon-stimulated upregulation of *Slc2a4* upon *linclRS2* knockdown. *LinclRS2* knockdown did not trigger transcriptional changes of key enzymes controlling beta-oxidation of fatty acids with the exception of CPT1A, whose expression levels were significantly lowered in insulin-stimulated primary hepatocytes. We observed no significant changes in expression levels of key enzymes involved in fatty acid synthesis upon *linclRS2* knockdown in insulin or forskolin and dexamethasone stimulated primary hepatocytes, yet detected significantly increased expression levels of ACACA and SREBP1 after glucagon stimulation. Most interestingly, *linclRS2* knockdown led to significantly increased expression levels of insulin signaling proteins IRS-1 and IRS-2 when primary hepatocytes were stimulated with glucagon.

Collectively, these results demonstrate that *linclRS2* influences the expression of multiple key metabolic genes in response to anabolic and catabolic metabolic signaling.

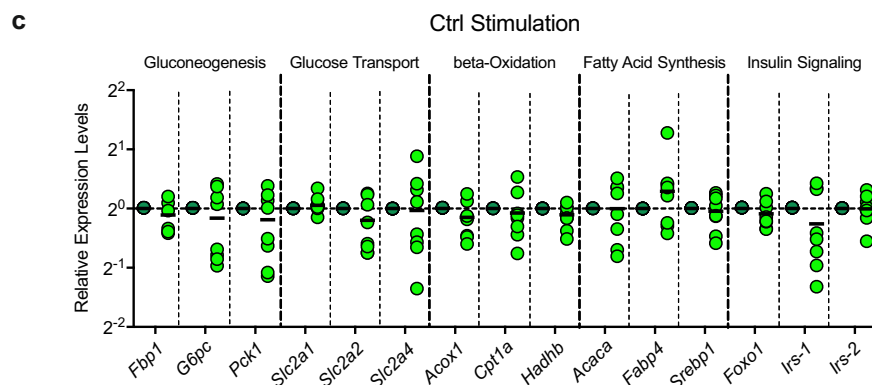
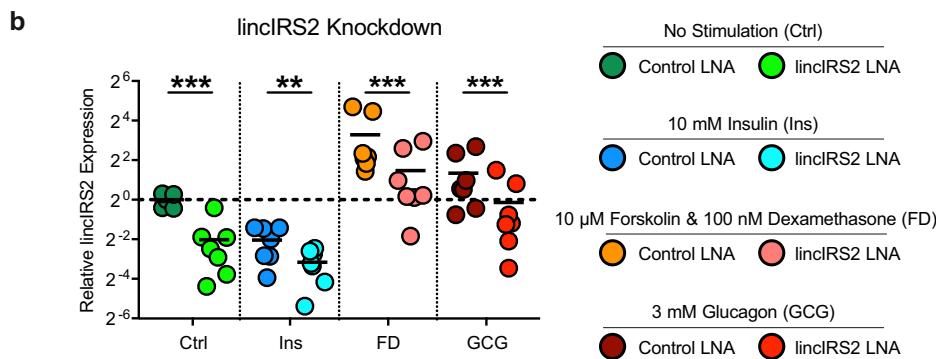
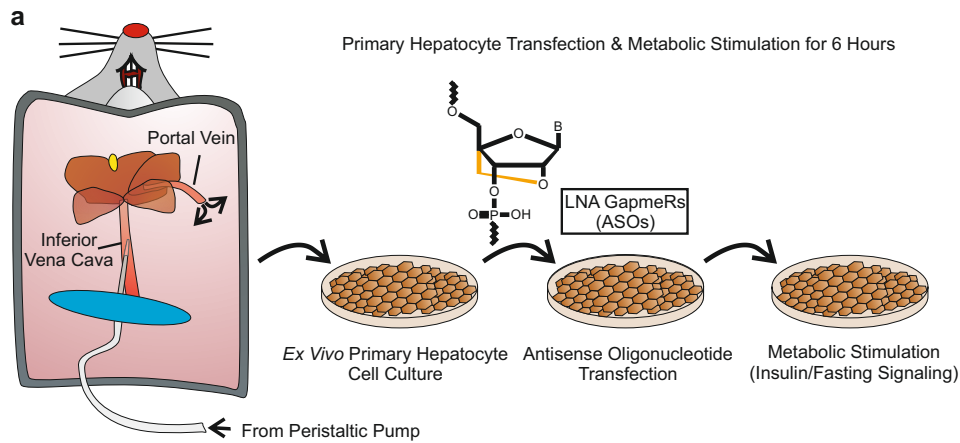


**Figure 23: Gene expression analysis of key metabolic genes upon lincIRS2 knockdown in primary hepatocytes (I).**

(a) Schematic representation of the experimental approach using 14-18 weeks-old C57BL/6 mice for isolation of primary hepatocytes, which were transfected with LNA GapmeR antisense oligonucleotides (LNA) and stimulated for 6 hrs with metabolic compounds. (b) qPCR gene expression analysis of lincIRS2 expression levels in transfected primary hepatocytes, which have been grown for 6 hrs in control growth medium (Ctrl) or control medium supplemented with 10 nM insulin (Ins), 10  $\mu$ M forskolin and 100 nM dexamethasone (FD) or 3 mM glucagon (GCG). Primary hepatocytes were transfected with scramble control LNAs or lincIRS2 LNAs specifically targeting exon 2 of the *lincIRS2* gene. Measurements for each biological replicate (n=8) were performed in 3 technical replicates.

The expression value for the biological replicates was calculated as mean of respective technical replicates. Graphs represent mean expression values with all data points shown. Statistical differences were calculated using paired two-tailed t-tests (P2T-TT). \*\* $p < 0.01$ ; \*\*\* $p < 0.001$ . (c) qPCR gene expression analysis of key metabolic genes in transfected primary hepatocytes grown in control growth medium for 6 hrs. Measurements for each biological replicate (n=8) were performed in 3 technical replicates. Graphs represent mean expression values with all data points shown.

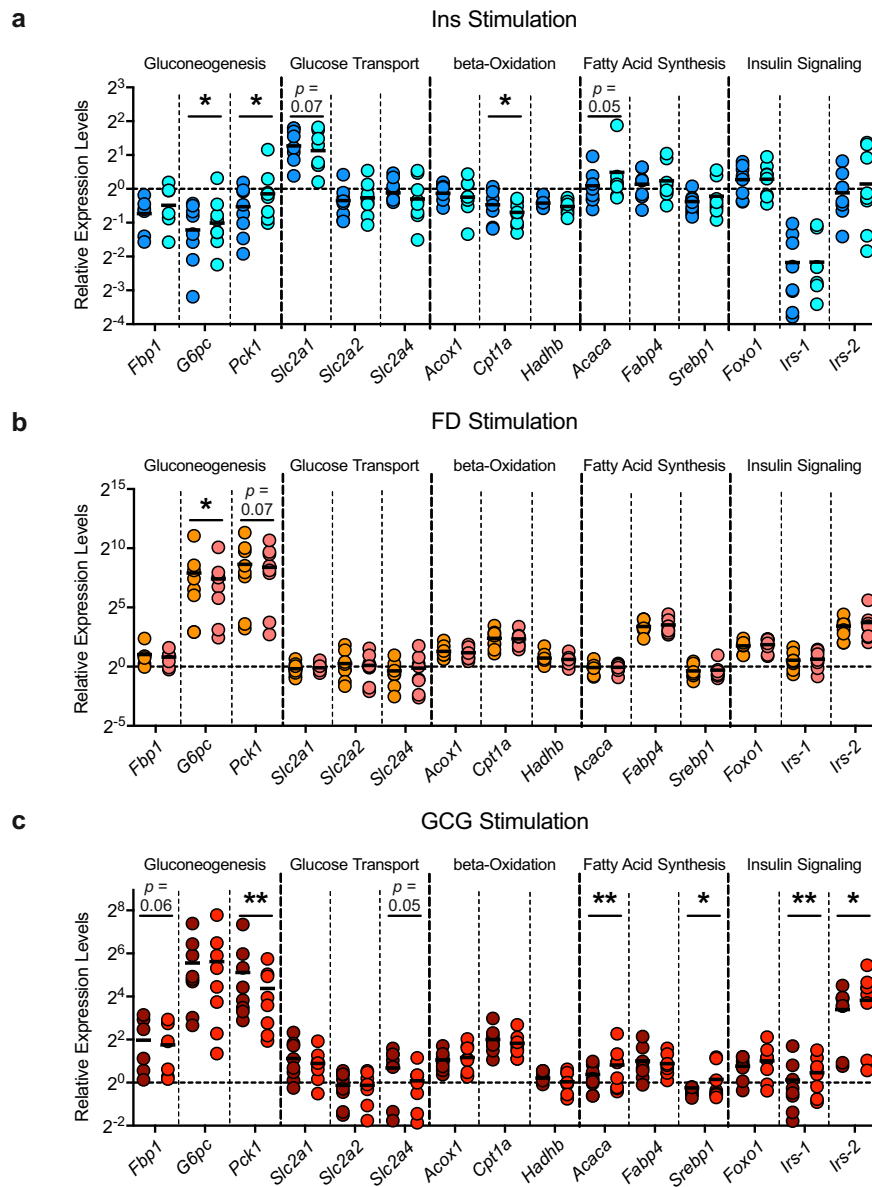


**Figure 24: Gene expression analysis of key metabolic genes upon *lincIRS2* knockdown in primary hepatocytes (II).**

(a-c) qPCR gene expression analysis of key metabolic genes in transfected primary hepatocytes grown for 6 hrs in growth medium supplemented with 10 nM insulin (a), 10  $\mu$ M forskolin and 100 nM dexamethasone (b) or 3 mM glucagon (c). Primary hepatocytes were transfected with scramble control LNAs or *lincIRS2* LNAs specifically targeting exon 2 of the *lincIRS2* gene. Measurements for each biological replicate (n=8) were performed in 3 technical replicates. The expression value for the biological replicates was calculated as mean of respective technical replicates. Graphs represent mean expression values with all data points shown. Statistical differences were calculated using paired two-tailed t-tests (P2T-TT). *p*-values are

given in the panels. \**p*<0.05; \*\**p*<0.01. For a legend of the respective samples see Figure 23b.

#### 4.5.5. Knockdown of *lincIRS2* indicates impaired insulin tolerance in LNA-treated mice

As genetic deletion of a lincRNA locus does not unequivocally prove that the transcript itself is needed for the observed effects in *lincIRS2* $\Delta\Delta$  mice, we additionally investigated the *in vivo* consequences of *lincIRS2* knockdown using anti-*lincIRS2* LNAs. Biweekly injection of C57BL/6 wildtype mice with anti-*lincIRS2* LNAs significantly reduced (range 38 % - 52 % reduction) hepatic *lincIRS2* expression (Figure 25b), with no significant alterations of body weight progression (Figure 25c). However, in contrast to hyperglycemic *lincIRS2* $\Delta\Delta$  mice, we did not detect changes in blood glucose levels between 11 weeks-old C57BL/6 mice treated with control or anti-*lincIRS2* LNAs (Figure 25d). With 11 and 12 weeks of age, respectively, LNA-treated mice were subjected to insulin and glucose tolerance tests to assess differential metabolic responses to intraperitoneal



insulin or glucose administration. Whereas we could not observe differences in glucose clearance between C57BL/6 mice treated with control or anti-lincIRS2 LNAs (Figure 25f), anti-lincIRS2 LNA-treated mice exhibited significantly lower insulin-induced reductions of blood glucose levels compared to control LNA-treated mice, demonstrating a strong tendency towards insulin resistance upon reductions of hepatic lincIRS2 transcript levels (Figure 25e).

These results further indicate that hepatic lincRNA *lincIRS2* is essential for physiological glucose homeostasis and demonstrate that both genomic *lincIRS2* deletion and transient lincIRS2 knockdown are sufficient to impair glucose metabolism *in vivo*, albeit to different degrees.

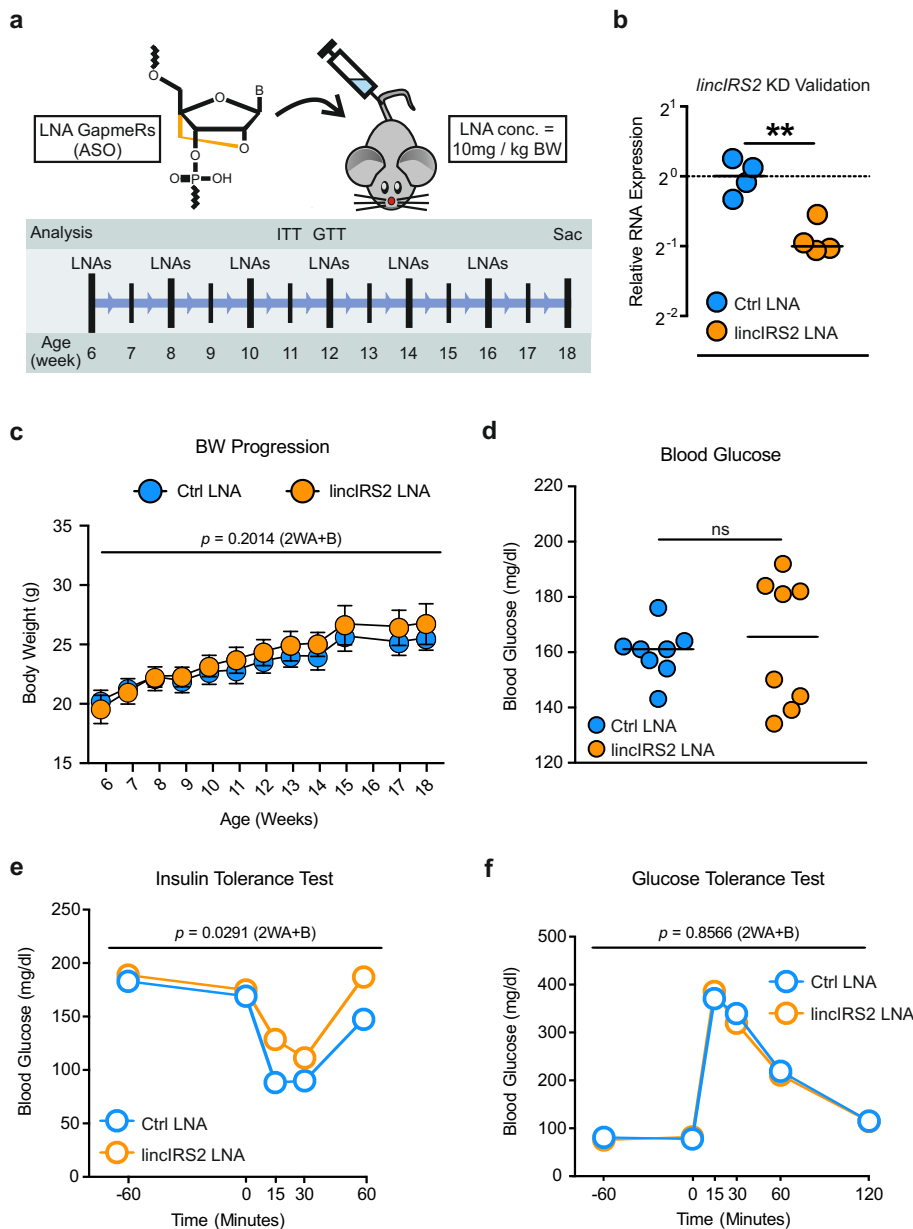


**Figure 25: Knockdown of lincIRS2 transcript levels does not elicit hyperglycemia, but impairs insulin tolerance.**

(a) Schematic representation of the experimental approach using male C57BL/6 mice, which were biweekly injected with 10mg/kg body weight of control or anti-lincIRS2 LNAs for 12 weeks (n=8 per group). All mice were subjected to insulin tolerance (ITT, 11 weeks of age) and glucose tolerance tests (GTT, 12 weeks of age) before sacrifice with 18 weeks of age. (b) qPCR gene expression analysis of lincIRS2 transcript levels in livers of male 18 weeks-old mice after 12 weeks of control (Ctrl LNA) or anti-lincIRS2 LNA (lincIRS2 LNA) treatment (n=4). Graphs represent mean expression values with all data points shown. (c) Body weight progression in male C57BL/6 mice subjected to biweekly injection of control (Ctrl LNA) or anti-lincIRS2 (lincIRS2 LNA) LNAs (n=8). Graphs represent mean body weight  $\pm$  s.e.m. (d) Blood glucose levels in male 11 weeks-old C57BL/6 mice subjected to control (Ctrl LNA) or anti-

lincIRS2 LNA (lincIRS2 LNA) treatment. Graphs represent mean blood glucose levels with all data points shown. (e+f) Blood glucose levels of male C57BL/6 mice subjected to control (Ctrl LNA) or anti-lincIRS2 LNA (lincIRS2 LNA) treatment (n=8) upon insulin (e) and glucose tolerance tests (f). The insulin tolerance test was performed with 11 weeks-old animals, the glucose tolerance test with 12 weeks-old animals. Insulin and glucose were administered at timepoint 0. Graphs represent mean blood glucose levels. Statistical differences were calculated using (b+d) unpaired two-tailed t-tests (UP2T-TT) or (c+e+f) two-way ANOVA with Bonferroni post-hoc test (2WA+B). p-values are given in the panels. \*\*p<0.01; ns, not significant.



#### 4.5.6. Knockdown of *lincIRS2* results in reduced AKT phosphorylation in liver

Before sacrificing the cohorts of LNA-treated C57BL/6 mice with 18 weeks of age, we intraperitoneally injected control LNA-treated and anti-*lincIRS2* LNA-treated mice with insulin or NaCl solutions to assess molecular effector mechanisms of hepatic *lincIRS2* upon acute insulin stimulation. As expected, when performing western blotting analyses of liver protein lysates, we observed insulin-induced phosphorylation of protein kinase AKT in both groups of LNA-treated C57BL/6 mice that were injected with insulin. However, compared to control LNA-treated mice, we detected significant reductions in insulin-evoked AKT phosphorylation (pAKT<sup>S473</sup>) in anti-*lincIRS2* LNA-treated mice, without changes in total AKT abundance (Figure 26).

This finding indicates that *lincIRS2* influences insulin-evoked metabolic responses by mediating phosphorylation of AKT. As phosphorylated AKT constitutes a direct upstream effector of gluconeogenic genes *G6pc* and *Pck1*, reduced AKT phosphorylation conforms with observed increases in expression of G6PC and PCK1 in *lincIRS2*-deficient mice.

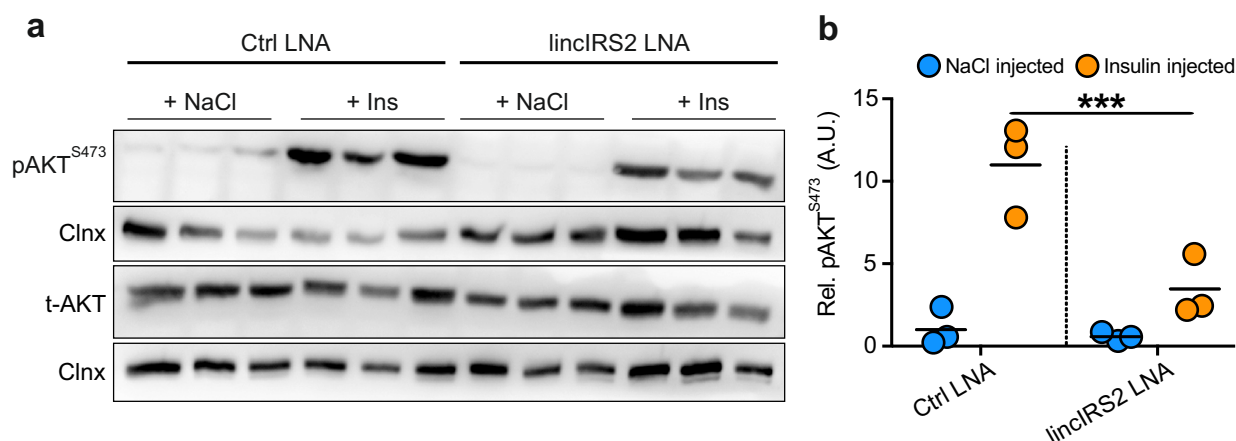


**Figure 26: Reduced insulin-induced AKT phosphorylation in *lincIRS2* LNA-treated mice.**

(a) Representative immunoblots of liver protein lysates isolated from 18 weeks-old C57BL/6 mice after 12 weeks of control LNA (Ctrl LNA) or anti-*lincIRS2* LNA (*lincIRS2* LNA) treatment. Before sacrifice, mice were injected with 2.5  $\mu$ L/g bodyweight of a 0.9 % NaCl solution (NaCl) or 0.1 U/mouse insulin (n=3 per group). (b) Densitometric quantification of AKT phosphorylation on serine residue 473 (pAKT<sup>S473</sup>) related to total AKT (t-AKT) and Calnexin (Clnx) abundance of the respective samples. Graphs represent mean expression values with all data points shown. Statistical differences were calculated using unpaired two-tailed t-tests (UP2T-TT). \*\*\* $p < 0.001$ .

## Chapter 5 - Discussion

### 5.1. Hepatic lncRNA expression adapts to chronic and acute nutrient challenges

In order to shed light on the global regulation of lncRNAs in response to metabolic conditions, such as chronic obesity, type 2 diabetes mellitus (T2DM) or short-term alterations of nutrient availability, we performed RNA-Sequencing (RNA-Seq) in livers of mouse models for chronic obesity and short-term alterations of nutrient availability as well as in human liver biopsies.

As a model system for chronic obesity, we exposed 6 weeks-old C57BL/6 mice for 30 weeks to high-fat diet (HFD) or low-fat diet (normal chow diet, NCD) feeding. As an independent model system for chronic obesity, we additionally used 10 weeks-old *LepR<sup>db/db</sup>* mutant mice, a widely used genetic model for obesity and T2DM [215], and their control breeding strain, 10 weeks-old *Dock7<sup>m/m</sup>* mutant mice [216]. When analysing differential gene expression of the respective model systems, we detected 50 hepatic lncRNAs significantly altered between HFD- and NCD-fed mice and 83 hepatic lncRNAs that exhibited significant differential expression levels between *LepR<sup>db/db</sup>* and *Dock7<sup>m/m</sup>* mutant mice. Global comparison of hepatic expression levels demonstrated a significant overrepresentation of downregulated lncRNAs compared to protein-coding mRNAs in response to HFD feeding and we could also observe the same anticorrelative global trend of lncRNA downregulation and mRNA upregulation in the genetic-evoked obesity model system, albeit less pronounced than in the diet-induced obesity model system.

To assess rapid transcriptional alterations of hepatic transcript expression upon short-term changes in nutrient availability, we performed RNA-Seq in livers of 16 weeks-old C57BL/6 mice that were subjected to 16 hrs *ad libitum* feeding, 16 hrs fasting or 16 hrs fasting followed by 6 hrs of *ad libitum* refeeding. Differential gene expression analysis detected 92 lncRNAs with altered hepatic expression levels between fasted and *ad libitum*-fed mice and 59 lncRNAs that were differentially expressed in livers of refed mice compared fasted mice. In line with the expression data of the chronic obesity mouse models, we again observed pronounced opposite transcriptional regulations for lncRNA and mRNA transcripts when comparing global differential gene expression. Global hepatic lncRNA regulation was significantly upregulated in fasted mice compared to *ad libitum* fed mice, whereas hepatic mRNAs showed a tendency to global downregulation upon fasting. Between refed mice and fasted mice, we observed an inverted trend to the fasting-induced upregulation of lncRNAs, including global downregulation of lncRNA and global upregulation of mRNA transcript expression.

To corroborate the findings of the murine RNA-Seq data sets, we finally performed RNA-Seq of human liver biopsies from a well-characterised cohort of lean, obese and T2DM patients [193]. Differential gene expression analysis detected 297 hepatic lncRNA transcripts that were differentially regulated between lean and obese patients. In addition, we identified 504 hepatic lncRNA transcripts that exhibited altered expression levels between lean and diabetic patients. Consistent with the results of the murine RNA-Seq data sets, we again observed opposite transcriptional regulations for lncRNAs and mRNAs in liver biopsies of the respective groups,

including a highly significant global downregulation of lncRNAs compared to mRNAs between lean and obese patients as well as between lean and T2DM.

Taken together, our extensive RNA-Seq analyses revealed that both chronic and acute nutrient challenges elicit alterations of hepatic lncRNA expression levels. We interpret these transcriptional changes in liver as consequence of the respective metabolic status, which in turn elicits adaptations of lncRNA expression to adjust metaboregulatory signaling circuits. As regulation of global lncRNA expression demonstrated significant downregulations in chronic obesity mouse models as well as in liver biopsies of metabolically compromised humans, we conclude that global lncRNA downregulation is associated with obesity-associated, metabolic impairments. However, if this global lncRNA repression constitutes a cause or consequence of the respective metabolic status remains to be investigated in further studies.

We also observed a significant global upregulation of hepatic lncRNA expression after 16 hrs of fasting and an inverted trend of global lncRNA downregulation when fasted mice were allowed to refeed for 6 hrs. This observation conforms with a previous study showing that the fasting-induced (24 hrs) upregulation of 237 hepatic lncRNAs were completely reversed by 4 hrs of refeeding [172], ultimately suggesting that lncRNA expression in liver is tightly and dynamically controlled in response to short-term alterations of nutrient availability.

Most interestingly, all RNA-Seq analyses identified a pronounced anticorrelative transcriptional regulation of lncRNAs and protein-coding mRNAs in liver. This finding not only indicates that the global regulation of lncRNA expression is independent from global mRNA expression, but also points to differences in the global genomic architecture of lncRNA and mRNA genes that could explain the differential transactivation by nutrient-sensitive signaling pathways. However, further studies are needed to identify the common gene architectures of metabolically-relevant lncRNA genes and the upstream effectors integrating nutritional cues into the global regulation of lncRNAs.

## 5.2. Selection procedure for liver-enriched lncRNAs proves sufficient to identify metabolically-instructive candidate transcripts

To identify metabolically-relevant lncRNAs that partake in the regulation of hepatic energy homeostasis, we designed a selection procedure considering 5 characteristics of lncRNA transcripts. The evaluated lncRNA characteristics included liver-specific expression, biological regulation across obesity and differentially-fed mouse models, predicted protein-coding potential, subcellular localisation of the RNA products as well as transcriptional regulation upon metabolic stimuli.

For identification of liver-specific lncRNAs, we analysed RNA-Seq data of seven metabolically active tissues of a NCD-fed cohort of 17-18 weeks-old C57BL/6 mice [221] and selected lncRNA transcripts, whose RNA-Seq reads were predominantly found in the liver samples. After considering significant regulations of the selected transcripts in the RNA-Seq data sets of both mouse models of chronic obesity as well as proper alignment to annotated genes, we identified 15 lncRNA transcripts for further characterisations. Of note, during the course of this study, one of the selected transcripts (C730036E19Rik) was described as lncLSTR, a liver-enriched transcript which

regulates liver lipid metabolism and whose expression is significantly reduced in mice fasted for 24 hrs, but recovered when fasted mice were allowed to refeed for 4 hrs [165]. This report is in line with the transcriptome data achieved in our study and provides an independent indication that the selected lncRNA candidates contain metabolically-relevant transcripts. As our RNA-Seq results could be affected by the low expression levels of most of our selected lncRNAs, we examined tissue-specific expression levels of the selected candidates by qPCR gene expression analysis in seven metabolically relevant tissues of 17-18 weeks-old NCD-fed C57BL/6 mice. Indeed, we found two candidates with pronounced expression in several non-hepatic tissues, but confirmed liver-specific expression of the remaining lncRNAs.

Differential expression of the selected lncRNAs across obesity and differentially-fed mouse models was analysed via qPCR gene expression analysis and identified significant regulations for the majority of the selected lncRNAs. Strikingly, we observed that fasting-induced transcriptional alterations of most of the lncRNAs were reversed when fasted mice were allowed to re-feed for 6 hrs, which further suggests dynamic transcriptional regulation of metaboregulatory lncRNAs in response to short-term changes in nutrient availability.

Since several recent studies reported lncRNA genes to encode for micropeptides [223, 224], we utilised two independent, web-based algorithms to predict the coding capacities of our selected lncRNAs [196, 197]. Remarkably, two selected lncRNAs exhibited protein-coding potential, whereas the remaining lncRNA candidates were not predicted to encode for (micro-)peptides.

Due to their abundant expression in multiple non-hepatic tissues or their predicted potential to encode for proteins, we discarded four lncRNA candidates and further characterised the remaining 11 lncRNAs by assessing the subcellular localisation of their transcripts in nuclear and cytoplasmic fractions of primary hepatocytes. We observed that most of the transcripts were predominantly found in nuclear fractions, while only one gene product strongly accumulated in cytoplasmic fractions. Of note, we also found several candidates with noticeable expression in both subcellular fractions, which indicates that the corresponding transcripts execute multiple functions in both the nuclear and cytoplasmic compartments.

Lastly, we investigated the transcriptional responses of four manually selected lncRNAs in primary hepatocytes upon 6 hrs stimulation with insulin or fasting-mimicking metabolites forskolin and dexamethasone. While we could not detect insulin-induced alterations in gene expression for B930025P03Rik and Gm13775, we monitored significantly repressed expression levels of 4833411C07Rik and Gm15441 upon insulin stimulation. In addition, 4833411C07Rik and Gm15441 were also found to be strongly regulated in response to fasting mimicking stimulation, albeit with different transcriptional consequences, as fasting stimulation elicited upregulation of 4833411C07Rik, but downregulation of Gm15441.

In conclusion, the evaluated characteristics of our selection procedure proved sufficient to identify two hepatic lncRNAs that are strongly affected by chronic obesity, alterations in feeding status and metabolic stimuli. However, also the other transcripts identified by our selection procedure could constitute impactful metabolic lncRNAs, as demonstrated for C730036E19Rik [165], and should be investigated in further studies. Remarkably, the list of lncRNAs identified by our selection procedure did not contain previously reported regulators of hepatic energy homeostasis

4632424N07 (termed lncLGR [166]), Gm10768 [173] or Gm16551 [172]. Yet, all of these lncRNAs were identified after fasting mice for 16 hrs or 24 hrs, respectively, and not upon chronic obesity as performed in our study. Most interestingly, the two lncRNAs 4833411C07Rik and Gm15441, which we selected for further molecular studies, were also identified in another report during the course of our study [173]. In that report, 4833411C07Rik and Gm15441 were identified as fasting-induced hepatic lncRNAs, which were strongly unregulated upon a 16 hrs fasting regime. These findings conform with the upregulated expression of 4833411C07Rik and Gm15441 that we detected in our RNA-Seq data of 16 hrs fasted mice and provide an independent indication that our selection procedure is sufficient to identify metaboregulatory hepatic lncRNAs.

### 5.3. Successful generation of *in vivo* mouse models to study lncRNA-mediated metabolic networks

To study the systemic impact of lncRNAs 4833411C07Rik (termed lincIRS2) and Gm15441 on liver energy homeostasis, we wanted to generate *in vivo* mouse models devoid of *lincIRS2* or *Gm15441* expression, respectively, using CRISPR/Cas9-mediated genome engineering. For precise design of targeting strategies, we complemented our liver-specific RNA-Seq data sets with publicly available liver chromatin immunoprecipitation sequencing (ChIP-Seq) data for histone 3 lysine 4 trimethylation (H3K4me3) and histone 3 lysine 27 acetylation (H3K27ac) chromatin marks, both of which are associated with active transcription of nearby genes [225].

The genomic *lincIRS2* locus demonstrated liver-specific expression in our RNA-Seq data sets, but also showed expression of another hepatic lncRNA, *Gm2814*, which is located in antisense direction on the opposing DNA strand and overlaps with exon 2 of *lincIRS2*. Of note, both lncRNA genes exhibited identical transcriptional regulations in both mouse models for chronic obesity, which indicates a putative conjoint expression of both genes by common regulatory genomic elements. When considering the publicly available ChIP-Seq data sets, we found H3K4me3 chromatin marks in close proximity to the transcriptional start sites (TSSs) of *lincIRS2* and *Gm2814* as well as broad H3K27ac chromatin marks along the respective gene bodies. We interpreted these accumulations of epigenetic histone modifications as reflections of active gene expression of both lncRNA genes in liver and considered the elimination of genomic sites with chromatin mark accumulations as advantaged aspect of possible targeting strategies. As we aimed to impact both isoforms expressed by *lincIRS2*, which differ in exon 3 and exon 4 composition, we decided to exclusively delete shared exon 1 to disrupt *lincIRS2* expression. Importantly, this targeting approach avoids removal of *Gm2814* transcriptional units, yet also results in collateral deletion of genomic sites with accumulation of H3K4me3 and H3K27ac chromatin marks.

For lncRNA Gm15441, we designed a very similar targeting strategy, as our RNA-Seq data also revealed expression of another transcript overlapping the *Gm15441* gene locus in antisense direction on the opposing DNA strand. Most interestingly, the overlapping gene is the well-studied protein-coding gene *Txnip*, which has been implicated in modulating energy metabolism by regulating cellular redox balance [226], hepatic glucose production [227] and diabetes in humans [228]. Tissue-specific RNA-Seq data sets demonstrated ubiquitous expression of *Txnip* in multiple

tissues, while *Gm15441* expression was predominantly restricted to liver, but could also be found in kidney, albeit to lesser extent. Liver-specific ChIP-Seq data showed accumulations of H3K4me3 and H3K27ac chromatin marks in close proximity to the *Txnip* TSS and along its gene body, but only marginal chromatin marks for active transcription at the *Gm15441* TSS. As this finding did not indicate associations of *Gm15441* expression with H3K4me3 or H3K27ac chromatin marks, we did not consider the removal of genomic sites with chromatin mark accumulations to disrupt *Gm15441* expression. Instead, and with respect to avoid disruptions of the *Txnip* locus, we decided to exclusively remove the genomic region encoding for exon 1 of *Gm15441*.

By using two web-based algorithms to design guideRNA (gRNA) sequences for CRISPR/Cas9 gene targeting, we identified several suitable spacer sequences flanking the first exons of *lincIRS2* and *Gm15441*, respectively. Considering differences in target specificity and potential off-target effects, we selected two 20-nucleotide and two 18-nucleotide spacer sequences for each 5'- and 3'-end of the genomic regions to be targeted and evaluated spacer sequence activity *in vitro* using sequence-specific T7 Endonuclease I assays and genotyping PCRs. Collectively, we could validate genome-editing capacity of four 20-nucleotide and five 18-nucleotide spacer sequences and decided to use the 20-nucleotide spacer sequences for the generation of lincRNA-deficient *in vivo* mouse models in order to maximise sequence-specific target recognition.

#### The *lincIRS2*<sup>Δ</sup> mouse line

The generation of *in vivo* lincRNA mouse models was performed utilising zygote pronuclear injection (PNI) of CRISPR/Cas9 components, including Cas9 protein, Cas9 mRNA and the respective target-specific gRNA components [217]. PNI using *lincIRS2*-targeting spacer sequences resulted in 7 pups, in which we could only detect a truncated *lincIRS2* allele with the expected size for a successful deletion event in one of the founder animals. Importantly, genotyping PCRs also showed the deleted *lincIRS2* allele in progeny of the previously mentioned founder animal, which demonstrated germline transmission of the edited allele. Yet, we could not detect edited *lincIRS2* alleles in the other founder animals or their offspring. To confirm the establishment of a new genome-edited mouse line, we examined the composition of the targeted genomic locus in the positive founder animal as well as in its F1 and F2 offspring. Indeed, DNA sequencing revealed identical genomic compositions among 21 sequenced animals and identified that our targeting approach led to a 422 bp genomic deletion, including the targeted 415 bp genomic region as well as 13 additional basepairs close to the 5' Cas9 cutting site. We interpret the loss of additional basepairs at the 5' Cas9 cutting site as consequence of multiple repair procedures of Cas9-induced double strand breaks, which is a common phenomena in CRISPR/Cas9 technology [176], but does not impinge on our targeting strategy.

When surveying physiological parameters of mice carrying the gene-edited *lincIRS2*<sup>Δ</sup> allele, we did not detect noticeable alterations in behaviour or morphology and found conventional breeding performance as well as genetic inheritance of the *lincIRS2*<sup>Δ</sup> allele with no significant deviations from Mendelian inheritance. Importantly, hepatic expression levels of lincIRS2 were significantly reduced in both heterozygous and homozygous *lincIRS2*<sup>Δ</sup> mice. Yet, whereas lincIRS2 expression was almost completely absent in homozygous *lincIRS2*<sup>Δ/Δ</sup> mice, lincIRS2 expression was reduced

to approximately half of the wildtype *linclRS2* expression in heterozygous *linclRS2<sup>wt/Δ</sup>* mice. This finding strongly indicates that both wildtype alleles of *linclRS2* are necessary for conventional *linclRS2* expression and that one wildtype allele alone is not sufficient to compensate for the lack of *linclRS2* expression by the *linclRS2<sup>Δ</sup>* allele. Remarkably, we also detected reductions in the expression levels of overlapping lncRNA *Gm2814*, which were similar to the respective reductions of *linclRS2* in heterozygous and homozygous *linclRS2<sup>Δ</sup>* mice. This observation points to an interconnected transcriptional regulation of lncRNA genes *linclRS2* and *Gm2814*, most probably by a common bidirectional promoter, parts of which have been removed by our genomic deletion.

#### The *Gm15441<sup>Δ</sup>* mouse line

PNI of CRISPR/Cas9 components using *Gm15441*-targeting spacer sequences resulted in 18 pups, some of which exhibited multiple alterations of the *Gm15441* locus, including truncated alleles in range of predicted deletion events, but also unpredicted edited alleles with slightly increased or decreased genomic sizes. Remarkably, we also observed four founder animals lacking the wildtype *Gm15441* allele, which indicates homozygous CRISPR/Cas9-induced alterations of the *Gm15441* locus or genomic deletions of primer binding sequences. When genotyping F1 and F2 offspring, we validated germline transmission of truncated *Gm15441* alleles in four founder animals. Of note, one of the founders giving rise to a stable *Gm15441<sup>Δ</sup>* mouse line did not show truncated alleles of *Gm15441* in genomic tail biopsy DNA, which demonstrates genetic mosaicism among gametic and somatic cells in the respective F0 individual. Identical genomic compositions among animals of the same founder line was successfully validated by DNA sequencing. However, we found minor variations of the targeted genomic deletions between all four founder lines, reflecting the error-prone repair of Cas9-induced DNA damage by endogenous cellular repair systems [177]. For further metabolic studies, we maintained one founder mouse line, which is defined by a 420 bp genomic deletion, including the targeted 407 bp genomic region as well as 13 additional nucleotides at the 5' Cas9 cutting site.

Homozygous as well as heterozygous mice carrying the selected gene-edited *Gm15441<sup>Δ</sup>* allele displayed no alterations in conventional fertility rates or exhibited obvious behavioural or developmental abnormalities. Additionally, the *Gm15441<sup>Δ</sup>* allele was inherited across generations with no significant deviations from Mendelian inheritance. Intriguingly, we detected highly significant reductions of *Gm15441* expression levels in livers of homozygous *Gm15441<sup>Δ/Δ</sup>* mice, yet did not observe changes of *Gm15441* expression in heterozygous *Gm15441<sup>wt/Δ</sup>* mice. This remarkable finding demonstrates that one wildtype allele of *Gm15441* is sufficient for conventional *Gm15441* transcript levels, which points to monoallelic expression of the *Gm15441* gene locus, as already described for some mammalian genes [221, 231], or compensatory feedback mechanisms that trigger transcriptional adaptations to meet physiological demands, which has been reported for several zebrafish and mouse models [232]. Most importantly, we did not observe transcriptional changes of overlapping protein-coding gene *Txnip* in heterozygous or homozygous *Gm15441<sup>Δ</sup>* animals, which displays successful abrogation of *Gm15441* expression, without perturbing expression of the adjacent *Txnip* locus.

Taken together, we demonstrate that the used protocols can result in the generation of multiple,

stable lncRNA-deficient mouse lines with slightly varying genomic compositions. Remarkably, deletion of the targeted genomic regions resulted in almost complete ablation of target lncRNA expression, but did not impact on fertility or elicit noticeable alterations in behaviour or development. In light of this, we conclude that the generated mouse models represent powerful model systems for *in vivo* characterisations of lncRNA-mediated signaling networks in hepatic metabolism.

#### 5.4. Genetic *lincIRS2* deficiency results in hyperglycemia and impacts on expression of key metabolic enzymes

To identify systemic metabolic consequences of genetic *lincIRS2* deficiency, we compared metabolic parameters between cohorts of *lincIRS2*<sup>ΔΔ</sup> mice with C57BL/6 mice. While we could not detect differences in body weight progression until 18 weeks of age, we found significantly increased blood glucose levels in male and female 11 weeks-old *lincIRS2*<sup>ΔΔ</sup> mice.

When performing intraperitoneal insulin and glucose tolerance tests at 11 and 12 weeks of age, respectively, we found that the previously observed defects in glycemic control of *lincIRS2*<sup>ΔΔ</sup> mice sustained after insulin and glucose challenges. Remarkably, 60 mins after insulin administration and 120 mins after glucose administration, we monitored similar blood glucose levels between C57BL/6 and *lincIRS2*<sup>ΔΔ</sup> mice, indicating that hyperglycemia of *lincIRS2*<sup>ΔΔ</sup> mice can temporarily abate to wildtype levels.

We next surveyed indirect calorimetric parameters between wildtype and homozygous *lincIRS2*<sup>ΔΔ</sup> mice, which could explain the hyperglycemia in *lincIRS2*<sup>ΔΔ</sup> mice. Three-day measurements of 16 weeks-old mice of the respective cohorts did not detect significant changes in energy expenditure or lipid versus carbohydrate substrate mobilisation. Yet, we observed a tendency towards higher rates of oxygen consumption and carbon dioxide production, and thus a tendency towards higher overall energy expenditure, in *lincIRS2*<sup>ΔΔ</sup> mice, which was not associated with increased nutrition or activity. However, owing to high biological variance among individuals in our study, further studies are necessary to examine possible increases in energy expenditure of *lincIRS2*<sup>ΔΔ</sup> mice.

In order to assess putative transcriptional alterations, which could account for the observed hyperglycemia in *lincIRS2*<sup>ΔΔ</sup> mice, we evaluated the expression of key metabolic genes in livers of 18 weeks-old C57BL/6 and heterozygous as well as homozygous *lincIRS2*<sup>Δ</sup> mice. Although *lincIRS2* deficiency did not result in significantly altered expression levels of metabolic genes encoding for glucose transporters or enzymes regulating fatty acid synthesis, we detected genotype-dependent changes in expression levels of genes controlling fatty acid beta-oxidation, insulin signaling and hepatic gluconeogenesis. Fatty acid beta-oxidation rate-limiting enzymes ACOX1 and CPT1A as well as insulin signaling proteins IRS-1, IRS-2 and FOXO1 displayed tendencies to elevated expression levels in both heterozygous *lincIRS2*<sup>wt/Δ</sup> and homozygous *lincIRS2*<sup>ΔΔ</sup> mice. Strikingly, we also detected strong genotype-dependent elevations of gluconeogenesis regulatory enzymes G6PC and PCK1 upon heterozygous and homozygous deletion of *lincIRS2*, which could explain hyperglycemia of *lincIRS2*<sup>ΔΔ</sup> mice due to increased rates of hepatic glucose production.



Collectively, the metabolic characterisation of *linclRS2<sup>ΔΔ</sup>* mice demonstrated that genetic *linclRS2* deficiency results in the development of significant hyperglycemia, including strong trends towards impaired insulin and glucose resistance and no significant differences in energy expenditure or lipid versus carbohydrate substrate mobilisation. Furthermore, genetic *linclRS2* deficiency impacted on the regulation of key metabolic genes controlling hepatic gluconeogenesis and fatty acid beta-oxidation, which could constitute alterations in metaboregulatory networks that ultimately lead to the observed hyperglycemia in *linclRS2<sup>ΔΔ</sup>* mice. As heterozygous and homozygous *linclRS2* deficiency resulted in derepressed gluconeogenic *G6pc*, *Pck1* and *Foxo1* as well as lipogenic *Acox1* and *Cpt1a* gene expression, we concluded that *linclRS2* is essential for the physiological control of hepatic glucose and lipid homeostasis *in vivo*.

## 5.5. Reduction of *linclRS2* levels affects gluconeogenic and lipogenic gene expression and reduces insulin-mediated AKT phosphorylation

As genetic *linclRS2*-deficiency does not unequivocally prove that the *linclRS2* transcript accounts for the observed alterations in metabolic signaling pathways, we monitored the transcriptional regulations of the previously examined set of key metabolic genes upon conditions of reduced *linclRS2* expression levels and in response to 6 hrs metabolic stimulations. We isolated primary hepatocytes from 14-18 weeks-old C57BL/6 mice and could significantly reduce *linclRS2* transcript levels using anti-*linclRS2* LNAs. When analysing primary hepatocytes grown in control medium, we did not detect changes in expression of key metabolic genes upon *linclRS2* knockdown. However, we observed alterations in transcriptional regulations of metabolic genes when LNA-treated primary hepatocytes were stimulated with insulin, glucagon or fasting mimicking metabolites forskolin and dexamethasone. Whereas genes encoding for glucose transporters displayed no significant changes in gene expression upon *linclRS2* knockdown in stimulated primary hepatocytes, we detected significantly elevated expression levels of fatty acid synthesis-controlling enzymes ACACA and SREBP1 in LNA-treated primary hepatocytes upon glucagon stimulation, suggesting that *linclRS2* mediates glucagon-triggered increases of lipogenesis. In line with the previous gene expression analysis of *linclRS2<sup>ΔΔ</sup>* mice, we also found transcriptional alterations of metabolic genes controlling fatty acid beta-oxidation, insulin signaling and gluconeogenesis upon *linclRS2* reduction in primary hepatocytes. This included significant changes in expression of lipolytic enzyme CPT1A upon insulin stimulation as well as significantly increased levels of insulin signaling proteins IRS-1 and IRS-2 when LNA-treated primary hepatocytes were stimulated with glucagon. Most interestingly, *linclRS2* knockdown in primary hepatocytes resulted in significantly altered expression levels of gluconeogenesis regulatory enzymes G6PC and PCK1, including reduced insulin-evoked gene repressions and lowered fasting-induced elevations in gene expression. We interpret these findings as additional evidence that *linclRS2* interacts with multiple metabolic signaling pathways, as already observed in *linclRS2<sup>ΔΔ</sup>* mice. These experiments furthermore indicate that *linclRS2* impacts on transcriptional alterations of gluconeogenic, lipolytic and lipogenic genes in response to anabolic and catabolic

metabolic stimuli, which could explain the impaired glucose homeostasis upon genetic *linclRS2* deletion.

To investigate the systemic metabolic consequences of *linclRS2* knockdown *in vivo*, we biweekly injected C57BL/6 mice with control or anti-*linclRS2* LNAs and compared the same metabolic parameters between the respective cohorts of mice, as previously done with *linclRS2*<sup>wt/wt</sup> and *linclRS2*<sup>ΔΔ</sup> mice. In anti-*linclRS2* LNA-treated mice, we observed no significant changes in body weight gain and could not detect elevations in blood glucose levels, as found in hyperglycemic *linclRS2*<sup>ΔΔ</sup> mice, which indicates that reducing *linclRS2* transcript levels is not sufficient to cause systemic hyperglycemia *in vivo*. When performing intraperitoneal insulin and glucose tolerance tests at 11 and 12 weeks of age, respectively, we observed no differences in glucose clearance between mice treated with control or anti-*linclRS2* LNAs, but a strong tendency towards insulin resistance upon *linclRS2* reduction, as seen in *linclRS2*<sup>ΔΔ</sup> mice. In line with the genetic loss of *linclRS2*, these results corroborate the conclusion that *linclRS2* is essential for physiological glucose homeostasis and demonstrate that both genomic *linclRS2* deletion and transient *linclRS2* knockdown lead to impaired glucose metabolism *in vivo*.

Before sacrifice at 18 weeks of age, we intraperitoneally injected LNA-treated mice with insulin or NaCl solutions to examine *linclRS2*-mediated differences in insulin-induced phosphorylation of protein kinase AKT, the major signaling protein controlling liver energy homeostasis. As expected, we observed strong elevations of AKT phosphorylation at serine residue 473 (pAKT<sup>S473</sup>) upon acute insulin stimulation in both groups of LNA-treated mice. However, when we compared AKT phosphorylation between control LNA and anti-*linclRS2* LNA treated mice, we detected significant reductions in insulin-evoked AKT phosphorylation in anti-*linclRS2* LNA-treated mice, without changes in total AKT abundance. Since pAKT<sup>S473</sup> represents a direct upstream effector regulating expression of gluconeogenic genes *G6pc* and *Pck1*, this finding suggests that *linclRS2* deficiency causes dampened insulin-induced AKT phosphorylation and in turn results in increased expression of *G6pc* and *Pck1*, as observed in anti-*linclRS2* LNA-treated primary hepatocytes and *linclRS2*-deficient mice.

In conclusion, these results demonstrate that reductions of *linclRS2* transcripts cause differences in transcriptional regulations of key metabolic genes in response to anabolic and catabolic metabolic signaling and lead to impaired glucose metabolism *in vivo*. Furthermore, lowered AKT phosphorylation upon *linclRS2* transcript reduction indicates that *linclRS2* is not only essential for proper glucose homeostasis, but also for insulin-evoked suppression of hepatic glucose production *in vivo*, which conforms with hyperglycemia development in *linclRS2*<sup>ΔΔ</sup> mice.

Collectively, we propose the concept that nutrient-sensitive lncRNA *linclRS2* is transcriptionally coupled to alterations of systemic nutrient states and controls liver energy homeostasis by impacting on insulin-induced phosphorylation of AKT and on transcriptional regulations of gluconeogenic, lipolytic and lipogenic genes in response to anabolic or catabolic metabolic signaling.

## 5.6. Future Perspectives

Our extensive RNA-Seq analyses demonstrated global regulations of hepatic lncRNAs in response to chronic and acute nutrient challenges as well as pronounced anticorrelative transcriptional regulations of lncRNAs and protein-coding mRNAs. As all of these findings indicate global transcriptional regulations of lncRNAs, which appear to be independent of protein-coding mRNA regulation, the role of lncRNA-specific upstream effector pathways needs to be addressed in future studies to identify transcription factors that facilitate adaptations of lncRNA expression. However, a simultaneous regulation of hundreds or thousands of lncRNA transcripts relies on the presence of common regulatory genomic elements within the respective lncRNA genes, and thus also the global genomic architecture of lncRNA loci, including transcription factor binding sites, proximal and long-range enhancers as well as accumulations of epigenetic marks and the overall chromatin state, should be investigated in more detail. Our RNA-Seq studies provide a rich source of global transcriptome data across different metabolic states and hence could be used to assess lncRNA-specific regulatory genomic elements.

When applying our selection criteria to the obtained transcriptome data, we identified 15 lncRNAs that are differentially regulated upon chronic obesity. Yet, we only selected two transcripts for further investigations and the remaining transcripts could also constitute metabolically-relevant mediators, as demonstrated in case of lncRNA candidate C730036E19Rik [165]. In addition, more lncRNA regulators of metabolism can be identified by our RNA-Seq studies, as our initial candidate selection procedure was only based on the chronic obesity RNA-Seq data, but not on the RNA-Seq data from differentially-fed mice. As shown by previous reports [172, 173], numerous lncRNAs are transcriptionally induced by fasting and thus hitherto undiscovered lncRNAs partaking in the regulation of cellular energy homeostasis can also be found in further analyses of our RNA-Seq data sets from differentially-fed mice.

### The *Gm15441*<sup>Δ</sup> mouse model system

During the course of this study, we generated an *in vivo* mouse model lacking exon 1 of lncRNA *Gm15441* and demonstrated that this genomic deletion resulted in significant reductions in *Gm15441* expression, without affecting expression of the adjacent protein-coding *Txnip* locus. However, we were not able to further characterise the systemic metabolic characteristics of *Gm15441*<sup>ΔΔ</sup> mice and further studies need to be conducted to evaluate putative consequences of genetic *Gm15441* deletion on liver energy homeostasis, including gene expression analysis of key metabolic genes as well as monitoring systemic metabolic parameters of *Gm15441*<sup>ΔΔ</sup> mice.

Importantly, although *Gm15441*<sup>ΔΔ</sup> mice did not display alterations in *Txnip* expression, the consequences of *Gm15441* deficiency on TXNIP protein levels should be assessed by western blotting analysis, as recent studies reported that lncRNAs can control mRNA translation of overlapping protein-coding genes at the post-transcriptional level [233, 234]. Of note, the transcriptional units of *Gm15441* contain the required functional RNA sequences, which have been shown to trigger increased mRNA translation of overlapping protein-coding genes, and a previous study also predicted that translation of *Txnip* would be affected by *Gm15441* transcripts [235].

### The *linclRS2*<sup>Δ</sup> mouse model system

We successfully generated an *in vivo* mouse model devoid of *linclRS2* expression and showed that genetic loss of exon 1 of *linclRS2* results in impaired glucose homeostasis and insulin-evoked suppression of hepatic glucose production *in vivo*. Yet, the genomic deletion also abrogated expression of overlapping lncRNA Gm2814, although transcriptional units of Gm2814 were not affected by our genomic deletion. For this reason, we can not exclude the possibility that removal of Gm2814 expression partly contributes to the observed hyperglycemic and insulin-intolerant phenotype of *linclRS2*<sup>ΔΔ</sup> mice. Hence, further studies are needed to validate that the observed physiological effects can be solely attributed to the genetic loss of *linclRS2* expression, such as gene expression analysis of metabolic gene expression in primary hepatocytes upon LNA-mediated knockdown of Gm2814 or metabolic characterisations of anti-Gm2814 LNA-treated mice. In our *in vivo* studies, we observed reductions in insulin-evoked AKT phosphorylation upon *linclRS2* knockdown and linked this phenomena to altered expression levels of gluconeogenic, lipolytic and lipogenic genes. Yet, phosphorylated AKT also directly impacts on several other metabolically-relevant downstream targets, such as GSK-3, which regulates glycogen synthesis [116], and TSC-2, which controls cell growth and protein synthesis via mTORC1 [117]. Thus, *linclRS2*<sup>ΔΔ</sup> mice or *linclRS2*<sup>ΔΔ</sup> primary hepatocytes can be used to identify the impact of *linclRS2* deficiency on glycogen metabolism, proliferation markers and protein homeostasis. As phosphorylation of AKT at serine residue 473 is mediated by mTORC2, which itself is regulated by insulin and nutrient availability [115], possible consequences of *linclRS2* deficiency on mTORC2 expression, abundance or function can also be addressed using our *linclRS2*<sup>ΔΔ</sup> mouse model. In addition to mTORC1 and mTORC2, *linclRS2*<sup>ΔΔ</sup> primary hepatocytes can be analysed with regard to alterations in abundance or phosphorylation of other major metabolic signaling proteins, such as FOXO1, IRS-1 and IRS-2. Due to its close genomic positioning to *linclRS2* and a common transcriptional regulation across mouse models of obesity and differential feeding, *Irs2* in particular represents a possible interaction partner of *linclRS2* and can be investigated in western blotting analysis of *linclRS2*<sup>ΔΔ</sup> primary hepatocytes or livers of *linclRS2*<sup>ΔΔ</sup> mice.

We detected alterations in gene expression of lipolytic and lipogenic genes upon *linclRS2* deficiency as well as reductions in insulin-evoked AKT phosphorylation, which besides to gluconeogenesis also controls lipogenesis [117]. Thus, *linclRS2*<sup>ΔΔ</sup> mice can also be used to further elucidate the impact of *linclRS2* on lipid homeostasis, for instance by monitoring lipid production and systemic levels of circulating fatty acids *in vivo*. Ultimately, *linclRS2*<sup>ΔΔ</sup> mice can be exposed to high-fat diet feeding and examined in regard to ameliorated or aggravated phenotypes of systemic glucose and lipid homeostasis.

### Considerations to detect molecular interaction partners of Gm15441 and *linclRS2*

To further explore global consequences of Gm15441 and *linclRS2* deficiency, livers from the respective *in vivo* mouse models can be utilised for protein mass spectrometry [236], RNA-Seq or ChIP-Seq studies, which could display potential differences in protein abundance, gene expression or chromatin modifications, respectively. Of note, primary hepatocytes of the respective mouse models can not only be used in studies examining differences in protein abundance and

phosphorylation or transcriptional alterations of metabolic genes upon metabolic stimulations, but also to identify putative global differences in chromatin architecture using chromosome conformation capture techniques [237]. Furthermore, possible genomic binding sites and RNA or protein interactions partners of the respective lncRNAs can be identified using lncRNA-specific RNA immunoprecipitation approaches, such as ligation of interacting RNA followed by high-throughput sequencing (LIGR-Seq) [238] or capture hybridization of RNA targets (CHART) technologies [221].

Taken together, the *Gm15441*- and *lincIRS2*-deficient mouse lines represent powerful *in vivo* model systems to study lncRNA-mediated cellular adaptations to acute and chronic metabolic cues and can be utilised in further studies to identify lncRNA-specific genomic or proteomic interaction partners.

## Chapter 6 - Appendix

### 6.1. Summary

Due to the current worldwide prevalence of overweight and obesity, an increasing number of individuals is affected by concomitant deregulations of glucose and lipid metabolism, which foster the development of obesity-associated diseases, such as cardiovascular pathologies, Alzheimer's disease, certain cancer subtypes, and type 2 diabetes mellitus. As central hub of energy metabolism, the liver orchestrates the production and storage of carbohydrates and lipids in response to nutrient availability and other metabolic stimuli. Yet, although a multitude of regulatory proteins and signaling pathways controlling liver metabolism have been identified in recent years, the molecular mechanisms by which the liver perceives the abundance or lack of nutrients and facilitates adaptations to the metabolic status remain poorly understood.

Long noncoding RNAs represent a hitherto insufficiently described class of RNA molecules, some of which have been attributed to vital developmental processes. However, just a few studies have identified long noncoding RNAs governing liver energy homeostasis and a multitude of long noncoding RNA genes have not yet been ascribed to specific molecular functions. In light of this, we monitored the expression levels of long noncoding RNAs in livers of mouse model systems for chronic obesity and short-term alterations of nutrient availability as well as in human liver biopsies, and detected that the global expression of long noncoding RNAs inversely correlates with the global expression of protein-coding mRNAs. In order to elucidate if the global anticorrelative regulation of long noncoding RNAs impacts on murine energy metabolism, we performed additional experiments in cell culture systems and identified two long noncoding RNA transcripts, which are significantly regulated upon chronic obesity, dynamically expressed in response to short-term nutritional changes and transcriptionally influenced by metabolic stimuli. Using CRISPR/Cas9-mediated genome engineering technology, we generated deleted alleles of the selected long noncoding RNA genes *Gm15441* and *linclRS2*, both of which result in ablated expression of the respective RNA molecule in *in vivo* mouse models. Finally, we demonstrate that *linclRS2* deficiency in *in vivo* mouse models leads to systemic hyperglycemia and impaired insulin tolerance, and provide evidence that *linclRS2* is essential for proper glucose and lipid homeostasis by influencing insulin-induced phosphorylation of key metabolic enzyme AKT and by regulating the expression of key gluconeogenic, lipolytic and lipogenic genes.

## 6.2. Zusammenfassung

Durch die globale Ausbreitung von Übergewicht und Fettleibigkeit ist der Stoffwechsel von einer stetig wachsenden Gruppe von betroffenen Personen vor große Herausforderungen gestellt, insbesondere durch pathologische Veränderungen des Glukose- und Fettstoffwechsels, welche die Entwicklung von Übergewichts-assoziierten Krankheiten wie Herz-Kreislaufkrankungen, Alzheimer, Krebs oder Typ 2 Diabetes fördern. Als zentrale Schaltstelle des Stoffwechsel koordiniert die Leber in Abhängigkeit zum jeweiligen Ernährungszustand die Aufnahme sowie die Produktion von Kohlenhydraten und Fetten. Doch obwohl bereits zahlreiche regulierende Proteine und Signalwege im Leberstoffwechsel identifiziert worden sind, bleiben viele Fragen über die Mechanismen, wie die Leber die Verfügbarkeit oder den Mangel an Nährstoffen erkennt und in entsprechende Anpassungen des Stoffwechsel anpasst, unbeantwortet.

Lange, nichtkodierende RNAs sind eine bislang unzureichend beschriebene Klasse von Molekülen, die zwar mit überlebenswichtigen Entwicklungsprozessen, jedoch noch nicht mit leberspezifischen Stoffwechselprozessen assoziiert worden sind. Wir haben daher die Expressionslevel von langen, nichtkodierenden RNAs in Lebern von verschiedenen Mausmodellen für chronisches Übergewicht und für kurzzeitig veränderten Ernährungszustand sowie in menschlichen Leberbiopsien überprüft und dabei herausgefunden, dass die globale Expression von langen, nichtkodierenden RNAs stets gegensätzlich zur globalen Expression von proteinkodierenden mRNAs reguliert wird. Um zu überprüfen, ob diese reziproke Regulation konkrete Auswirkungen auf den systematischen Stoffwechsel in der Maus hat, haben wir weitere Untersuchungen im Zellkulturmodell unternommen und letztlich zwei, besonders regulierte, lange, nichtkodierenden RNAs identifiziert. Durch Nutzung der CRISPR/Cas9 Technologie zur Editierung von Genomsequenzen haben wir deletierte Allele der beiden selektierten RNA Gene Gm15441 und lincIRS2 erzeugt, welche im Mausmodell zur nahezu vollständigen Ablation der Expression der jeweiligen RNA Moleküle führen. Abschließend demonstrieren wir, dass die vollständige Abwesenheit des lincIRS2 Transkriptes in erhöhten Blutzuckerwerten und verminderter Insulintoleranz im Mausmodell resultiert, und zeigen Resultate, welche nahelegen, dass das lincIRS2 RNA Molekül entscheidend in der Regulation des leberspezifischen Glukose- und Fettstoffwechsel mitwirkt, indem es Veränderungen des Ernährungszustandes mit der Genexpression von Glukose- und Fettstoffwechselproteinen koppelt und die Insulin-induzierte Phosphorylierung vom metabolischen Schlüsselenzym AKT beeinflusst.

### 6.3. Supplemental figures

Quality Control Summary for RNA-Seq Analysis  
Run 1929 (Obesity Model Livers)

ID	Label	# Reads	# Aligned	Dupl Removed	MapQ ≥ 30	Stranded	miRNA	rRNA	Other nRNA	Ins Size
1079	misty_16	196.7 M	177.5 M	112.9 M	101.3 M	0,0 %	1.9 M	3.1 M	27.6 M	1881.9 ± 3616.9
1080	misty_17	200.6 M	180.7 M	116.9 M	105.8 M	0,0 %	2.9 M	4.9 M	26.1 M	1829.4 ± 2978.1
1081	misty_18	201.7 M	183.5 M	119.3 M	108.0 M	0,0 %	2.3 M	2.6 M	28.8 M	1709 ± 2833.6
1082	dbdb_20	202.8 M	182.9 M	114.4 M	104.6 M	0,0 %	3.5 M	9.6 M	19.8 M	2597.2 ± 4312.1
1083	dbdb_21	195.3 M	179.8 M	96.0 M	87.7 M	0,0 %	3.1 M	5.4 M	20.4 M	2198.3 ± 3970.2
1084	dbdb_22	238.9 M	222.5 M	118.4 M	107.2 M	0,0 %	3.8 M	5.5 M	24.1 M	2815.8 ± 4048.2
1085	NCD_6	197.7 M	179.7 M	122.8 M	113.2 M	0,0 %	2.8 M	6.1 M	21.4 M	2113 ± 4134
1086	NCD_7	186.9 M	168.6 M	110.1 M	100.3 M	0,0 %	2.0 M	3.3 M	22.2 M	2237.9 ± 4343
1087	NCD_8	204.9 M	186.8 M	119.6 M	109.2 M	0,0 %	3.2 M	7.0 M	22.6 M	2228.7 ± 3970.6
1088	HFD_2	204.3 M	186.2 M	120.6 M	111.5 M	0,0 %	2.6 M	4.1 M	21.5 M	2759.3 ± 5189.4
1089	HFD_7	184.3 M	167.9 M	111.2 M	102.9 M	0,0 %	2.4 M	3.5 M	19.1 M	2356.9 ± 4631.3
1094	HFD_6	198.0 M	177.3 M	117.7 M	109.2 M	0,0 %	2.8 M	6.8 M	19.1 M	2072.6 ± 3827.4

Quality Control Summary for RNA-Seq Analysis  
Run 1960 (Feeding Experiment)

ID	Label	# Reads	# Aligned	Dupl Removed	MapQ ≥ 30	Stranded	miRNA	rRNA	Other nRNA	Ins Size
2807	AL2	127.2 M	120.6 M	56.0 M	51.7 M	0,0 %	9.8 M	21.3 M	10.6 M	986.3 ± 2641
2808	AL3	121.6 M	113.7 M	54.5 M	50.0 M	0,0 %	9.2 M	18.1 M	11.6 M	5490.5 ± 140806.9
2809	AL4	143.3 M	134.8 M	61.9 M	56.8 M	0,0 %	10.9 M	22.6 M	13.8 M	957.7 ± 2816.3
2810	AL5	149.1 M	136.9 M	62.5 M	58.4 M	0,0 %	9.4 M	24.9 M	11.5 M	687.8 ± 1886.2
2811	FA1	133.4 M	125.0 M	59.2 M	54.4 M	0,0 %	9.2 M	22.1 M	12.1 M	903.3 ± 2476.1
2812	FA2	148.7 M	140.5 M	64.3 M	59.1 M	0,0 %	10.4 M	23.1 M	13.8 M	724.7 ± 2084.4
2813	FA3	124.4 M	117.0 M	56.0 M	52.1 M	0,0 %	8.1 M	20.4 M	10.3 M	989.6 ± 2990.3
2814	FA5	134.4 M	127.9 M	58.4 M	54.1 M	0,0 %	8.3 M	23.3 M	12.1 M	870 ± 2513.6
2815	RF1	134.6 M	128.5 M	58.6 M	53.8 M	0,0 %	10.3 M	21.6 M	11.8 M	1108.1 ± 3287.2
2816	RF2	127.9 M	121.4 M	59.5 M	55.5 M	0,0 %	8.5 M	20.3 M	10.2 M	837.2 ± 2412.2
2817	RF3	149.5 M	141.1 M	65.5 M	60.5 M	0,0 %	10.0 M	22.8 M	12.3 M	976.1 ± 2970.3
2818	RF4	149.9 M	142.4 M	66.7 M	62.0 M	0,0 %	9.6 M	22.9 M	13.0 M	781.1 ± 2198.5

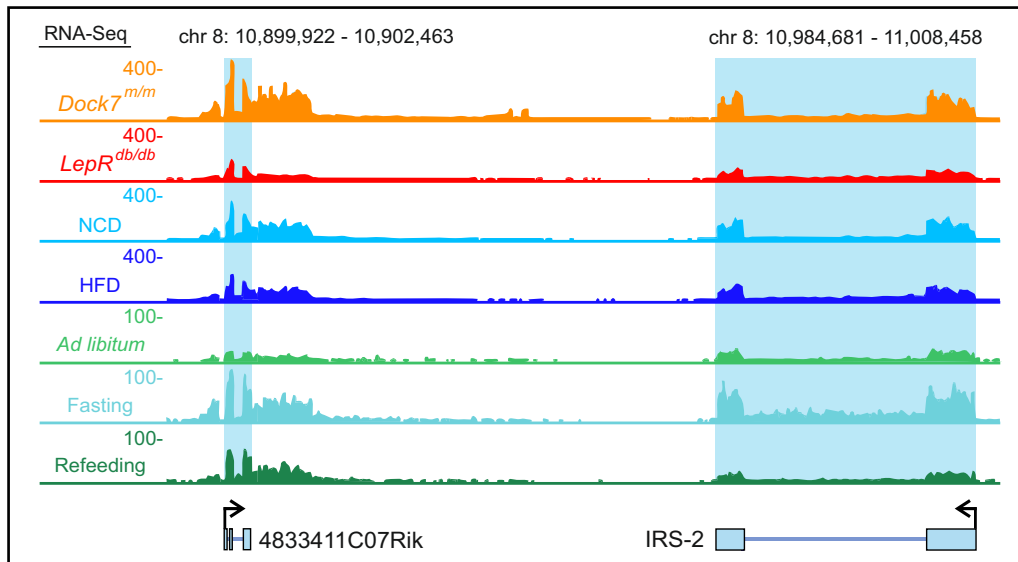
Quality Control Summary for RNA-Seq Analysis  
Run 1995 (Human Livers)

ID	Label	# Reads	# Aligned	Dupl Removed	MapQ ≥ 30	Stranded	miRNA	rRNA	Other nRNA	Ins Size
3045	0381WSC	146.5 M	139.9 M	59.0 M	52.5 M	97,9 %	7.6 M	22.4 M	17.0 M	179.9 ± 138.7
3046	1651HRU	139.0 M	132.7 M	57.2 M	50.4 M	98,0 %	7.6 M	25.1 M	15.7 M	159.5 ± 111.5
3047	1311WER	132.6 M	124.5 M	61.1 M	55.2 M	96,7 %	7.6 M	20.8 M	18.1 M	156.8 ± 84.7
3048	3141AZE	137.9 M	131.3 M	66.1 M	60.1 M	96,3 %	8.1 M	17.9 M	20.1 M	154.0 ± 59.8
3049	0311RAN	136.9 M	131.1 M	66.2 M	61.4 M	97,5 %	6.6 M	19.6 M	18.1 M	148.5 ± 47.3
3050	0861NSC	135.6 M	130.0 M	61.6 M	56.1 M	97,6 %	6.5 M	21.2 M	16.6 M	154.6 ± 91.6
3051	1941JRO	127.6 M	122.0 M	62.8 M	56.6 M	96,9 %	6.1 M	21.4 M	15.9 M	161.4 ± 87.0
3052	0121STR	129.6 M	123.7 M	67.2 M	61.5 M	96,9 %	7.4 M	17.5 M	18.5 M	170.6 ± 120.4
3053	0951LZU	140.1 M	134.2 M	61.7 M	55.5 M	97,5 %	7.6 M	23.0 M	16.7 M	176.6 ± 137.8
3054	1781DGR	148.6 M	142.3 M	66.8 M	59.6 M	97,4 %	8.7 M	20.1 M	18.9 M	172.9 ± 107.9
3055	1701GBO	139.1 M	133.8 M	65.5 M	60.3 M	98,0 %	7.1 M	20.8 M	16.6 M	188.0 ± 139.1
3056	3011FHE	144.8 M	138.3 M	72.7 M	66.2 M	97,5 %	7.8 M	21.5 M	19.3 M	179.1 ± 116.8

**Supplemental Figure 1: Summarised read information for RNA-Seq analyses.**

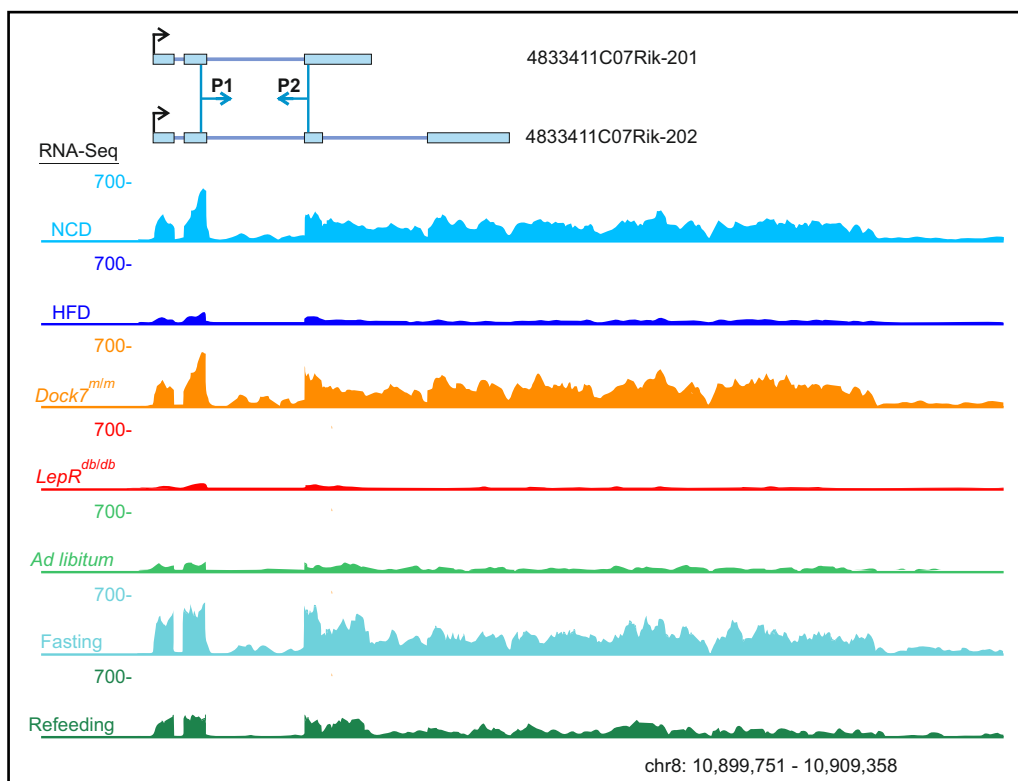
Summarised read information for RNA-Seq analyses of liver RNA derived from obesity mouse models, differentially-fed mouse models and human liver biopsies.





**Supplemental Figure 2: Hepatic expression of lincIRS2 and IRS-2 in the mouse models of chronic obesity and differential feeding.**

Liver RNA-Seq tracks showing the genomic locus of lincRNA candidate 4833411C07Rik (lincIRS2) and neighboring gene insulin receptor substrate 2 (IRS-2) as well as their hepatic expression levels in the mouse models of chronic obesity (*Dock7<sup>m/m</sup>* [orange], *LepR<sup>db/db</sup>* [red], NCD [light blue] and HFD [dark blue]) and differential feeding (*Ad libitum* [light green], Fasting [azure], Refeeding [dark green]). Indicated chromosomal coordinates relate to the respective light blue regions. The distance between 4833411C07Rik and IRS-2 is approximately 82 kb.



**Supplemental Figure 3: Overview of the *lincIRS2* locus, including both transcript isoforms.**

Liver RNA-Seq tracks showing the genomic locus of lincRNA candidate 4833411C07Rik (lincIRS2) as well as its hepatic expression levels in the mouse models of chronic obesity (*Dock7<sup>m/m</sup>* [orange], *LepR<sup>db/db</sup>* [red], NCD [light blue] and HFD [dark blue]) and differential feeding (*Ad libitum* [light green], Fasting [azure], Refeeding [dark green]). Blue boxes indicate annotated exons of transcript isoforms 4833411C07Rik-201 and 4833411C07Rik-202. Blue arrows indicate PCR primers P1 and P2 used for qPCR gene expression analysis.

Nils Hansmeier scientist		Kornfeld workgroup		PNI project		146 AZ			
Project 4833411C07Rik_KO (BHS_)									
Date	males	females	Average Lysis rate	Foster ID	Transferdate	Pregnant	dob	born Pups	alive Pups
14.06.2017	20 C57BL/6NRj	20 C57BL/6NRj	26%	222	14.06.2017	not pregnant	03.07.2017		
				152	14.06.2017	not pregnant	03.07.2017		
				221	14.06.2017	pregnant	03.07.2017	4	4
				87	14.06.2017	pregnant	03.07.2017	3	3
CrispR Deletion gRNA= 800nM (2x 400nM, 400nM, nM, nM) Cas9 mRNA= 30ng/μl Cas9 protein= 200nM									
				Embryos transferred	Number of Transfers	Pregnant	Pups born	alive Pups	
				115	4	1	7	7	

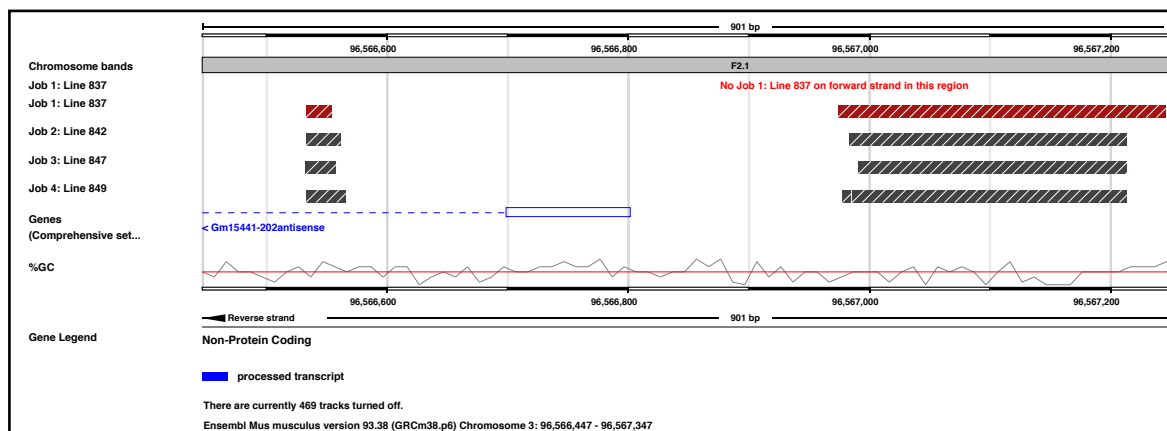
#### Supplemental Figure 4: Outcome of PNI targeting *lincIRS2* exon 1.

Outcome of PNI using CRISPR/Cas9 components to target exon 1 of lncRNA candidate *lincIRS2*, depicting average lysis rate of zygotes, number of transferred 2-cell stage embryos and born founder animals.

Nils Hansmeier scientist		Kornfeld workgroup		PNI project		145 AZ			
Project Gm15441_KO (BHR_)									
Date	males	females	Average Lysis rate	Foster ID	Transferdate	Pregnant	dob	born Pups	alive Pups
07.06.2017	20 C57BL/6NRj	20 C57BL/6NRj	31%	141	08.06.2017	not pregnant	27.06.2017		
				119	08.06.2017	pregnant	27.06.2017	6	6
				96	08.06.2017	pregnant	27.06.2017	5	5
				99	08.06.2017	pregnant	27.06.2017	4	4
				107	08.06.2017	pregnant	27.06.2017	3	3
CrispR Deletion gRNA= 800nM (2x 400nM, 400nM, nM, nM) Cas9 mRNA= 30ng/μl Cas9 protein= 200nM									
				Embryos transferred	Number of Transfers	Pregnant	Pups born	alive Pups	
				106	5	4	18	18	

#### Supplemental Figure 5: Outcome of PNI targeting *Gm15441* exon 1.

Outcome of PNI using CRISPR/Cas9 components to target exon 1 of lncRNA candidate *Gm15441*, depicting average lysis rate of zygotes, number of transferred 2-cell stage embryos and born founder animals.



#### Supplemental Figure 6: Comparison of generated *Gm15441*<sup>ΔA</sup> mouse lines.

Overview of Ensembl genome browser tracks depicting generated *Gm15441*<sup>ΔA</sup> alleles. Error-prone NHEJ repair of Cas9-induced DSBs resulted in minor variations of truncated *Gm15441*<sup>ΔA</sup> alleles in the four stable *Gm15441*<sup>ΔA</sup> mouse lines (Line 837, Line 842, Line 847 and Line 849). The deletion size for the respective mouse lines is as follows: Line 837, 420 bp; Line 842, 422 bp; Line 847, 433 bp; Line 849, 411 bp. The *Gm15441*<sup>ΔA</sup> mouse line described in this work is Line 837.

## 6.4. Bibliography

1. World-Health-Organization, *Global Health Observatory Data*. [Internet] <http://www.who.int/gho/en/>, cited 2018 Aug 7.
2. World-Health-Organization, *Global Database on Body Mass Index*. [Internet] <http://apps.who.int/gmi/index.jsp>, cited 2018 Aug 7.
3. Jura, M. and L.P. Kozak, Obesity and related consequences to ageing. *Age* (Dordr), 2016. 38(1): p. 23.
4. Bray, G.A. and D.S. Gray, *Obesity. Part I--Pathogenesis*. *West J Med*, 1988. 149(4): p. 429-41.
5. Drenick, E.J., et al., Excessive mortality and causes of death in morbidly obese men. *Jama*, 1980. 243(5): p. 443-5.
6. Afshin, A., et al., Health Effects of Overweight and Obesity in 195 Countries over 25 Years. *N Engl J Med*, 2017. 377(1): p. 13-27.
7. Speliotes, E.K., et al., Association analyses of 249,796 individuals reveal 18 new loci associated with body mass index. *Nat Genet*, 2010. 42(11): p. 937-48.
8. Hruby, A. and F.B. Hu, *The Epidemiology of Obesity: A Big Picture*. *Pharmacoeconomics*, 2015. 33(7): p. 673-89.
9. Wadden, T.A., et al., Lifestyle modification for obesity: new developments in diet, physical activity, and behavior therapy. *Circulation*, 2012. 125(9): p. 1157-70.
10. Koh, K.A., et al., The hunger-obesity paradox: obesity in the homeless. *J Urban Health*, 2012. 89(6): p. 952-64.
11. Devaux, M. and F. Sassi, Social inequalities in obesity and overweight in 11 OECD countries. *Eur J Public Health*, 2013. 23(3): p. 464-9.
12. Northstone, K., et al., Prepubertal start of father's smoking and increased body fat in his sons: further characterisation of paternal transgenerational responses. *Eur J Hum Genet*, 2014. 22(12): p. 1382-6.
13. Ravelli, A.C., et al., Obesity at the age of 50 y in men and women exposed to famine prenatally. *Am J Clin Nutr*, 1999. 70(5): p. 811-6.
14. Drake, A.J. and R.M. Reynolds, Impact of maternal obesity on offspring obesity and cardiometabolic disease risk. *Reproduction*, 2010. 140(3): p. 387-98.
15. Wang, Y., et al., Will all Americans become overweight or obese? estimating the progression and cost of the US obesity epidemic. *Obesity* (Silver Spring), 2008. 16(10): p. 2323-30.
16. Whitlock, G., et al., Body-mass index and cause-specific mortality in 900 000 adults: collaborative analyses of 57 prospective studies. *Lancet*, 2009. 373(9669): p. 1083-96.
17. Berrington de Gonzalez, A., et al., Body-mass index and mortality among 1.46 million white adults. *N Engl J Med*, 2010. 363(23): p. 2211-9.
18. Peeters, A., et al., Obesity in adulthood and its consequences for life expectancy: a life-table analysis. *Ann Intern Med*, 2003. 138(1): p. 24-32.

19. Mokdad, A.H., et al., Actual causes of death in the United States, 2000. *Jama*, 2004. 291(10): p. 1238-45.
20. Flint, A.J., et al., Excess weight and the risk of incident coronary heart disease among men and women. *Obesity (Silver Spring)*, 2010. 18(2): p. 377-83.
21. Lu, Y., et al., Metabolic mediators of the effects of body-mass index, overweight, and obesity on coronary heart disease and stroke: a pooled analysis of 97 prospective cohorts with 1.8 million participants. *Lancet*, 2014. 383(9921): p. 970-83.
22. Urbina, E.M. and S.D. de Ferranti, Lipid Screening in Children and Adolescents. *Jama*, 2016. 316(6): p. 589-91.
23. Bianchini, F., R. Kaaks, and H. Vainio, Weight control and physical activity in cancer prevention. *Obes Rev*, 2002. 3(1): p. 5-8.
24. Larsson, S.C. and A. Wolk, Overweight, obesity and risk of liver cancer: a meta-analysis of cohort studies. *Br J Cancer*, 2007. 97(7): p. 1005-8.
25. Larsson, S.C. and A. Wolk, Obesity and the risk of gallbladder cancer: a meta-analysis. *Br J Cancer*, 2007. 96(9): p. 1457-61.
26. Larsson, S.C. and A. Wolk, Overweight and obesity and incidence of leukemia: a meta-analysis of cohort studies. *Int J Cancer*, 2008. 122(6): p. 1418-21.
27. Calle, E.E., et al., Overweight, obesity, and mortality from cancer in a prospectively studied cohort of U.S. adults. *N Engl J Med*, 2003. 348(17): p. 1625-38.
28. Olsen, C.M., et al., Obesity and the risk of epithelial ovarian cancer: a systematic review and meta-analysis. *Eur J Cancer*, 2007. 43(4): p. 690-709.
29. Discacciati, A., N. Orsini, and A. Wolk, Body mass index and incidence of localized and advanced prostate cancer--a dose-response meta-analysis of prospective studies. *Ann Oncol*, 2012. 23(7): p. 1665-71.
30. Polednak, A.P., Estimating the number of U.S. incident cancers attributable to obesity and the impact on temporal trends in incidence rates for obesity-related cancers. *Cancer Detect Prev*, 2008. 32(3): p. 190-9.
31. Gance, L.G., et al., Impact of obesity on mortality and complications in trauma patients. *Ann Surg*, 2014. 259(3): p. 576-81.
32. Huttunen, R. and J. Syrjanen, Obesity and the risk and outcome of infection. *Int J Obes (Lond)*, 2013. 37(3): p. 333-40.
33. Liu, T., et al., The effect of obesity on outcomes in trauma patients: a meta-analysis. *Injury*, 2013. 44(9): p. 1145-52.
34. Young, K.M., C.M. Gray, and L.G. Bekker, Is obesity a risk factor for vaccine non-responsiveness? *PLoS One*, 2013. 8(12): p. e82779.
35. Procaccini, C., et al., Role of metabolism in neurodegenerative disorders. *Metabolism*, 2016. 65(9): p. 1376-90.
36. Anstey, K.J., et al., Body mass index in midlife and late-life as a risk factor for dementia: a meta-analysis of prospective studies. *Obes Rev*, 2011. 12(5): p. e426-37.
37. Kaur, J., A comprehensive review on metabolic syndrome. *Cardiol Res Pract*, 2014. 2014: p. 943162.

38. Nolan, P.B., et al., Prevalence of metabolic syndrome and metabolic syndrome components in young adults: A pooled analysis. *Prev Med Rep*, 2017. 7: p. 211-215.
39. Engin, A., The Definition and Prevalence of Obesity and Metabolic Syndrome. *Adv Exp Med Biol*, 2017. 960: p. 1-17.
40. Carr, D.B., et al., Intra-abdominal fat is a major determinant of the National Cholesterol Education Program Adult Treatment Panel III criteria for the metabolic syndrome. *Diabetes*, 2004. 53(8): p. 2087-94.
41. Martin, K.A., M.V. Mani, and A. Mani, New targets to treat obesity and the metabolic syndrome. *Eur J Pharmacol*, 2015. 763(Pt A): p. 64-74.
42. (NCD-RisC), N.R.F.C., Trends in adult body-mass index in 200 countries from 1975 to 2014: a pooled analysis of 1698 population-based measurement studies with 19.2 million participants. *Lancet*, 2016. 387(10026): p. 1377-1396.
43. Abdullah, A., et al., The magnitude of association between overweight and obesity and the risk of diabetes: a meta-analysis of prospective cohort studies. *Diabetes Res Clin Pract*, 2010. 89(3): p. 309-19.
44. US-Department-of-Health-and-Human-Services-Diabetes-Fact-Sheet, *National Diabetes Information Clearinghouse*. [Internet] <http://diabetes.niddk.nih.gov/dm/pubs/overview>, cited 2018 Aug 8.
45. International-Diabetes-Foundation, *IDF Diabetes Atlas, eight edition, 2017*. [Internet] <http://diabetesatlas.org/resources/2017-atlas.html>, cited 2018 Aug 8.
46. Das, S.K. and S.C. Elbein, *The Genetic Basis of Type 2 Diabetes*. *Cellscience*, 2006. 2(4): p. 100-131.
47. American-Diabetes-Association, Diagnosis and classification of diabetes mellitus. *Diabetes Care*, 2014. 37 Suppl 1: p. S81-90.
48. Organization, W.H. *Global reports on diabetes*. [Internet] <http://www.who.int/diabetes/global-report/en/> cited 2018 Aug 8.
49. Ponziani, F.R., et al., *Physiology and pathophysiology of liver lipid metabolism*. *Expert Rev Gastroenterol Hepatol*, 2015. 9(8): p. 1055-67.
50. Adeva-Andany, M.M., et al., Liver glucose metabolism in humans. *Biosci Rep*, 2016. 36(6).
51. De Bartolo, L., et al., Biotransformation and liver-specific functions of human hepatocytes in culture on RGD-immobilized plasma-processed membranes. *Biomaterials*, 2005. 26(21): p. 4432-41.
52. Schwegler, J., *Der Mensch - Anatomie und Physiologie (4th ed.)*. Thieme. ISBN-13: 978-3-13-100154-2, 2006.
53. Scharl, M.G., M; von Eckardstein, A., *Biochemie und Molekularbiologie des Menschen (1st ed.)*. Urban & Fischer. ISBN-13: 978-3-437-43690-1, 2009.
54. Nguyen, P., et al., *Liver lipid metabolism*. *J Anim Physiol Anim Nutr (Berl)*, 2008. 92(3): p. 272-83.
55. Jones, J.G., *Hepatic glucose and lipid metabolism*. *Diabetologia*, 2016. 59(6): p. 1098-103.
56. Moore, M.C., et al., Regulation of hepatic glucose uptake and storage in vivo. *Adv Nutr*, 2012. 3(3): p. 286-94.

57. Rui, L., *Energy metabolism in the liver*. Compr Physiol, 2014. 4(1): p. 177-97.
58. Sharabi, K., et al., Molecular pathophysiology of hepatic glucose production. Mol Aspects Med, 2015. 46: p. 21-33.
59. Roder, P.V., et al., Pancreatic regulation of glucose homeostasis. Exp Mol Med, 2016. 48: p. e219.
60. Ekberg, K., et al., Contributions by kidney and liver to glucose production in the postabsorptive state and after 60 h of fasting. Diabetes, 1999. 48(2): p. 292-8.
61. Rines, A.K., et al., Targeting hepatic glucose metabolism in the treatment of type 2 diabetes. Nat Rev Drug Discov, 2016. 15(11): p. 786-804.
62. Rojas, J.M. and M.W. Schwartz, Control of hepatic glucose metabolism by islet and brain. Diabetes Obes Metab, 2014. 16 Suppl 1: p. 33-40.
63. Bays, H., L. Mandarino, and R.A. DeFronzo, Role of the adipocyte, free fatty acids, and ectopic fat in pathogenesis of type 2 diabetes mellitus: peroxisomal proliferator-activated receptor agonists provide a rational therapeutic approach. J Clin Endocrinol Metab, 2004. 89(2): p. 463-78.
64. Samuel, V.T. and G.I. Shulman, Mechanisms for insulin resistance: common threads and missing links. Cell, 2012. 148(5): p. 852-71.
65. Shaywitz, A.J. and M.E. Greenberg, CREB: a stimulus-induced transcription factor activated by a diverse array of extracellular signals. Annu Rev Biochem, 1999. 68: p. 821-61.
66. Liang, H. and W.F. Ward, PGC-1alpha: a key regulator of energy metabolism. Adv Physiol Educ, 2006. 30(4): p. 145-51.
67. Nerlov, C., C/EBPs: recipients of extracellular signals through proteome modulation. Curr Opin Cell Biol, 2008. 20(2): p. 180-5.
68. Chen, L. and G. Yang, PPARs Integrate the Mammalian Clock and Energy Metabolism. PPAR Res, 2014. 2014: p. 653017.
69. Yang, H. and L. Yang, Targeting cAMP/PKA pathway for glycemic control and type 2 diabetes therapy. J Mol Endocrinol, 2016. 57(2): p. R93-r108.
70. Mao, Z. and W. Zhang, Role of mTOR in Glucose and Lipid Metabolism. Int J Mol Sci, 2018. 19(7).
71. Thorens, B. and M. Mueckler, *Glucose transporters in the 21st Century*. Am J Physiol Endocrinol Metab, 2010. 298(2): p. E141-5.
72. Seyer, P., et al., Hepatic glucose sensing is required to preserve beta cell glucose competence. J Clin Invest, 2013. 123(4): p. 1662-76.
73. Santer, R., et al., The mutation spectrum of the facilitative glucose transporter gene SLC2A2 (GLUT2) in patients with Fanconi-Bickel syndrome. Hum Genet, 2002. 110(1): p. 21-9.
74. Thorens, B., Glucose transporters in the regulation of intestinal, renal, and liver glucose fluxes. Am J Physiol, 1996. 270(4 Pt 1): p. G541-53.
75. Gras, D., et al., *GLUT1 deficiency syndrome: an update*. Rev Neurol (Paris), 2014. 170(2): p. 91-9.
76. Kotani, K., et al., GLUT4 glucose transporter deficiency increases hepatic lipid production and peripheral lipid utilization. J Clin Invest, 2004. 114(11): p. 1666-75.

77. Hatting, M., et al., *Insulin regulation of gluconeogenesis*. Ann N Y Acad Sci, 2018. 1411(1): p. 21-35.
78. Barthel, A. and D. Schmolli, Novel concepts in insulin regulation of hepatic gluconeogenesis. Am J Physiol Endocrinol Metab, 2003. 285(4): p. E685-92.
79. Kim, S.G., G.R. Buel, and J. Blenis, Nutrient regulation of the mTOR complex 1 signaling pathway. Mol Cells, 2013. 35(6): p. 463-73.
80. Inoue, H., et al., Role of hepatic STAT3 in brain-insulin action on hepatic glucose production. Cell Metab, 2006. 3(4): p. 267-75.
81. She, P., et al., Phosphoenolpyruvate carboxykinase is necessary for the integration of hepatic energy metabolism. Mol Cell Biol, 2000. 20(17): p. 6508-17.
82. Burgess, S.C., et al., Impaired tricarboxylic acid cycle activity in mouse livers lacking cytosolic phosphoenolpyruvate carboxykinase. J Biol Chem, 2004. 279(47): p. 48941-9.
83. Valera, A., et al., Transgenic mice overexpressing phosphoenolpyruvate carboxykinase develop non-insulin-dependent diabetes mellitus. Proc Natl Acad Sci U S A, 1994. 91(19): p. 9151-4.
84. Hommes, F.A., et al., Two cases of phosphoenolpyruvate carboxykinase deficiency. Acta Paediatr Scand, 1976. 65(2): p. 233-40.
85. Vidnes, J. and O. Sovik, Gluconeogenesis in infancy and childhood. III. Deficiency of the extramitochondrial form of hepatic phosphoenolpyruvate carboxykinase in a case of persistent neonatal hypoglycaemia. Acta Paediatr Scand, 1976. 65(3): p. 307-12.
86. Vieira, P., et al., Novel homozygous PCK1 mutation causing cytosolic phosphoenolpyruvate carboxykinase deficiency presenting as childhood hypoglycemia, an abnormal pattern of urine metabolites and liver dysfunction. Mol Genet Metab, 2017. 120(4): p. 337-341.
87. Yip, J., et al., Cerebral Gluconeogenesis and Diseases. Front Pharmacol, 2016. 7: p. 521.
88. Visinoni, S., et al., Increased glucose production in mice overexpressing human fructose-1,6-bisphosphatase in the liver. Am J Physiol Endocrinol Metab, 2008. 295(5): p. E1132-41.
89. Hopwood, N.J., I. Holzman, and A.L. Drash, *Fructose-1,6-diphosphatase deficiency*. Am J Dis Child, 1977. 131(4): p. 418-21.
90. Faiyaz-UI-Haque, M., et al., Novel FBP1 gene mutations in Arab patients with fructose-1,6-bisphosphatase deficiency. Eur J Pediatr, 2009. 168(12): p. 1467-71.
91. Ijaz, S., et al., Genetic analysis of fructose-1,6-bisphosphatase (FBPase) deficiency in nine consanguineous Pakistani families. J Pediatr Endocrinol Metab, 2017. 30(11): p. 1203-1210.
92. Mutel, E., et al., Targeted deletion of liver glucose-6 phosphatase mimics glycogen storage disease type 1a including development of multiple adenomas. J Hepatol, 2011. 54(3): p. 529-37.
93. Rajas, F., et al., Lessons from new mouse models of glycogen storage disease type 1a in relation to the time course and organ specificity of the disease. J Inher Metab Dis, 2015. 38(3): p. 521-7.
94. Penhoat, A., et al., Intestinal gluconeogenesis is crucial to maintain a physiological fasting glycemia in the absence of hepatic glucose production in mice. Metabolism, 2014. 63(1): p. 104-11.
95. Froissart, R., et al., *Glucose-6-phosphatase deficiency*. Orphanet J Rare Dis, 2011. 6: p. 27.

96. Bartlett, K. and S. Eaton, *Mitochondrial beta-oxidation*. Eur J Biochem, 2004. 271(3): p. 462-9.
97. Houten, S.M. and R.J. Wanders, A general introduction to the biochemistry of mitochondrial fatty acid beta-oxidation. J Inherit Metab Dis, 2010. 33(5): p. 469-77.
98. Nyman, L.R., et al., Homozygous carnitine palmitoyltransferase 1a (liver isoform) deficiency is lethal in the mouse. Mol Genet Metab, 2005. 86(1-2): p. 179-87.
99. Longo, N., C. Amat di San Filippo, and M. Pasquali, *Disorders of carnitine transport and the carnitine cycle*. Am J Med Genet C Semin Med Genet, 2006. 142c(2): p. 77-85.
100. Vluggens, A., et al., Reversal of mouse Acyl-CoA oxidase 1 (ACOX1) null phenotype by human ACOX1b isoform [corrected]. Lab Invest, 2010. 90(5): p. 696-708.
101. Ferdinandusse, S., et al., Clinical, biochemical, and mutational spectrum of peroxisomal acyl-coenzyme A oxidase deficiency. Hum Mutat, 2007. 28(9): p. 904-12.
102. Ibdah, J.A., et al., Lack of mitochondrial trifunctional protein in mice causes neonatal hypoglycemia and sudden death. J Clin Invest, 2001. 107(11): p. 1403-9.
103. Clayton, P.T., et al., Hyperinsulinism in short-chain L-3-hydroxyacyl-CoA dehydrogenase deficiency reveals the importance of beta-oxidation in insulin secretion. J Clin Invest, 2001. 108(3): p. 457-65.
104. Thumser, A.E., J.B. Moore, and N.J. Plant, Fatty acid binding proteins: tissue-specific functions in health and disease. Curr Opin Clin Nutr Metab Care, 2014. 17(2): p. 124-9.
105. Horton, J.D., J.L. Goldstein, and M.S. Brown, SREBPs: activators of the complete program of cholesterol and fatty acid synthesis in the liver. J Clin Invest, 2002. 109(9): p. 1125-31.
106. Abu-Elheiga, L., et al., Mutant mice lacking acetyl-CoA carboxylase 1 are embryonically lethal. Proc Natl Acad Sci U S A, 2005. 102(34): p. 12011-6.
107. Hotamisligil, G.S., et al., Uncoupling of obesity from insulin resistance through a targeted mutation in aP2, the adipocyte fatty acid binding protein. Science, 1996. 274(5291): p. 1377-9.
108. Shimomura, I., Y. Bashmakov, and J.D. Horton, Increased levels of nuclear SREBP-1c associated with fatty livers in two mouse models of diabetes mellitus. J Biol Chem, 1999. 274(42): p. 30028-32.
109. Pettinelli, P., et al., Enhancement in liver SREBP-1c/PPAR-alpha ratio and steatosis in obese patients: correlations with insulin resistance and n-3 long-chain polyunsaturated fatty acid depletion. Biochim Biophys Acta, 2009. 1792(11): p. 1080-6.
110. Moon, Y.A., et al., The Scap/SREBP pathway is essential for developing diabetic fatty liver and carbohydrate-induced hypertriglyceridemia in animals. Cell Metab, 2012. 15(2): p. 240-6.
111. Titchenell, P.M., M.A. Lazar, and M.J. Birnbaum, Unraveling the Regulation of Hepatic Metabolism by Insulin. Trends Endocrinol Metab, 2017. 28(7): p. 497-505.
112. White, M.F., Regulating insulin signaling and beta-cell function through IRS proteins. Can J Physiol Pharmacol, 2006. 84(7): p. 725-37.
113. Boucher, J., A. Kleinridders, and C.R. Kahn, Insulin receptor signaling in normal and insulin-resistant states. Cold Spring Harb Perspect Biol, 2014. 6(1).
114. Alessi, D.R., et al., Characterization of a 3-phosphoinositide-dependent protein kinase which phosphorylates and activates protein kinase Balpha. Curr Biol, 1997. 7(4): p. 261-9.



115. Sarbassov, D.D., et al., Phosphorylation and regulation of Akt/PKB by the rictor-mTOR complex. *Science*, 2005. 307(5712): p. 1098-101.
116. Ramnanan, C.J., et al., Brain insulin action augments hepatic glycogen synthesis without suppressing glucose production or gluconeogenesis in dogs. *J Clin Invest*, 2011. 121(9): p. 3713-23.
117. Duvel, K., et al., Activation of a metabolic gene regulatory network downstream of mTOR complex 1. *Mol Cell*, 2010. 39(2): p. 171-83.
118. Tzivion, G., M. Dobson, and G. Ramakrishnan, FoxO transcription factors; Regulation by AKT and 14-3-3 proteins. *Biochim Biophys Acta*, 2011. 1813(11): p. 1938-45.
119. Matsumoto, M., et al., Impaired regulation of hepatic glucose production in mice lacking the forkhead transcription factor Foxo1 in liver. *Cell Metab*, 2007. 6(3): p. 208-16.
120. Lu, M., et al., Insulin regulates liver metabolism in vivo in the absence of hepatic Akt and Foxo1. *Nat Med*, 2012. 18(3): p. 388-95.
121. Haeusler, R.A., K.H. Kaestner, and D. Accili, FoxOs function synergistically to promote glucose production. *J Biol Chem*, 2010. 285(46): p. 35245-8.
122. Kim, D.H., et al., FoxO6 integrates insulin signaling with gluconeogenesis in the liver. *Diabetes*, 2011. 60(11): p. 2763-74.
123. Clausen, J.O., et al., Insulin resistance: interactions between obesity and a common variant of insulin receptor substrate-1. *Lancet*, 1995. 346(8972): p. 397-402.
124. Bottomley, W.E., et al., IRS2 variants and syndromes of severe insulin resistance. *Diabetologia*, 2009. 52(6): p. 1208-11.
125. Araki, E., et al., Alternative pathway of insulin signalling in mice with targeted disruption of the IRS-1 gene. *Nature*, 1994. 372(6502): p. 186-90.
126. Withers, D.J., et al., Disruption of IRS-2 causes type 2 diabetes in mice. *Nature*, 1998. 391(6670): p. 900-4.
127. Dong, X., et al., Irs1 and Irs2 signaling is essential for hepatic glucose homeostasis and systemic growth. *J Clin Invest*, 2006. 116(1): p. 101-14.
128. Post-transcriptional processing generates a diversity of 5'-modified long and short RNAs. *Nature*, 2009. 457(7232): p. 1028-32.
129. Clark, M.B., et al., *The reality of pervasive transcription*. *PLoS Biol*, 2011. 9(7): p. e1000625; discussion e1001102.
130. Noller, H.F., *Ribosomal RNA and translation*. *Annu Rev Biochem*, 1991. 60: p. 191-227.
131. Matera, A.G., R.M. Terns, and M.P. Terns, Non-coding RNAs: lessons from the small nuclear and small nucleolar RNAs. *Nat Rev Mol Cell Biol*, 2007. 8(3): p. 209-20.
132. Farazi, T.A., S.A. Juraneck, and T. Tuschl, The growing catalog of small RNAs and their association with distinct Argonaute/Piwi family members. *Development*, 2008. 135(7): p. 1201-14.
133. Okamura, K. and E.C. Lai, *Endogenous small interfering RNAs in animals*. *Nat Rev Mol Cell Biol*, 2008. 9(9): p. 673-8.
134. Bartel, D.P., MicroRNAs: target recognition and regulatory functions. *Cell*, 2009. 136(2): p. 215-33.

135. Iyer, M.K., et al., The landscape of long noncoding RNAs in the human transcriptome. *Nat Genet*, 2015. 47(3): p. 199-208.
136. Fang, S., et al., NONCODEV5: a comprehensive annotation database for long non-coding RNAs. *Nucleic Acids Res*, 2018. 46(D1): p. D308-d314.
137. Chen, L.L., Linking Long Noncoding RNA Localization and Function. *Trends Biochem Sci*, 2016. 41(9): p. 761-772.
138. Derrien, T., et al., The GENCODE v7 catalog of human long noncoding RNAs: analysis of their gene structure, evolution, and expression. *Genome Res*, 2012. 22(9): p. 1775-89.
139. Yin, Q.F., et al., Long noncoding RNAs with snoRNA ends. *Mol Cell*, 2012. 48(2): p. 219-30.
140. Qu, S., et al., Circular RNA: A new star of noncoding RNAs. *Cancer Lett*, 2015. 365(2): p. 141-8.
141. Gendrel, A.V. and E. Heard, Noncoding RNAs and epigenetic mechanisms during X-chromosome inactivation. *Annu Rev Cell Dev Biol*, 2014. 30: p. 561-80.
142. Cusanelli, E. and P. Chartrand, Telomeric repeat-containing RNA TERRA: a noncoding RNA connecting telomere biology to genome integrity. *Front Genet*, 2015. 6: p. 143.
143. Kanduri, C., Long noncoding RNAs: Lessons from genomic imprinting. *Biochim Biophys Acta*, 2016. 1859(1): p. 102-11.
144. Fatica, A. and I. Bozzoni, Long non-coding RNAs: new players in cell differentiation and development. *Nat Rev Genet*, 2014. 15(1): p. 7-21.
145. Marchese, F.P., I. Raimondi, and M. Huarte, The multidimensional mechanisms of long noncoding RNA function. *Genome Biol*, 2017. 18(1): p. 206.
146. Wang, K.C., et al., A long noncoding RNA maintains active chromatin to coordinate homeotic gene expression. *Nature*, 2011. 472(7341): p. 120-4.
147. Goyal, N., D. Kesharwani, and M. Datta, Lnc-ing non-coding RNAs with metabolism and diabetes: roles of lncRNAs. *Cell Mol Life Sci*, 2018. 75(10): p. 1827-1837.
148. Geuens, T., D. Bouhy, and V. Timmerman, The hnRNP family: insights into their role in health and disease. *Hum Genet*, 2016. 135(8): p. 851-67.
149. Ribeiro, D.M., et al., Protein complex scaffolding predicted as a prevalent function of long non-coding RNAs. *Nucleic Acids Res*, 2018. 46(2): p. 917-928.
150. Yang, L., et al., lncRNA-dependent mechanisms of androgen-receptor-regulated gene activation programs. *Nature*, 2013. 500(7464): p. 598-602.
151. Marin-Bejar, O., et al., Pint lincRNA connects the p53 pathway with epigenetic silencing by the Polycomb repressive complex 2. *Genome Biol*, 2013. 14(9): p. R104.
152. Wang, Z., et al., The long noncoding RNA Chaer defines an epigenetic checkpoint in cardiac hypertrophy. *Nat Med*, 2016. 22(10): p. 1131-1139.
153. Rinn, J.L., et al., Functional demarcation of active and silent chromatin domains in human HOX loci by noncoding RNAs. *Cell*, 2007. 129(7): p. 1311-23.
154. Liu, B., et al., A cytoplasmic NF-kappaB interacting long noncoding RNA blocks I kappa B phosphorylation and suppresses breast cancer metastasis. *Cancer Cell*, 2015. 27(3): p. 370-81.

155. Gong, C. and L.E. Maquat, lncRNAs transactivate STAU1-mediated mRNA decay by duplexing with 3' UTRs via Alu elements. *Nature*, 2011. 470(7333): p. 284-8.
156. Yoon, J.H., et al., LincRNA-p21 suppresses target mRNA translation. *Mol Cell*, 2012. 47(4): p. 648-55.
157. Cesana, M., et al., A long noncoding RNA controls muscle differentiation by functioning as a competing endogenous RNA. *Cell*, 2011. 147(2): p. 358-69.
158. Lee, S., et al., Noncoding RNA NORAD Regulates Genomic Stability by Sequestering PUMILIO Proteins. *Cell*, 2016. 164(1-2): p. 69-80.
159. Nakagawa, S., et al., Malat1 is not an essential component of nuclear speckles in mice. *Rna*, 2012. 18(8): p. 1487-99.
160. Wilusz, J.E., S.M. Freier, and D.L. Spector, 3' end processing of a long nuclear-retained noncoding RNA yields a tRNA-like cytoplasmic RNA. *Cell*, 2008. 135(5): p. 919-32.
161. Cabili, M.N., et al., Integrative annotation of human large intergenic noncoding RNAs reveals global properties and specific subclasses. *Genes Dev*, 2011. 25(18): p. 1915-27.
162. Ellis, B.C., L.D. Graham, and P.L. Molloy, CRNDE, a long non-coding RNA responsive to insulin/IGF signaling, regulates genes involved in central metabolism. *Biochim Biophys Acta*, 2014. 1843(2): p. 372-86.
163. Lin, A., et al., The LINK-A lncRNA interacts with PtdIns(3,4,5)P3 to hyperactivate AKT and confer resistance to AKT inhibitors. *Nat Cell Biol*, 2017. 19(3): p. 238-251.
164. Li, D., et al., Identification of a novel human long non-coding RNA that regulates hepatic lipid metabolism by inhibiting SREBP-1c. *Int J Biol Sci*, 2017. 13(3): p. 349-357.
165. Li, P., et al., A liver-enriched long non-coding RNA, lncLSTR, regulates systemic lipid metabolism in mice. *Cell Metab*, 2015. 21(3): p. 455-67.
166. Ruan, X., et al., A Long Non-coding RNA, lncLGR, Regulates Hepatic Glucokinase Expression and Glycogen Storage during Fasting. *Cell Rep*, 2016. 14(8): p. 1867-75.
167. Lanz, R.B., et al., A steroid receptor coactivator, SRA, functions as an RNA and is present in an SRC-1 complex. *Cell*, 1999. 97(1): p. 17-27.
168. Xu, B., et al., Multiple roles for the non-coding RNA SRA in regulation of adipogenesis and insulin sensitivity. *PLoS One*, 2010. 5(12): p. e14199.
169. Liu, S., et al., SRA gene knockout protects against diet-induced obesity and improves glucose tolerance. *J Biol Chem*, 2014. 289(19): p. 13000-9.
170. Chen, G., et al., lncRNA SRA promotes hepatic steatosis through repressing the expression of adipose triglyceride lipase (ATGL). *Sci Rep*, 2016. 6: p. 35531.
171. Zhu, X., et al., Upregulation of lncRNA MEG3 promotes hepatic insulin resistance via increasing FoxO1 expression. *Biochem Biophys Res Commun*, 2016. 469(2): p. 319-25.
172. Yang, L., et al., Integrative Transcriptome Analyses of Metabolic Responses in Mice Define Pivotal lncRNA Metabolic Regulators. *Cell Metab*, 2016. 24(4): p. 627-639.
173. Cui, X., et al., The long non-coding RNA Gm10768 activates hepatic gluconeogenesis by sequestering microRNA-214 in mice. *J Biol Chem*, 2018. 293(11): p. 4097-4109.
174. Li, K., et al., MicroRNA-214 suppresses gluconeogenesis by targeting activating transcriptional factor 4. *J Biol Chem*, 2015. 290(13): p. 8185-95.

175. Jinek, M., et al., A programmable dual-RNA-guided DNA endonuclease in adaptive bacterial immunity. *Science*, 2012. 337(6096): p. 816-21.
176. Ran, F.A., et al., Genome engineering using the CRISPR-Cas9 system. *Nat Protoc*, 2013. 8(11): p. 2281-2308.
177. Yang, H., H. Wang, and R. Jaenisch, Generating genetically modified mice using CRISPR/Cas-mediated genome engineering. *Nat Protoc*, 2014. 9(8): p. 1956-68.
178. Doudna, J.A. and E. Charpentier, Genome editing. The new frontier of genome engineering with CRISPR-Cas9. *Science*, 2014. 346(6213): p. 1258096.
179. Briner, A.E., et al., Guide RNA functional modules direct Cas9 activity and orthogonality. *Mol Cell*, 2014. 56(2): p. 333-339.
180. Friedland, A.E., et al., Heritable genome editing in *C. elegans* via a CRISPR-Cas9 system. *Nat Methods*, 2013. 10(8): p. 741-3.
181. Bassett, A.R. and J.L. Liu, CRISPR/Cas9 and genome editing in *Drosophila*. *J Genet Genomics*, 2014. 41(1): p. 7-19.
182. Hwang, W.Y., et al., Efficient genome editing in zebrafish using a CRISPR-Cas system. *Nat Biotechnol*, 2013. 31(3): p. 227-9.
183. Yang, H., et al., One-step generation of mice carrying reporter and conditional alleles by CRISPR/Cas-mediated genome engineering. *Cell*, 2013. 154(6): p. 1370-9.
184. Rupaimoole, R. and F.J. Slack, MicroRNA therapeutics: towards a new era for the management of cancer and other diseases. *Nat Rev Drug Discov*, 2017. 16(3): p. 203-222.
185. Kurreck, J., RNA interference: from basic research to therapeutic applications. *Angew Chem Int Ed Engl*, 2009. 48(8): p. 1378-98.
186. Fischer, S.E., RNA Interference and MicroRNA-Mediated Silencing. *Curr Protoc Mol Biol*, 2015. 112: p. 26.1.1-5.
187. Lundin, K.E., O. Gissberg, and C.I. Smith, Oligonucleotide Therapies: The Past and the Present. *Hum Gene Ther*, 2015. 26(8): p. 475-85.
188. Burnett, J.C. and J.J. Rossi, RNA-based therapeutics: current progress and future prospects. *Chem Biol*, 2012. 19(1): p. 60-71.
189. Sanghvi, Y.S., A status update of modified oligonucleotides for chemotherapeutics applications. *Curr Protoc Nucleic Acid Chem*, 2011. Chapter 4: p. Unit 4.1.1-22.
190. Campbell, J.M., T.A. Bacon, and E. Wickstrom, Oligodeoxynucleoside phosphorothioate stability in subcellular extracts, culture media, sera and cerebrospinal fluid. *J Biochem Biophys Methods*, 1990. 20(3): p. 259-67.
191. Modarresi, F., et al., Inhibition of natural antisense transcripts in vivo results in gene-specific transcriptional upregulation. *Nat Biotechnol*, 2012. 30(5): p. 453-9.
192. Lundin, K.E., et al., Biological activity and biotechnological aspects of locked nucleic acids. *Adv Genet*, 2013. 82: p. 47-107.
193. Eissing, L., et al., De novo lipogenesis in human fat and liver is linked to ChREBP-beta and metabolic health. *Nat Commun*, 2013. 4: p. 1528.

194. Drost, H.G. and J. Paszkowski, *Biomart: genomic data retrieval with R*. Bioinformatics, 2017. 33(8): p. 1216-1217.
195. Langmead, B. and S.L. Salzberg, Fast gapped-read alignment with Bowtie 2. Nat Methods, 2012. 9(4): p. 357-9.
196. Wang, L., et al., CPAT: Coding-Potential Assessment Tool using an alignment-free logistic regression model. Nucleic Acids Res, 2013. 41(6): p. e74.
197. Kong, L., et al., CPC: assess the protein-coding potential of transcripts using sequence features and support vector machine. Nucleic Acids Res, 2007. 35(Web Server issue): p. W345-9.
198. Haeussler, M., et al., Evaluation of off-target and on-target scoring algorithms and integration into the guide RNA selection tool CRISPOR. Genome Biol, 2016. 17(1): p. 148.
199. Hsu, P.D., et al., DNA targeting specificity of RNA-guided Cas9 nucleases. Nat Biotechnol, 2013. 31(9): p. 827-32.
200. Trapnell, C., et al., Differential gene and transcript expression analysis of RNA-seq experiments with TopHat and Cufflinks. Nat Protoc, 2012. 7(3): p. 562-78.
201. Love, M.I., W. Huber, and S. Anders, Moderated estimation of fold change and dispersion for RNA-seq data with DESeq2. Genome Biol, 2014. 15(12): p. 550.
202. Kinsella, R.J., et al., Ensembl BioMart: a hub for data retrieval across taxonomic space. Database (Oxford), 2011. 2011: p. bar030.
203. Roehr, J.T., C. Dieterich, and K. Reinert, Flexbar 3.0 - SIMD and multicore parallelization. Bioinformatics, 2017. 33(18): p. 2941-2942.
204. Koressaar, T. and M. Remm, Enhancements and modifications of primer design program Primer3. Bioinformatics, 2007. 23(10): p. 1289-91.
205. Untergasser, A., et al., *Primer3--new capabilities and interfaces*. Nucleic Acids Res, 2012. 40(15): p. e115.
206. Wagle, P., M. Nikolic, and P. Frommolt, QuickNGS elevates Next-Generation Sequencing data analysis to a new level of automation. BMC Genomics, 2015. 16: p. 487.
207. Dobin, A., et al., STAR: ultrafast universal RNA-seq aligner. Bioinformatics, 2013. 29(1): p. 15-21.
208. Trapnell, C., L. Pachter, and S.L. Salzberg, *TopHat: discovering splice junctions with RNA-Seq*. Bioinformatics, 2009. 25(9): p. 1105-11.
209. Livak, K.J. and T.D. Schmittgen, Analysis of relative gene expression data using real-time quantitative PCR and the 2(-Delta Delta C(T)) Method. Methods, 2001. 25(4): p. 402-8.
210. Cashman, N.R., et al., Neuroblastoma x spinal cord (NSC) hybrid cell lines resemble developing motor neurons. Dev Dyn, 1992. 194(3): p. 209-21.
211. Durham, H.D., S. Dahrouge, and N.R. Cashman, Evaluation of the spinal cord neuron X neuroblastoma hybrid cell line NSC-34 as a model for neurotoxicity testing. Neurotoxicology, 1993. 14(4): p. 387-95.
212. Drexler, H.G. and C.C. Uphoff, Mycoplasma contamination of cell cultures: Incidence, sources, effects, detection, elimination, prevention. Cytotechnology, 2002. 39(2): p. 75-90.
213. Hummel, K.P., M.M. Dickie, and D.L. Coleman, *Diabetes, a new mutation in the mouse*. Science, 1966. 153(3740): p. 1127-8.

214. Robertson, D.M. and A.A. Sima, Diabetic neuropathy in the mutant mouse [C57BL/ks(db/db)]: a morphometric study. *Diabetes*, 1980. 29(1): p. 60-7.
215. Chen, H., et al., Evidence that the diabetes gene encodes the leptin receptor: identification of a mutation in the leptin receptor gene in db/db mice. *Cell*, 1996. 84(3): p. 491-5.
216. Truett, G.E., et al., *Misty (m) affects growth traits*. *Am J Physiol*, 1998. 275(1 Pt 2): p. R29-32.
217. Troder, S.E., et al., An optimized electroporation approach for efficient CRISPR/Cas9 genome editing in murine zygotes. *PLoS One*, 2018. 13(5): p. e0196891.
218. Moreno-Mateos, M.A., et al., CRISPRscan: designing highly efficient sgRNAs for CRISPR-Cas9 targeting in vivo. *Nat Methods*, 2015. 12(10): p. 982-8.
219. Yates, A., et al., *Ensembl 2016*. *Nucleic Acids Res*, 2016. 44(D1): p. D710-6.
220. Trapnell, C., et al., Transcript assembly and quantification by RNA-Seq reveals unannotated transcripts and isoform switching during cell differentiation. *Nat Biotechnol*, 2010. 28(5): p. 511-5.
221. Schmidt, E., et al., LincRNA H19 protects from dietary obesity by constraining expression of monoallelic genes in brown fat. *Nat Commun*, 2018. 9(1): p. 3622.
222. McIntyre, L.M., et al., RNA-seq: technical variability and sampling. *BMC Genomics*, 2011. 12: p. 293.
223. Nelson, B.R., et al., A peptide encoded by a transcript annotated as long noncoding RNA enhances SERCA activity in muscle. *Science*, 2016. 351(6270): p. 271-5.
224. Stein, C.S., et al., Mitoregulin: A lincRNA-Encoded Microprotein that Supports Mitochondrial Supercomplexes and Respiratory Efficiency. *Cell Rep*, 2018. 23(13): p. 3710-3720.e8.
225. Sims, R.J., 3rd, K. Nishioka, and D. Reinberg, Histone lysine methylation: a signature for chromatin function. *Trends Genet*, 2003. 19(11): p. 629-39.
226. Nishiyama, A., et al., Identification of thioredoxin-binding protein-2/vitamin D(3) up-regulated protein 1 as a negative regulator of thioredoxin function and expression. *J Biol Chem*, 1999. 274(31): p. 21645-50.
227. Chutkow, W.A., et al., Thioredoxin-interacting protein (Txnip) is a critical regulator of hepatic glucose production. *J Biol Chem*, 2008. 283(4): p. 2397-406.
228. Ferreira, N.E., et al., Thioredoxin interacting protein genetic variation is associated with diabetes and hypertension in the Brazilian general population. *Atherosclerosis*, 2012. 221(1): p. 131-6.
229. Brandl, C., et al., Creation of targeted genomic deletions using TALEN or CRISPR/Cas nuclease pairs in one-cell mouse embryos. *FEBS Open Bio*, 2015. 5: p. 26-35.
230. Fu, Y., et al., Improving CRISPR-Cas nuclease specificity using truncated guide RNAs. *Nat Biotechnol*, 2014. 32(3): p. 279-284.
231. Khamlichi, A.A. and R. Feil, Parallels between Mammalian Mechanisms of Monoallelic Gene Expression. *Trends Genet*, 2018.
232. El-Brolosy, M., et al., Genetic compensation is triggered by mutant mRNA degradation. *bioRxiv*, 2018.

233. Zucchelli, S., et al., SINEUPs: A new class of natural and synthetic antisense long non-coding RNAs that activate translation. *RNA Biol*, 2015. 12(8): p. 771-9.
234. Schein, A., et al., Identification of antisense long noncoding RNAs that function as SINEUPs in human cells. *Sci Rep*, 2016. 6: p. 33605.
235. Carrieri, C., et al., Long non-coding antisense RNA controls Uchl1 translation through an embedded SINEB2 repeat. *Nature*, 2012. 491(7424): p. 454-7.
236. Wang, S., et al., Long Non-Coding RNA CYP4B1-PS1-001 Inhibits Proliferation and Fibrosis in Diabetic Nephropathy by Interacting with Nucleolin. *Cell Physiol Biochem*, 2018. 49(6): p. 2174-2187.
237. Li, G.Y., et al., Long non-coding RNAs AC026904.1 and UCA1: a "one-two punch" for TGF-beta-induced SNAI2 activation and epithelial-mesenchymal transition in breast cancer. *Theranostics*, 2018. 8(10): p. 2846-2861.
238. Sharma, E., et al., Global Mapping of Human RNA-RNA Interactions. *Mol Cell*, 2016. 62(4): p. 618-26.

## 6.5. Acknowledgements

A study like this is impossible to be done by a single person, at least not within 4 years time, and thus I would like to express my deepest gratitude to all the people who helped with data analysis, animal handling, scientific troubleshooting or general discussions.

First of all, I want to thank Prof. Dr. Jan-Wilhelm Kornfeld, who supervised this project during the last 4 years and provided great help to bring it to a successful ending.

Moreover, I have to thank all the past and present members of the Kornfeld Lab, which made the Kornfeld Lab a very *special* place to work at. In particular, most cordial thanks go to - soon to be PhDs - Elena Schmidt and Sajjad Khani, who stayed with me in Cologne when the Kornfeld Lab moved to Odense, and not only contributed to intensive daily discussions during the last 10 months, but also helped with large-scale preparations of mouse cohorts. I wish you all the best for your next career steps !

Hugh thanks go to Dr. Paul Klemm, Prof. Dr. Peter Frommolt and Prof. Dr. Christoph Dieterich, who conducted the bioinformatic analyses of our RNA-Seq data sets and data integration.

Many thanks also go to Dr. Simon Tröder and Prof. Dr. Branko Zevnik, who provided the infrastructure for CRISPR/Cas9 gene targeting and supervised the pronuclear microinjections.

Furthermore, I thank the head of the animal facility, Dr. Karina Schöfisch, for constant support in questions of animal care and legal ordinance and Jens Alber for technical assistance with indirect calorimetry measurements. Additionally, I want to thank all members of the MPI-MR for providing such a prolific scientific environment and in particular Dr. Rachel Lippert for proofreading this thesis and my azizam Nasim Biglari for personal assistance in tough times.

With overflowing gratitude I want to thank my parents, who made it possible for me to follow my personal interests and go study, and thus ultimately paved the way to the work presented here. Infinite thanks also belongs to all my other family members and friends, especially Oliver Paßgang, Michael Petera and Larissa Klingel. Without your loyal support over the years, I would have never achieved anything in life and you were the force that made me survive the ordeal of performing a PhD study !

*I've seen the calloused, I know the jaded  
I've been disheartened, I've lost control  
But I never crumbled in the face of adversity*

Hatebreed - Hollow Ground (Perseverance, 2002)



## 6.6. Eidesstattliche Erklärung

Ich versichere, dass ich die von mir vorgelegte Dissertation selbstständig angefertigt, die benutzten Quellen und Hilfsmittel vollständig angegeben und die Stellen der Arbeit - einschließlich Tabellen, Karten und Abbildungen -, die anderen Werken im Wortlaut oder dem Sinn nach entnommen sind, in jedem Einzelfall als Entlehnung kenntlich gemacht habe; dass diese Dissertation noch keiner anderen Fakultät oder Universität zur Prüfung vorgelegen hat; dass sie - abgesehen von unten angegebenen Teilpublikationen - noch nicht veröffentlicht ist sowie, dass ich eine solche Veröffentlichung vor Abschluss des Promotionsverfahrens nicht vornehmen werde. Die Bestimmungen der Promotionsordnung sind mir bekannt. Die von mir vorgelegte Dissertation ist von Prof. Dr. Jan-Wilhelm Kornfeld betreut worden.

---

Köln, 01. Oktober 2018

Nils Rouven Hansmeier

## 6.7. Curriculum vitae

### Personal Information

Name: Nils Rouven Hansmeier      Address: Zur Goldbrede 43, 59269 Beckum  
Date of Birth: 18. 07. 1987      Email: [Nils.Hansmeier@sf.mpg.de](mailto:Nils.Hansmeier@sf.mpg.de)

### University Education

**Master of Science in Molecular Biomedicine**      Jan 2014  
Westphalian Wilhelm University of Münster, Münster, Germany  
Thesis Title: "Analysis of Molecular Mechanisms Active in the Early Morphogenesis during Murine Fetal Lymphangiogenesis"  
Cumulative GPA: 3.46/4.0 (excellent)

**Bachelor of Science in Biosciences**      Sep 2011  
Westphalian Wilhelm University of Münster, Münster, Germany  
Thesis Title: "Investigations of Apoptosis during Zebrafish Germ Cell Development"  
Cumulative GPA: 3.48/4.0 (excellent)

### Publications

Schmidt E, Dhaouadi I, Gaziano I, Oliverio M, Klemm P, Awazawa M, Mitterer G, Fernandez-Rebollo E, Pradas-Juni M, Wagner W, Hammerschmidt P, Loureiro R, Kiefer C, **Hansmeier N**, Khani S, Bergami M, Heine M, Ntini E, Frommolt P, Zentis P, Orom U, Heeren J, Blueher M, Bilban M, Kornfeld JW.  
LincRNA H19 Protects from Dietary Obesity by Constraining Expression of Monoallelic Genes in Brown Fat. **Nat Commun.** 2018, Sep 6; 9(1):3622. (doi: 10.1038/s41467-018-05933-8)

Oliverio M, Schmidt E, Mauer J, Beitel C, **Hansmeier N**, Khani S, Konietzka S, Pradas-Juni M, Brodesser S, Van TM, Bartsch D, Brönneke HS, Heine M, Hilpert H, Tarcitano E, Garinis GA, Frommolt P, Heeren J, Mori MA, Brüning JC, Kornfeld JW.  
Dicer1-miR-328-Bace1 Signalling Controls Brown Adipose Tissue Differentiation and Function. **Nat Cell Biol.** 2016 Mar; 18(3):328-36. (doi: 10.1038/ncb3316)

### Awards and Fellowships

**ISTT Registration Award** for 14th Transgenic Technology Meeting      Jul 2017  
International Society for Transgenic Technologies  
Competitive Selection Procedure for Student Members  
[www.transtechsociety.org](http://www.transtechsociety.org)

**3 Year PhD Fellowship**      Oct 2014  
Cologne Graduate School of Ageing Research  
Competitive Selection Procedure (12 out of 500+ applicants)  
[www.ageing-grad-school.de](http://www.ageing-grad-school.de)

### Scientific Permissions

Special Authorization for Animal Research      May 2017  
Liver Perfusion under Anesthetics  
Council for Environment and Consumer Protection - City of Cologne, Germany

**Course of Laboratory Animal Science**      Nov 2012  
Equal to FELASA-B Standards  
Central Animal Experimentation Facility, University Hospital Münster, Germany

### Professional Memberships and Activities

International Society for Transgenic Technologies      since Jan 2017  
National Health & Exercise Science Association      since Aug 2016